Contributions to the experimental investigation and numerical description of soil cyclic behavior

M.Sc. Jose Alejandro Duque Felfle

A dissertation submitted for the degree of Doctor of Philosophy

Supervisor: prof. RNDr. David Mašín, Ph.D.

Charles University, Faculty of Science
Institute of Hydrogeology, Engineering Geology and Applied Geophysics
Prague, 2021

Declaration

I hereby declare that the present thesis was prepared and elaborated on my own. The work presented in this thesis has not be submitted for the application of any different professional degree. In the case of jointly-authored publications, the proper credit was always explicitly indicated. All cited references and sources of information are listed at the end of this thesis.

In Prague, September 2021

Jose Alejandro Duque Felfle

Acknowledgements

First and foremost, I would like to thank my supervisor prof. RNDr. David Mašín, Ph.D., whose invaluable guidance, patience, support and motivation was indispensable during the course of my doctoral degree.

I would also like to thank professor William Fuentes, for his guidance and fruitful discussions during some stages of my doctoral research. Furthermore, I would like to express my sincere gratitude to professor Maciej Ochmański for several scientific discussions. I thank to my colleagues Marco Loche, Tomáš Kadlíček, Jakub Roháč, Jan Jerman and Gianvito Scaringi for making a friendly working environment during my doctoral studies.

Last but not least, I express my gratitude to my parents and brothers for their continuous support and motivation.

The present dissertation was supported by the Charles University Grant Agency (GAUK) with project number 200120 and the INTER-EXCELLENCE project LTACH19028 by the Czech Ministry of Education, Youth and Sports.

List of publications

During my doctoral studies, I worked on 7 research articles. Out of them, 6 as first author in which I made the main contributions. At the moment of the thesis submission, 3 of the articles are already published and the remaining ones are under review. The articles are summarized as follows:

- Duque, J., Ochmański, M., Mašín, D., Hong, Y., Wang, L. On the behavior of monopiles subjected to multiple episodes of cyclic loading and reconsolidation in cohesive soils. *Computers and Geotechnics* 134, 104049, 2021.
- Duque, J., Mašín, D., Fuentes, W. Improvement to the intergranular strain model for larger numbers of repetitive cycles. *Acta Geotechnica* 15, 3593–3604, 2020.
- Ochmański, M., Mašin, D., Duque, J., Hong, Y., Wang, L. Performance of tripod foundations for offshore wind turbines: a numerical study. *Géotechnique letters* 11(3), 1-9, 2021.
- Duque, J., Roháč, J., Mašín, D., Najser, J. Experimental investigation on Malaysian kaolin under monotonic and cyclic loading: inspection of undrained Miner's rule and drained cyclic preloading. *Submitted to Acta Geotechnica*, 2021.
- Duque, J., Roháč, J., Mašín, D., Najser, J., Opršal, J. Experimental investigation on Zbraslav sand under monotonic and cyclic loading: on the influence of cyclic preloadings. *Submitted to Acta Geotechnica*, 2021.
- Duque, J., Tafili, M., Seidalinov, G., Mašín, D., Fuentes, W. Inspection of four advanced constitutive models for fine-grained soils under monotonic and cyclic loading. *Submitted to Acta Geotechnica*, 2021.
- Duque, J., Fuentes, W., Yang, M., Mašín, D., Taiebat, M. Characteristic limitations of advanced plasticity and hypoplasticity models for cyclic loading of sands. *Submitted to Acta Geotechnica*, 2021.

Contents

List of Tables

List of Figures

Abstract

A wide range of geotechnical structures are subjected to episodes of cyclic loading. Among them, we can for example mention onshore and offshore foundations subjected to environmental loadings, pavements subjected to traffic loading, filling-emptying cycles on silos and water tanks, among many others. In order to develop constitutive models or numerical tools that accurately reproduce the soil behavior on the aforementioned geotechnical problems, a deep understanding on how soil behaves under cyclic loading is necessary. This behavior is, however, not trivial since non-linearity, small strain stiffness, stiffness degradation, cyclic hysteresis and recent stress history play a significant role.

This dissertation presents some contributions to the experimental evidence and numerical description of soil cyclic behavior. It begins with comprehensive experimental databases on Malaysian kaolin and Zbraslav sand. In each database, several monotonic and cyclic tests were performed and analyzed considering a wide range of initial conditions and loading characteristics. In particular, the influence of the deviatoric stress amplitude, soil plasticity, initial stress ratio, drained cyclic preloading and sequence of packages of cycles with different deviatoric stress amplitudes was investigated on Malaysian kaolin. On Zbraslav sand, the influence of the deviatoric stress amplitude and different types of drained or undrained cyclic preloadings was investigated. The experimental databases will be freely available at the soilmodels.com website [89].

The thesis further presents a detailed analysis and comparison of the prediction capabilities, advantages and limitations of some of the most well-known and advanced constitutive models for cyclic loading on fine-grained soils: Anamnesis, anisotropic hypoplasticity with ISA, SANICLAY-B and three surface kinematic hardening model. Subsequently, the characteristic limitations of four advanced constitutive models for coarse-grained soils: hypoplasticity with intergranular strain, hypoplasticity with ISA, SANISAND and SANISAND-MSf are detailed and discussed. The aforementioned works remark the main components of the models that require improvements and provide discussion and analysis of them, which are of great value both for practical applications (to know under which conditions the models predict reliable results) and for future developments. The results suggest a huge success in the reproduction of monotonic loading but several issues in many simulations under cyclic loading. Among them, poor prediction capabilities when the model simulates conditions different to the ones in which it was calibrated, overshooting effects, improper accumulation of plastic strains, spoiled dilatancy-contractancy characteristics, or in general, poorly reproduced stiffness.

An improved version of the intergranular strain model by Niemunis and Herle [170] is further presented. It presents improved capabilities in the prediction of strains and/or pore water pressure accumulation under cyclic loading. Finally, two case studies consisting of a monopile and a tripod subjected to multiple episodes of cyclic loading were simulated. The analyses focus on their deformation mechanism and the capabilities of the considered constitutive models to reproduce the centrifuge results.

Chapter 1

Introduction

This dissertation corresponds to a cumulative (collection of articles) thesis. The research articles presented in this thesis have been funded by the Czech-China bilateral project LTACH19028 Inter-Excellence (Inter-Action) entitled "*Failure mechanism and hazard mitigation of wind turbine structure subjected to extreme environmental loadings*". Therefore, the outcome of this thesis followed from my research performed on the project. The document was organized to follow a logical (not chronological) structure. Experimental results have thus been introduced first, followed by constitutive modelling and concluded by numerical simulations of boundary value problems.

1.1 Outline and contributions

Chapter 2 presents the article entitled "*Experimental investigation on Malaysian kaolin under monotonic and cyclic loading: inspection of undrained Miner's rule and drained cyclic preloading*". This article presents a comprehensive experimental database on a high-plasticity kaolin. The influence of the deviatoric stress amplitude, soil plasticity, initial stress ratio, drained cyclic preloading and sequence of packages of cycles with different deviatoric stress amplitudes in the undrained cyclic resistance of the material was investigated. I have set the experimental plan, performed the kaolin characterization, executed the cyclic experiments, processed and analyzed the experimental results and prepared the first draft of the manuscript; Dr. Jakub Roháč performed the monotonic triaxial tests and provided technical assistance in the laboratory; Dr. David Mašín and Dr. Jan Najser provided technical discussions about the experimental results and assistance in revising the manuscript; Dr. David Mašín came up with the idea of the modified Stewart's approach method. This article was submitted for publication in the journal *Acta Geotechnica*.

An experimental database under monotonic and cyclic loading on Zbraslav sand is presented in Chapter 3. This chapter corresponds to the article entitled "*Experimental investigation on Zbraslav sand under monotonic and cyclic loading: on the influence of cyclic preloadings*". In this article, multiple monotonic and cyclic triaxial tests were performed on Zbraslav sand. Special attention was given to undrained cyclic triaxial tests with and without drained/undrained cyclic preloadings. The undrained cyclic resistance was quantified depending of the amount of the drained/undrained cyclic preloadings. I have set the experimental plan, performed the sand characterization, executed the cyclic experiments, processed and analyzed the experimental results and prepared the first draft of the manuscript; Dr. Jakub Roháč prepared and saturated the sand samples for the cyclic tests; Mr. Jakub Opršal performed the monotonic triaxial tests; Dr. David Mašín and Dr. Jan Najser provided technical discussions about the experimental results and assistance in revising the manuscript. This article was submitted for publication in the journal

Acta Geotechnica.

Chapter 4 presents the article entitled "*Inspection of four advanced constitutive models for fine-grained soils under monotonic and cyclic loading*", in which several monotonic and cyclic triaxial tests were analyzed and simulated with four advanced constitutive models for anisotropic fine-grained soils, developed under different mathematical frameworks: the anisotropic hypoplastic model (AHP+ISA) proposed by Fuentes et al. [71], the SANICLAY-B elasto-plastic model by Seidalinov and Taiebat [203], the Anamnesis (CAM) model by Tafili [230] and the three surface kinematic hardening model proposed by Stallebrass and Taylor [219] with transverse isotropic elasticity (A3-SKH). This article remarks the main advantages and limitations of different advanced constitutive models for fine-grained soils under monotonic and cyclic conditions. Therefore, it gives hints to end-users to in which boundary conditions the models are reliable. Furthermore, it provides discussions about the model components responsible for the reproduction of some experimental observations that are accounted for or missing. I planned the article, performed the calibration using element test simulations with the AHP+ISA and A3-SKH models, processed and edited the graphs of all experiments and simulations, and prepared the first draft of the manuscript. Dr. Merita Tafili and Dr. Gaziz Seidalinov provided technical discussions about the results and the element test simulations with the Anamnesis and SANICLAY-B models, respectively. Dr. Merita Tafili, Dr. Gaziz Seidalinov, Dr. David Mašín and Dr. William Fuentes provided valuable discussions about the results and technical assistance in revising the manuscript. This article was submitted for publication in the journal *Acta Geotechnica*.

The article entitled "*Characteristic limitations of advanced plasticity and hypoplasticity models for cyclic loading of sands*" is presented in chapter 5. It presents a comprehensive investigation about the characteristic limitations of two advanced hypoplastic and two advanced elasto-plastic constitutive models for granular soils. The results of this article remarks some important issues of the constitutive models which should be addressed. In addition, it remarks to end-users the main conditions in which each model are not reliable. I and Dr. William Fuentes planned the article. I performed the element test simulations with the two hypoplastic and the SANISAND constitutive models. Furthermore, I prepared the first draft of the manuscript. Dr. Ming Yang re-calibrated the SANISAND model and provided simulations with the SANISAND-MSf constitutive model. Dr. David Mašín, Dr. William Fuentes and Dr. Mahdi Taiebat provided valuable discussions about the results and technical assistance in revising the manuscript. This article was submitted for publication in the journal *Acta Geotechnica*.

Chapter 6 presents the article entitled "*Improvement to the intergranular strain model for larger numbers of repetitive cycles*". It corresponds to an improved version of the intergranular strain model by Niemunis and Herle [170], while considering the extension by Wegener and Herle [260]. The proposed improved model predicted with more accuracy the accumulation of pore water pressure in undrained cyclic triaxial tests and accumulated strains in drained cyclic triaxial tests than the former versions. I and Dr. David Mašín planned the article. I and Dr. William Fuentes performed the element test simulations. I prepared the first draft of the manuscript. Dr. David Mašín and Dr. William Fuentes provided technical assistance in proposing the form of the new equations, results interpretation and revising the manuscript. This article was published in the journal *Acta Geotechnica* [50].

Numerical results of back-calculation of some centrifuge tests are presented in Chapter 7. The analysis involve monopiles subjected to intermittent episodes of cyclic loading and reconsolidation. It corresponds to the article entitled "*On the behavior of monopiles subjected to multiple episodes of cyclic loading and reconsolidation in cohesive soils*". In this article, an advanced hypoplastic constitutive model for clays was firstly calibrated based on undrained monotonic and cyclic triaxial tests. Then, the model was used to back-calculate the centrifuge tests. The simulation results suggest that the constitutive model was able to accurately reproduce the accumulation rates under cyclic loading. However, it was not able to reproduce the stiffness recovery after each subsequent reconsolidation episode. I and Dr. Maciej

Ochmański performed the simulations. I performed the analysis of the results, edited the graphs and prepared the first draft of the manuscript. Dr. David Mašín provided valuable discussions about the results and technical assistance in revising the manuscript. Dr. Yi Hong and Dr. Lizhong Wang provided the results of the centrifuge tests. This article was published in the journal *Computers and Geotechnics* [172].

Chapter 8 presents the article entitled "*Performance of tripod foundations for offshore wind turbines: a numerical study*". It shows numerical simulations of a suction bucket foundation for offshore wind turbines. Special attention was given to the so-called "healing effect" observed after many loading cycles. A comparison between centrifuge tests and numerical back-calculations was as well included. Dr. Maciej Ochmański and Dr. David Mašín planned the article; Dr. Maciej Ochmański performed the simulations. I provided technical assistance in the constitutive model calibration and results interpretation. Dr. Yi Hong and Dr. Lizhong Wang provided the results of the centrifuge tests. This article was published in the journal *Géotechnique letters* [52].

Chapters 9 and 10 conclude the dissertation by remarking the main conclusions of the work and an outlook on possible further works.

1.2 Notation and relevant variables

Scalar magnitudes are denoted by italic fonts (e.g. a, b), vectors with bold lowercase fonts (e.g. $\mathbf{a}, \mathbf{b}$), second-rank tensors with bold capital letter or bold symbols (e.g. $\mathbf{A}$, $\mathbf{B}$), higher ranked tensors with special fonts (e.g. E, L). Components of these tensors are denoted through indicial notation (e.g. A_{ij}). δ_{ij} is the Kronecker delta, also represented with ($1_{ij} = \delta_{ij}$). The unit fourth-rank tensor for symmetric tensors is denoted by I, where $\mathsf{I}_{ijkl} = \frac{1}{2}\left(\delta_{ik}\delta_{jl} + \delta_{il}\delta_{jk}\right)$. The following operations hold: $\mathbf{A} : \mathbf{B} = A_{ij}B_{ij}$, $\mathbf{A} \otimes \mathbf{B} = A_{ij}B_{kl}$, $\| \mathbf{A} \| = \sqrt{A_{ij}A_{ij}}$, $\overrightarrow{\square} = \frac{\square}{\|\square\|}$, $\mathbf{A}^{\text{dev}} = \mathbf{A} - \frac{1}{3}(\text{tr}\mathbf{A})\mathbf{1}$, $\hat{\mathbf{A}} = \frac{\mathbf{A}}{\text{tr}(\mathbf{A})}$. Roscoe's variables are defined as $p = \text{tr}(\boldsymbol{\sigma})/3$, $q = \sqrt{\frac{3}{2}} \| \boldsymbol{\sigma}^{\text{dev}} \|$, $\varepsilon_v = \text{tr}(\boldsymbol{\varepsilon})$ and $\varepsilon_s = \sqrt{\frac{2}{3}} \| \boldsymbol{\varepsilon}^{\text{dev}} \|$. Under triaxial conditions, Roscoe's invariants are defined as $p = (\sigma_a + 2\sigma_r)/3$, $q = (\sigma_a - \sigma_r)$ and $\varepsilon_v = (\varepsilon_a + 2\varepsilon_r)$, $\varepsilon_q = 2(\varepsilon_a - \varepsilon_r)/3$. The subscripts a and r denote the axial and radial directions, respectively. The isometric stresses are defined as $P = \sqrt{3}p$ and $Q = \sqrt{2/3}q$. The stress ratio η is defined as $\eta = q/p$.

Chapter 2

Experimental database on Malaysian kaolin under monotonic and cyclic loading - Article 1

Summary of the article

This article presents a comprehensive experimental database on a high-plasticity Malaysian kaolin. The material was prepared from a kaolin dry powder in the so-called reconstituted state defined by Burland [26]. Initially, a detailed characterization of the material is presented. It includes the liquid limit, plastic limit, grain size distribution, mineralogical composition and microstructure of the kaolin. Subsequently, the procedure for the samples preparation and the method to verify the homogeneity of pre-consolidated samples for triaxial tests are described.

The mechanical behavior of the kaolin at large strain was analyzed by means of undrained monotonic triaxial tests with different initial mean effective pressures and overconsolidation ratios. The results on normally consolidated samples show a contractive behavior and a clear critical state line. In addition, the monotonic results show strain softening after $\varepsilon_1 \approx 15\%$, which is probably related with the development of shear bands and strain localization at large deformations. Furthermore, the results suggest a more dilative response and higher undrained shear strengths with increasing overconsolidation ratio. An oedometric compression test with multiple unloading-reloading cycles was also included to analyze the compressibility of the material.

The next part of the article focuses on the undrained cyclic response of the kaolin under a wide range of initial conditions. Firstly, undrained cyclic triaxial tests with variation of the deviatoric stress amplitude were performed. The results suggest that increasing the deviatoric stress amplitude remarkably reduces the number of cycles to reach the failure criterion $|\varepsilon_1| = 10\%$. A comparison analysis of the obtained results with experimental data from the literature on samples with different plasticity index was also included. It suggests that with all other conditions remaining the same, an increase in soil plasticity leads to a remarkable increment in the number of cycles to reach failure conditions. Subsequently, undrained cyclic triaxial tests on samples with anisotropic initial states were performed and analyzed. The results suggest that increasing the initial stress ratio of the tests leads to a reduction in the number of cycles to reach the failure criterion.

Undrained cyclic triaxial tests with packages of cycles in distinct sequences were performed to inspect the validity of Miner's rule under undrained cyclic conditions. The results suggest that under undrained

cyclic conditions, the sequence of the loading applications does matter. A modified Stewart's approach was proposed for the estimation of accumulated strains and pore water pressure on tests with packages of cycles in different sequences based on single-amplitude tests. Finally, undrained cyclic triaxial tests with drained cyclic preloadings were included and analyzed. The results suggest that the application of a drained preloading remarkably increases the undrained cyclic resistance of the material.

Experimental investigation on Malaysian kaolin under monotonic and cyclic loading: inspection of undrained Miner's rule and drained cyclic preloading

Duque, J.[1], Roháč, J.[1], Mašín, D.[1], Najser, J.[1]

[1]Charles University, Prague, Czech Republic

Abstract

The results of an experimental investigation on Malaysian kaolin under monotonic and cyclic loading are presented. In the tests, a wide range of initial conditions was varied in order to investigate their influence on the mechanical behavior of the kaolin. The response under monotonic loading was analyzed by means of undrained monotonic triaxial tests with different initial mean effective pressures and overconsolidation ratios. The experimental plan under cyclic loading includes an oedometer test with multiple unloading-reloading cycles and twenty one undrained cyclic triaxial tests with either isotropic or anisotropic consolidation. In the latter tests, the influence of the initial stress ratio, deviator stress amplitude, drained cyclic preloading and sequence of packages of cycles with different deviator stress amplitudes has been investigated. The experimental results suggest that the variation of the aforementioned test conditions leads to remarkable changes in the accumulation rates of pore water pressure and strains. In addition, it was found that the so-called Miner's rule (independence of accumulated strains on loading sequence) is not valid under undrained cyclic conditions. A modified Stewart's approach was proposed for the estimation of the accumulated pore water pressure and strains on undrained cyclic tests with packages of cycles with different deviator stress amplitudes, demonstrating that constitutive models developed using single-magnitude loading packages can be used in simulations of problems with variable cyclic loading magnitude.

2.1 Introduction

Many geotechnical structures founded on water-saturated fine-grained soils, such as offshore foundations, are subjected to complex cyclic loading scenarios [71, 97, 221, 263]. Reliable predictions of their behavior require robust constitutive models for soils, able to accurately reproduce its main features under a wide range of loading types and initial conditions [50, 153, 230]. For the development, improvement and calibration of constitutive models for fine-grained soils, different experimental databases on soils with different characteristics (e.g. plasticity, structure, mineralogical composition, among others) are necessary. Such databases should include a wide range of initial conditions on samples subjected to monotonic and cyclic loading. This study summarizes a comprehensive experimental investigation on a high-plasticity Malaysian kaolin, which has been widely implemented in many geotechnical model tests (e.g. [96, 110, 126, 281, 295]) and is the standard fine-grained soil used in many geotechnical centrifuge facilities.

The so-called Miner's rule [155], which states that the application of packages of cycles of different magnitudes in different sequences does not affect the final accumulation of strains, has been widely validated on sands subjected to drained cyclic loading on experimental tests e.g. [12, 119, 139, 222, 267, 270] and it has also been predicted by various numerical models e.g. [221, 263, 270]. However, the recent work by Staubach and Wichtmann [221] showed through numerical simulations with the High Cycle Accumulation Model by Niemunis et al. [171], that Miner's rule is not valid under not fully drained conditions, and that experimental corroboration of these numerical results is necessary. For that reason, some undrained cyclic triaxial tests with packages of cycles in distinct sequences were performed to inspect the validity of

Miner's rule under undrained cyclic conditions.

In order to evaluate the behavior of the kaolin at different strain ranges, distinct types of tests were performed under monotonic and cyclic loading. Initially, undrained monotonic triaxial tests were performed considering different initial mean effective pressures and overconsolidation ratios for the characterization of the behavior at large deformations. The experimental plan under cyclic loading includes an oedometric compression test with multiple unloading-reloading episodes and twenty one undrained cyclic triaxial tests on samples with either isotropic or anisotropic consolidation. In the cyclic triaxial tests, the influence of the initial stress ratio, deviator stress amplitude, drained cyclic preloading and sequence of packages of cycles with different deviator stress amplitudes was investigated.

The structure of the article is as follows: first, the main characteristics of the kaolin and the samples preparation procedure is described. Then, the results of the undrained monotonic triaxial tests are presented and discussed. Subsequently, the results of the oedometer and undrained cyclic triaxial tests are given and analyzed. At the end, the main findings of the experimental results are remarked. The experimental database presented in this study will be freely available at the soilmodels.com website [89], and it is expected to be used for the development, improvement and calibration of constitutive models for fine-grained soils.

2.2 Material description and samples preparation

This section describes the main characteristics of the Malaysian kaolin adopted in the experiments. It was purchased as a dry powder from the company "Kaolin (Malaysia) SDN BHD" and presents a specific gravity $G_s = 2.71$, a liquid limit $LL = 65\%$, a plastic limit $PL = 40\%$, and therefore a plasticity index $PI = LL - PL = 25\%$. According to the position of the kaolin in the Casagrande plasticity diagram, it is classified as a silt with high plasticity (MH), see Figure 2.1a. The grain size distribution of the kaolin was obtained from sieve and sedimentation analysis and it is composed by fine-sand (2%), silt (70%) and clay (28%) particles, see Figure 2.1b. In terms of mineralogy, the kaolin is composed of quartz (5.5%), muscovite (48%), kaolinite (46%) and rutile (0.5%), see Figure 2.2. The microstructure of the kaolin is formed by plate-like microaggregates, see Figure 2.3.

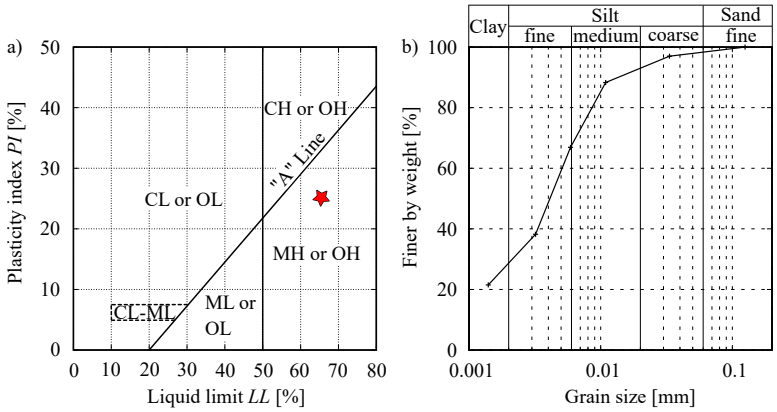

Figure 2.1: Characterization of the Malaysian kaolin: a) position in the Casagrande plasticity diagram, b) grain size distribution

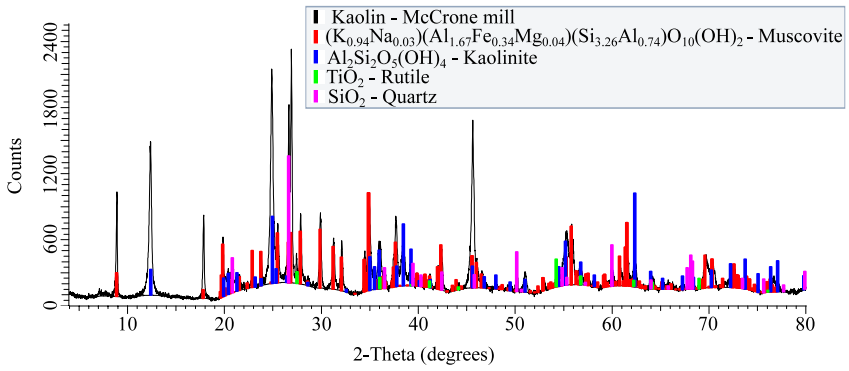

Figure 2.2: X-ray diffraction results

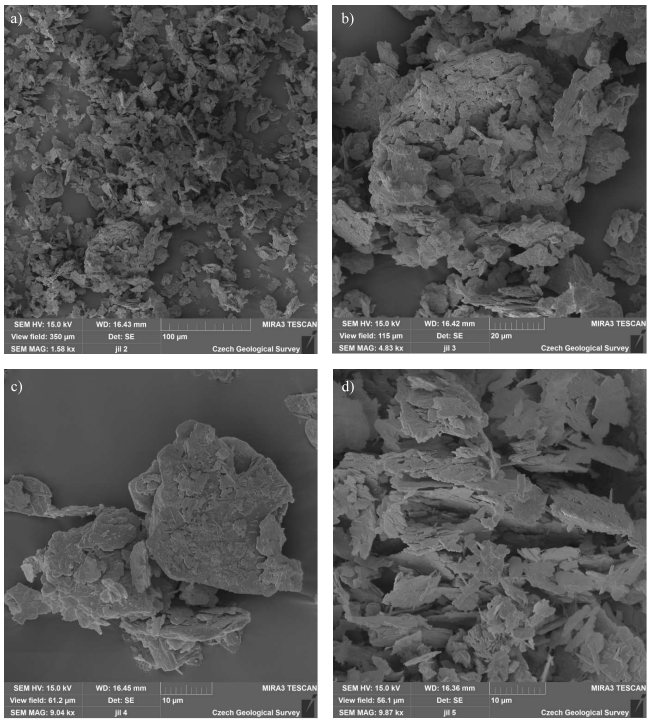

Figure 2.3: Scanning Electron Microscope (SEM) results

All samples were prepared by mixing the kaolin dry powder with distilled water having an initial water content of $w_i = 1.8LL$. The slurry was then deposited in a plexiglas cylinder with diameter $d = 50$ mm. Subsequently, it was pre-consolidated by gradually increasing the axial stress until a maximum value of 100 kPa. Some preliminary samples were used to test the homogenization of the pre-consolidated samples ($h \approx 150$ mm), following the procedure described by Wichtmann and Triantafyllidis [275]. For that purpose, samples were cut out in five layers, and in each one, multiple measurements of the water content were performed. The results suggest that the water contents in the pre-consolidated samples were fairly homogeneous, see Figure 2.4. After the pre-consolidation, samples were cut out with a height $h = 100$ mm (a high-to-diameter ratio of $h/d = 2$) and mounted into the triaxial device. Samples were sandwiched with porous stones and filter papers. All samples were water-saturated with a back pressure of 500 kPa, which always provided Skempton's B-coefficient greater than 0.98. All triaxial tests were performed at a controlled temperature of 20° C.

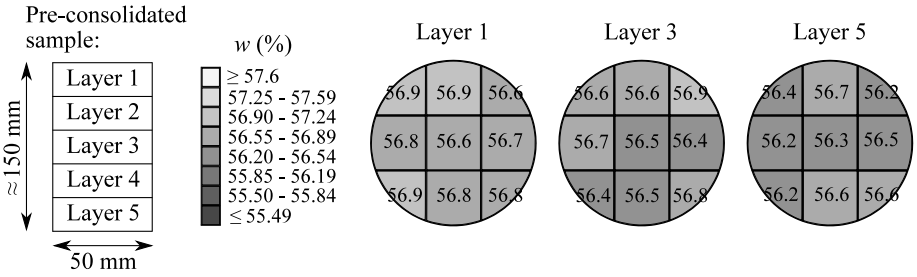

Figure 2.4: Variation of the water content in pre-consolidated samples for triaxial tests

2.3 Tests with monotonic loading

The testing program under monotonic loading is summarized in Table 2.1. The table includes the main characteristics and initial conditions of each test, such as test name, test type, initial mean effective pressure $p_0 = (\sigma'_a + 2\sigma'_r)/3$, initial deviator stress $q_0 = (\sigma'_a - \sigma'_r)$, initial overconsolidation ratio $\mathrm{OCR}_0 = p_{\max}/p_0$, initial void ratio e_0 measured at the consolidation mean effective pressure, before the shearing stage and displacement rate ν.

Table 2.1: Tests with monotonic loading

Test name	Test type	p_0 [kPa]	q_0 [kPa]	OCR_0 [-]	e_0 [-]	ν [mm/min]
UMT1	UMT	100	0	1	1.475	0.016
UMT2	UMT	200	0	1	1.385	0.016
UMT3	UMT	300	0	1	1.299	0.016
UMT4	UMT	400	0	1	1.216	0.016
UMT5	UMT	200	0	3	1.228	0.016
UMT6	UMT	200	0	5	1.170	0.016

Four undrained monotonic triaxial tests (UMT) were initially performed on normally consolidated samples with isotropic consolidation ($q_0 = 0$ kPa) and variation of the initial mean effective pressure $p_0 = \{100, 200, 300, 400\}$ kPa. The results of these tests suggest a contractive behavior, see Figure 2.5a. In addition, the results show a clear critical state line (CSL) in the $q - p$ space, calculated following the relations by the Mohr-Coulomb criterion $M_c = 6\,\mathrm{sin}\varphi_c/(3 - \mathrm{sin}\varphi_c)$, with $\varphi_c = 23.5°$. Figure 2.5b presents the stress-strain space where a significant increase of the undrained shear strength with increasing initial mean effective pressure is observed. The results also show strain softening after $\varepsilon_1 \approx 15\%$, which is probably related with the development of shear bands and strain localization at large deformations.

In order to evaluate the influence of the initial overconsolidation ratio, two additional tests were performed on isotropically consolidated samples ($p_0 = 200$ kPa, $q_0 = 0$ kPa) and $\mathrm{OCR}_0 = \{3, 5\}$. To achieve the desired initial overconsolidation ratio, samples were isotropically preloaded under drained conditions to $p_{\max} = 600$ and 1000 kPa. Then, a drained isotropic unloading till $p_0 = 200$ kPa was performed, resulting in the desired initial overconsolidation ratios. The effective stress paths are presented in Figure 2.6a and suggest that an increase in the initial overconsolidation ratio produce a more dilative response and higher undrained shear strengths. In addition, the results on overconsolidated samples also follows the critical state line obtained from tests on normally consolidated samples, although large peak friction angle is observed on sample with highest preconsolidation. Strain softening was also observed after $\varepsilon_1 \approx 15\%$, see Figure 2.6b. The results obtained on normally and overconsolidated samples are in good agreement with

previous experimental studies on fine-grained soils [65, 178, 206, 210, 230, 237, 263].

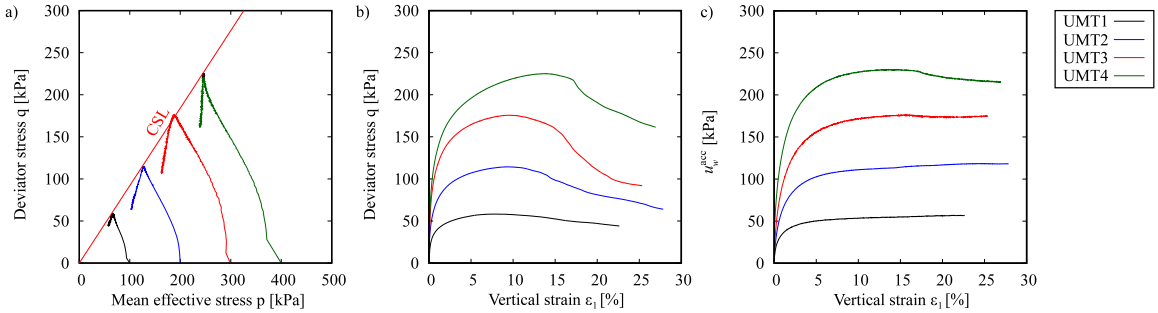

Figure 2.5: Undrained monotonic triaxial tests UMT1-UMT4 on normally consolidated samples with isotropic consolidation ($q_0 = 0$ kPa) and variation of the initial mean effective pressure $p_0 = \{100, 200, 300, 400\}$ kPa

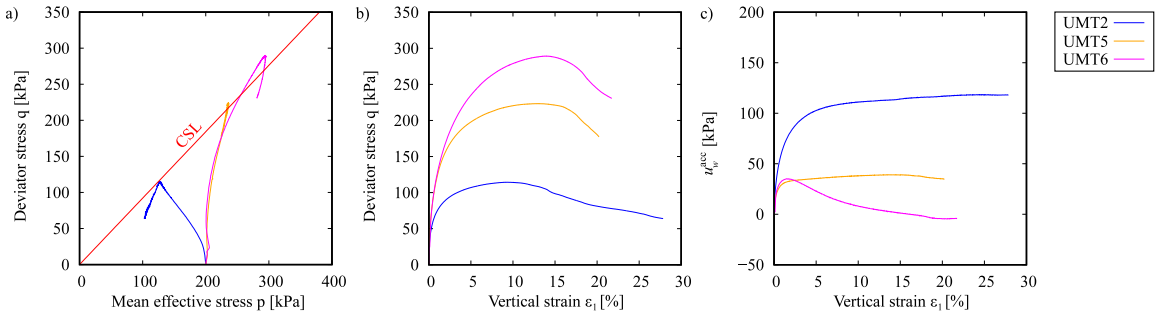

Figure 2.6: Undrained monotonic triaxial tests UMT2,UMT5,UMT6 on samples with isotropic consolidation ($p_0 = 200$ kPa, $q_0 = 0$ kPa) and variation of the initial overconsolidation ratio $\mathrm{OCR}_0 = \{1, 3, 5\}$

2.4 Tests with cyclic loading

The testing program under cyclic loading is summarized in Table 2.2. Initially, a stress-controlled oedometric compression test (OED) with multiple unloading-reloading cycles was performed in order to investigate the compressibility of the kaolin. In this test, the kaolin slurry was directly placed in the oedometer ring without any pre-consolidation. The oedometer test started with an initial void ratio $e_0 = 2.106$ and an axial stress $\sigma_1 = 2.5$ kPa. The loading/reloading paths increases the axial stress to: a) $\sigma_1 = 120$ kPa, b) $\sigma_1 = 400$ kPa, c) $\sigma_1 = 800$ kPa and d) $\sigma_1 = 1600$ kPa. All unloading paths reached always $\sigma_1 = 2.5$ kPa. The oedometric results are presented in Figure 2.7 and show a hysterethic behavior at each unloading-reloading cycle, which differs from typical results observed in loose granular soils, where almost linear behavior is observed during the unloading-reloading paths e.g. [63, 262, 263, 274].

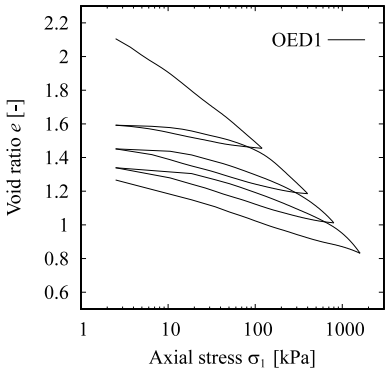

Figure 2.7: Oedometric compression test OED1 with multiple unloading-reloading cycles, $e - \sigma_1$ space

Twenty one undrained cyclic triaxial tests (UCT) were performed with either isotropic ($\eta_0 = q_0/p_0 = 0$) or anisotropic ($\eta_0 \neq 0$) consolidation and considering variation of the deviator stress amplitude $q^{\text{amp}} = (q^{\max} - q^{\min})/2$, drained cyclic preloading and sequence of packages of cycles with distinct deviator stress amplitudes. All undrained cyclic triaxial tests were performed with a loading frequency of 0.1 Hz, typical of offshore conditions [131, 215, 254, 297]. The cyclic tests were stopped when the failure criterion, hereafter defined as $|\varepsilon_1| = 10\%$, or equivalently, a shear strain of $|\gamma| = 15\%$ was reached.

2.4.1 UCT with isotropic consolidation and variation of the deviator stress amplitude

Seven undrained cyclic triaxial tests UCT1-UCT7 were performed on normally consolidated samples with isotropic consolidation ($p_0 = 200$ kPa, $q_0 = 0$ kPa, $\eta_0 = 0$) and variation of the deviator stress amplitude 30 kPa $\leq q^{\text{amp}} \leq$ 80 kPa. Their initial total and effective stresses are schematically presented in Figure 2.8. A typical result on test UCT4 with deviator stress amplitude of $q^{\text{amp}} = 50$ kPa is given in Figure 2.9. The results suggest that the liquefaction state ($p = q = 0$) was not reached with the kaolin, see Figure 2.9a. In addition, the kaolin does not exhibit eight-shaped effective stress paths in the final phase of tests with isotropic consolidation, which are usually observed on fine-grained soils with low plasticity [22, 237, 263, 275] but "erased" with increasing plasticity [21, 105]. The material does not show any significant inclination of the effective stress paths, which is related with an almost negligible inherent anisotropy [234–236]. The relaxation of the mean effective stress, or equivalently, the excess pore water pressure accumulation u_w^{acc}, presents three very different accumulation rates, see Figure 2.9b. At the beginning of the test, a high rate of pore water pressure accumulation is observed (stage "A"). Then, the accumulation rate decreases and gets almost constant during stage "B". Finally, at the end of the test, the accumulation rate increases again during stage "C". The stress-strain behavior is analyzed in the $q - \varepsilon_1$ space in Figure 2.9c. The results suggest that the vertical strains accumulate at a very small

Table 2.2: Tests with cyclic loading

Test name	Test type	p_0 [kPa]	q_0 [kPa]	η_0 [-]	q^{amp} [kPa]	CSR [-]	OCR_0 [-]	e_0 [-]	N_f [-]
OED1	OED	-	-	-	-	-	-	2.106	-
UCT1	UCT	200	0	0	30	0.075	1.00	1.327	>>25000
UCT2	UCT	200	0	0	40	0.100	1.00	1.334	4700
UCT3	UCT	200	0	0	45	0.113	1.00	1.338	416
UCT4	UCT	200	0	0	50	0.125	1.00	1.340	343
UCT5	UCT	200	0	0	60	0.150	1.00	1.311	36
UCT6	UCT	200	0	0	70	0.175	1.00	1.342	12
UCT7	UCT	200	0	0	80	0.200	1.00	1.312	6
UCT8	UCT	220	60	0.27	20	0.045	1.00	1.323	>>8000
UCT9	UCT	220	60	0.27	30	0.068	1.00	1.314	5376
UCT10	UCT	220	60	0.27	40	0.091	1.00	1.361	147
UCT11	UCT	220	60	0.27	60	0.136	1.00	1.339	14
UCT12†	UCT	200	0	0	40-45-50	-	1.00	1.344	300
UCT13†	UCT	200	0	0	45-40-50	-	1.00	1.353	300
UCT14†	UCT	200	0	0	50-45-40	-	1.00	1.336	300
UCT15†	UCT	220	60	0.27	20-30-40	-	1.00	1.366	300
UCT16†	UCT	220	60	0.27	30-20-40	-	1.00	1.340	300
UCT17†	UCT	220	60	0.27	40-30-20	-	1.00	1.348	300
UCT18†	UCT	135	60	0.44	40	0.148	1.79	1.314	100
UCT19‡	UCT	200	0	0	40	0.100	1.00	1.332/1.312	12916
UCT20‡	UCT	200	0	0	60	0.150	1.00	1.311/1.291	296
UCT21‡	UCT	200	0	0	80	0.200	1.00	1.346/1.280	21

† These tests did not reach the failure criterion and 100 cycles were performed at each deviator stress amplitude, ‡ Drained cyclic preloading

rate until reaching the stage "C" (see Figure 2.9b), in which the double strain amplitude grows quickly with each subsequent cycle until reaching the defined failure criterion, see Figure 2.9d. The results also suggest that the vertical strain accumulation is higher in the extension side than in the compression side.

The detailed results of undrained cyclic triaxial tests UCT1-UCT7 are presented in Figures 2.10 and 2.11, and are summarized in Figure 2.12. They suggest a remarkable increase in the accumulation rate of vertical strains and pore water pressures with increasing deviator stress amplitudes. For example, while 25000 cycles were not enough to get close to failure conditions on test UCT1 with $q^{amp} = 30$ kPa, only 6 cycles were required to reach failure conditions on test UCT7 with $q^{amp} = 80$ kPa. In addition, smallest deviator stress amplitudes leads to higher final magnitudes of the normalized accumulated pore water pressure u_w^{acc}/p_0, see Figure 2.12a. In some tests, a reduction of the deviator stress amplitude at large strains occurred as a consequence of apparatus load controller procedure. The analysis of the cyclic stress ratio $CSR = q^{amp}/(2p_0)$ against the number of cycles to reach the failure criterion N_f is presented in Figure 2.12c. The results suggest a remarkable reduction in N_f with increasing CSR. The previous behavior was well described ($R^2 = 0.96$) by a potential function in the form $CSR = aN_f^b$, with $a = 0.227$ and $b = -0.104$. Finally, the degradation of the secant Young's modulus $E = q^{amp}/\varepsilon_1^{amp}$ in the cycles $N = 2 - 5$ is presented in Figure 2.12d. The results of tests UCT8-UCT11 with anisotropic consolidation and variation of the deviator stress amplitude, were borrowed from the next section and also included in the aforementioned figure. The experiments suggest a significant reduction of the secant Young's modulus E with increasing vertical strain amplitude ε_1^{amp}. The observed behavior on undrained cyclic triaxial tests with isotropic consolidation is in good agreement with previous experimental results

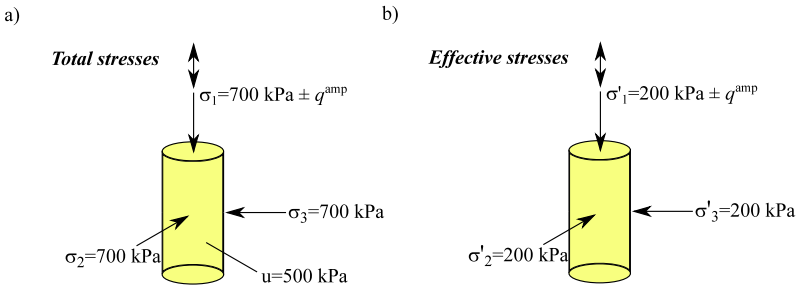

Figure 2.8: Typical initial stress states on tests with isotropic consolidation and constant deviator stress amplitude

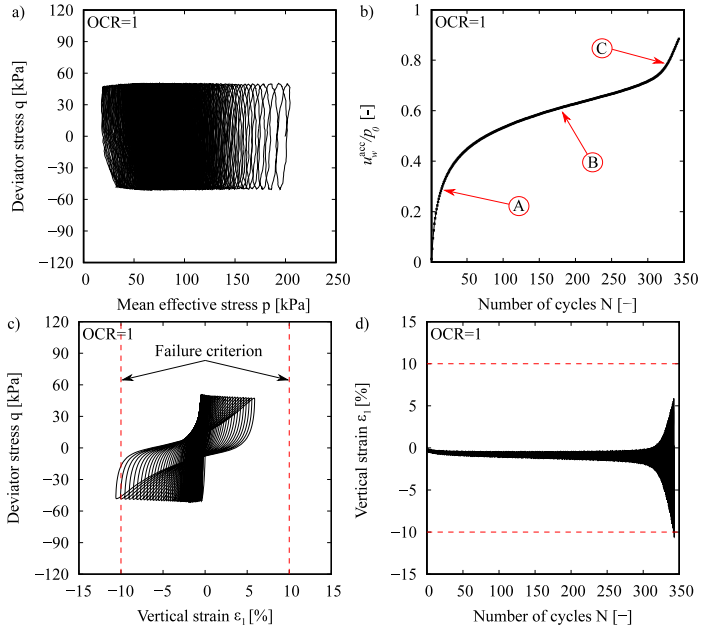

Figure 2.9: Typical results of an undrained cyclic triaxial test (UCT4) with isotropic consolidation ($p_0 = 200$ kPa, $q_0 = 0$ kPa, $\eta_0 = 0$) and constant deviator stress amplitude of $q^{\mathrm{amp}} = 50$ kPa

reported on fine-grained soils, e.g. [21, 22, 25, 31, 69, 85, 237, 263, 264].

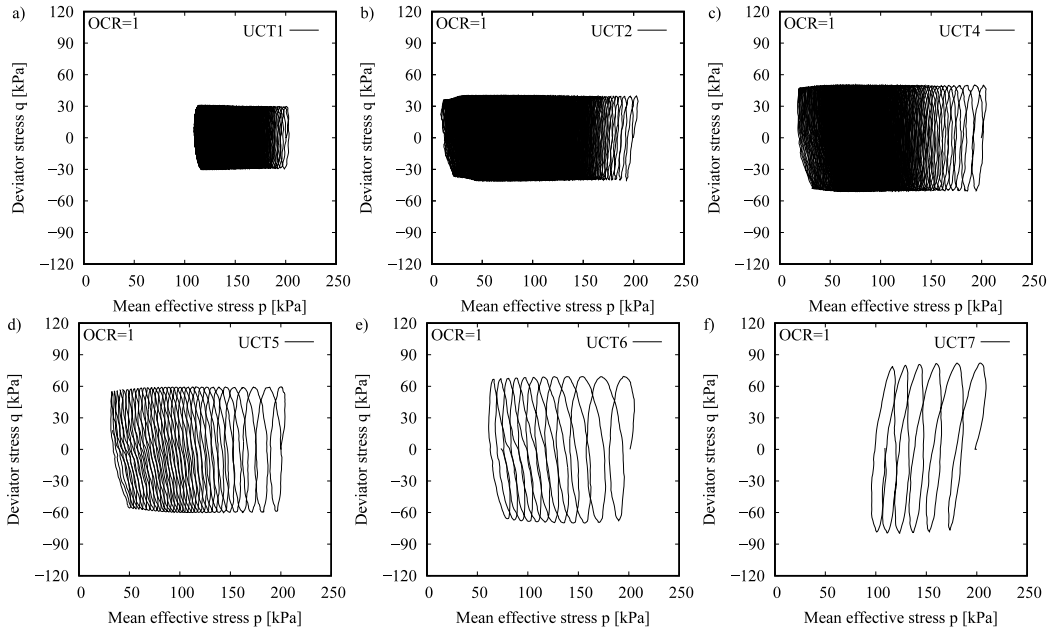

Figure 2.10: Undrained cyclic triaxial tests UCT1, UCT2 and UCT4-UCT7 with isotropic consolidation ($p_0 = 200$ kPa, $q_0 = 0$ kPa, $\eta_0 = 0$) and variation of the deviator stress amplitude $q^{\text{amp}} = \{30, 40, 50, 60, 70, 80\}$ kPa, $q - p$ space

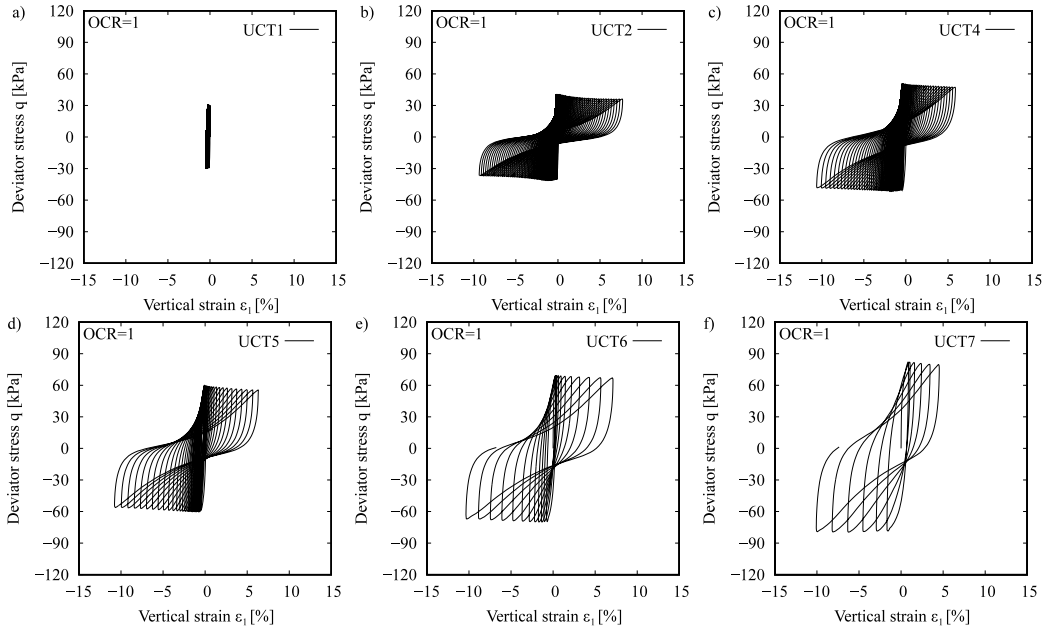

Figure 2.11: Undrained cyclic triaxial tests UCT1, UCT2 and UCT4-UCT7 with isotropic consolidation ($p_0 = 200$ kPa, $q_0 = 0$ kPa, $\eta_0 = 0$) and variation of the deviator stress amplitude $q^{\text{amp}} = \{30, 40, 50, 60, 70, 80\}$ kPa, $q - \varepsilon_1$ space

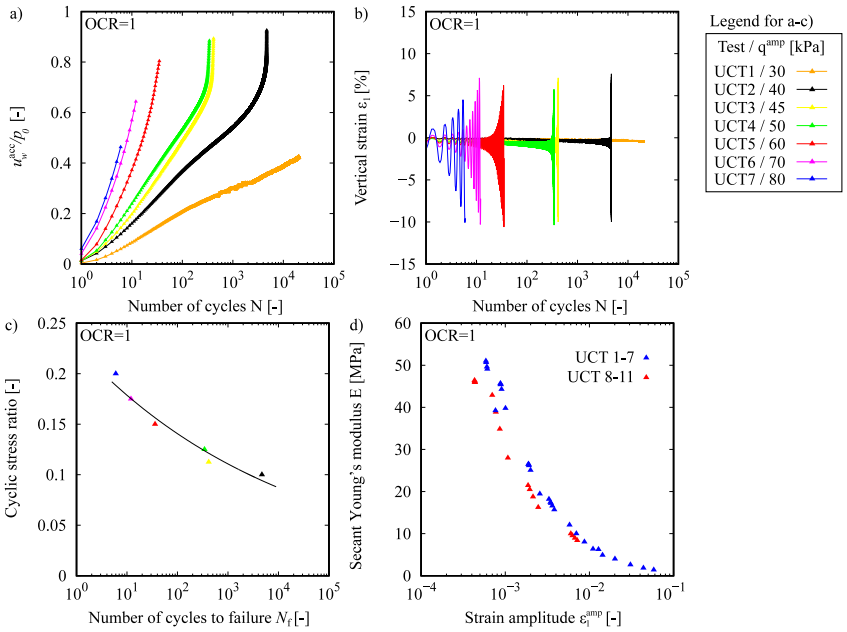

Figure 2.12: Summary of undrained cyclic triaxial tests UCT1-UCT7 with isotropic consolidation ($p_0 = 200$ kPa, $q_0 = 0$ kPa, $\eta_0 = 0$) and variation of the deviator stress amplitude $q^{amp} = \{30, 40, 45, 50, 60, 70, 80\}$ kPa: a) normalized accumulated pore water pressure u_w^{acc}/p_0 against the number of cycles N, b) vertical strain ε_1 against the number of cycles N, c) cyclic stress ratio CSR against the number of cycles to reach failure N_f, d) degradation of the secant Young's modulus E against the vertical strain amplitude ε_1^{amp}

The influence of soil plasticity in the accumulation rates of pore water pressure and strains, and therefore, in the number of cycles to reach failure conditions ($|\varepsilon_1| = 10\%$) is now inspected. For that purpose, the previously presented results on Malaysian kaolin ($PI = 25\%$) were combined with cyclic results on normally consolidated samples reported by Wichtmann and Triantafyllidis [275] in Karlsruhe kaolin ($PI = 12.2\%$), Wichtmann et al. [264] in Onsøy clay ($PI = 33.7\%$) and Hyodo et al. [105] in Hiroshima-B clay ($PI = 72.8\%$). Even though that more data is available in the literature, different failure criteria were considered in different works. Therefore, only the results using the same failure criterion were considered. The analysis of the influence of soil plasticity in the number of cycles to reach failure conditions is summarized in Figure 2.13. The results suggest that, with all other conditions remaining the same, an increase in soil plasticity leads to a remarkable increment in the number of cycles to reach failure conditions.

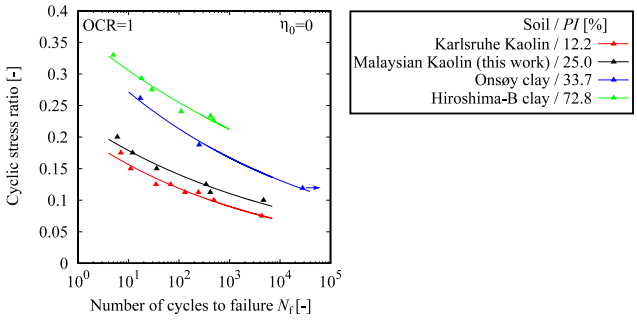

Figure 2.13: Influence of soil plasticity in the number of cycles to reach failure conditions N_f

2.4.2 UCT with anisotropic consolidation and variation of the deviator stress amplitude

In order to analyze the behavior on samples with initial anisotropic stresses, typical of marine clays deposits in their in-situ sedimentary process [105, 131], four undrained cyclic triaxial tests UCT8-UCT11 on normally consolidated samples with anisotropic consolidation ($p_0 = 220$ kPa, $q_0 = 60$ kPa, $\eta_0 = 0.27$) and variation of the deviator stress amplitude 20 kPa $\leq q^{\text{amp}} \leq$ 60 kPa were performed. A typical result on test UCT9 with constant deviator stress amplitude of $q^{\text{amp}} = 30$ kPa is given in Figure 2.14 for illustration purposes. Some observations regarding the experimental results are worthy to remark: in contrast to samples with isotropic initial stresses, the normalized accumulated pore water pressure u_w^{acc}/p_0 evolves at a high rate at the beginning of the test, but it is strongly reduced thereafter towards an asymptotic value $p > 0$, see Figure 2.14a,b. Three very different strain accumulation rates are observed on tests with anisotropic consolidation, which are denoted as "A", "B" and "C" in Figure 2.14d. The experimental results also suggest that the vertical strains progressively grows in each subsequent cycle even when the accumulation of pore water pressure almost stabilized.

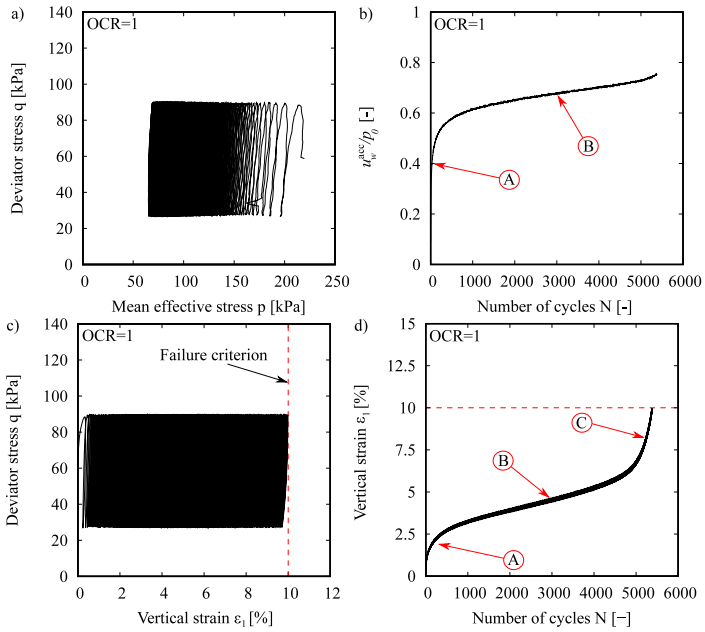

Figure 2.14: Typical results of an undrained cyclic triaxial test (UCT9) with anisotropic consolidation ($p_0 = 220$ kPa, $q_0 = 60$ kPa, $\eta_0 = 0.27$) and constant deviator stress amplitude of $q^{\text{amp}} = 30$ kPa

The detailed results of undrained cyclic triaxial tests UCT8-UCT11 are presented in Figures 2.15 and 2.16, and are summarized in Figure 2.17. Similar to samples with isotropic consolidation, the accumulation rates of strains and pore water pressure increase with increasing deviator stress amplitude, see Figure 2.17a,b. In addition, smallest deviator stress amplitudes generate higher final magnitudes of the normalized accumulated pore water pressure u_w^{acc}/p_0. Due to device limitations, the first two cycles on tests UCT10-UCT11 did not reach the desired deviator stress amplitudes, but worked fine thereafter. The analysis of the CSR $- N_f$ curves is presented in Figure 2.17c. The results suggest that increasing the magnitude of the initial stress ratio η_0, remarkably reduces the number of cycles to reach the failure criterion N_f. The results of tests with anisotropic consolidation were fairly well described ($R^2 = 0.95$) with the potential equation CSR $= aN_f^b$, with $a = 0.175$ and $b = -0.113$. The results on samples with anisotropic consolidation are in good agreement with former studies on fine-grained soils, e.g. [22, 105, 107, 179, 263, 275].

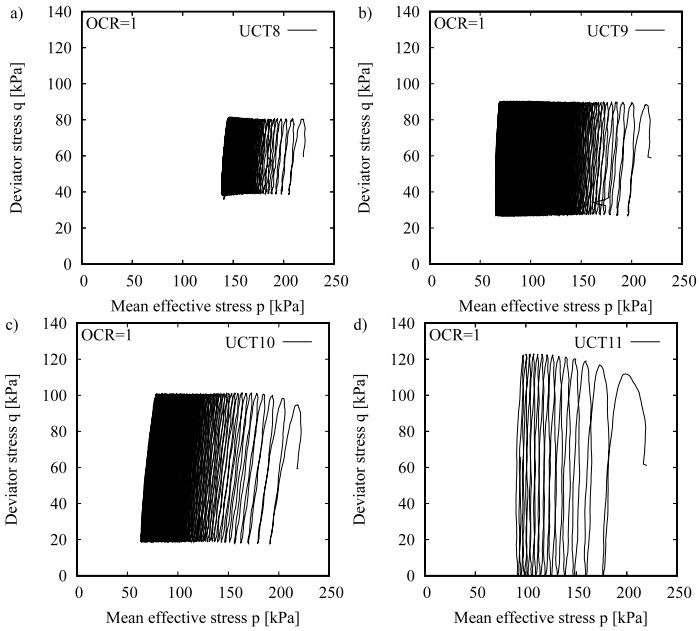

Figure 2.15: Undrained cyclic triaxial tests UCT8-UCT11 with anisotropic consolidation ($p_0 = 220$ kPa, $q_0 = 60$ kPa, $\eta_0 = 0.27$) and variation of the deviator stress amplitude $q^{\text{amp}} = \{20, 30, 40, 60\}$ kPa, $q - p$ space

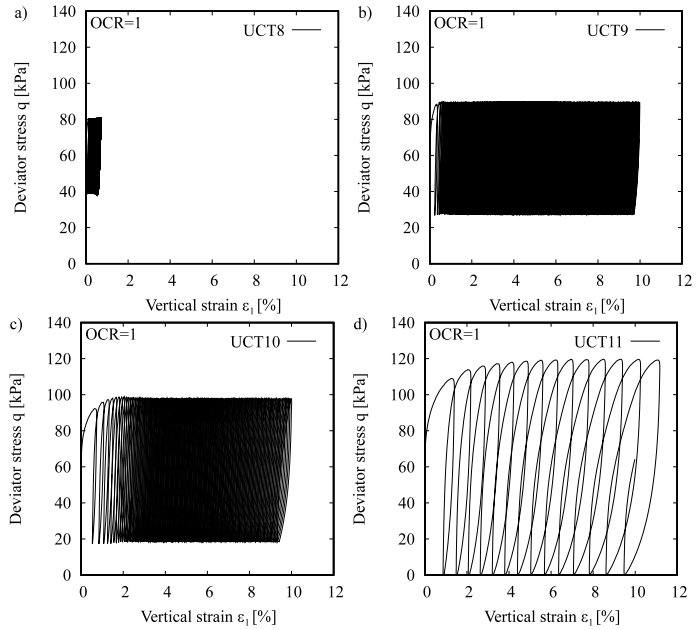

Figure 2.16: Undrained cyclic triaxial tests UCT8-UCT11 with anisotropic consolidation ($p_0 = 220$ kPa, $q_0 = 60$ kPa, $\eta_0 = 0.27$) and variation of deviator the stress amplitude $q^{\text{amp}} = \{20, 30, 40, 60\}$ kPa, $q - \varepsilon_1$ space

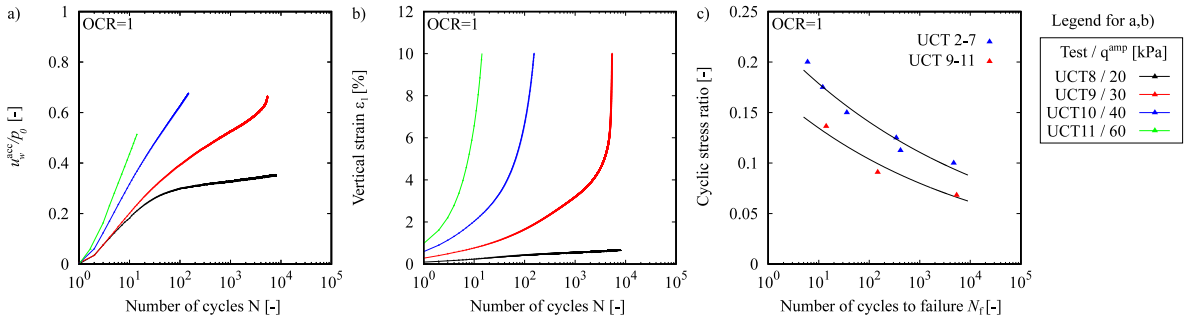

Figure 2.17: Summary of undrained cyclic triaxial tests UCT8-UCT11 with anisotropic consolidation ($p_0 = 220$ kPa, $q_0 = 60$ kPa, $\eta_0 = 0.27$) and variation of deviator the stress amplitude $q^{\text{amp}} = \{20, 30, 40, 60\}$ kPa: a) normalized accumulated pore water pressure u_w^{acc}/p_0 against the number of cycles N, b) vertical strain ε_1 against the number of cycles N, c) cyclic stress ratio CSR against the number of cycles to reach failure N_f

2.4.3 UCT with isotropic or anisotropic consolidation and packages of cycles

Geotechnical structures, such as pavements and offshore foundations, are subjected to irregular cyclic loading histories of very different amplitudes. Some attempts to analyze/simplify these type of loadings scenarios have been proposed by e.g. [119, 157, 222, 270], in which the irregular cyclic loading is bundled into packages of cycles with constant amplitudes and then treated sequentially, see Figure 2.18 for illustration purposes. These methods should be applied only on granular soils and under fully drained cyclic conditions, in which Miner's rule [155] (i.e. the sequence of the packages does not affect the final strain accumulation) have been experimentally validated e.g. [12, 139, 222, 267, 270]. Unfortunately, Miner's rule has not been inspected on fine-grained soils nor under undrained conditions.

In this section, the validity of Miner's rule under undrained conditions is evaluated. For that purpose, three undrained cyclic triaxial tests UCT12-UCT14 were performed on normally consolidated samples with isotropic consolidation ($p_0 = 200$ kPa, $q_0 = 0$ kPa, $\eta_0 = 0$) and packages of cycles in the sequences $q^{\text{amp}} = \{40 \rightarrow 45 \rightarrow 50\}$, $\{45 \rightarrow 40 \rightarrow 50\}$ and $\{50 \rightarrow 45 \rightarrow 40\}$ kPa. Each package of cycles considered $N = 100$ cycles, for a total of $N = 300$ cycles in each test. The magnitudes of the deviator stress amplitudes were carefully selected, based on the tests presented in previous sections, in order to avoid cyclic mobility. The experimental results of tests UCT12-UCT14 are presented in Figures 2.19 and 2.20, and are summarized in Figure 2.21. The results suggest that the order of the packages of cycles plays a major role in the final accumulation of pore water pressure and strains (i.e. Miner's rule is not valid under undrained conditions). Packages with decreasing order of the deviator stress amplitude produce the higher accumulation, while packages with ascending order of loads produce the lowest accumulation. A similar conclusion was found in the numerical simulations by Staubach and Wichtmann [221], in which they found that Miner's rule does not apply under partially drained conditions and that the magnitude of the final accumulation was mainly controlled by the amplitude of the firsts packages of cycles.

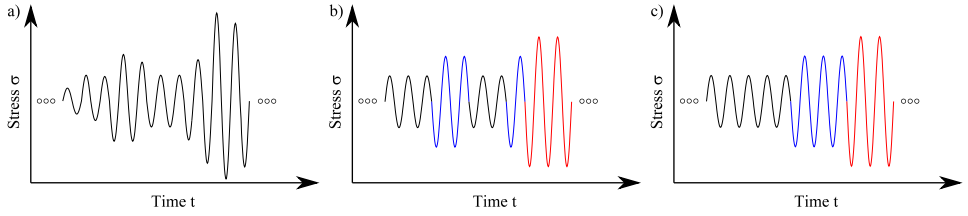

Figure 2.18: Simplification of a loading history into packages of cycles with constant amplitudes

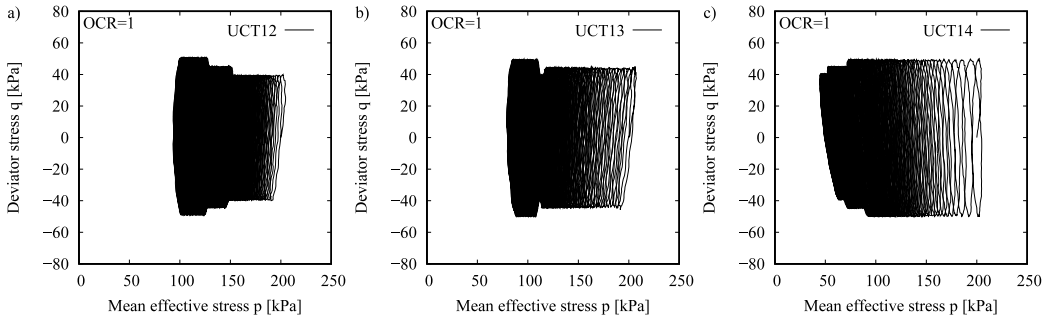

Figure 2.19: Undrained cyclic triaxial tests UCT12-UCT14 with isotropic consolidation ($p_0 = 200$ kPa, $q_0 = 0$ kPa, $\eta_0 = 0$) and variable deviator stress amplitude: a) $q^{\text{amp}} = \{40 \rightarrow 45 \rightarrow 50\}$ kPa, b) $q^{\text{amp}} = \{45 \rightarrow 40 \rightarrow 50\}$ kPa, c) $q^{\text{amp}} = \{50 \rightarrow 45 \rightarrow 40\}$ kPa, $q - p$ space

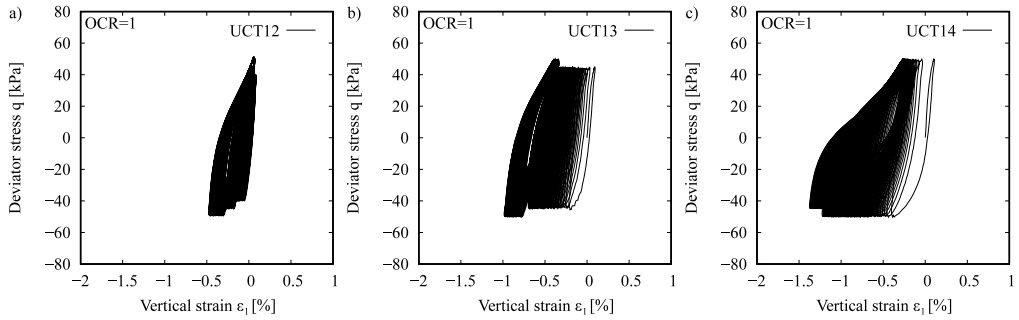

Figure 2.20: Undrained cyclic triaxial tests UCT12-UCT14 with isotropic consolidation ($p_0 = 200$ kPa, $q_0 = 0$ kPa, $\eta_0 = 0$) and variable deviator stress amplitude: a) $q^{\text{amp}} = \{40 \rightarrow 45 \rightarrow 50\}$ kPa, b) $q^{\text{amp}} = \{45 \rightarrow 40 \rightarrow 50\}$ kPa, c) $q^{\text{amp}} = \{50 \rightarrow 45 \rightarrow 40\}$ kPa, $q - \varepsilon_1$ space

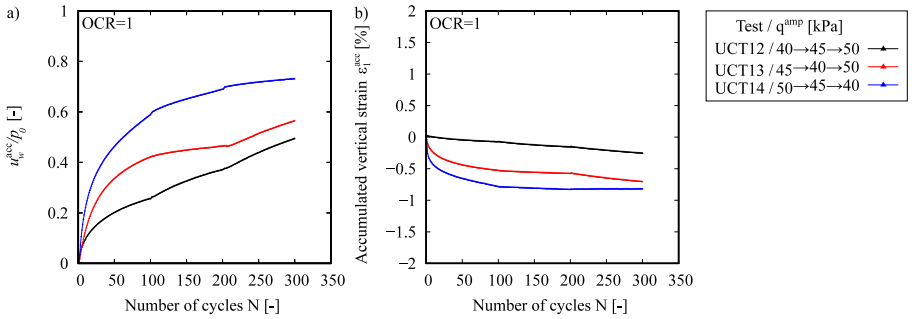

Figure 2.21: Summary of undrained cyclic triaxial tests UCT12-UCT14 with isotropic consolidation ($p_0 = 200$ kPa, $q_0 = 0$ kPa, $\eta_0 = 0$) and variable deviator stress amplitude: a) average normalized accumulated pore water pressure u_w^{acc}/p_0 against the number of cycles N, b) accumulated vertical strain $\varepsilon_1^{\text{acc}}$ against the number of cycles N

Three additional undrained cyclic triaxial tests UCT15-UCT17 on normally consolidated samples with anisotropic consolidation ($p_0 = 220$ kPa, $q_0 = 60$ kPa, $\eta_0 = 0.27$) and packages of cycles in the sequences $q^{\text{amp}} = \{20 \rightarrow 30 \rightarrow 40\}$, $\{30 \rightarrow 20 \rightarrow 40\}$ and $\{40 \rightarrow 30 \rightarrow 20\}$ kPa were performed. Each package of cycles considered $N = 100$ cycles, for a total of $N = 300$ cycles in each test. The results of these tests are summarized in Figures 2.22-2.24, and are consistent with previous tests with isotropic consolidation, in which the sequence of the packages influences the final accumulation of strains and pore water pressure.

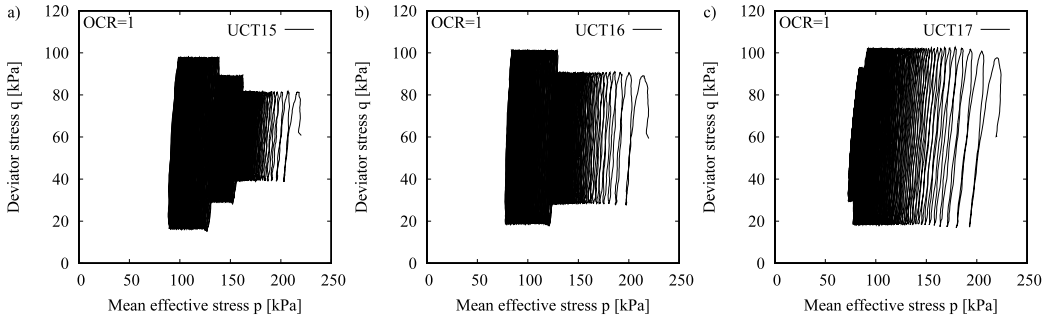

Figure 2.22: Undrained cyclic triaxial tests UCT15-UCT17 with anisotropic consolidation ($p_0 = 220$ kPa, $q_0 = 60$ kPa, $\eta_0 = 0.27$) and variable deviator stress amplitude: a) $q^{\text{amp}} = \{20 \rightarrow 30 \rightarrow 40\}$ kPa, b) $q^{\text{amp}} = \{30 \rightarrow 20 \rightarrow 40\}$ kPa, c) $q^{\text{amp}} = \{40 \rightarrow 30 \rightarrow 20\}$ kPa, $q - p$ space

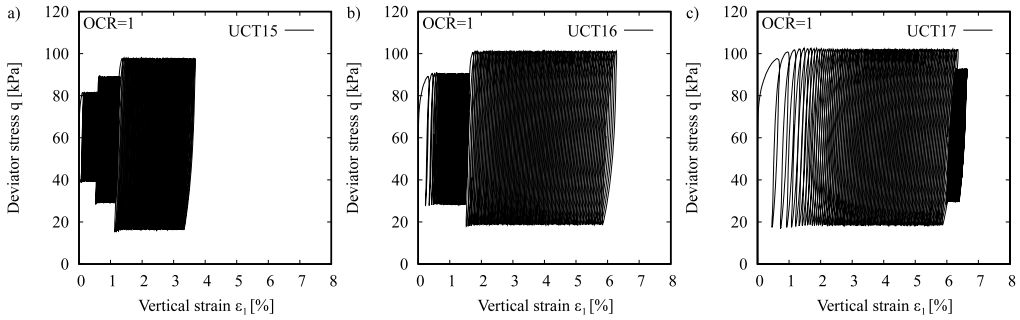

Figure 2.23: Undrained cyclic triaxial tests UCT15-UCT17 with anisotropic consolidation ($p_0 = 220$ kPa, $q_0 = 60$ kPa, $\eta_0 = 0.27$) and variable deviator stress amplitude: a) $q^{\text{amp}} = \{20 \rightarrow 30 \rightarrow 40\}$ kPa, b) $q^{\text{amp}} = \{30 \rightarrow 20 \rightarrow 40\}$ kPa, c) $q^{\text{amp}} = \{40 \rightarrow 30 \rightarrow 20\}$ kPa, $q - \varepsilon_1$ space

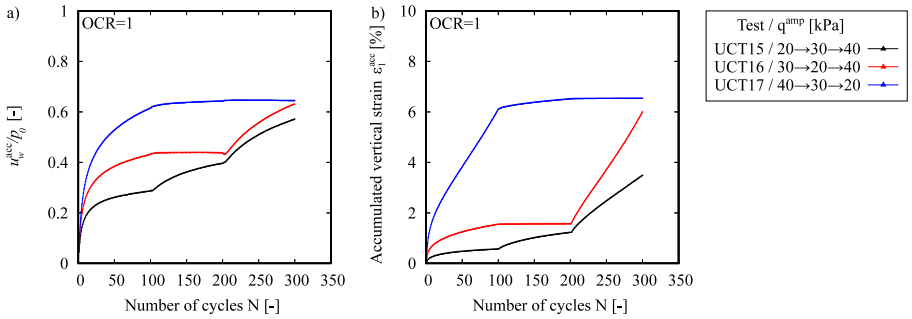

Figure 2.24: Summary of undrained cyclic triaxial tests UCT15-UCT17 with anisotropic consolidation ($p_0 = 220$ kPa, $q_0 = 60$ kPa, $\eta_0 = 0.27$) and variable deviator stress amplitude: a) average normalized accumulated pore water pressure u_w^{acc}/p_0 against the number of cycles N, b) accumulated vertical strain $\varepsilon_1^{\text{acc}}$ against the number of cycles N

Unlike in drained tests, in undrained tests each package is characterized by different initial mean effective stress p_0 due to pore water pressure generated in preceding package. An attempt was performed to identify whether the differences in the final accumulations of tests with packages of cycles were only generated by the different initial p_0 with each package of cycles or not. For that purpose, undrained cyclic triaxial tests UCT18 was performed to replicate the initial conditions of the last 100 cycles of test UCT15 ($p_0 = 135$ kPa, $q_0 = 60$ kPa, $\eta_0 = 0.444$ and $q^{\text{amp}} = 40$ kPa). In order to achieve the initial mean effective pressure $p_0 = 135$ kPa, a drained unloading from $p_0 = 220$ kPa was performed. The results of tests UCT18 and UCT15 are presented in Figure 2.25, and suggest that although the pore water pressure accumulation is rather similar, the vertical strain accumulation is totally different in magnitude and initial rate, see Figure 2.26. This suggest that the history of previous undrained cyclic loading plays a major role in the subsequent undrained behavior of the material.

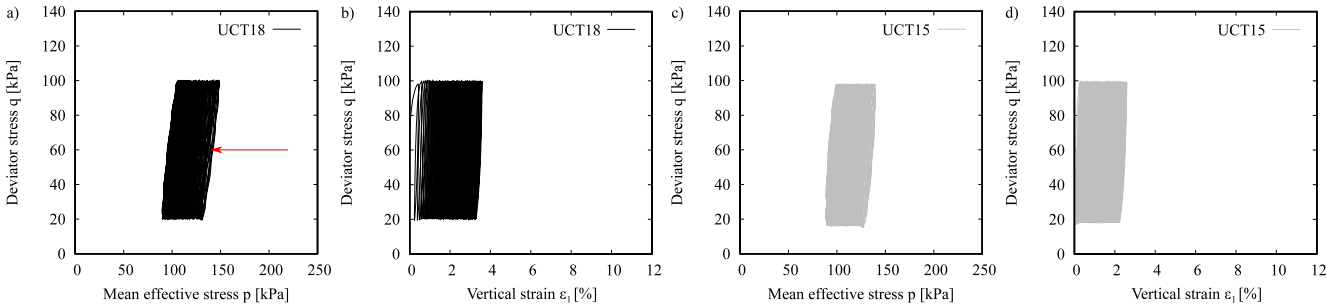

Figure 2.25: a,b) undrained cyclic triaxial test UCT18 with $p_0 = 135$ kPa, $q_0 = 60$ kPa, $\eta_0 = 0.444$ and $q^{\text{amp}} = 40$ kPa, c,d) last 100 cycles of test UCT15 with $p_0 = 135$ kPa, $q_0 = 60$ kPa, $\eta_0 = 0.444$ and $q^{\text{amp}} = 40$ kPa

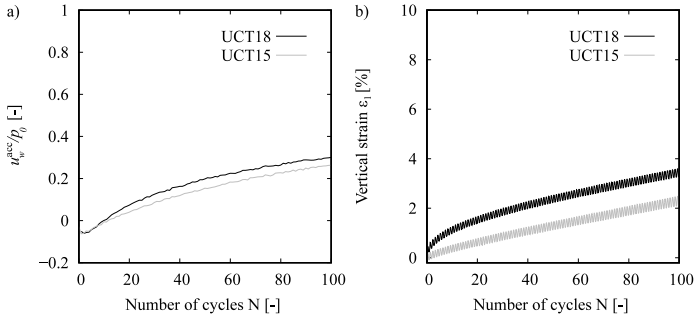

Figure 2.26: Summary of undrained cyclic triaxial test UCT18 with $p_0 = 135$ kPa, $q_0 = 60$ kPa, $\eta_0 = 0.444$, $q^{\text{amp}} = 40$ kPa and last 100 cycles of test UCT15 with $p_0 = 135$ kPa, $q_0 = 60$ kPa, $\eta_0 = 0.444$ and $q^{\text{amp}} = 40$ kPa: a) normalized accumulated pore water pressure u_w^{acc}/p_0 against the number of cycles N, b) vertical strain ε_1 against the number of cycles N

2.4.4 Modified Stewart's approach for undrained cyclic conditions

Stewart [222] proposed a method for the prediction of the accumulated strains under drained cyclic conditions with different loading amplitudes, based on the Miner's rule [155]. This approach have been experimentally validated on model piles founded in granular soils and subjected to drained cyclic loading with variable stress amplitudes e.g. [92, 129, 132, 135]. However, the results of the previous section suggest that Miner's rule is not valid under undrained conditions. Therefore, Stewart's approach can not be applied under undrained cyclic conditions, since it leads to the same final accumulation of strains independently of the loading sequence. For that reason, in this section a Modified Stewart's Approach (MSA) for the calculation of the accumulated pore water pressure and strains under undrained cyclic loading is proposed. The modified method is schematized in Figure 2.27 and is based on an assumption that the strain and pore water pressure accumulation rates depend on the loading magnitude and the actual accumulated pore water pressure. The explanation of the method will be given based on a simple example. Initially, Figure 2.27a presents the normalized accumulated pore water pressure u_w^{acc}/p_0 in three tests with the same initial conditions but different stress amplitudes $\{q_1^{\text{amp}}, q_2^{\text{amp}}, q_3^{\text{amp}}\}$, with $q_1^{\text{amp}} < q_2^{\text{amp}} < q_3^{\text{amp}}$ and N_1, N_2 and N_3 represent the number of cycles with each stress amplitude, respectively. Firstly, N_1 cycles are performed with the lowest deviator stress amplitude q_1^{amp}, which generates a normalized accumulated pore water pressure of u_{w1}^{acc}/p_0. Subsequently, a horizontal projection is performed to achieve the same normalized accumulated pore water pressure with the accumulation curve of the test with the subsequent stress amplitude q_2^{amp}. The number of cycles to reach u_{w1}^{acc}/p_0 with the accumulation curve of

q_2^{amp} is denoted as $N_{1,2}^*$. Then, starting from u_{w1}^{acc}/p_0 and $N_{1,2}^*$, N_2 cycles are performed considering the accumulation curve of the test with q_2^{amp}, leading to a normalized accumulated pore water pressure of u_{w2}^{acc}/p_0. Note that $N_{2,eq} = N_{1,2}^* + N_2$. Afterwards, a new horizontal projection is performed to intersect the accumulation curve of the test with q_3^{amp} at u_{w2}^{acc}/p_0. The number of equivalent cycles to reach the aforementioned scenario is denoted as $N_{2,3}^*$. Finally, N_3 cycles are performed considering the accumulation curve of the test with q_3^{amp}, leading to a final normalized accumulated pore water pressure of u_{w3}^{acc}/p_0. Figure 2.27b presents the construction of a test with the loading sequence $q^{amp} = \{q_1^{amp} \rightarrow q_2^{amp} \rightarrow q_3^{amp}\}$. The curve was constructed by assembly the three sections calculated with the aforementioned procedure. On the other hand, the procedure to compute the accumulated strains with each stress amplitude is presented in Figure 2.27c. It starts with N_1 cycles with q_1^{amp} which generates an accumulate strain of $\varepsilon_{1,1}^{acc}$. Subsequently, starting from $N_{1,2}^*$ a total of N_2 cycles are performed following the strain accumulation curve of the test with q_2^{amp} leading to $\varepsilon_{1,2}^{acc}$. Note that the accumulated strain $\varepsilon_{1,1}^{acc}$ is different to the accumulated strain obtained from the strain accumulation curve of q_2^{amp} after $N_{1,2}^*$ cycles. This difference is hereafter denoted as $\Delta\varepsilon_{1-2}$. In the same way, the difference between $\varepsilon_{1,2}^{acc}$ and the accumulated strains after $N_{2,3}^*$ cycles with the accumulation curve of the test with q_3^{amp} is defined as $\Delta\varepsilon_{2-3}$. Later, starting from $N_{2,3}^*$ a number of N_3 cycles are performed following the accumulation curve of the test with q_3^{amp}, leading to a final strain accumulation of $\varepsilon_{1,3}^{acc}$. Depending on the loading sequence, the magnitudes of $\Delta\varepsilon_{1-2}$ and $\Delta\varepsilon_{2-3}$ are different and lead to different final magnitudes of the accumulated strains. Finally, the strain accumulation curve is constructed by assembly the different strain sections calculated with the aforementioned procedure, see Figure 2.27c,d.

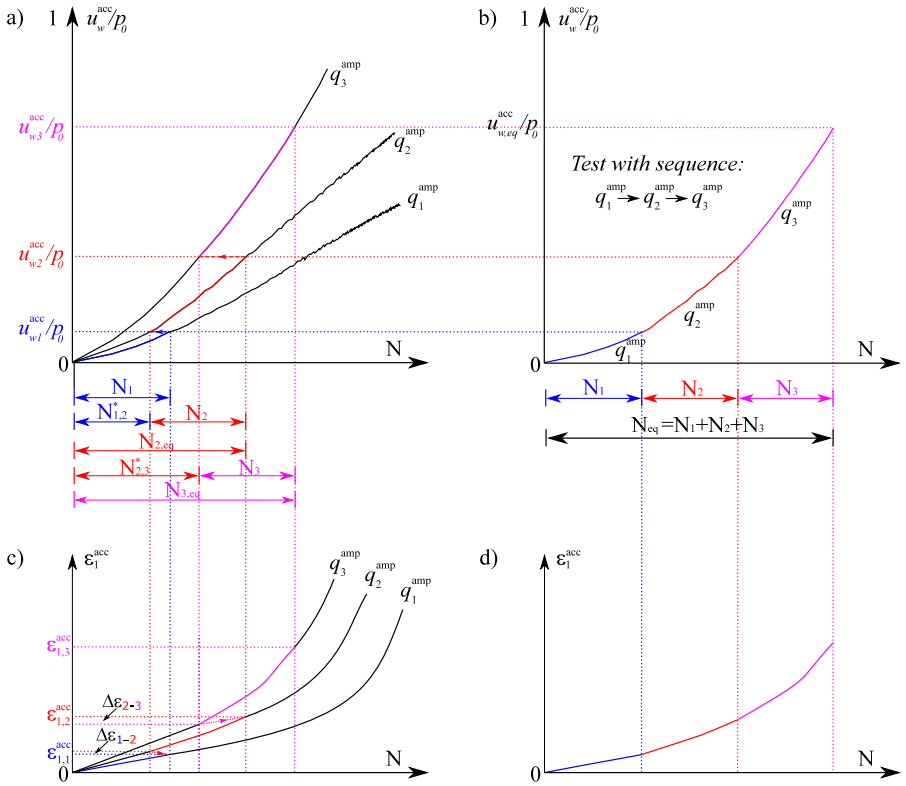

Figure 2.27: Schematic representation of the modified Stewart's approach under undrained cyclic conditions: a,b) normalized accumulated pore water pressure u_w^{acc}/p_0 against the number of cycles N, c,d) accumulated vertical strain ε_1^{acc} against the number of cycles N.

The previously described procedure was used for the prediction of tests UCT12-UCT14 with isotropic

consolidation and packages of cycles with variation of the deviator stress amplitude in different sequences. The pore water pressure and strains accumulation curves for the tests with single amplitudes were taken from section 2.4.1. The results of the analysis with the MSA are presented in Figure 2.28. They suggest that the predicted accumulated pore water pressure is in relatively good agreement with the experiments, predicting almost an average value of tests UCT12-UCT14. In addition, a reasonable prediction of the accumulated strains was also obtained. These findings are particularly interesting from a constitutive modelling point of view, since constitutive models are mainly developed and validated using experimental results of cyclic tests with a single loading amplitude tests. Validity of MSA indicates that models developed using single loading package magnitudes can be used in simulations of problems where loading magnitudes vary. It should be remarked that a small repeatability issue was found between the test and prediction of UCT12 since the first 100 cycles of both should be identical.

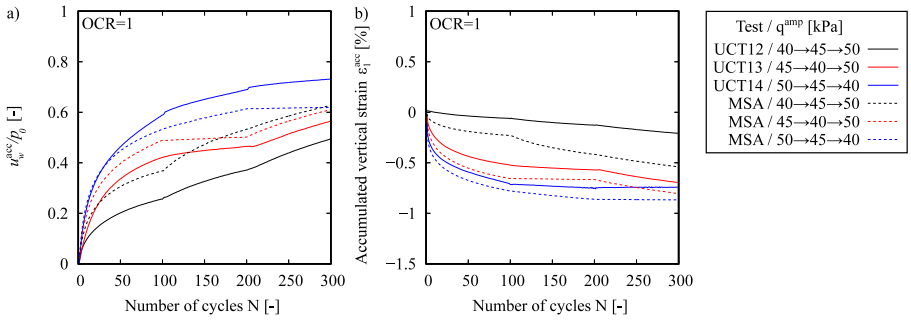

Figure 2.28: Comparison between tests UCT12-UCT14 with packages of undrained cycles and the predictions using the modified Stewart's approach based on single amplitude tests: a) normalized accumulated pore water pressure u_w^{acc}/p_0 against the number of cycles N, b) accumulated vertical strain ε_1^{acc} against the number of cycles N

2.4.5 Repeatability

In order to inspect the repeatability of cyclic tests, the first 100 cycles of tests UCT8-UCT10 with $q^{amp} = \{20, 30, 40\}$ kPa (in which a considerable accumulation of both, pore water pressure and strains was found) were compared against the first 100 cycles of tests UCT15-UCT17 with the same deviator stress amplitude. The results are presented in Figure 2.29 and suggest a quite high repeatability. The small variation between the tests is probably related to slight variations in the initial void ratios of the samples.

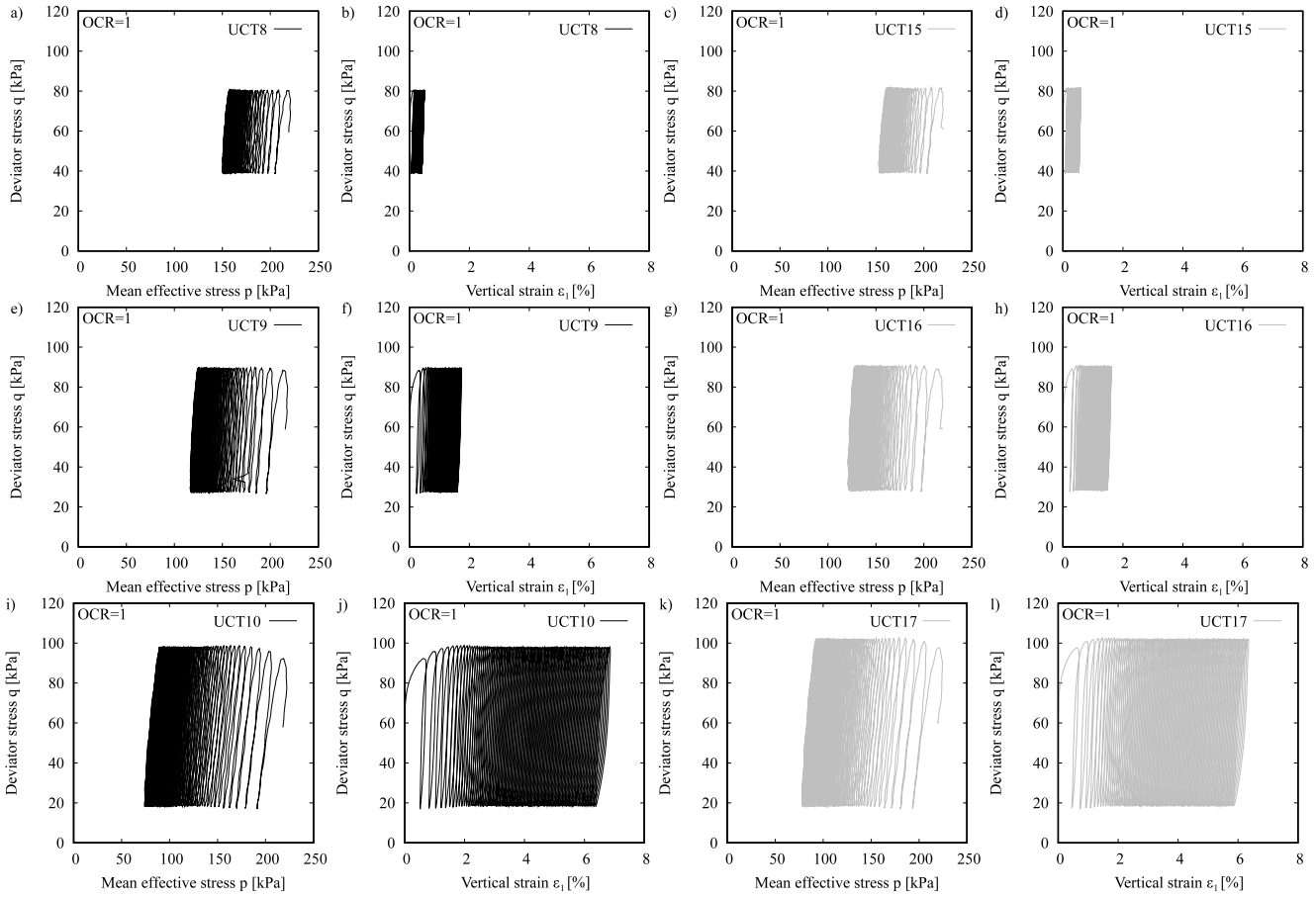

Figure 2.29: Repeatability of the first 100 cycles on undrained cyclic triaxial tests UCT8-UCT10 (black colour) and UCT15-UCT17 (gray colour)

2.4.6 UCT with isotropic consolidation and drained cyclic preloading

Former studies on granular soils suggest that drained previous loading episodes (e.g. drained cyclic preloadings) increase the shear resistance on the subsequent undrained shearing stage and modify the dilative-contractive behavior of the material e.g. [16, 43, 45, 46, 48, 77]. However, few efforts have been made to analyze the effect of drained cyclic preloadings on the subsequent undrained cyclic behavior on fine-grained soils. In this section, the influence of a previous drained episode (a drained cyclic preloading) in the subsequent undrained cyclic behavior is analyzed. For that purpose, undrained cyclic triaxial tests UCT19-UCT21 were performed considering the same initial conditions as tests UCT2, UCT5 and UCT7 but considering a drained cyclic preloading. The performed drained cyclic preloadings are schematized in Figure 2.30 with red arrows.

The results of tests UCT19-UCT21 are presented in Figures 2.30 and 2.31, and are summarized in Figure 2.32. They suggest that a drained cyclic preloading considerably reduces the accumulation rates of strains and pore water pressure, and therefore, increases the number of cycles to reach failure conditions. Furthermore, the inclination of the effective stress paths is affected by the drained monotonic preloading due to induced anisotropy. These results are in agreement with former experimental studies on Hostun sand by Doanh et al. [43, 45, 63]. In addition, increasing the deviator stress amplitude of the test (and therefore, of the drained cyclic preloading) generates higher strains in the preloading stage and leads to higher strain accumulation in the compression side than in the extension side, which differs from tests

without a drained cyclic preloading, see section 2.4.1. The obtained results are in good agreement with former studies on granular soils e.g. [5, 181, 182]. The drastic change in the strain accumulation tendency and the reduction in the accumulation rates are likely not related with the small reduction in void ratio, but rather may be attributed to effects of recent stress history and fabric changes due to stress/strain induced anisotropy.

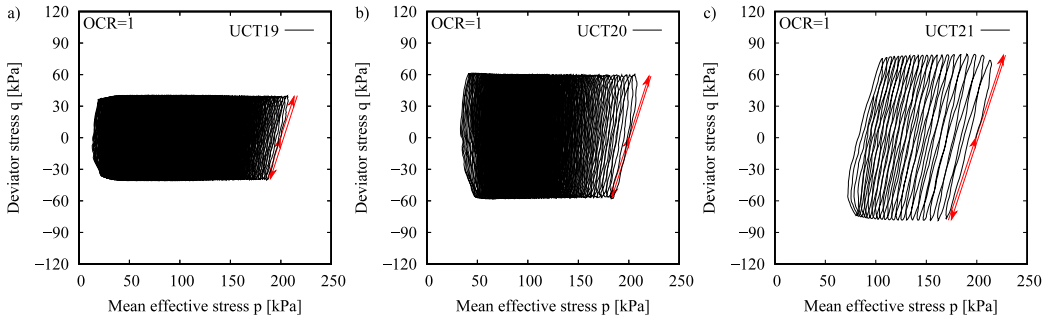

Figure 2.30: Undrained cyclic triaxial tests UCT19-UCT21 with isotropic consolidation ($p_0 = 200$ kPa, $q_0 = 0$ kPa, $\eta_0 = 0$), drained cyclic preloading and variation of the deviator stress amplitude $q^{\text{amp}} = \{40, 60, 80\}$ kPa, $q - p$ space

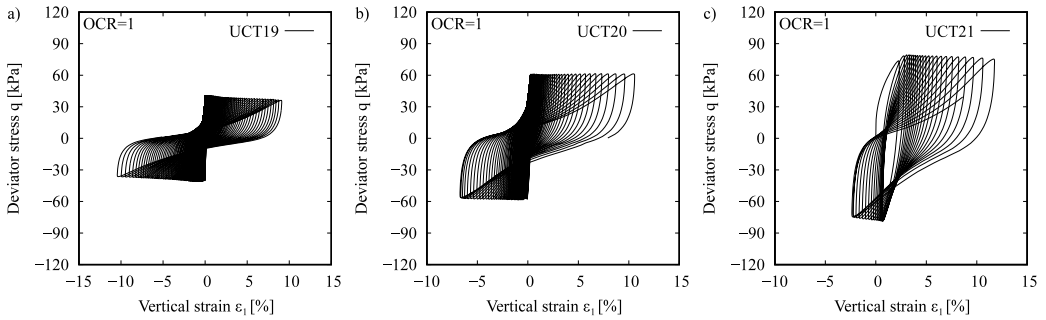

Figure 2.31: Undrained cyclic triaxial tests UCT19-UCT21 with isotropic consolidation ($p_0 = 200$ kPa, $q_0 = 0$ kPa, $\eta_0 = 0$), drained cyclic preloading and variation of the deviator stress amplitude $q^{\text{amp}} = \{40, 60, 80\}$ kPa, $q - \varepsilon_1$ space

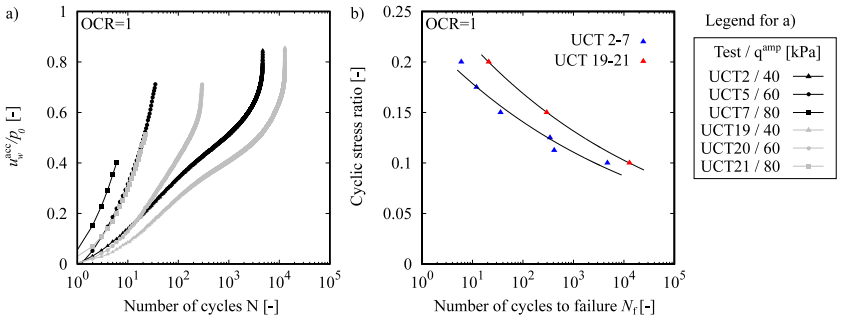

Figure 2.32: Comparison of undrained cyclic triaxial tests with and without a drained cyclic preloading, isotropic consolidation ($p_0 = 200$ kPa, $q_0 = 0$ kPa, $\eta_0 = 0$) and variation of the deviator stress amplitude $q^{\text{amp}} = \{40, 60, 80\}$ kPa: a) normalized accumulated pore water pressure u_w^{acc}/p_0 against the number of cycles N, b) cyclic stress ratio CSR against the number of cycles to reach failure N_f

2.5 Summary and conclusions

A comprehensive experimental investigation on a high-plasticity Malaysian kaolin under monotonic and cyclic loading was presented. Undrained monotonic triaxial tests were performed for the characterization under monotonic loading. Furthermore, an oedometric compression test with multiple unloading-reloading cycles and twenty one undrained cyclic triaxial tests with different initial conditions were performed to investigate the cyclic response of the material. The main findings of the study are summarized as:

- Undrained monotonic triaxial tests on normally consolidated samples showed a contractive behavior. Increasing the mean effective pressure generates higher undrained shear strengths. An increase in the initial overconsolidation ratio leads to more dilative responses and higher undrained shear strengths.
- The results of undrained cyclic triaxial tests suggest a remarkable influence of the deviator stress amplitude in the accumulation rates of pore water pressure and strains, and therefore, in the number of cycles to reach failure conditions. A similar effect was found with the initial stress ratio η_0, in which an increase of η_0 drastically reduces the number of cycles to reach failure conditions.
- Like tests on medium to high plasticity soils from the literature, the state with zero effective stress, hence the liquefaction state, was not reached with the kaolin. In addition, the Malaysian kaolin does not exhibit eight-shaped effective stress paths in the final phase of tests with isotropic consolidation, which are usually observed on some fine-grained soils.
- The comparison of the obtained results with some former studies suggest that, with all other conditions remaining the same, soil plasticity considerably increases the number of cycles to reach failure.
- Undrained cyclic tests with packages of cycles in different sequences suggest that, independently of η_0, Miner's rule is not valid under undrained conditions. A modified Stewart's approach was proposed for the estimation of the accumulated pore water pressure and strains on the tests with variable loading magnitudes. Its validity suggests that constitutive models developed using single-magnitude loading packages can be used in simulations of problems with variable cyclic loading magnitudes.
- Undrained cyclic triaxial tests with a drained cyclic preloading presented a substantial reduction in the accumulation rates of strains and pore water pressure, and therefore, an increase the number of cycles to reach failure conditions. These behavior is associated with effects of recent stress history and fabric changes due to stress/strain induced anisotropy.

The experimental database presented in this study will be freely available at the soilmodels.com website [89].

2.6 Acknowledgements

The authors appreciate the financial support given by the INTER-EXCELLENCE project LTACH19028 by the Czech Ministry of Education, Youth and Sports. The first author appreciates the financial support given by the Charles University Grant Agency (GAUK) with project number 200120. The first and third authors acknowledge the institutional support by the Center for Geosphere Dynamics (UNCE/SCI/006).

Notation

Symbol	Name
B	Skempton's coefficient
CSR	cyclic stress ratio
d	diameter
e	void ratio
E	secant Young's modulus
G_s	specific gravity
h	height
LL	liquid limit
M_c	critical state slope in compression
N	number of cycles
N_f	number of cycles to reach the failure criterion
OCR	overconsolidation ratio
p	mean effective stress
$p_{\max}$	maximum mean effective stress
PI	plasticity index
PL	plastic limit
q	deviator stress
q^{amp}	deviator stress amplitude
R^2	coefficient of determination
u_w^{acc}	accumulated pore water pressure
u_w^{acc}/p_0	normalized accumulated pore water pressure
w	water content
ε_1	vertical strain
$\varepsilon_1^{\mathrm{amp}}$	vertical strain amplitude
$\varepsilon_1^{\mathrm{acc}}$	accumulated vertical strain
φ_c	critical state friction angle
γ	shear strain
η	stress ratio
ν	displacement rate
σ'_a	axial stress
σ'_r	radial stress

Chapter 3

Experimental database on Zbraslav sand under monotonic and cyclic loading - Article 2

Summary of the article

This article presents a comprehensive experimental database on Zbraslav sand. The material was collected from a borrow pit in the district of Zbraslav, Prague, Czech Republic. Initially, a detailed characterization of the material was presented. It includes maximum and minimum void ratios, grain size distribution, angle of repose, grains shape and mineralogical composition of the sand. Subsequently, the samples preparation and saturation procedure is described. Most of the triaxial tests were performed on dense samples ($D_r \approx 70$ %), which is a density often found at offshore sites [5, 14, 15].

The mechanical behavior of the sand at large strains was analyzed by means of undrained monotonic triaxial tests with different initial mean effective pressures and relative densities. The results suggest a significant increase of the maximum deviatoric stress with increasing initial mean effective pressure. The results also show strain softening after $\varepsilon_1 \approx 15\%$. A set of oedometric compression tests with different initial relative densities and multiple unloading-reloading cycles was also included to analyze the compressibility of the material.

The main focus of the article lies on the undrained cyclic response of Zbraslav sand under a wide range of cyclic conditions. Initially, undrained cyclic triaxial tests with variation of the deviatoric stress amplitude were performed. The results suggest that increasing the deviatoric stress amplitude remarkably reduces the number of cycles to reach the failure criterion $|\varepsilon_1| = 10\%$. Then, undrained cyclic triaxial tests with drained or undrained cyclic preloadings were included and analyzed. The experimental results suggested that drained cyclic preloadings remarkably modified the subsequent rate of pore water pressure accumulation and increased the number of cycles to reach the defined failure criterion without affecting the shape of the stress-strain hysteresis. On the other hand, undrained cyclic preloadings presented a threshold which separated positive and negative effects in the subsequent undrained cyclic resistance.

Experimental investigation on Zbraslav sand under monotonic and cyclic loading: on the influence of cyclic preloadings

Duque, J.[1], Roháč, J.[1], Mašín, D.[1], Najser, J.[1], Opršal, J.[1]

[1]Charles University, Prague, Czech Republic

Abstract

This article presents a comprehensive experimental investigation on Zbraslav sand under monotonic and cyclic loading. Initially, the material response at large strains was investigated by means of undrained monotonic triaxial tests with different initial mean effective stresses and relative densities. A set of oedometric compression tests with multiple unloading-reloading cycles and different initial relative densities was as well included to evaluate the material compressibility. In addition, several undrained cyclic triaxial tests were performed and analyzed under a wide range of initial conditions. In the aforementioned tests, the undrained cyclic resistance was investigated considering different types of drained or undrained cyclic preloadings and reconsolidation stages. The experimental results suggested that drained cyclic preloadings remarkably modified the subsequent rate of pore water pressure accumulation and increased the number of cycles to reach the defined failure criterion without affecting the shape of the stress-strain hysteresis. On the other hand, undrained cyclic preloadings presented a threshold which separated positive and negative effects in the subsequent undrained cyclic resistance. A comparison of the undrained cyclic resistance variation depending on the number of drained or undrained cyclic preloadings was also included.

3.1 Introduction

Some geotechnical analyses involve foundations subjected to short episodes of fast and high-magnitude cyclic loading, followed by long periods where the magnitude of the cyclic loading is strongly reduced or negligible. Examples of these loading scenarios are offshore foundations under storm conditions, followed by long episodes of calm environmental conditions and foundations during and after seismic episodes [103, 120, 190, 207]. During these episodes, if the soil is loaded under undrained conditions, it accumulates pore water pressure which is afterwards dissipated while it reconsolidates [5, 14, 52, 126]. The experimental evidence suggests that the subsequent soil mechanical behavior is strongly influenced by its previous loading/unloading episodes, effect which is usually referred as stress-strain history [3, 8, 127, 158, 182, 218]. Therefore, to develop constitutive models and numerical tools which properly predict the behavior of foundations involving different types of loading scenarios and reconsolidations episodes, a proper understanding and reproduction of the influence of the stress-strain history in the subsequent soil mechanical behavior is crucial.

Some of the earliest experimental investigations on the influence of preloadings (e.g. drained preloadings or undrained preloadings with reconsolidation episodes) in the subsequent monotonic and cyclic behavior of granular soils were performed by Finn et al. [64], Lee and Albaisa [130] and Toki and Kitago [244]. They reported that the application of preloadings impact the subsequent liquefaction resistance. Later, Ishihara and Okada [114, 115] performed undrained cyclic tests on very loose sand samples and found that the liquefaction resistance can be improved or worsen depending if the effective stress path of the preloading goes beyond the phase transformation line. If so, the preloading was denominated "large preloading" and large strains are expected together with a reduction in the liquefaction resistance. If

not, it is defined as "small preloading" and small strains are expected accompanied with an improvement in the liquefaction resistance. Some consecutive experimental studies agree with these observations on granular soils e.g. [174, 200, 201, 213, 217, 228, 249]. However, their analysis was usually limited to undrained cyclic preloadings with two extreme cases: a) pretty few cycles that lead to very small values of the pore water pressure ratio $r_u = u_w^{acc}/p_0$ or b) too many cycles that lead to liquefaction (i.e. $r_u = 1$). In addition, recent experimental studies e.g. [102, 181, 182] reported different conclusions depending on the sand characteristics and initial density of the samples. In particular, the conclusions found in the literature regarding the variation of the undrained cyclic resistance on tests with undrained cyclic preloadings that lead to pore water pressure ratios in the range $0.2 < r_u < 1$ or in tests with dense samples are contradictory. Therefore, more investigation is still needed in order to quantify the variation of the undrained cyclic resistance considering a wide range of undrained cyclic preloadings. In addition, it is particularly important to define a stress/strain threshold that separates positive and negative effects due to the undrained cyclic preloadings. Regarding drained preloadings, while a wide number of research focused on the influence of a drained monotonic preloading in the subsequent undrained monotonic behavior e.g. [6, 16, 43–46, 48, 63, 77, 263], rather few efforts have been devoted to quantify the influence of drained cyclic preloadings in the subsequent undrained cyclic resistance e.g. [5, 175, 271]. Accordingly, more investigation is needed to analyze and quantify the subsequent undrained cyclic resistance variation depending on the number of drained or undrained cyclic preloadings.

The structure of the article is as follows: first, a detailed characterization of the material properties and characteristics is presented. Afterwards, undrained monotonic triaxial tests with different initial mean effective stresses and relative densities are given for the characterization of the material at large strains. Then, several oedometric compression tests with different initial relative densities and considering multiple unloading-reloading episodes are presented for the characterization of the material compressibility. Subsequently, a set of undrained cyclic triaxial tests were performed on dense samples with variation of the deviatoric stress amplitude to characterize the undrained cyclic resistance of the sand. Finally, several undrained cyclic triaxial tests with different types of drained or undrained cyclic preloadings were performed to investigate their influence on the subsequent undrained cyclic resistance. The experimental results suggested that drained cyclic preloadings remarkably modified the subsequent rate of pore water pressure accumulation and increased the number of cycles to reach the defined failure criterion without affecting the shape of the stress-strain hysteresis. On the other hand, undrained cyclic preloadings presented a threshold which separated positive and negative effects in the subsequent undrained cyclic resistance. The experimental data presented in this article will be freely available at the soilmodels.com website [89].

3.2 Material description and samples preparation

The testing material corresponds to Zbraslav sand. It was collected from a borrow pit in the district of Zbraslav, Prague, Czech Republic. The location was in the Mindel terrace of river Moldau at an altitude of 250 m.a.s.l, in the forest area north of Zbraslav quarry, 80 m east from the building "Nad Kamínkou 1575". Zbraslav sand is a common testing material and has been used in many former works e.g. [19, 59–62, 90, 148], just to mention a few. As the original location where Zbraslav sand was extracted by Feda [59–62] is not accessible any more, we tested samples extracted from several other locations from the same Mindel terrace of Moldau, selecting finally the sample with grain size distribution close to the original Zbraslav sand site (see Figure 3.1a). This sand presents the following characteristics: specific gravity $G_s = 2.65$, maximum void ratio $e_{\max} = 0.893$, minimum void ratio $e_{\min} = 0.520$, mean diameter $D_{50} = 0.531$ mm, uniformity coefficient $C_{\mathrm{u}} = 3.19$ and coefficient of curvature $C_{\mathrm{c}} = 0.98$. In addition, Zbraslav sand presents a critical state friction angle $\varphi_c = 34°$, which was determined as the mean value from several measurements with the cone pluviation test on very loose ($D_r \approx 0$ %) dry sand. The aforementioned tests were performed following the procedure described in former works e.g.

[90, 153, 262, 273]. According to the Unified Soil Classification System (USCS) the tested sand is classified as poorly graded sand (SP). Zbraslav sand presents almost no fines ($< 1\%$) and its grain size distribution is presented in Figure 3.1a. The sand grains present subangular shape, see Figure 3.1b and Figure 3.2. In terms of mineralogy, Zbraslav sand is composed of quartz (75%), albite (12.5%), microcline (10.5%) and muscovite (2%), see Figure 3.3.

Samples for triaxial tests were prepared following the procedure described by Wichtmann et al. [272], in which the dry material was deposited in its loosest state and was further compacted by tapping to achieve the desired initial relative density. Samples were prepared considering a diameter $d \approx 50$ mm and a height $h \approx 100$ mm (a high-to-diameter ratio of $h/d = 2$). All samples were sandwiched with porous stones and filter papers. The saturation procedure for triaxial samples is similar to the one reported by Wichtmann [262] and Lade [125]. Initially, dry samples were placed in the triaxial cell and were saturated with CO_2. Then, the back and cell pressures were increased to 10 and 20 kPa, respectively. Under these stresses, samples were saturated with distilled deaerated water (i.e. we let deaerated water flow through the sample under these stresses very carefully, in order not to change the stress states). Subsequently, the back and cell pressures were increased to 500 and 510 kPa, respectively. Finally, we again let flow distilled deaerated water through the sample under this back pressure. The aforementioned procedure always provided Skempton's coefficient $B \geq 0.99$, which confirms a full water-saturation. After the saturation, samples were isotropically consolidated at the corresponding initial mean effective stress of each test. All triaxial tests were performed at a controlled temperature of 20° C.

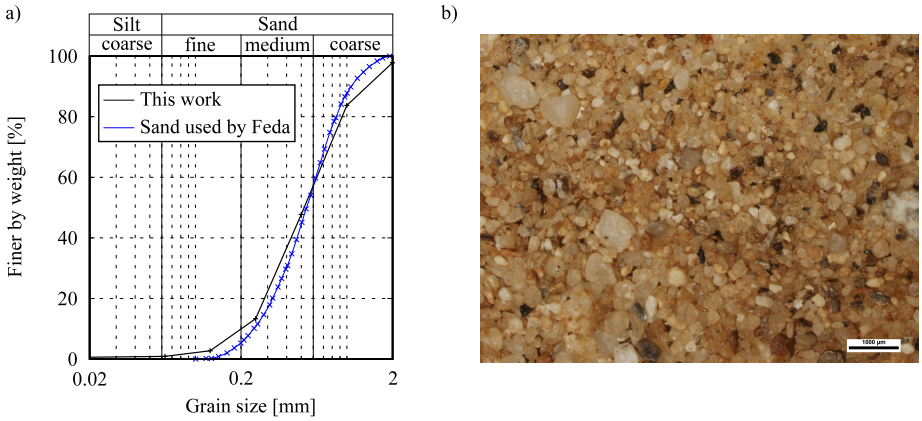

Figure 3.1: Characterization of Zbraslav sand: a) grain size distribution, b) grains of the sand in an optical microscope

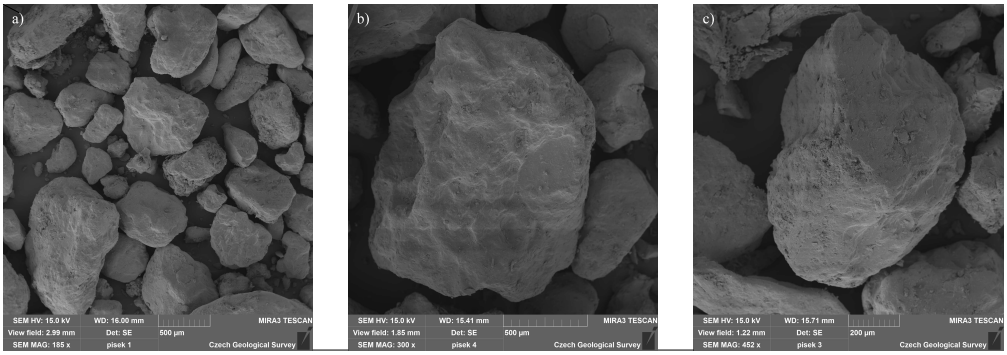

Figure 3.2: Scanning Electron Microscope (SEM) results

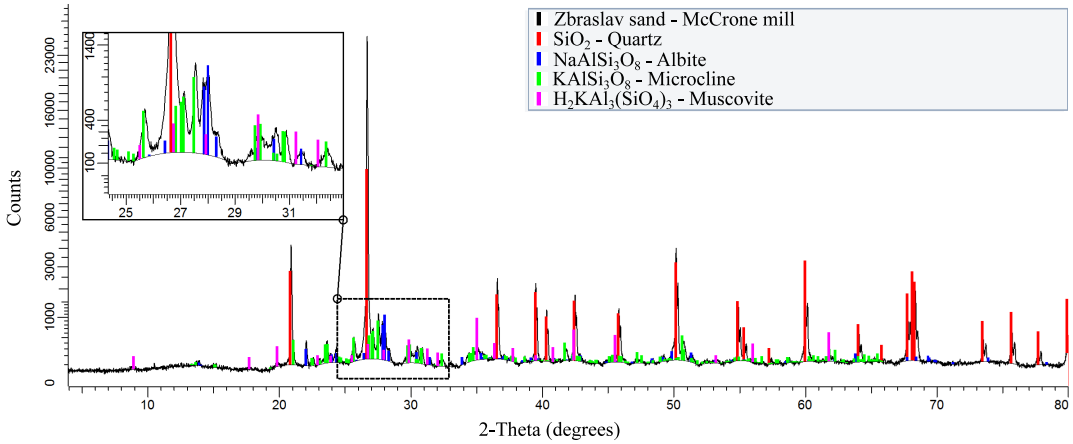

Figure 3.3: X-ray diffraction results

3.3 Tests with monotonic loading

The testing program under monotonic loading is summarized in Table 3.1, and is composed by undrained triaxial tests. The table includes the main characteristics and initial conditions of each test, such as test name, initial mean effective stress $p_0 = (\sigma'_1 + 2\sigma'_3)/3$, initial deviatoric stress $q_0 = (\sigma'_1 - \sigma'_3)$, initial void ratio e_0 measured at the consolidation mean effective stress (before the shearing stage) and initial relative density $D_r = (e_{\max} - e_0)/(e_{\max} - e_{\min}) \cdot 100\%$. The monotonic triaxial tests were performed with a displacement rate $\nu = 0.1$ mm/min.

Initially, four undrained monotonic triaxial tests UMT1-UMT4 were performed on dense samples ($D_r \approx$ 70 %) with isotropic consolidation ($\eta_0 = q_0/p_0 = 0$) and variation of the initial mean effective stress $p_0 = \{100, 200, 300, 400\}$ kPa. The results of these tests suggest a contractive behavior at the initial stage of the tests, followed by dilation after the effective stress path crosses the Phase Transformation Line (PTL), see Figure 3.4a. The inclination of the phase transformation line follows $M_{PTL} = 1.133$ in the $q - p$ plane. Two additional undrained monotonic triaxial tests UMT5-UMT6 were performed considering different initial relative densities. Their results are presented in Figure 3.4c,d and suggest that increasing the initial relative density of the samples leads to a less contractive behavior in the initial part of the shearing stage and higher maximum deviatoric stresses. The results also show strain softening after $\varepsilon_1 \approx 15\%$. The obtained results on undrained monotonic triaxial tests are in good agreement with former studies on granular soils e.g. [106, 113, 156, 229, 253, 262, 263, 291].

Table 3.1: Programme of monotonic triaxial tests

Test name	p_0 [kPa]	η_0 [kPa]	e_0 [-]	D_r [%]
UMT1	100	0	0.632	70.0
UMT2	200	0	0.617	74.0
UMT3	300	0	0.610	75.8
UMT4	400	0	0.621	73.0
UMT5	200	0	0.740	41.0
UMT6	200	0	0.801	24.7

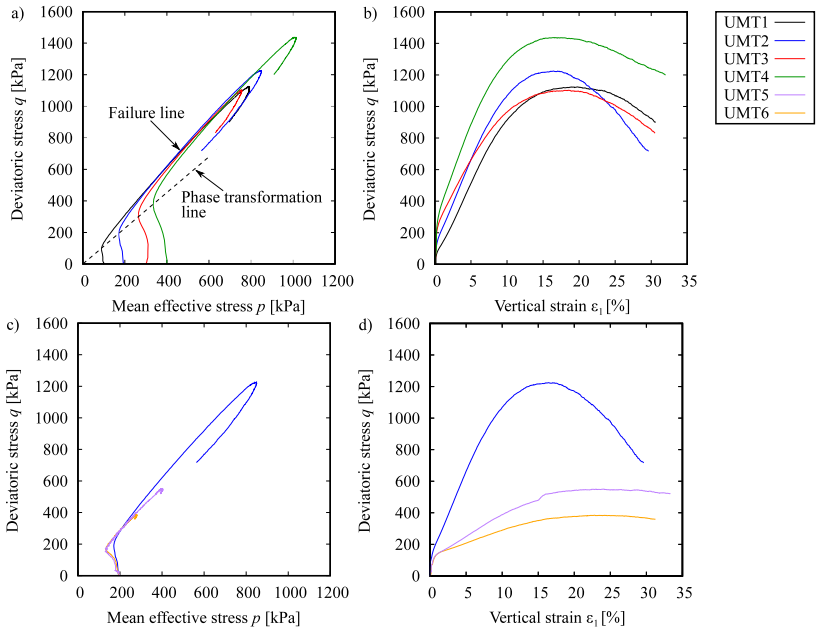

Figure 3.4: Undrained monotonic triaxial tests with isotropic consolidation ($\eta_0 = 0$): a,b) UMT1-UMT4 tests with variation of the initial mean effective stress $p_0 = \{100, 200, 300, 400\}$ kPa, c,d) UMT2, UMT5 and UMT6 with variation of the initial density

3.4 Tests with cyclic loading

3.4.1 Oedometric compression tests with unloading-reloading cycles

Nine stress-controlled oedometric compression tests (OED) were performed with different initial relative densities 17.4 % $\leq D_r \leq$ 82.8 % and considering multiple unloading-reloading cycles to investigate the compressibility of Zbraslav sand. The initial conditions of each oedometric compression test are summarized in Table 3.2. All oedometric compression tests started with an initial axial stress $\sigma_1 = 2.5$ kPa and increased the axial stress to: a) $\sigma_1 = 120$ kPa, b) $\sigma_1 = 400$ kPa, c) $\sigma_1 = 800$ kPa and d) $\sigma_1 = 1600$ kPa. All unloading paths reached always an axial stress of $\sigma_1 = 2.5$ kPa. Some typical results on samples with loose, medium dense and dense initial relative densities are presented in Figure 3.5. The results suggest that higher initial relative densities lead to lower reductions in the void ratio and lower accumulation of vertical strains. The obtained results are in good agreement with former studies on granular soils e.g. [63, 128, 263, 266, 274].

Table 3.2: Programme of oedometric compression tests with multiple unloading-reloading cycles

Test name	e_0 [-]	D_r [%]
OED1	0.828	17.4
OED2	0.827	17.7
OED3	0.803	24.1
OED4	0.714	48.0
OED5	0.711	48.8
OED6	0.710	49.1
OED7	0.584	82.8
OED8	0.593	80.4
OED9	0.598	79.1

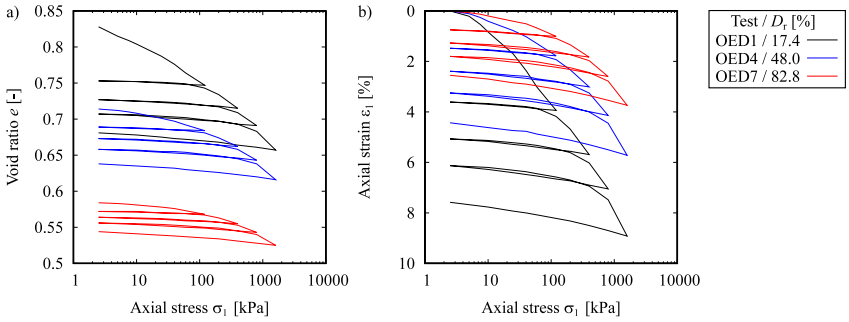

Figure 3.5: Typical results of oedometric compression tests with multiple unloading-reloading cycles and different initial relative densities: a) OED1 ($e_0 = 0.828$, $D_r = 17.4\%$), b) OED4 ($e_0 = 0.714$, $D_r = 48\%$) and c) OED7 ($e_0 = 0.584$, $D_r = 82.8\%$)

3.4.2 Undrained cyclic triaxial tests

Fourteen undrained cyclic triaxial tests (UCT) with isotropic consolidation ($\eta_0 = 0$) were performed considering different deviatoric stress amplitudes $q^{\text{amp}} = (q^{\max} - q^{\min})/2$ and types of cyclic preloadings. The detailed characteristics of each undrained cyclic triaxial test are summarized in Table 3.3. In tests with preloadings, the following variables were always indicated: initial void ratio $e_{0_{bp}}$ and relative density $D_{r_{bp}}$ before the preloading (i.e. before the first undrained shearing stage or before the drained episodes), preloading limit criterion P_{LC} (i.e. criterion to finish the preloading stage) and deviatoric stress amplitude of the preloading $q^{\text{amp}}_{\text{preloading}}$. The undrained cyclic tests were stopped when the failure criterion, hereafter defined as $|\varepsilon_1| = 10\%$, or equivalently, a shear strain of $|\gamma| = 15\%$ was reached. Note that the table differentiates between the number of cycles to reach the failure criterion N_f and the number of cycles to reach initial liquefaction N_{il} (i.e. to reach $r_u \approx 1$). All undrained cyclic triaxial tests were performed on dense samples ($D_r \approx 70\,\%$), density often found at offshore sites [5, 14, 15]. The undrained cyclic tests were performed with a loading frequency of 0.1 Hz, typical of offshore conditions [5, 131, 215, 254, 273, 297]. The drained cycles were performed with a small loading frequency of 0.001 Hz in order to ensure fully drained conditions.

Tests with variation of the deviatoric stress amplitude

Four undrained cyclic triaxial tests UCT1-UCT4 were initially performed on samples with isotropic consolidation ($p_0 = 200$ kPa, $q_0 = 0$, $\eta_0 = 0$) and variation of the deviatoric stress amplitude 45 kPa $\leq q^{\text{amp}} \leq$

Table 3.3: Programme of undrained cyclic triaxial tests

Test name	$e_{0_{bp}}$ [-]	$D_{r_{bp}}$ [%]	e_0 [-]	D_r [%]	p_0 [kPa]	q^{amp} [kPa]	CSR [-]	P_{LC} [-]	$q^{\text{amp}}_{\text{preloading}}$ [kPa]	N_{il} [-]	N_f [-]
UCT1	-	-	0.625	71.95	200	45	0.1125	-	-	215	220
UCT2	-	-	0.634	69.48	200	50	0.125	-	-	138	143
UCT3	-	-	0.650	65.18	200	60	0.150	-	-	18	21
UCT4	-	-	0.640	67.83	200	70	0.175	-	-	6	11
UCT5	0.631	70.42	0.628	71.11	200	60	0.15	$r_u = 0.25$	60	46	55
UCT6	0.641	67.66	0.634	69.39	200	60	0.15	$r_u = 0.50$	60	136	143
UCT7	0.637	68.81	0.623	72.54	200	60	0.15	$r_u = 0.75$	60	128	135
UCT8	0.643	67.16	0.640	67.87	200	50	0.125	$r_u = 0.25$	50	336	345
UCT9	0.641	67.51	0.601	78.33	200	60	0.15	$\varepsilon_1 = 5\%$	60	98	114
UCT10	0.636	69.02	0.590	81.31	200	60	0.15	$\varepsilon_1 = 7.5\%$	60	10	32
UCT11	0.638	68.46	0.591	81.11	200	60	0.15	$\varepsilon_1 = 10\%$	60	9	25
UCT12	0.632	70.09	0.631	70.29	200	60	0.15	$N_d = 1$	60	25	28
UCT13	0.638	68.41	0.637	68.68	200	60	0.15	$N_d = 5$	60	74	78
UCT14	0.629	70.86	0.626	71.55	200	60	0.15	$N_d = 20$	60	346	351

70 kPa ($0.1125 \leq \text{CSR} = q^{\text{amp}}/(2p_0) \leq 0.175$). A schematic representation of their initial total and effective stresses is presented in Figure 3.6. For illustration purposes, a typical result on test UCT1 with deviatoric stress amplitude of $q^{\text{amp}} = 45$ kPa is presented in Figure 3.7. The typical evolution of the total and effective stresses is presented in Figure 3.7a. Some observations regarding the experimental results are worthy to remark: the final stage of tests with isotropic consolidation (cyclic mobility phase) exhibit butterfly-shaped effective stress paths, see Figure 3.7c. Three remarkably different accumulation rates of the relaxation of the mean effective stress, or analogously, the accumulated pore water pressure u_w^{acc} are observed, see Figure 3.7c,d. Initially, a fast accumulation of the pore water pressure is evidenced. This stage was denoted as "A". Later, during stage "B" the pore water pressure accumulates at a lower (and almost constant) rate. At the end of the test, the accumulation rate increases again during stage "C". The analysis of the stress-strain behavior is presented in Figure 3.7e. Similar to former results reported using undrained cyclic triaxial tests, and differing from typical results on undrained cyclic simple shear tests, the vertical strain accumulation is asymmetric with higher accumulation in the extension side compared with the compression side e.g. [104, 177, 246, 262, 263]. The results also indicate that accumulation of axial strains grows at a very small rate until reaching the stage "C", after which the axial strain amplitude quickly grows with each subsequent cycle until reaching the defined failure criterion $|\varepsilon_1| = 10\%$, see Figure 3.7b,d,f.

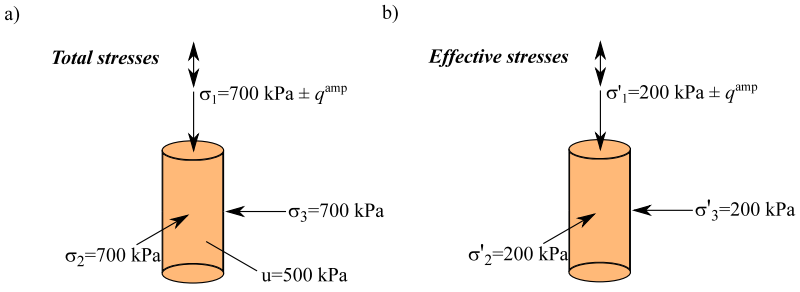

Figure 3.6: Typical initial total and effective stresses

Figures 3.8 and 3.9 present the results of undrained cyclic triaxial tests UCT1-UCT4. A remarkable increase in the accumulation rate of strains and pore water pressure, and therefore, a reduction in the number of cycles to reach the failure criterion is observed with increasing deviatoric stress amplitude, see Figure 3.9a,b. This is evident by comparing tests UCT1 with $q^{\text{amp}} = 45$ kPa and UCT4 with $q^{\text{amp}} = 70$ kPa, in which the number of cycles to reach initial liquefaction N_{il} changed from 215 to 6, respectively. This tendency is also evident in Figure 3.9c, which presents the analysis of the Cyclic Stress Ratio (CSR)

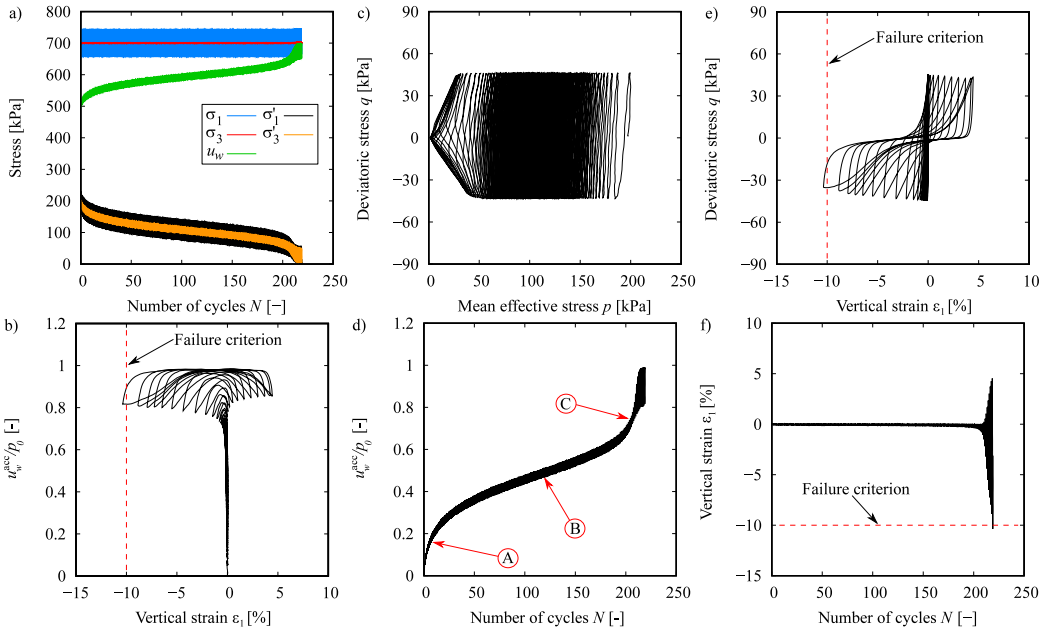

Figure 3.7: Typical results of an undrained cyclic triaxial test (UCT1) with isotropic consolidation ($p_0 = 200$ kPa, $q_0 = 0$, $\eta_0 = 0$) and deviatoric stress amplitude of $q^{\text{amp}} = 45$ kPa

against N_{il}. The reduction in N_{il} with increasing CSR was fairly well described ($R^2 = 0.99$) by a potential function in the form $\text{CSR} = aN_f^b$, with $a = 0.2129$ and $b = -0.115$. Finally, Figure 3.9d presents the variation of the secant Young's modulus $E = q^{\text{amp}}/\varepsilon_1^{\text{amp}}$ after the first cycle (i.e. $N \geq 2$). The results suggest a significant degradation of the secant Young's modulus E with increasing vertical strain amplitude $\varepsilon_1^{\text{amp}}$. The obtained results on undrained cyclic triaxial tests with isotropic consolidation and variation of the deviatoric stress amplitude are in good agreement with former experimental results reported on granular soils, e.g. [70, 80, 104, 205, 247, 248, 276, 284, 285].

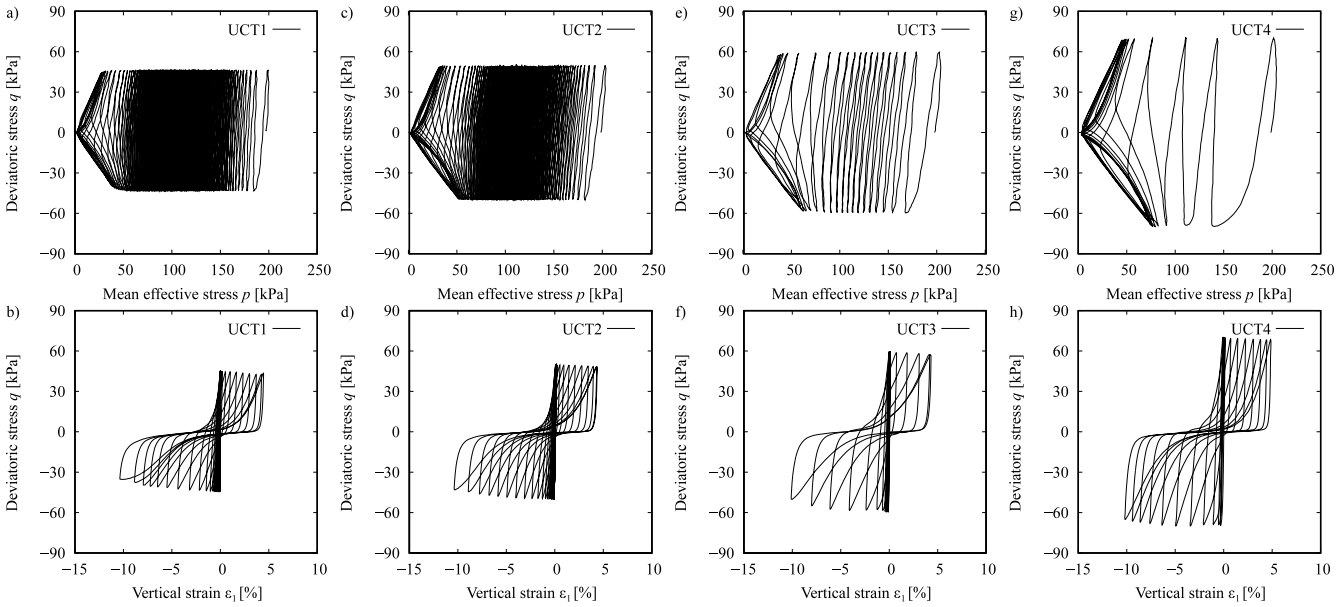

Figure 3.8: Undrained cyclic triaxial tests UCT1-UCT4 with isotropic consolidation ($p_0 = 200$ kPa, $q_0 = 0$, $\eta_0 = 0$) and variation of the deviatoric stress amplitude $q^{\text{amp}} = \{45, 50, 60, 70\}$ kPa

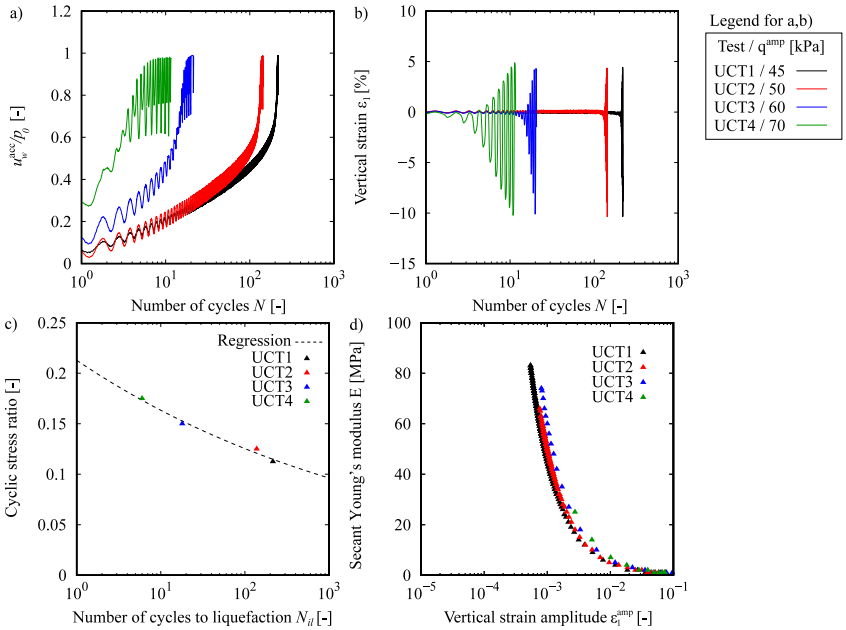

Figure 3.9: Summary of undrained cyclic triaxial tests UCT1-UCT4 with isotropic consolidation ($p_0 = 200$ kPa, $q_0 = 0$, $\eta_0 = 0$) and variation of the deviatoric stress amplitude $q^{\text{amp}} = \{45, 50, 60, 70\}$ kPa: a) normalized accumulated pore water pressure u_w^{acc}/p_0 against the number of cycles N, b) vertical strain ε_1 against the number of cycles N, c) cyclic stress ratio CSR against the number of cycles to reach initial liquefaction N_{il}, d) degradation of the secant Young's modulus E against the vertical strain amplitude $\varepsilon_1^{\text{amp}}$

Tests with undrained cyclic preloadings

This section evaluates the influence of undrained cyclic preloadings in the subsequent undrained cyclic resistance. For that purpose, undrained cyclic triaxial tests UCT5-UCT7 and UCT9-UCT11 were performed considering the same initial conditions as test UCT3 (i.e. isotropic consolidation with $p_0 = 200$ kPa and deviatoric stress amplitude $q^{\text{amp}} = 60$ kPa) but considering different preloading limit criteria, see Table 3.3. The tests of this section were performed with the following sequence: undrained cyclic shearing until reaching the corresponding preloading limit criteria (at $q = 0$): $r_u = \{0.25, 0.5, 0.75\}$ (with $\varepsilon_1 < 1.5$ %) or $\varepsilon_1 = \{5, 7.5, 10\}$ % (with $r_u = 1$). Subsequently, the samples were isotropically re-consolidated until the initial mean effective stress of the tests ($p = 200$ kPa). Finally, samples were re-sheared under undrained cyclic conditions until the failure criterion $|\varepsilon_1| = 10\%$ was reached, see Figure 3.10 for illustration purposes.

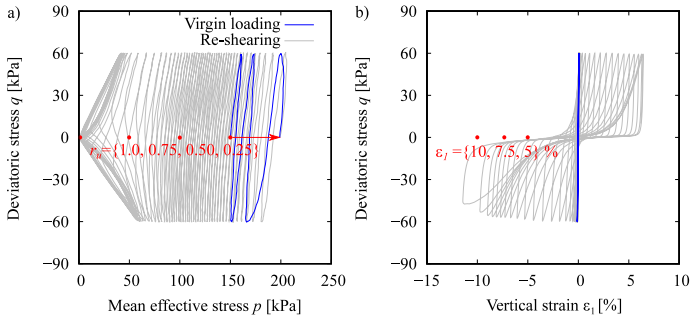

Figure 3.10: Schematic representation of the preloading limit criteria and the tests sequence

The results suggest that undrained cyclic preloadings that lead to $r_u = \{0.25, 0.5, 0.75\}$ (with $\varepsilon_1 < 1.5$ %) provides a remarkable improvement in the subsequent undrained cyclic resistance, see Figure 3.11c-h. Regarding the results in the stress-strain space, there are not noticeable differences in the shape of the hysteresis between tests with and without undrained cyclic preloadings. However, the number of mobilized cycles to reach the failure criterion $|\varepsilon_1| = 10\%$ clearly increases in the samples that were subjected to undrained cyclic preloadings (i.e. on tests with undrained cyclic preloadings the vertical strain accumulation presents a lower rate after cyclic mobility). The remarked increase in the undrained cyclic resistance can not be attributed to the small increase in relative density during the reconsolidation stage ($\Delta D_{r,average} \approx 2$ %, see Table 3.3) but may be related with stronger fabric structures generated by the undrained cyclic preloadings and reconsolidation stages. The obtained results on tests with undrained cyclic preloadings that do not lead to initial liquefaction are in good agreement with former studies on granular soils e.g. [58, 114, 115, 181, 182]. In addition, the improvement in the undrained cyclic resistance after episodes of undrained cyclic loading and reconsolidation stages is in accordance with the centrifuge results reported by Lai et al. [126] and discussed in [52].

Increasing the number of undrained cyclic preloadings eventually lead to initial liquefaction ($r_u = 1$) with a progressive increase in the vertical strain accumulation in extension and compression. In this state, three different preloading limit criteria were considered: $\varepsilon_1 = \{5, 7.5, 10\}$ %, see Figure 3.12. In the aforementioned figure, only the results of the re-shearing stage were included to facilitate its interpretation since on some tests, similar number of cycles were found on both stages. It is clear that there is a strain threshold in which the subsequent liquefaction resistance is worsen even though that there is a high increase in relative density ($\Delta D_{r,average} \approx 11$ %) in the reconsolidation stage. This strain threshold is achieved after large vertical strains of $\varepsilon_1 > 5$ % in which the effective stress paths are fully mobilized and presents butterfly-shaped loops that already crossed the critical and phase transformation lines. This experimental evidence is in disagreement with the conclusions reported by Ishihara and Okada [114, 115]

on loose granular samples but in agreement with the conclusions reported by Porcino et al. [181, 182] on dense samples (similar to the ones considered in this study). On the other hand, similar to the results reported by Yamada et al. [282] and Porcino et al. [181, 182], undrained cyclic preloadings that lead to large strains affect the subsequent undrained behavior in the stress-strain space (notice that higher magnitude of the vertical strain preloading limit criteria lead to subsequent lower strain accumulation in the compression side).

The summary of the tests with undrained cyclic preloadings is presented in Figure 3.13. In particular, the normalized accumulated pore water pressure is presented in Figure 3.13a. It shows that preloadings of $r_u = \{0.25, 0.5\}$ drastically reduces the initial rate of the pore water pressure accumulation and increases the number of cycles to reach initial liquefaction. The application of subsequent undrained cyclic episodes lead to the preloading limit criteria of $r_u = 0.75$ and $\varepsilon_1 = 5$ %, after which the initial pore water pressure accumulation rate starts at a similar rate than the non-preloaded samples but then is reduced leading to higher number of cycles to reach initial liquefaction. Finally, for preloading limit criteria of $\varepsilon_1 = \{7.5, 10\}$ % a faster rate of the pore water pressure is observed accompanied with a drastic reduction in the number of cycles to reach initial liquefaction, see Figure 3.13b. On the other hand, Figure 3.13c presents the analysis of the Cyclic Number Ratio CNR $= N_{il,preloaded}/N_{il,non-preloaded}$, in which a clear improvement on the liquefaction resistance is found up to a strain threshold after which the application of more undrained cyclic preloadings lead to a reduction in the subsequent liquefaction resistance. The results show that the maximum improvement in the liquefaction resistance is found on the test with undrained cyclic preloadings that lead to $r_u = 0.5$, stage in which the non-preloaded sample approximately presents the slower pore water pressure accumulation rate.

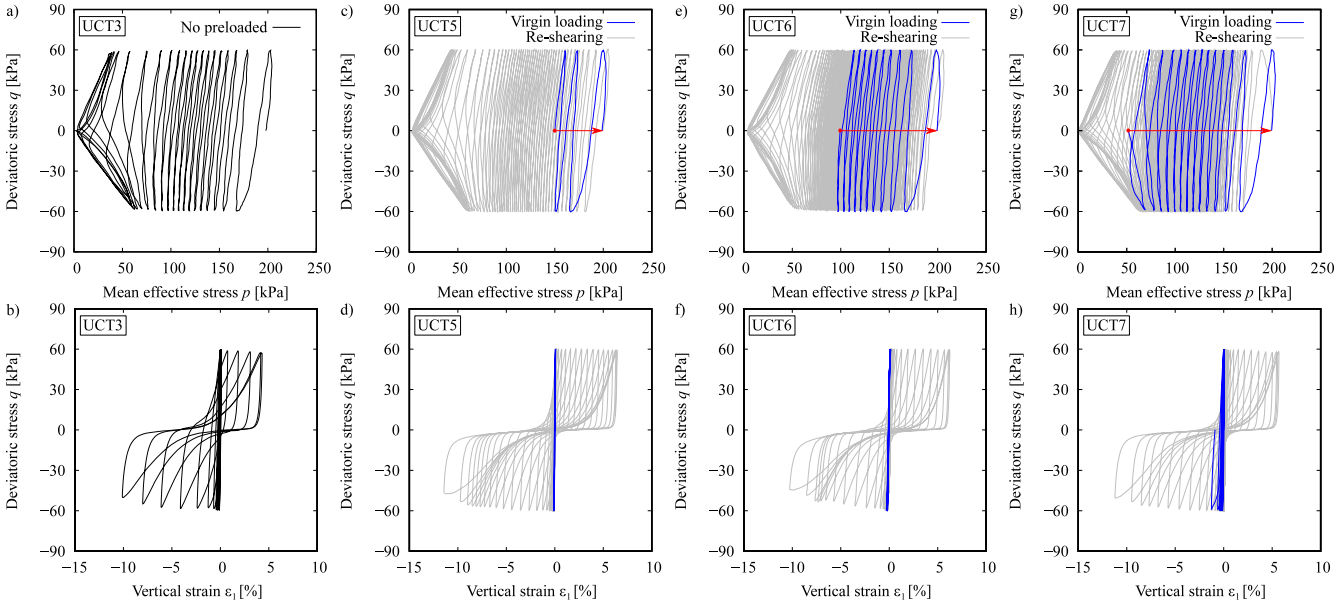

Figure 3.11: Undrained cyclic triaxial tests UCT3, UCT5-UCT7 with isotropic consolidation ($p_0 = 200$ kPa, $q_0 = 0$, $\eta_0 = 0$) and deviatoric stress amplitude $q^{\text{amp}} = 60$ kPa: a,b) no preloading, and undrained cyclic preloading till: c,d) $r_u = 0.25$, e,f) $r_u = 0.50$, g,h) $r_u = 0.75$

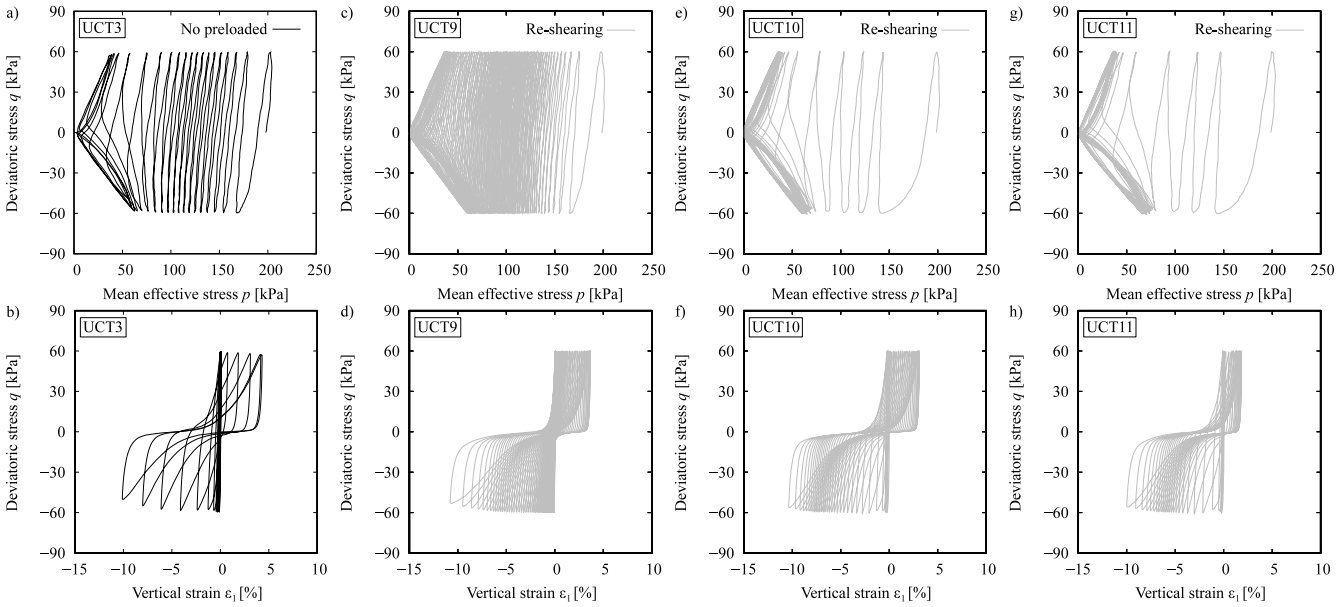

Figure 3.12: Undrained cyclic triaxial tests UCT3, UCT9-UCT11 with isotropic consolidation ($p_0 = 200$ kPa, $q_0 = 0$, $\eta_0 = 0$) and deviatoric stress amplitude $q^{\text{amp}} = 60$ kPa: a,b) no preloading, and undrained cyclic preloading till: c,d) $\varepsilon_1 = 5$ %, e,f) $\varepsilon_1 = 7.5$ %, g,h) $\varepsilon_1 = 10$ %

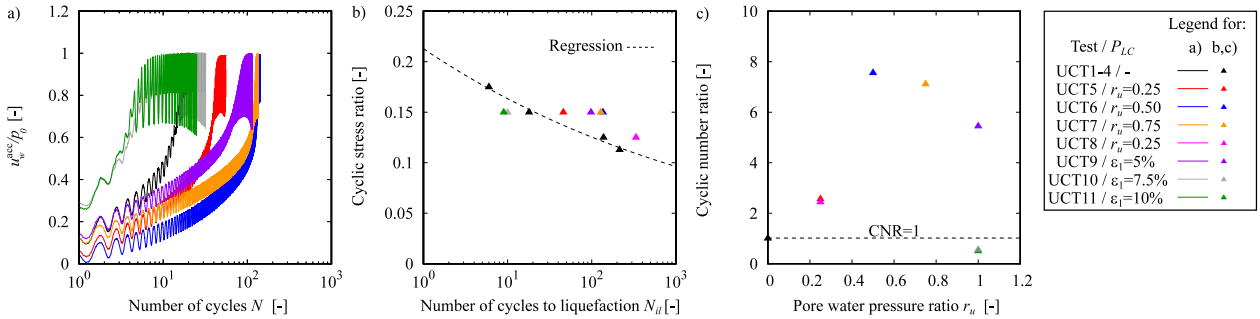

Figure 3.13: Summary of undrained cyclic triaxial tests UCT3 and UCT5-UCT11 with isotropic consolidation ($p_0 = 200$ kPa, $q_0 = 0$, $\eta_0 = 0$) and different undrained cyclic preloadings: a) normalized accumulated pore water pressure u_w^{acc}/p_0 against the number of cycles N, b) cyclic stress ratio CSR against the number of cycles to reach initial liquefaction N_{il}, c) cyclic number ratio CNR against the pore water pressure ratio r_u

Tests with drained cyclic preloadings

This section evaluates the influence of stress-controlled drained cyclic preloadings in the subsequent undrained cyclic resistance. For that purpose, undrained cyclic triaxial tests UCT12-UCT14 were performed considering the same initial conditions as test UCT3 but considering $N_d = \{1, 5, 20\}$ symmetric drained cyclic preloadings with $q^{\text{amp}}_{\text{preloading}} = 60$ kPa. In the drained preloadings, the radial stress σ_3 was maintained constant while the axial stress σ_1 evolved cyclically with $\sigma^{\text{amp}}_{1,\text{preloading}} = q^{\text{amp}}_{\text{preloading}}$.

The results of tests UCT3 and UCT12-UCT14 are presented in Figure 3.14 and are summarized in Figure 3.15. The performed drained cyclic preloadings are schematized in color red. Similar to the results reported by Wichtmann and Triantafyllidis [275], the application of a drained preloading (i.e. $N_d = 1$) moderately affect the subsequent pore water pressure accumulation and the number of cycles to reach initial liquefaction. However, and in accordance with [275], the test with $N_d = 1$ follows the same CSR-N_{il} curve of non-preloaded samples, see Figure 3.15c. Increasing the number of drained cyclic preloadings N_d prior to the subsequent undrained cyclic shearing considerably reduces the initial rate of pore water pressure accumulation, and therefore, increases the number of cycles to reach initial liquefaction (and the failure criterion $|\varepsilon_1| = 10\%$). For example, while test UCT3 without preloadings required $N_{il} = 18$, test UCT14 with $N_d = 20$ required $N_{il} = 346$. Regarding the results in the stress-strain space, there are not noticeable differences in the shape of the hysteresis between tests with and without drained cyclic preloadings. However, the number of mobilized cycles to reach the failure criterion $|\varepsilon_1| = 10\%$ increases with increasing N_d (i.e. the vertical strain accumulation presents a lower rate after cyclic mobility on tests with increasing N_d). The obtained results are in good agreement with former studies on granular soils e.g. [5, 175, 271]. The drastic change in the pore water pressure accumulation tendency and in the number of cycles to reach failure conditions can not be explained by the small reduction in void ratio during the drained stage (see Table 3.3), and may be attributed to effects of recent stress/strain history and fabric changes due to stress/strain induced anisotropy.

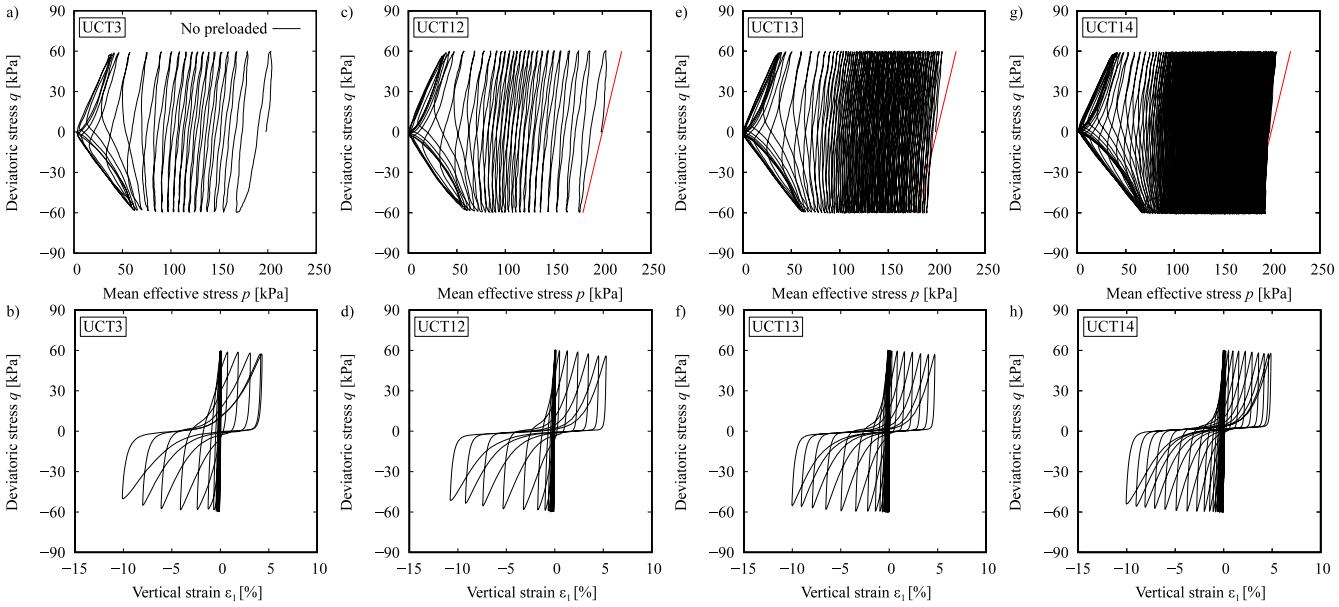

Figure 3.14: Undrained cyclic triaxial tests UCT3, UCT12-UCT14 with isotropic consolidation ($p_0 = 200$ kPa, $q_0 = 0$, $\eta_0 = 0$), deviatoric stress amplitude $q^{\text{amp}} = 60$ kPa and variation of the number of drained cyclic preloadings: a,b) no preloading, c,d) $N_d = 1$, e,f) $N_d = 5$, g,h) $N_d = 20$

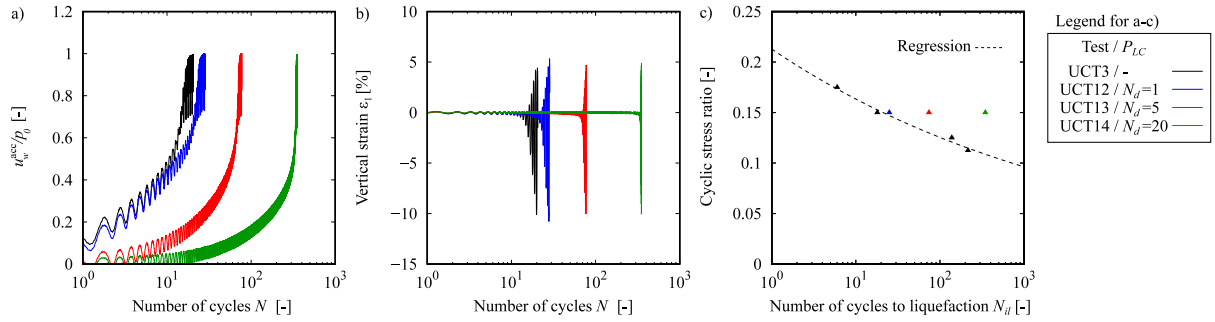

Figure 3.15: Undrained cyclic triaxial tests UCT3, UCT12-UCT14 with isotropic consolidation ($p_0 = 200$ kPa, $q_0 = 0$, $\eta_0 = 0$), deviatoric stress amplitude $q^{\text{amp}} = 60$ kPa and variation of the number of drained cyclic preloadings: a) normalized accumulated pore water pressure u_w^{acc}/p_0 against the number of cycles N, b) vertical strain ε_1 against the number of cycles N, c) cyclic stress ratio CSR against the number of cycles to reach initial liquefaction N_{il}

An analysis of the influence of the number of drained or undrained cyclic preloadings in the subsequent liquefaction resistance is presented in Figure 3.16. It can be noted that increasing the number of drained cyclic preloadings leads to an almost linear increase in the cyclic number ratio. On the other hand, as remarked in section 3.4.2, the application of undrained cyclic preloadings lead to an improvement in the cyclic number ratio up to a threshold in which the application of more undrained preloadings leads to negative effects. Interestingly, both drained and undrained preloadings produce a similar effect on the cyclic number ratio in the initial part of the curve.

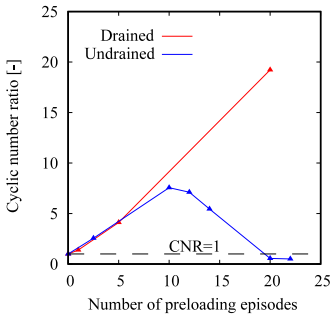

Figure 3.16: Influence of the number of drained or undrained cyclic preloadings with $q^{\text{amp}}_{\text{preloading}} = 60$ kPa in the cyclic number ratio

3.5 Summary and conclusions

This article presented the results of an experimental investigation on Zbraslav sand under monotonic and cyclic loading. Initially, monotonic triaxial and oedometric compression tests were performed for the basic characterization of the material. Furthermore, undrained cyclic triaxial tests with and without cyclic preloadings were performed to investigate the undrained cyclic resistance of the material. The main findings of the study are summarized as:

- Undrained monotonic triaxial tests on medium dense samples showed a contractive behavior followed by dilation. Increasing the initial relative density of the samples leads to a less compressive response at the initial phase of the tests and a higher maximum deviatoric stress.
- The results of undrained cyclic triaxial tests with isotropic consolidation suggest a remarkable influence of the deviatoric stress amplitude in the accumulation rates of pore water pressure and strains, and therefore, in the number of cycles to reach failure conditions. Their final phase is characterized by butterfly-shaped effective stress paths accompanied with a progressive increase of the axial strain amplitude in each subsequent cycle. The vertical strain accumulation is asymmetric with higher accumulation in the extension side compared with the compression side.
- The application of undrained cyclic preloadings lead to a remarkable improvement in the subsequent liquefaction resistance up to a strain threshold. The magnitude of this threshold seems to be much higher in the case of dense samples. In addition, the application of undrained cyclic preloadings that lead to large vertical strains affects the tendency of the subsequent strain accumulation.
- Undrained cyclic triaxial tests with drained cyclic preloadings presented a substantial reduction in the initial rate of pore water pressure accumulation, and therefore, an increase in the number of cycles to reach initial liquefaction. These changes can not be explained by the small reduction in void ratio during the drained stage and may be attributed to effects of recent stress/strain history and fabric changes due to stress/strain induced anisotropy.
- A comparison between the influence of the number of drained or undrained cyclic preloadings in the subsequent liquefaction resistance showed different trends. While increasing the number of drained cyclic preloadings always lead to an increase in the cyclic number ratio, the application of undrained cyclic preloadings lead to an improvement in the cyclic number ratio up to a threshold in which the application of more undrained preloadings lead to negative effects.

The experimental data presented in this article will be freely available at the soilmodels.com website [89], and is expected to be used for the validation and improvement of constitutive models on scenarios involving different types of cyclic preloadings.

3.6 Acknowledgements

The authors appreciate the financial support given by the grant No. 21-35764J of the Czech Science Foundation and the financial support by the INTER-EXCELLENCE project LTACH19028 by the Czech Ministry of Education, Youth and Sports. The first author appreciates the financial support given by the Charles University Grant Agency (GAUK) with project number 200120. The first and third authors acknowledge the institutional support by the Center for Geosphere Dynamics (UNCE/SCI/006).

Notation

Symbol	Name
B	Skempton's coefficient
C_c	coefficient of curvature
C_u	uniformity coefficient
CO_2	carbon dioxide
CSR	cyclic stress ratio
CNR	cyclic number ratio
d	diameter
D_r	initial relative density
$D_{r_{bp}}$	initial relative density before the preloading
D_{50}	mean particles diameter
e	void ratio
e_0	initial void ratio
$e_{0_{bp}}$	initial void ratio before preloading
e_max	maximum void ratio
e_min	minimum void ratio
E	secant Young's modulus
G_s	specific gravity
h	height
M_{PTL}	slope of the phase transformation line
N	number of cycles
N_{il}	number of cycles to reach initial liquefaction
N_f	number of cycles to reach the failure criterion
PTL	phase transformation line
p	mean effective stress
P_{LC}	preloading limit criterion
q	deviatoric stress
q^amp	deviatoric stress amplitude
r_u	pore water pressure ratio
R^2	coefficient of determination
u_w^acc	accumulated pore water pressure
u_w^acc/p_0	normalized accumulated pore water pressure
ε_1	vertical strain
$\varepsilon_1^\mathrm{amp}$	vertical strain amplitude
φ_c	critical state friction angle
γ	shear strain
η	stress ratio
ν	displacement rate
σ_1	axial stress
σ_3	radial stress

Chapter 4

Inspection of four advanced constitutive models for fine-grained soils under monotonic and cyclic loading - Article 3

Summary of the article

Reliable predictions of complex geotechnical problems subjected to monotonic and cyclic loading require robust constitutive models for soils, able to predict the mechanical response of the material under a wide range of monotonic and cyclic conditions. This has motivated the development of numerous constitutive models for soils under different mathematical frameworks. While most models have succeeded in capturing certain aspects of the stress-strain response under a number of idealized loading paths, certain issues are revealed when simulating loading scenarios of complex nature or when tested under wide range of monotonic and cyclic conditions. Therefore, the main advantages and limitations of each constitutive model should be very well known before their application on boundary value problems.

Based on several monotonic and cyclic triaxial tests on Karlsruhe kaolin, the present article conducts a direct comparison between experiments and the corresponding simulation results with four advanced constitutive models for fine-grained soils basing their formulation on different mathematical frameworks: the anisotropic hypoplastic model with intergranular strain anisotropy by Fuentes et al. [71], the SANICLAY-B elasto-plastic model by Seidalinov and Taiebat [203], the constitutive Anamnesis model by Tafili [230] and the three surface kinematic hardening model proposed by Stallebrass and Taylor [219] with transverse isotropic elasticity. The experiments and simulations were performed considering a wide range of cyclic conditions which include variation of the deviatoric stress amplitude, initial stress ratio, overconsolidation ratio, axial strain amplitude and cutting direction (and therefore its bedding plane orientation). The presented results elaborate on the specific capabilities and limitations of these advanced models in simulating several essential aspects of the cyclic behavior of fine-grained soils.

Inspection of four advanced constitutive models for fine-grained soils under monotonic and cyclic loading

Duque, J.[1], Tafili, M.[2], Seidalinov, G.[3], Mašín, D.[1], Fuentes, W.[4]

[1]Charles University, Prague, Czech Republic

[2]Ruhr-Universität Bochum, Germany

[3]Fugro Germany Land GmbH, Germany

[4]Findeter, Bogotá, Colombia

Abstract

A wide range of geotechnical structures founded in fine-grained soils are subjected to complex cyclic loading scenarios. The prediction of their behavior has motivated the development of several constitutive models for soils under different mathematical frameworks. Some success has been achieved under certain simplified cyclic conditions. However, the performance of the models is usually not satisfactory when dealing with a wide range of test conditions, such as variation of the loading amplitudes, initial effective stresses, initial stress ratios, overconsolidation ratios, direction of the loading with respect to the bedding plane, among others. Even though this issue is well-known by model developers, few efforts have been made in the literature to analyze and discuss this and other models' limitations. This article investigates the strengths and weaknesses of four advanced constitutive models for anisotropic fine-grained soils, namely: the anisotropic hypoplastic model by Fuentes et al. [71], the SANICLAY-B elasto-plastic model by Seidalinov and Taiebat [203], the constitutive Anamnesis model by Tafili [230] and the three surface kinematic hardening model proposed by Stallebrass and Taylor [219] with transverse isotropic elasticity. In order to achieve that, simulation results with the models are qualitatively and quantitatively compared against a large number of experimental results under monotonic and cyclic loading on an anisotropic kaolin reported by Wichtmann and Triantafyllidis [275].

4.1 Introduction

The study of cyclic loading on saturated clayey natural deposits is of high interest for the analysis of different geotechnical problems, as for example, offshore and onshore structures subjected to environmental loads, filling-emptying cycles on silos and water tanks, pavements under traffic loading, among many others [72, 75, 76, 166, 275]. Some particular characteristics observed on the cyclic behavior of natural clays take relevance on numerical predictions of these geotechnical problems, such as the accumulation rate of strains and pore water pressure [9, 21, 22, 25, 31, 85, 105, 164, 237], the stress attractors states in the sense of Gudehus [86, 88], the inherent and induced anisotropy [151, 153, 154, 232], among other observations. In particular, the material anisotropy affects the mechanical behavior depending on the angle between the loading direction and the bedding plane resulting from the material formation process [71, 118, 198, 234, 236]. At large strain amplitudes, it leads to different strengths, stiffnesses and dilatancy-contractancy characteristics [73, 233, 263]. On the other hand, under small strain amplitudes, it affects the small strain stiffness [51, 71, 169, 196], the accumulation rates of strains and pore water pressure [2, 231, 234, 237, 263] and the inclination of the effective stress paths under undrained cyclic loading [49, 230, 232, 275].

Reliable predictions of the aforementioned geotechnical problems dealing with water saturated fine-grained soils require robust constitutive models able to predict their behavior under undrained cyclic conditions.

Their accuracy depends on their capabilities, which should include at least the above-mentioned observations. Authors of different models capable to reproduce monotonic and cyclic loading on fine-grained soils, have formulated models with different mathematical structures to allow the reproduction of some anisotropic effects. It is difficult to classify models for cyclic loading in fine-grained soils, but some key ingredients considered in their formulation provide some hints about their capabilities and limitations. For example, it is expected that models including Cam-Clay type yield surfaces, able to harden kinematically, are capable to simulate the influence of anisotropy on the stiffness and strength, but cannot provide different small strain stiffnesses depending on the bedding plane orientation. On the other hand, models accounting for anisotropic elastic tensors, do consider the dependence of small strain stiffness with the bedding plane orientation, but do not guarantee correct assessment on cycles close to the critical state, where fabric changes due to large deformations are important. Finally, the prediction of the accumulation rate of strains and pore water pressure, which is known to depend on the loading direction, depends on the special features of the plastic strain rate formulation.

Contrasting with many works in the literature, the present one aims to show and analyze the main advantages and limitations of some available constitutive models, claiming to reproduce the monotonic and cyclic behavior of anisotropic fine-grained soils. This is achieved by analyzing the simulations with four different models for cyclic loading for anisotropic fine-grained soils, basing their formulations on different mathematical structures, namely: the anisotropic hypoplastic model extended with Intergranular Strain Anisotropy (AHP+ISA) by Fuentes et al. [71], the SANICLAY-B elasto-plastic model by Seidalinov and Taiebat [203], the Anamnesis model by Tafili [230] and the three surface kinematic hardening model by Stallebrass and Taylor [219], adopting the well-known relations for transverse isotropic elasticity by Graham and Houlsby [84]. Simulations will be performed and compared with monotonic and cyclic tests on an anisotropic kaolin reported by Wichtmann and Triantafyllidis [275]. The experiments include an oedometer test with multiple unloading-reloading cycles, five undrained monotonic triaxial tests and sixteen undrained cyclic triaxial tests with different controls and initial conditions on samples having vertical and horizontal cutting directions.

The structure of the paper is as follows: first, the main characteristics of each inspected constitutive model are given. Then, a brief description of the numerical implementations is presented. Subsequently, the testing material and selected experiments for simulation purposes are described. After that, the performance of the models is evaluated through the comparison between experimental results and element test simulations. At the end, the weaknesses and strengths of each model are remarked. The notation and convention is as follows: scalar magnitudes (e.g. a, b) are denoted by italic fonts, vectors (e.g. $\mathbf{a}, \mathbf{b}$) with bold lowercase fonts, second-rank tensors (e.g. $\mathbf{A}$, $\mathbf{B}$) with bold capital letter or bold symbols, higher ranked tensors with special fonts (e.g. E, L). Components of the tensors are denoted through indicial notation (e.g. A_{ij}). The Kronecker delta is represented with $1_{ij} = \delta_{ij}$. Components of the effective stress tensor $\boldsymbol{\sigma}$ or strain tensor $\boldsymbol{\varepsilon}$ in compression are positive. In the triaxial space, Roscoe's invariants are defined as $p = (\sigma_a + 2\sigma_r)/3$, $q = (\sigma_a - \sigma_r)$ and $\varepsilon_v = (\varepsilon_a + 2\varepsilon_r)$, $\varepsilon_q = 2(\varepsilon_a - \varepsilon_r)/3$, respectively. The subscripts a and r denote the axial and radial directions, respectively. The stress ratio η is defined as $\eta = q/p$.

4.2 Brief description of the constitutive models

In this section, four existing constitutive models able to describe the behavior of anisotropic clays under monotonic and cyclic loading are briefly explained. We begin with the anisotropic hypoplastic model for clays by Fuentes et al. [71], hereafter referred as AHP+ISA. Its formulation is basically based on extending the anisotropic hypoplastic model for clays by Mašín [151], with the Intergranular Strain Anisotropy (ISA) approach by Fuentes and Triantafyllidis [74]. The resulting model presents some important features

compared to the former version by Mašín [151], such as the reduction of overshooting effects and improved capabilities on the reproduction of pore water pressure under undrained cyclic loading. It also incorporates a transversely isotropic stiffness tensor to account for anisotropic effects on the small strain behavior. Its calibration requires a number of 15 parameters, which are listed in Table 4.1.

Table 4.1: Parameters of the AHP+ISA model for kaolin

φ_c	ξ	λ^*	κ^*	N	ν	α_G	A_g	n_g	R	β_{h0}	β_{hmax}	χ_0	χ_{max}	C_a
[°]	[-]	[-]	[-]	[-]	[-]	[-]	[-]	[-]	[-]	[-]	[-]	[-]	[-]	[-]
26	5.7	0.087	0.013	1.215	0.35	1.9	135	1	0.00035	0.42	1.2	4.3	17	0.018

The SANICLAY-B is an anisotropic critical state model proposed by Seidalinov and Taiebat [202, 203]. This model corresponds to an improved version of the SANICLAY model by Dafalias et al. [40] with the following characteristics: it accounts for a new bounding surface formulation based on a proper repositioning mechanism of the projection center in order to improve cyclic loading simulations. In addition, it considers a damage parameter to describe the stiffness degradation upon cyclic mobility effects. Mechanisms describing the isotropic and rotational hardening as well as the elastic behavior are similar to the ones proposed by Dafalias et al. [40]. The resulting model presents in general improved capabilities on the reproduction of undrained cyclic loading and cyclic mobility effects. It requires 11 parameters which are presented in Table 4.2.

Table 4.2: Parameters of the SANICLAY-B model for kaolin

M_c	M_e	λ	κ	ν	N	h_0	a_d	C	x	k_i
[−]	[-]	[-]	[-]	[-]	[-]	[-]	[-]	[-]	[-]	[-]
0.9	0.84	0.17	0.01	0.2	0.93	50	3	3	1.64	0

The recently proposed Anamnesis model by Tafili [230], hereafter denoted as CAM, is also analyzed in the present work due to the following features. Its formulation incorporates a transversal hypoelastic stiffness tensor to consider anisotropic small strain effects. For this purpose, the existent hypoelastic stiffness is transformed (rotated and scaled) after defining the bedding plane orientation. The strain rate is decomposed into a hypoplastic and a time-dependent one. The hypoplastic strain rate accounts for induced anisotropic effects by considering a back-stress type tensor while the viscous strain rate considers a similar formulation to the ISA-Clay model by [69]. In general, the model incorporated a yield surface, the so-called historiotropic surface, through which the model can be classified also as elastoplastic. Hence, the mathematical formulation of CAM combines the two pioneer developments - hypoplasticity and elastoplasticity. This novel formulation is able to reproduce fairly well the stress-strain behavior of anisotropic clays under cyclic loading, including some viscous effects such as creep and stress relaxation. The model accounts for 15 parameters which are presented in Table 4.3.

Table 4.3: Parameters of the CAM model for kaolin

φ_c	λ	κ	e_{i0}	ν_h	α	I_v	n_{peak}	n_{ptl}	n_o	n_{oi}	c_B	C_2	$n_{Y,D0}$	β_d
[°]	[−]	[−]	[−]	[−]	[−]	[−]	[−]	[−]	[−]	[−]	[−]	[−]	[−]	[−]
26	0.055	0.03	1.158	0.3	1.7	0.02	5.5	8	15	2	0.5	30	0.8	2

An extended version of the three surface kinematic hardening model proposed by Stallebrass and Taylor [219] is herein considered and analyzed. The extended model, hereafter denoted as the A3-SKH model, results from adopting the well-known relations for transverse isotropic elasticity by Graham and Houlsby

[84]. The A3-SKH model incorporates a bounding surface describing the limit of all admissible stress state, and includes two kinematic surfaces, corresponding to the yield and history surfaces, with similar (but not equal) formulations and hardening mechanisms to the ones proposed by Al Tabbaa and Wood [4]. The three surfaces share the same geometrical shape (elliptical), but different sizes. The A3-SKH model consists of 11 parameters which are presented in Table 4.4.

Table 4.4: Parameters of the A3-SKH model for kaolin

φ_c	λ^*	κ^*	N	A_g	n_g	m	α	T	S	ψ
[°]	[-]	[-]	[-]	[-]	[-]	[-]	[-]	[-]	[-]	[-]
26	0.087	0.013	1.215	135	1	0.2	1.9	0.25	0.08	2.1

It is worthy to remark, that the calibration procedure of the model's parameters was performed by its corresponding model developer, to achieve their best performance. Numerical implementations of the CAM and AHP+ISA models considered a substepping explicit scheme, with very small strain increments to provide numerical convergence. They were written using FORTRAN following the "UMAT" syntax from the commercial software ABAQUS Standard. Element test simulations with the CAM and AHP+ISA models were performed with the software INCREMENTAL DRIVER by Niemunis [167]. On the other hand, element test simulations with the SANICLAY-B model were performed using the nonlinear finite-difference code Fast Lagrangian Analysis of Continua (FLAC), while a Forward-Euler scheme was employed for the A3-SKH model. The element test simulations with the A3-SKH model were performed with the element test driver TRIAX developed by Mašín [152].

4.3 Test material and experiments

Experimental results on the anisotropic kaolin reported by Wichtmann and Triantafyllidis [275] are used to analyze the models capabilities. This kaolin has been found to present an anisotropic microstructure arrangement according to some previous studies using scanning electron microscope (SEM) [79]. It is classified as a low plasticity silt (ML), see Figure 4.1, and presents the following characteristics: specific gravity of $G_s = 2.675$, liquid limit of $LL = 47.2\%$, plastic limit of $PL = 35.0\%$, and plasticity index of $PI = 12.2\%$. Samples were prepared by mixing a kaolin dry powder with demineralized water with an initial water content $w_i = 2.5\,LL$. Then, samples were pre-consolidated with a maximum vertical stress of $\sigma_1 = 100$ kPa. In order to inspect its anisotropic properties, cylindrical samples with dimensions $d = h = 50$ mm (diameter and height, respectively) were cut out and tested considering different bedding plane's orientation in the following way: "vertical samples" were cut out vertically and present horizontal bedding plane, while "horizontal samples" were cut out horizontally and present vertical bedding plane, see Figure 4.2. For a more detailed description of the experimental procedure, readers are referred to [275].

Table 4.5 summarizes the testing program reported in [275] and used in the present work. An oedometric compression test with three unloading-reloading cycles, five undrained monotonic triaxial tests and sixteen undrained cyclic triaxial tests are considered. The undrained monotonic triaxial tests were performed on normally consolidated samples considering different initial mean effective pressures $p_0 = \{50, 100, 200, 300, 400\}$ kPa. The first series of the undrained cyclic triaxial tests consist of six tests with different deviatoric stress amplitudes $q^{\text{amp}} = \{30, 40, 45, 50, 60, 70\}$ kPa and isotropic initial stress of $p_0 = 200$ kPa. The testing program under undrained cyclic loading also includes the following variations: four tests with anisotropic initial stresses $\eta_0 = q_0/p_0 = \{0.25, 0.125, -0.125, -0.25\}$ and $p_0 = 200$ kPa; three tests with different initial overconsolidation ratios OCR $= \{1.5, 2.0, 2.5\}$ and two tests controlled with axial strain cycles and different axial strain amplitudes $\varepsilon_1^{\text{amp}} = \{1, 2\}$ %. Finally, a sample with

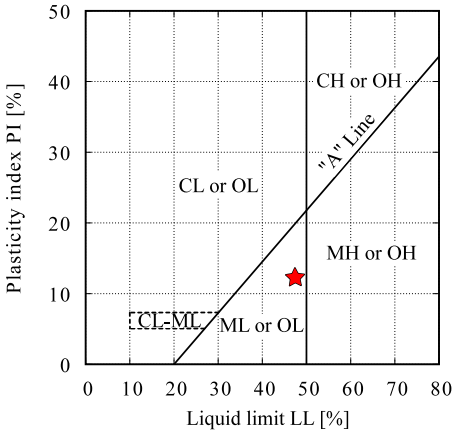

Figure 4.1: Position of the kaolin in the Casagrande plasticity diagram

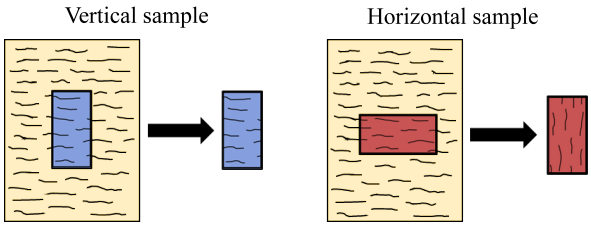

Figure 4.2: Schematic cutting direction of samples

vertical bedding plane (cut out in the horizontal direction) with $p_0 = 200$ kPa subjected to undrained deviatoric cyclic loading with $q^{\text{amp}} = 45$ kPa is considered.

Table 4.5 includes the number of simulated cycles by the models N_s and the number of cycles to reach $|\varepsilon_1| = 10\%$ in the experiments N_f. The authors decided to limit their simulations to a maximum number of $N_s = 150$ considering that numerical errors resulting from the integration of incremental based models are accumulated upon increasing number of cycles [165, 166, 262, 263]. To avoid this issue, models depending explicitly on the number of cycles, e.g. [20, 82, 141, 171, 197, 263], are a more appropriate approach when $N_s > 150$. For the particular case of the SANICLAY-B model, some simulations were stopped before 150 cycles due to the fact that the model produced excessive accumulation of strains for larger number of cycles, as it was developed for earthquake applications where smaller number of cycles are expected.

Table 4.5: Testing program with the kaolin reported by Wichtmann and Triantafyllidis [275]

Test name	p_0 [kPa]	q_0 [kPa]	q^{amp} [kPa]	$\varepsilon_1^{\text{amp}}$ [%]	N_s [-]	N_f [-]	OCR [-]	e_0 [-]	Cutting direction
O1*	-	-	-	-	-	-	-	1.424	Vertical
M1†	50	0	-	-	-	-	1.33	1.434	Vertical
M2†	100	0	-	-	-	-	1.00	1.332	Vertical
M3†	200	0	-	-	-	-	1.00	1.332	Vertical
M4†	300	0	-	-	-	-	1.00	1.244	Vertical
M5†	400	0	-	-	-	-	1.00	1.214	Vertical
C1‡	200	0	30	-	150	>4368	1.00	1.250	Vertical
C2‡	200	0	40	-	150	492	1.00	1.147	Vertical
C4‡	200	0	45	-	131	131	1.00	1.193	Vertical
C5‡	200	0	50	-	68	68	1.00	1.145	Vertical
C7‡	200	0	60	-	11	11	1.00	1.202	Vertical
C8‡	200	0	70	-	7	7	1.00	1.121	Vertical
C26‡	200	50	30	-	150	319	1.00	1.249	Vertical
C27‡	200	25	30	-	150	>2272	1.00	1.319	Vertical
C28‡	200	-25	30	-	150	>7286	1.00	1.248	Vertical
C29‡	200	-50	30	-	150	>2418	1.00	1.248	Vertical
C37‡	100	0	30	-	115	115	1.50	1.239	Vertical
C38‡	100	0	30	-	115	531	2.00	1.200	Vertical
C39‡	100	0	30	-	115	904	2.50	1.146	Vertical
C41‡	200	0	45	-	150	614	1.00	1.252	Horizontal
C43‡	300	0	-	1	150	-	1.00	1.046	Vertical
C44‡	300	0	-	2	150	-	1.00	1.057	Vertical

* Oedometric compression test
† Undrained monotonic triaxial test
‡ Undrained cyclic triaxial test

4.4 Element test simulations with the inspected models

The experimental tests listed in Table 4.5 are now used for simulation purposes. Initial conditions of the state variables of each model were found after reproducing the preloading history of each test.

4.4.1 Oedometric compression test

Simulations of the oedometric test O1 (see Table 4.5), which includes three unloading-reloading cycles and some creep stages (see test description in [69]), is in the following analyzed. The experimental path is compared to simulations in Figure 4.3. It is recalled, that the only model able to capture the time-dependent behavior, such as creep, is the CAM model, as shown in Figure 4.3a. This is attributed to the incorporation of a viscous strain rate and a proper calibration of the viscous parameter I_v. Stiffness characteristics at medium and large strains were also well reproduced by the CAM model, while an underestimation on the stiffness is observed at the beginning of each reloading path, see Figure 4.3a. The unloading-reloading episodes with the CAM model does not reproduce the hysteretic behavior but an almost linear behavior. The AHP+ISA model delivered a slightly stiffer response due to the effect of the intergranular strain. However, this model was able to successfully account for the hysteresis exhibited by the experiment at the unloading-reloading cycles, see Figure 4.3b. Simulation results with the SANICLAY-B model are presented in Figure 4.3c and show an accurate prediction of the compressive behavior, while an overestimation of the unloading-reloading (secant) stiffness. This issue is related to the fact that the parameters controlling the unloading stiffness were calibrated to reproduce its best performance on undrained cyclic triaxial tests. The SANICLAY-B model was also able to predict hysteretic effects upon unloading-reloading cycles. The A3-SKH model was able to accurately reproduce the compressive behavior and hysteretic effects. However, a small overestimation of the stiffness was found upon the unloading-reloading paths since the unloading stiffness was also calibrated based on undrained cyclic triaxial tests. No overshooting effects were found in these particular simulations.

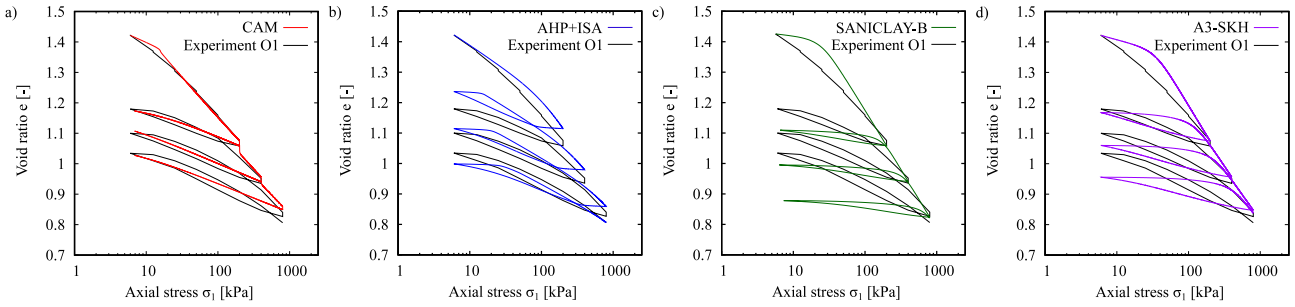

Figure 4.3: Simulations of the oedometric test O1 with three unloading-reloading cycles, $e - \sigma_1$ space: a) CAM, b) AHP+ISA, c) SANICLAY-B, d) A3-SKH

4.4.2 Undrained monotonic triaxial tests

Simulations of five undrained monotonic triaxial tests (see M1-M5 in Table 4.5) on normally consolidated samples with different initial mean effective pressures $p_0 = \{50, 100, 200, 300, 400\}$ kPa were performed for calibration purposes. They in general show an agreement with the experiments, however, a few observations are worthy to remark: the experiments show that the peak is reached at large deformations $\varepsilon_1 > 10\%$. This behavior was only well captured by the CAM model and the A3-SKH model, since they consider hardening mechanisms which are still active upon medium and large strains. In contrast, the AHP+ISA and SANICLAY-B reached a peak behavior at lower strains since they lack of the aforemen-

tioned mechanisms, and instead, these models rendered an almost constant deviatoric stress after the peak has been reached. This effect is much more pronounced on the SANICLAY-B model due to its stiffer response, since parameters controlling the small strain stiffness were selected with special focus to reproduce the undrained cyclic loading and not the monotonic loading.

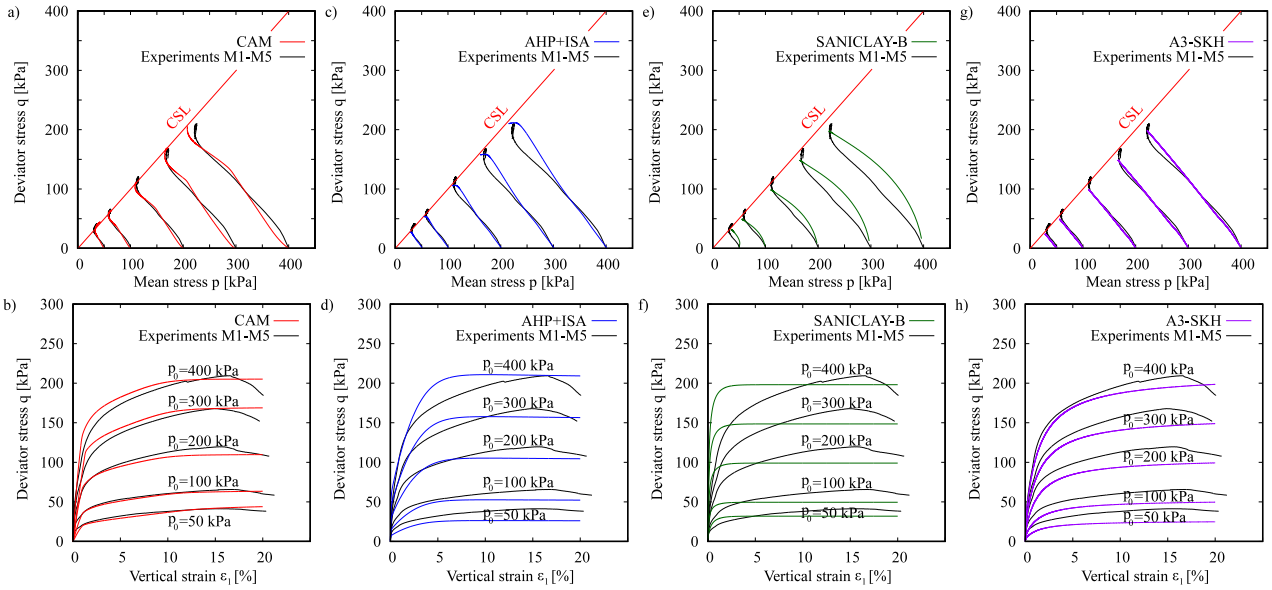

Figure 4.4: Simulations of undrained monotonic triaxial tests M1-M5 on normally consolidated samples with isotropic consolidation ($q_0 = 0$ kPa, $\eta_0 = 0$) and variation of the initial mean effective pressures $p_0 = \{50, 100, 200, 300, 400\}$ kPa: a,b) CAM, c,d) AHP+ISA, e,f) SANICLAY-B, g,h) A3-SKH

4.4.3 Undrained cyclic triaxial tests

In the present section, constitutive models are now inspected under undrained cyclic loading. Variation of the deviatoric stress amplitude, initial stress ratio, overconsolidation ratio, axial strain amplitude, and finally, cutting direction (and therefore its bedding plane orientation) are considered.

Variation of deviatoric stress amplitude

In the following, simulations of undrained cyclic triaxial tests on normally consolidated samples after isotropic consolidation ($p_0 = 200$ kPa, $q_0 = 0$ kPa) considering different deviatoric stress amplitudes $q^{\text{amp}} = \{30, 40, 45, 50, 60, 70\}$ kPa are carefully analyzed. The experimental results as well as their respective simulations in the $q - p$ space are presented in Figure 4.5. From the plots, one immediately notes, that the liquefaction state $p = q = 0$ is not reached in any experiment. Instead, cycles close to the critical state line exhibit "eight-shaped" effective stress loops accompanied with the development of large strain amplitudes. This "eight-shaped" effective stress loops were only predicted by the CAM model, attributed to the consideration of an interaction between inherent anisotropy and dilatancy of the material on its flow rule formulation.

The experiments suggest that the pore water pressure accumulation rate, and therefore the number of cycles to reach the failure criterion (e.g. $|\varepsilon_1| = 10\%$), strongly depends on the magnitude of the deviatoric stress amplitude. On one hand, it is noted that test C1 presenting the lowest deviatoric stress amplitude ($q^{\text{amp}} = 30$ kPa) did not reach $|\varepsilon_1| = 10\%$ after a number of $N = 4368$ cycles. On the other hand, test C8 presenting the highest deviatoric stress amplitude ($q^{\text{amp}} = 70$ kPa) reached the failure criterion $|\varepsilon_1| = 10\%$

after only 7 cycles. From the simulations, one may conclude the following: the CAM model predicts well the mean effective stress reduction upon the cycles under different deviatoric stress amplitudes, see Figure 4.5e-h. This is attributed to the rotation mechanism of the historiotropic flow surface, which affects directly the hypoplastic volumetric strain rate and thus the pore pressure accumulation rate. The AHP+ISA model was able to reproduce accurately the variation of the mean effective stress accumulation rate, see Figure 4.5i-l. This behavior was achieved due to the evolution of function χ, controlling directly the accumulation rate, which increases its value from parameters χ_0 to χ_{max} upon increasing number of cycles. Pore water pressure generation of the critical state-based elasto plastic models (SANICLAY-B and A3-SKH models) is controlled by the adopted plastic potentials, such that compressive plastic volumetric strains imply positive pore water pressure generation and dilative plastic volumetric strains imply negative pore water pressure generation if undrained (constant volume) conditions are imposed. As a matter of fact, due to the adopted model structure defined by kinematic hardening (for A3-SKH) and mapping rules (for SANICLAY-B), these models predict zero plastic volumetric strains not only at the critical state defined by mean effective stress, void ratio and stress ratio, but even if stress ratio is lower than the one corresponding to critical state. Therefore, pore water pressure accumulation stops as soon as mean effective stress reaches critical state value (for current void ratio). This behavior limits the applicability of these models on problems with cyclic loading, whereby the accumulation of excess pore water pressure is essential.

The effective stress paths show a remarked inclination in the $q-p$ space caused by the material's inherent anisotropy. This effect was successfully captured by the CAM and AHP+ISA models, due to the incorporation of a bedding plane-dependent hypoelastic stiffness. It should be mentioned, that these parameters were calibrated to reproduce satisfactorily the small shear stiffness anisotropy, and not the resulting inclination of the effective stress paths on undrained elastic cycles. Therefore, this inclination is considered as a model prediction. While the CAM model incorporates the parameter α to simulate the material's anisotropy, the AHP+ISA model employs parameter α_G for the same purpose. The SANICLAY-B model was not able to reproduce the inclination of the effective stress paths since it considers isotropic (hypo-)elasticity. On the other hand, the A3-SKH model incorporates a transversely isotropic hypoelastic stiffness, but it is evident that the observed effective stress paths inclination does not coincide with the experiments because only the elastic part of the model accounts for inherent anisotropy, and the elastic range of the model is very small. Therefore, the overall response of the model is governed by the elastic and plastic components.

The experimental results in stress-strain space are presented in Figure 4.6a-d. They suggest that the vertical strain accumulation runs at a slow rate until reaching cyclic mobility, in which the double strain amplitude quickly grows with each subsequent cycle. Simulation results with the CAM model suggest that the accumulation of vertical strains before the mobilized cycles was particularly well predicted. The amplitude and shape of the stress-strain hysteresis at cyclic mobility are accurately described, however, the model accumulates in extension despite the accumulation of the experiments in compression. On the other hand, the AHP+ISA predicts a bias in strain accumulation on the compression side after reaching the last mobilized cycles. This behavior is associated with the effect of the Lode's angle on the critical state surface (with different compression and extension critical state slopes). The bias in strain accumulation after cyclic mobility is actually a common limitation of most hypoplastic models and remarks the need to reformulate the dilatancy-contractancy changes at large strain amplitudes (due to the rearrangement of the particles) and the stiffness degradation of most of these type of models [50, 68]. This issue limits the capabilities of the model on problems where the behavior at large deformations take relevance, such as analysis under seismic conditions with a number of cycles. Simulation results with the SANICLAY-B model are presented in Figure 4.6m-p and suggest that this is the only model which realistically reproduces the accumulation of vertical strains both before and after cyclic mobility. Finally, simulations results with the A3-SKH model suggest that the model does not present a bias in strain accumulation, but fails to

reproduce the increasing magnitude of the axial strain in double amplitude with each subsequent cycle.

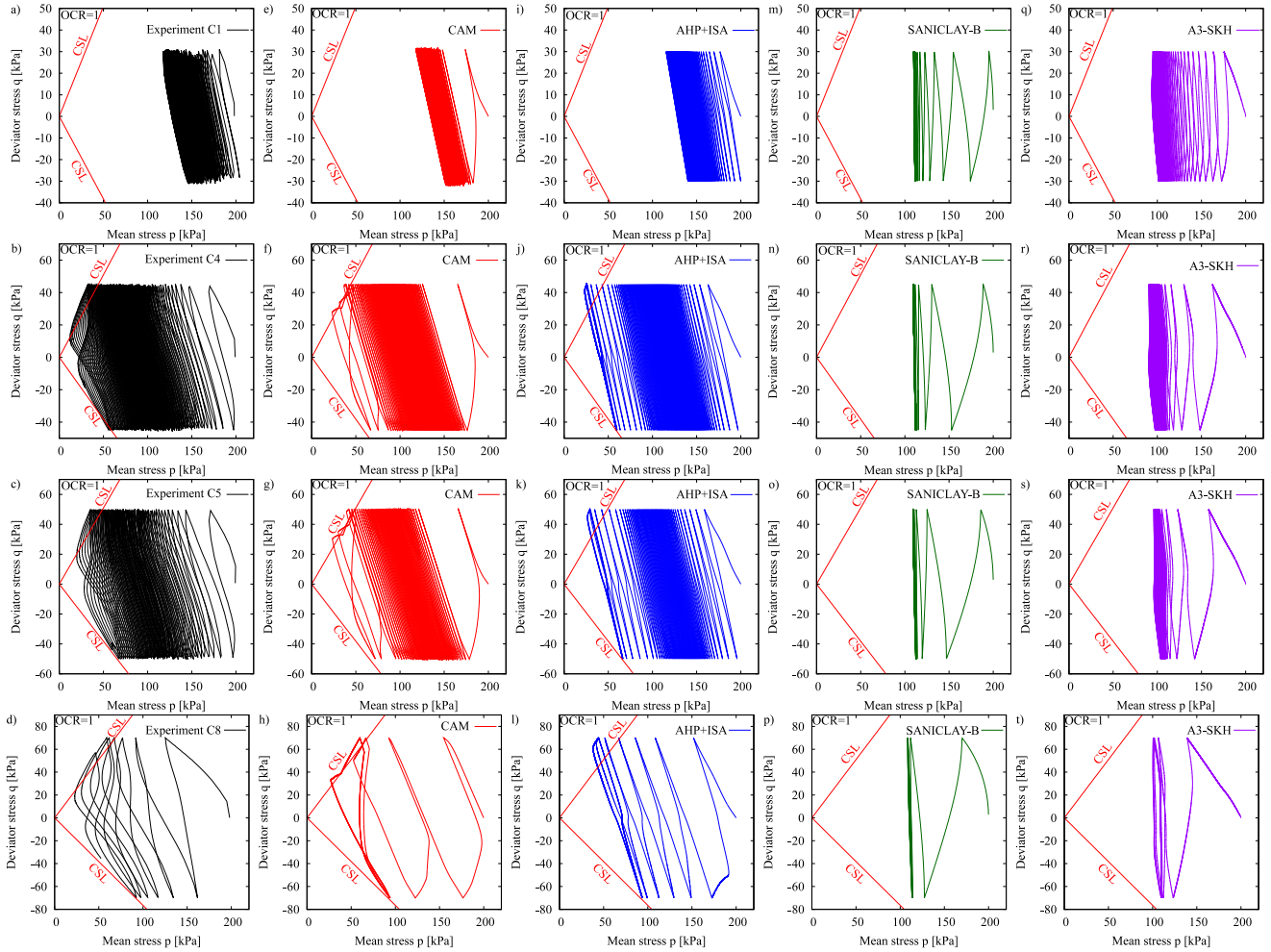

Figure 4.5: Simulations of undrained cyclic triaxial tests C1-C8 on normally consolidated samples with isotropic consolidation ($p_0 = 200$ kPa, $q_0 = 0$ kPa, $\eta_0 = 0$) and variation of the deviatoric stress amplitude $q^{\text{amp}} = \{30, 45, 50, 70\}$ kPa, $q - p$ space: a-d) experiments by Wichtmann and Triantafyllidis [275], e-h) CAM, i-l) AHP+ISA, m-p) SANICLAY-B, q-t) A3-SKH

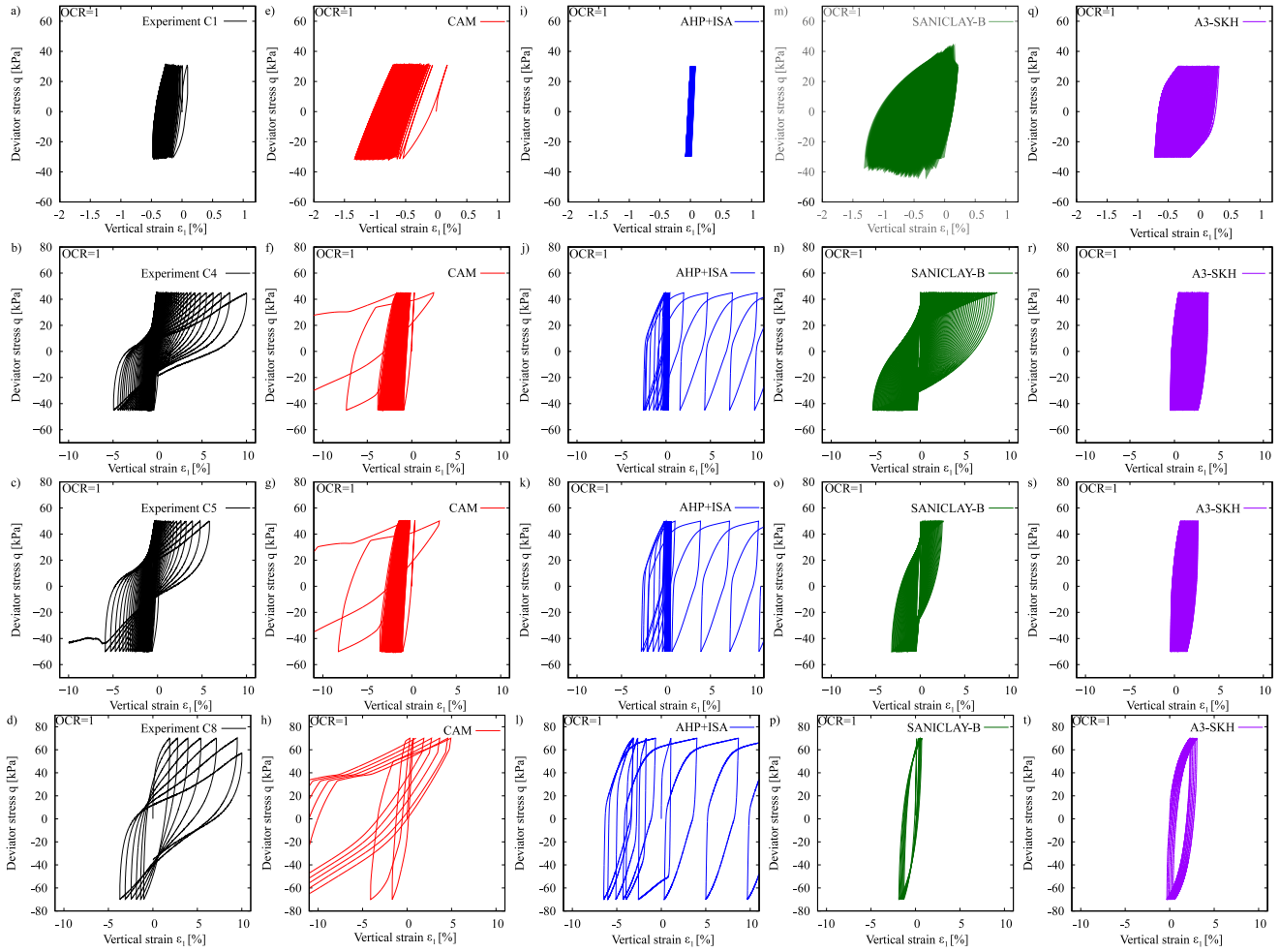

Figure 4.6: Simulations of undrained cyclic triaxial tests C1-C8 on normally consolidated samples with isotropic consolidation ($p_0 = 200$ kPa, $q_0 = 0$ kPa, $\eta_0 = 0$) and variation of the deviatoric stress amplitude $q^{\text{amp}} = \{30, 45, 50, 70\}$ kPa, $q - \varepsilon_1$ space: a-d) experiments by Wichtmann and Triantafyllidis [275], e-h) CAM, i-l) AHP+ISA, m-p) SANICLAY-B, q-t) A3-SKH

The analysis of the accumulated pore water pressure p_w (computed at the middle of each cycle) is presented in Figure 4.7. The results suggest that the CAM and AHP+ISA models were able to reproduce the strong dependency of the pore water pressure accumulation on the deviatoric stress amplitude q^{amp}. On the other hand, the SANICLAY-B and A3-SKH models reproduced a similar pore water pressure accumulation independently of the deviatoric stress amplitude. The proper reproduction of the pore water pressure accumulation with different deviatoric stress amplitudes is a complex task from the constitutive description point of view. Wichtmann [263] reported that even advanced models as the anisotropic visco-hypoplastic model for clays by Niemunis et al. [169], have problems to accurately reproduce a wide range of cyclic conditions with a single set of parameters.

In order to analyze the number of cycles to reach the state at which large strain amplitudes are developed, two failure criteria are hereafter considered: a) axial strain in single amplitude of $\varepsilon_1^{\text{SA}} = 10\%$, and b) axial strain in double amplitude of $\varepsilon_1^{\text{DA}} = 10\%$, see Figure 4.8a,b. The analysis of the cyclic stress ratio $\text{CSR} = q^{\text{amp}}/(2p_0)$ against the number of cycles to reach failure N_{f} is presented in Figure 4.9. For the construction of the experimental curves, the results of tests C1-C8 (with variation of q^{amp} and $p_0 = 200$ kPa) were considered and are presented as black triangles. In addition, a potential fitting regression was

also included as a continuous solid black line. Simulations with the CAM model suggest an accurate performance for both failure criteria. On the other hand, the AHP+ISA model was only able to reach the failure criterion $\varepsilon_1^{\mathrm{SA}} = 10\%$ with a reasonable performance. The SANICLAY-B model was able to reach both failure criteria but with a much steeper strength curves than the experiment. Finally, the A3-SKH model was not able to reach any of the failure criteria.

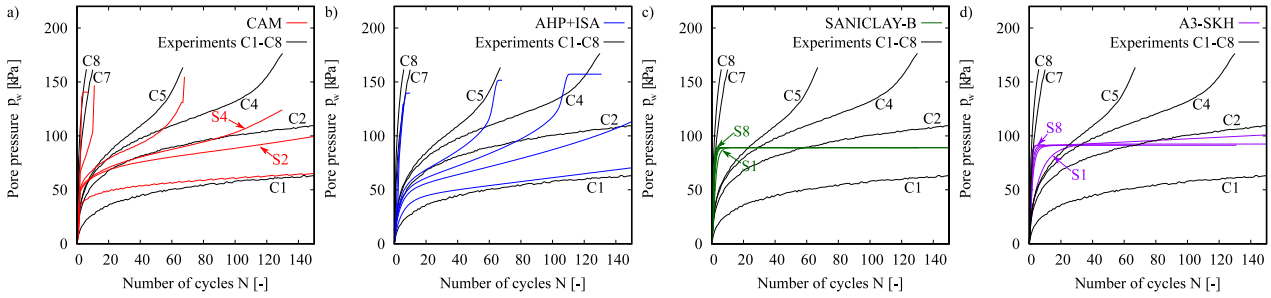

Figure 4.7: Simulations of the accumulated pore water pressure in undrained cyclic triaxial tests C1-C8 on normally consolidated samples with isotropic consolidation ($p_0 = 200$ kPa, $q_0 = 0$ kPa, $\eta_0 = 0$) and variation of the deviatoric stress amplitude $q^{\mathrm{amp}} = \{30, 40, 45, 50, 60, 70\}$ kPa: a) CAM, b) AHP+ISA, c) SANICLAY-B, d) A3-SKH

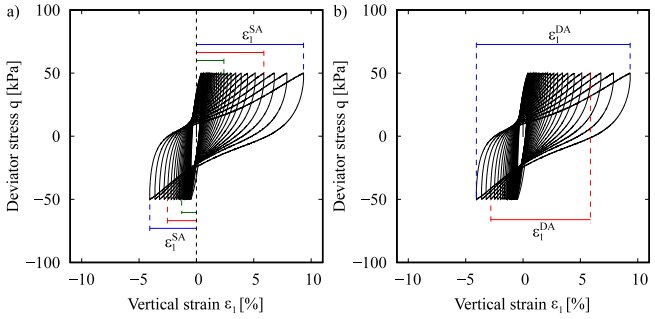

Figure 4.8: Description of the selected failure criteria: a) $\varepsilon_1^{\mathrm{SA}} = 10\%$, b) $\varepsilon_1^{\mathrm{DA}} = 10\%$

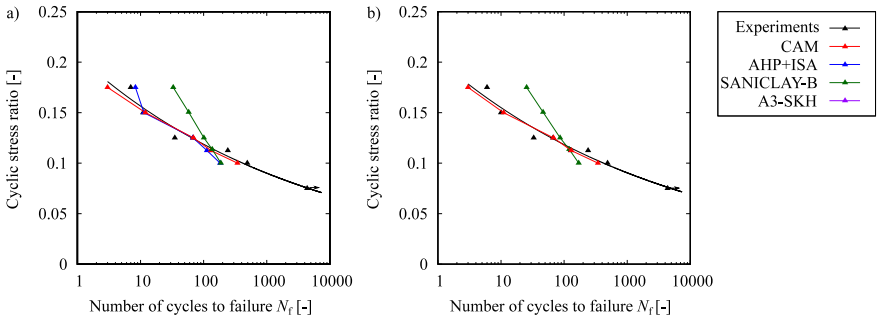

Figure 4.9: CSR-N_{f} curves for different failure criteria: a) $\varepsilon_1^{\mathrm{SA}} = 10\%$, b) $\varepsilon_1^{\mathrm{DA}} = 10\%$

Variation of the initial stress ratio

The influence of the initial stress ratio in the cyclic behavior is now analyzed. For that purpose, undrained cyclic triaxial tests C26-C29 on normally consolidated samples with constant deviatoric stress amplitude of $q^{\text{amp}} = 30$ kPa and anisotropic initial stress ratios $\eta_0 = \{0.25, 0.125, -0.125, -0.25\}$ are considered. The experiments followed an initial isotropic consolidation until $p_0 = 200$ kPa. Then, the axial stress was increased or decreased to achieve the desired initial stress ratio η_0, where the anisotropic consolidation was performed. The experimental results are presented in Figures 4.10a-d and 4.11a-d, and suggest that greater magnitude of the initial stress ratio $|\eta_0|$ generates a faster accumulation of vertical strains, and therefore, a reduction in the number of cycles to reach failure conditions.

Simulations results with the CAM model showed an accurate accumulation of vertical strains and pore water pressure. Some small discrepancies are found in the reduction of the mean effective pressure upon cycles in test C29, with the lower initial stress ratio, see Figure 4.10h. The mentioned discrepancy suggests once more, that the rotation rate of the historiotropic surface in extension should differ from that in compression. On the other hand, simulations results with the AHP+ISA model show an overestimation of vertical strains and pore water pressure accumulation during the first cycles in tests with initial average stress ratios in the triaxial compression regime ($\eta_0 > 0$). In addition, an underestimation of vertical strains and pore water pressure accumulation was found on test C29. This opens the discussion whether parameter β, controlling the strain amplitude required to degrade the stiffness, depends on the stress ratio. Simulations with the SANICLAY-B model suggest an excessive accumulation of vertical strains in all tests with anisotropic consolidation ($\eta_0 \neq 0$). In addition, and similar to tests with isotropic initial stresses, the model only accumulates pore water pressure during the first cycles and remains constant thereafter. Simulation results with the A3-SKH model also suggest an excessive strain accumulation in all tests of this series. Furthermore, the model reproduced lower pore water pressure accumulation on tests C26 and C29 with higher magnitudes of the initial stress ratio $|\eta_0|$, which is opposite to the observed behaviour in the experiments after 150 cycles. A summary of the excess pore water pressure curves is presented in Figure 4.12, and suggests that the performance of the models is less accurate on tests with anisotropic consolidation than in tests with isotropic consolidation.

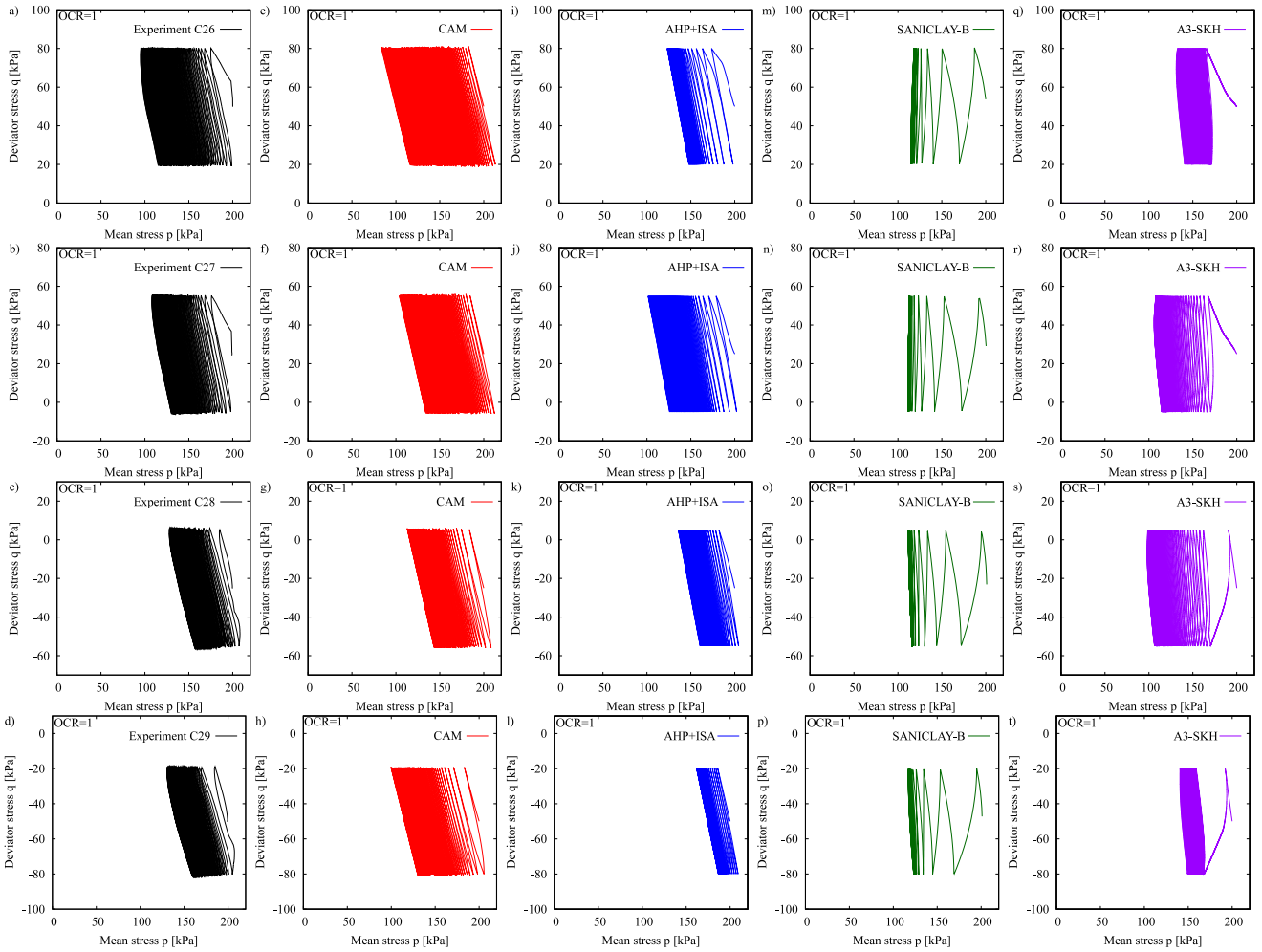

Figure 4.10: Simulations of undrained cyclic triaxial tests C26-C29 on normally consolidated samples with constant deviatoric stress amplitude $q^{\text{amp}} = 30$ kPa, variation of the initial stress ratio $\eta_0 = \{0.25, 0.125, -0.125, -0.25\}$ and $p_0 = 200$ kPa, $q - p$ space: a-d) experiments by Wichtmann and Triantafyllidis [275], e-h) CAM, i-l) AHP+ISA, m-p) SANICLAY-B, q-t) A3-SKH

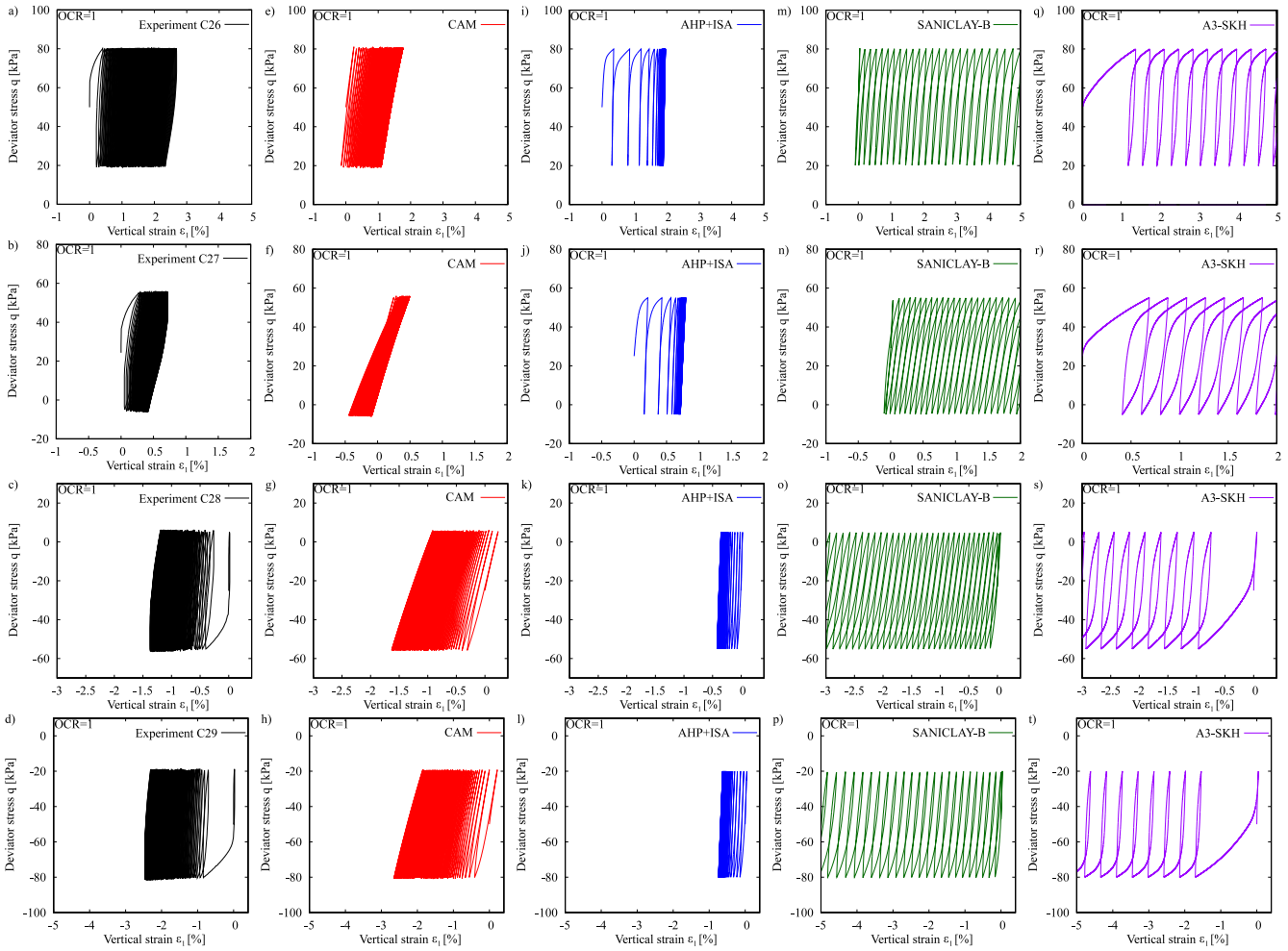

Figure 4.11: Simulations of undrained cyclic triaxial tests C26-C29 on normally consolidated samples with constant deviatoric stress amplitude $q^{\text{amp}} = 30$ kPa, variation of the initial stress ratio $\eta_0 = \{0.25, 0.125, -0.125, -0.25\}$ and $p_0 = 200$ kPa, $q - \varepsilon_1$ space: a-d) experiments by Wichtmann and Triantafyllidis [275], e-h) CAM, i-l) AHP+ISA, m-p) SANICLAY-B, q-t) A3-SKH

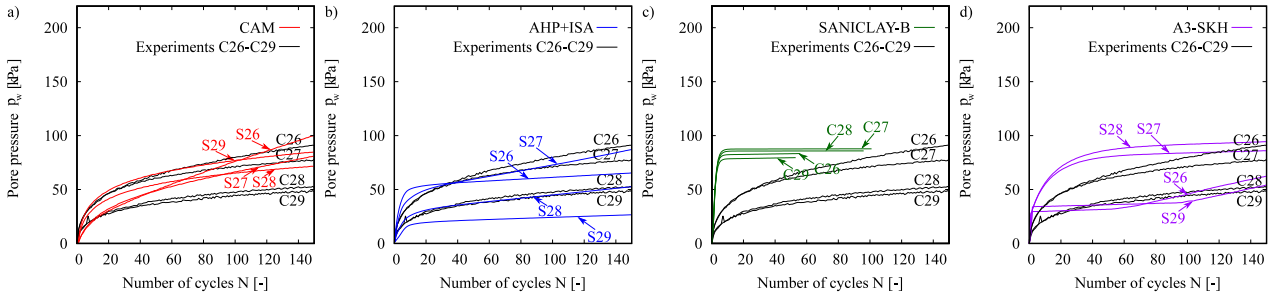

Figure 4.12: Accumulated pore water pressure in the simulations of undrained cyclic triaxial tests C26-C29 on normally consolidated samples with constant deviatoric stress amplitude $q^{\text{amp}} = 30$ kPa, variation of the initial stress ratio $\eta_0 = \{0.25, 0.125, -0.125, -0.25\}$ and $p_0 = 200$ kPa: a) CAM, b) AHP+ISA, c) SANICLAY-B, d) A3-SKH

Variation of the initial overconsolidation ratio

The influence of the initial overconsolidation ratio on the behavior under cyclic loading is of crucial interest, considering that most natural clay deposits are composed of strata with different OCR degrees. For that reason, experiments C37-C39 were numerically simulated considering the same initial mean effective pressure $p_0 = 100$ kPa and deviatoric stress amplitude of $q^{\text{amp}} = 30$ kPa, but preloading the samples up to reach different initial overconsolidation ratios OCR $= \{1.5, 2.0, 2.5\}$. The analysis of these tests were performed considering 115 cycles, since this was the number of cycles required in test C37 to reach failure ($\varepsilon_1^{\text{SA}} = 10\%$). Therefore, considering the same number of cycles, the influence of the initial overconsolidation ratio in the strains and pore water pressure accumulation can be easily compared in tests C38-C39.

The experimental results are presented in Figures 4.13a-c and 4.14a-c. From these tests, it is noted, that as the initial oversonsolidation ratio increases, a higher dilatant response including negative pore pressure is in the first cycle obtained, and a reduction of the pore pressure on the subsequent cycles is observed. From the simulation results with the CAM model one may conclude, that the negative pore pressure in the first cycle was not reproduced. Despite of this, the model was able to capture fairly well the pore pressure accumulation in the subsequent cycles, resulting in a significantly less pronounced reduction of the mean effective stress with increasing initial overconsolidation ratio, as observed in the experiments. The mobilized cycles presenting eight-shaped loops in the $q-p$ space shown on test C37 was also reproduced by the CAM model. On the other hand, the AHP+ISA model managed to reach failure conditions on test C37, however, a bias in strain accumulation on the compression side was reproduced by the model and the eight-shaped loop in the $q-p$ space was not captured. Both drawbacks are explained by the non-consideration of the fabric rearrangement in the flow rule and the drastic reduction of the plastic strain rate produced by the intergranular strain formulation. Simulation results of tests C38 and C39 showed a moderate reduction in the accumulation rate and an inability to reproduce the negative pore water pressure accumulation experimentally observed in the first cycle. Finally, simulation results with both SANICLAY-B as well as the A3-SKH model showed that they were able to reproduce the dilative response observed in the first cycle due to their flow rule formulation. However, simulation results of test C39, with the higher OCR, shows an always increasing negative pore water pressure, which is not observed in the experiment, see Figure 4.13l,o. A summary of the pore water pressure accumulation on tests C37-C39 is presented in Figure 4.15. The results suggest that the influence of the OCR on the pore water pressure accumulation is partly well predicted by the CAM model and AHP+ISA, and less accurate by the SANICLAY-B and A3-SKH models.

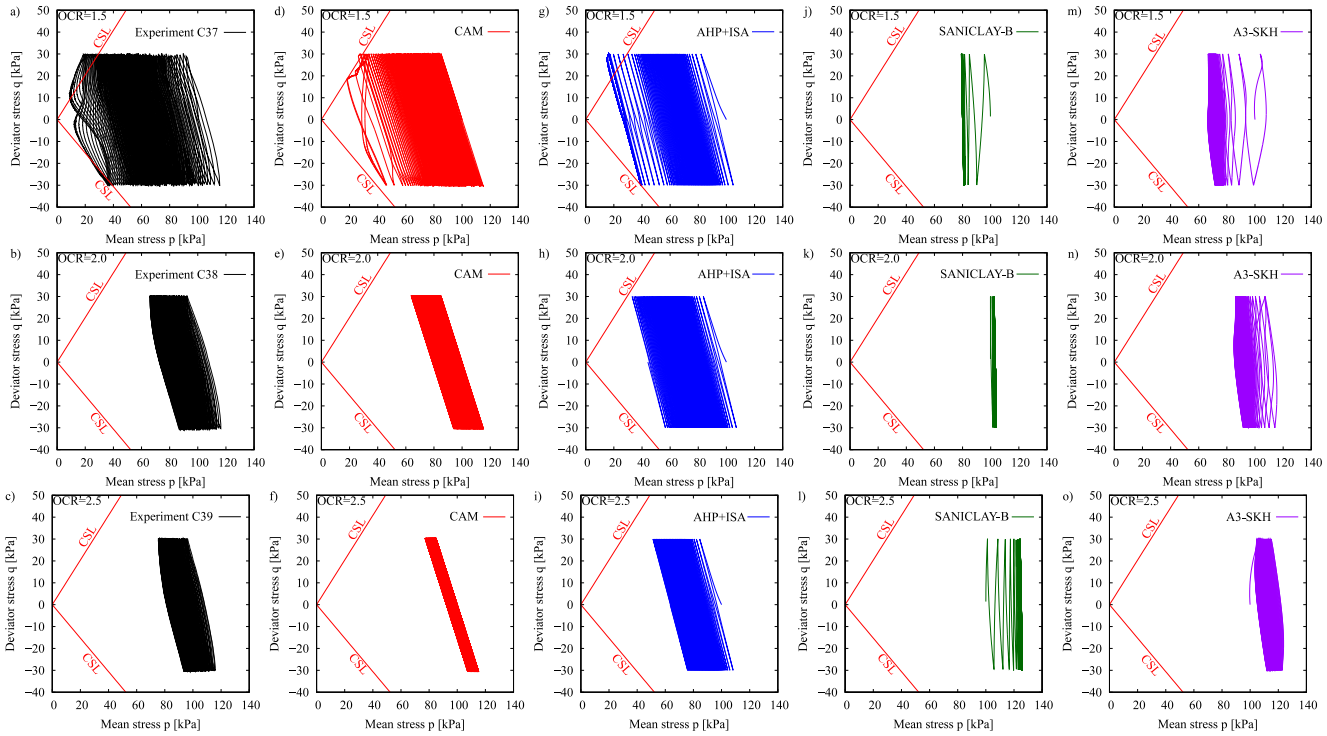

Figure 4.13: Simulations of undrained cyclic triaxial tests C37-C39 with constant deviatoric stress amplitude $q^{\text{amp}} = 30$ kPa, isotropic consolidation ($p_0 = 100$ kPa, $q_0 = 0$ kPa, $\eta_0 = 0$) and variation of the initial overconsolidation ratios OCR $= \{1.5, 2.0, 2.5\}$, $q - p$ space: a-c) experiments by Wichtmann and Triantafyllidis [275], d-f) CAM, g-i) AHP+ISA, j-l) SANICLAY-B, m-o) A3-SKH

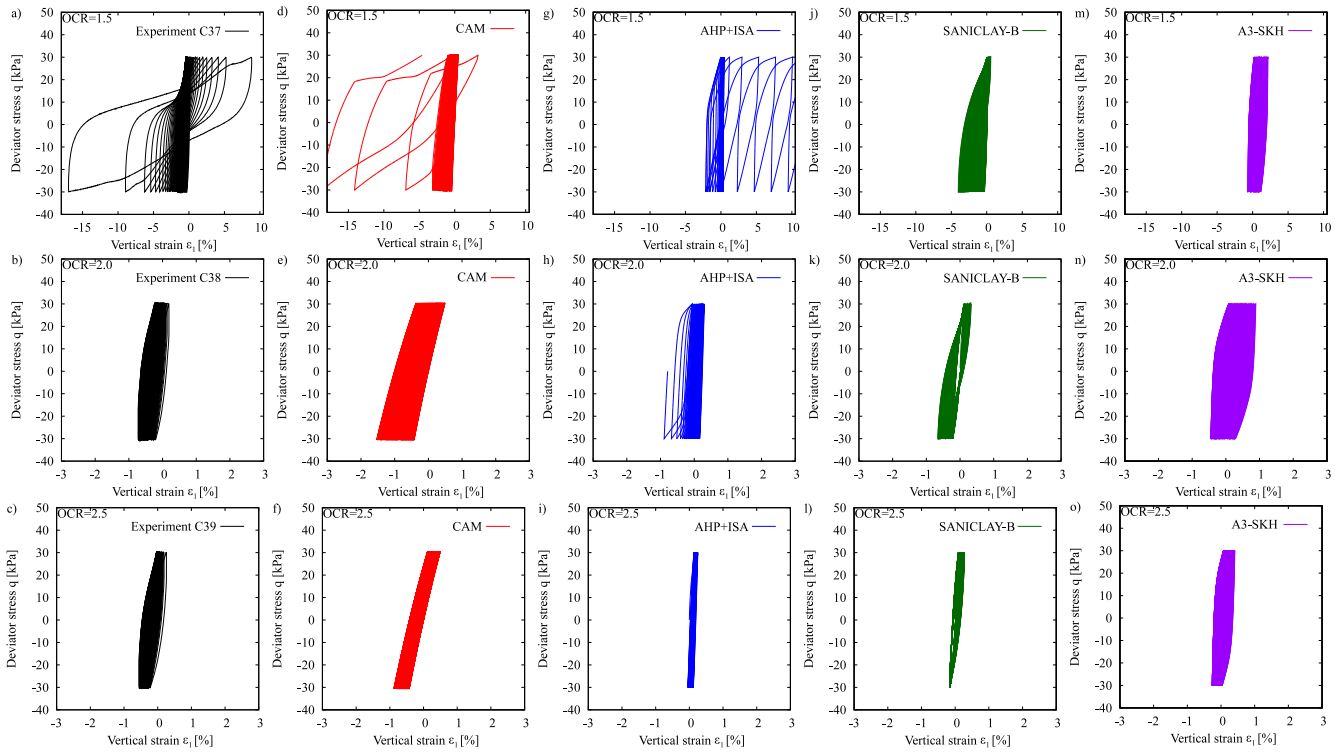

Figure 4.14: Simulations of undrained cyclic triaxial tests C37-C39 with constant deviatoric stress amplitude $q^{\text{amp}} = 30$ kPa, isotropic consolidation ($p_0 = 100$ kPa, $q_0 = 0$ kPa, $\eta_0 = 0$) and variation of the initial overconsolidation ratios OCR $= \{1.5, 2.0, 2.5\}$, $q - \varepsilon_1$ space: a-c) experiments by Wichtmann and Triantafyllidis [275], d-f) CAM, g-i) AHP+ISA, j-l) SANICLAY-B, m-o) A3-SKH

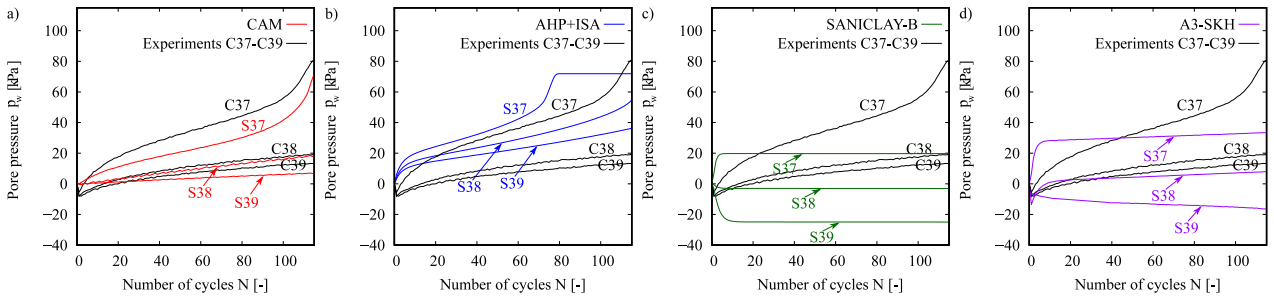

Figure 4.15: Accumulated pore water pressure in the simulations of undrained cyclic triaxial tests C37-C39 with constant deviatoric stress amplitude $q^{\text{amp}} = 30$ kPa, isotropic consolidation ($p_0 = 100$ kPa, $q_0 = 0$ kPa, $\eta_0 = 0$) and variation of the initial overconsolidation ratios OCR $= \{1.5, 2.0, 2.5\}$: a) CAM, b) AHP+ISA, c) SANICLAY-B, d) A3-SKH

Variation of the axial strain amplitude

The next analysis corresponds to undrained cyclic triaxial tests C43-C44. In contrast to previous laboratory data, these tests were performed with strain-controlled cycles, see Figures 4.16a,b and 4.17a,b. The kaolin samples were initially isotropically consolidated with a mean effective stress of $p_0 = 300$ kPa. Subsequently, they were cyclic loaded under a constant axial strain amplitude of $\varepsilon_1^{\text{amp}} = \{1, 2\}$ %. Note that the state with zero effective stress ($p = q = 0$) was not reached in any test. The material exhibits "fir tree" loops when approaching to failure conditions, see Figure 4.16a,b. The experiments show that the increasing number of cycles leads to an increase in the excess pore water pressure accumulation and a progressive reduction of the deviatoric stress amplitude q^{amp} from its maximum magnitude in the first cycle. In addition, an increase in the cyclic axial strain amplitude of the tests generates a higher final accumulation of pore water pressure.

Simulation results with the CAM model suggest that it succeeds to reduce the mean effective stress towards an asymptotic value $p > 0$. However, after a certain number of cycles (after $N \approx 20$), the model produces higher pore pressure accumulation for lower axial strain amplitudes, which is in disagreement with the experiments. The progressive reduction of the deviatoric stress amplitude upon the cycles observed in the stress-strain space was captured by the model, although it shows a faster degradation on the extension side ($q < 0$). Simulations with the AHP+ISA model suggest similar conclusions, in which the test with the higher strain amplitude produce lower pore water pressure accumulation. However, the almost symmetric reduction of the deviatoric stress observed in the stress-strain space was much better reproduced by this model. Finally, simulation results with SANICLAY-B and A3-SKH model suggest the same findings obtained on tests with stress-controlled cycles, where the accumulation of pore water pressure is strongly reduced at $p \approx p_c/2$. Due to this attractor, the deviatoric stress amplitude was not sufficiently degraded. However, the experimental observation that the maximum deviatoric stress was reached in the first cycle, independently of the axial strain amplitude of the test, was only reproduced by the SANICLAY-B model. Figure 4.18 summarizes the accumulation of the pore water pressure on tests C43-C44. In general, the influence of the cyclic axial strain amplitude is moderately reproduced by the CAM and AHP+ISA model, and much less accurate by the SANICLAY-B and A3-SKH models.

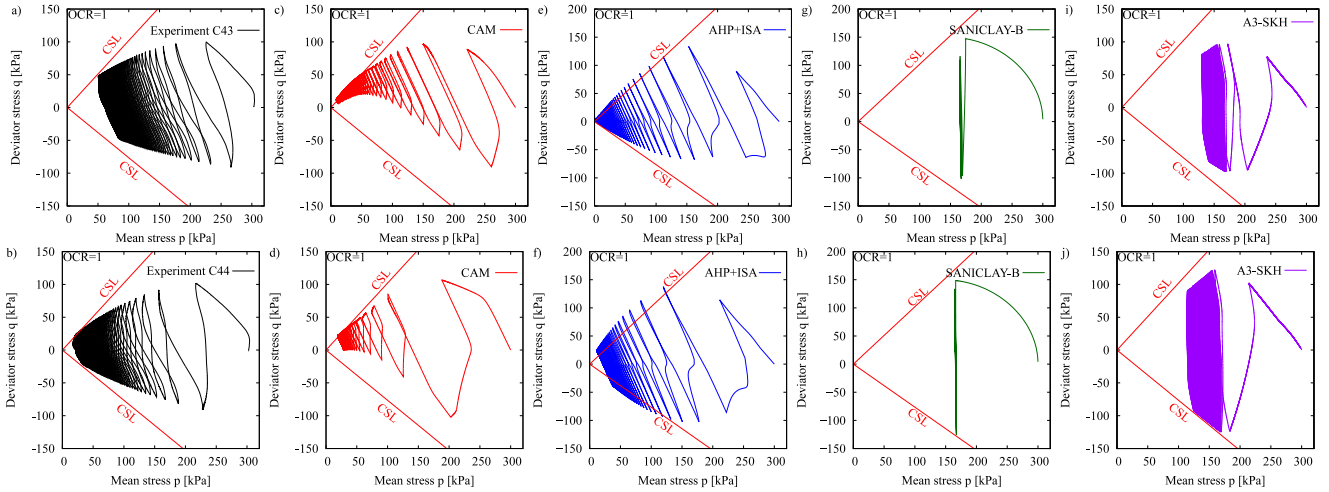

Figure 4.16: Simulations of undrained cyclic triaxial tests C43-C44 on normally consolidated samples with isotropic consolidation ($p_0 = 300$ kPa, $q_0 = 0$ kPa, $\eta_0 = 0$) and variation of the axial strain cycles amplitude $\varepsilon_1^{\text{amp}} = \{1, 2\}$ %, $q - p$ space: a,b) experiments by Wichtmann and Triantafyllidis [275], c,d) CAM, e,f) AHP+ISA, g,h) SANICLAY-B, i,j) A3-SKH

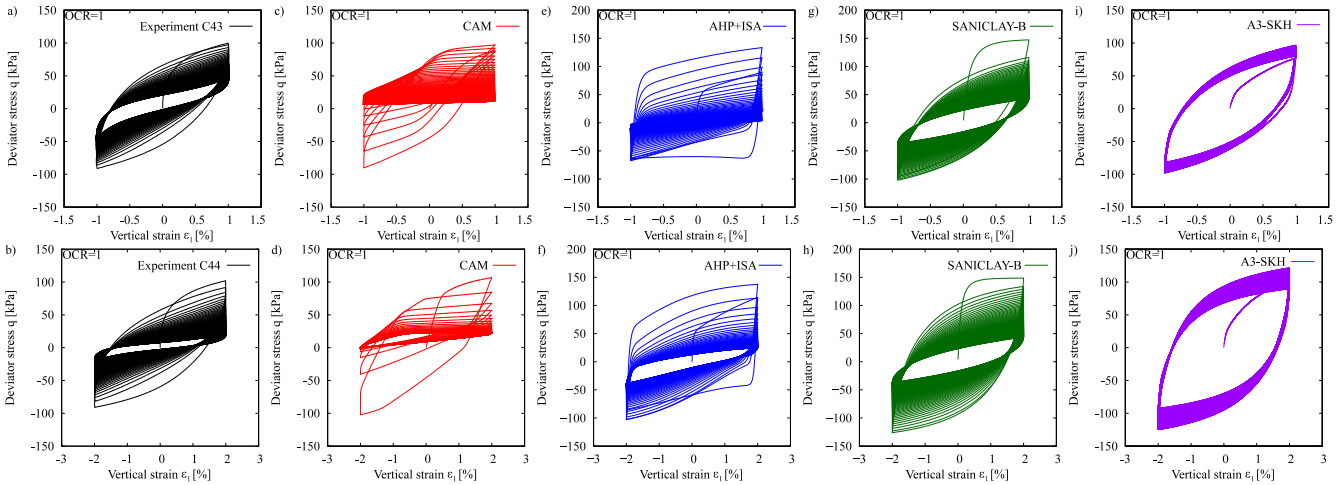

Figure 4.17: Simulations of undrained cyclic triaxial tests C43-C44 on normally consolidated samples with isotropic consolidation ($p_0 = 300$ kPa, $q_0 = 0$ kPa, $\eta_0 = 0$) and variation of the axial strain cycles amplitude $\varepsilon_1^{\text{amp}} = \{1, 2\}$ %, $q - \varepsilon_1$ space: a,b) experiments by Wichtmann and Triantafyllidis [275], c,d) CAM, e,f) AHP+ISA, g,h) SANICLAY-B, i,j) A3-SKH

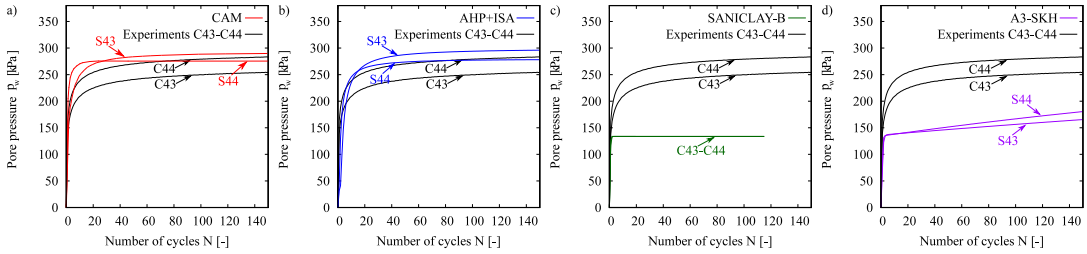

Figure 4.18: Accumulated pore water pressure in the simulations of undrained cyclic triaxial tests C43-C44 on normally consolidated samples with isotropic consolidation ($p_0 = 300$ kPa, $q_0 = 0$ kPa, $\eta_0 = 0$) and variation of the axial strain cycles amplitude $\varepsilon_1^{\text{amp}} = \{1, 2\}$ %: a) CAM, b) AHP+ISA, c) SANICLAY-B, d) A3-SKH

Variation of the cutting direction

The last simulation corresponds to the experiment C41 corresponding to an undrained cyclic triaxial test with the same initial conditions as test C4 ($p_0 = 200$ kPa, $\eta_0 = 0$, $q^{\text{amp}} = 45$ kPa) but having horizontal cutting direction of the sample (vertical bedding plane), see Figure 4.2. The experimental results on test C41 are presented in Figure 4.20a,b and showed a very different behavior in comparison to test C4: a) a stiffer response, b) the number of cycles required to reach failure conditions is considerably higher, c) the strain accumulation is mainly obtained in extension, and d) the effective stress paths of the undrained cycles have an opposite inclination, see figure 4.19. All these experimental evidences are expected to be reproduced by anisotropic models for fine-grained soils. The CAM model was able to reproduce the opposite inclination of the effective stress path in the $q-p$ space. In addition, the accumulation of vertical strains as well as the excess pore water pressure accumulation were reasonably well predicted, see Figure 4.20d and Figure 4.21a. Also, the AHP+ISA model reproduced the inclination of the effective stress path in the $q - p$ space. In addition, the reduction of the mean effective stress was particularly well reproduced. However, an overestimation of the vertical strains was found during the first cycles, similar to the results obtained on tests with anisotropic consolidation. The SANICLAY-B model did not capture

the opposite inclination as other models, considering that it does not incorporate any anisotropic elastic tensor. It also showed a much faster accumulation of pore pressures than the experiments during the first cycles. Finally, simulation results with the A3-SKH model captured partly well the inclination of the $p-q$ path with a less pronounced slope than the experiments. Similar to the SANICLAY-B model, the pore pressure generation on the first cycles was faster than the experiments. A summary of the accumulated pore water pressure curves are presented in Figure 4.21 and suggest accurate predictions with the CAM and AHP+ISA models, while a faster accumulation with the A3-SKH and SANICLAY-B models. The experimental result in the stress-strain space is presented in Figure 4.20b. It suggest that after each cycle the maximum vertical strain in compression and extension always increase, similar to tests with isotropic consolidation and vertical cutting direction, see section 4.4.3. Only the SANICLAY-B model agrees with this experimental observation but with a higher magnitude of the vertical strains. CAM and AHP+ISA models predict a lower magnitude of the vertical strain accumulation but increasing only towards compression, similar to tests with anisotropic consolidation. The vertical strain accumulation with the A3-SKH model increases during the first cycles but remains almost constant thereafter.

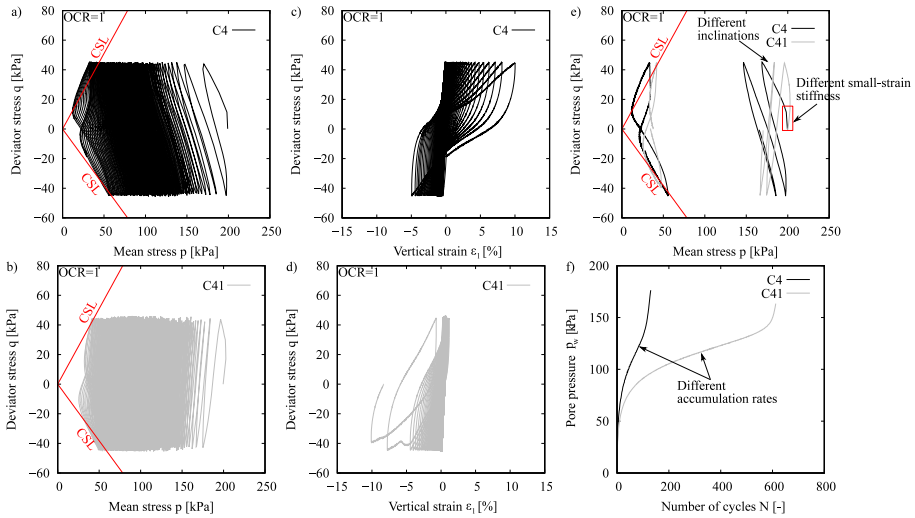

Figure 4.19: Comparison of undrained cyclic triaxial tests C4 and C41 on normally consolidated samples with constant deviatoric stress amplitude $q^{\text{amp}} = 45$ kPa, isotropic consolidation ($p_0 = 200$ kPa, $q_0 = 0$ kPa, $\eta_0 = 0$) and vertical (C4) or horizontal cutting direction (C41)

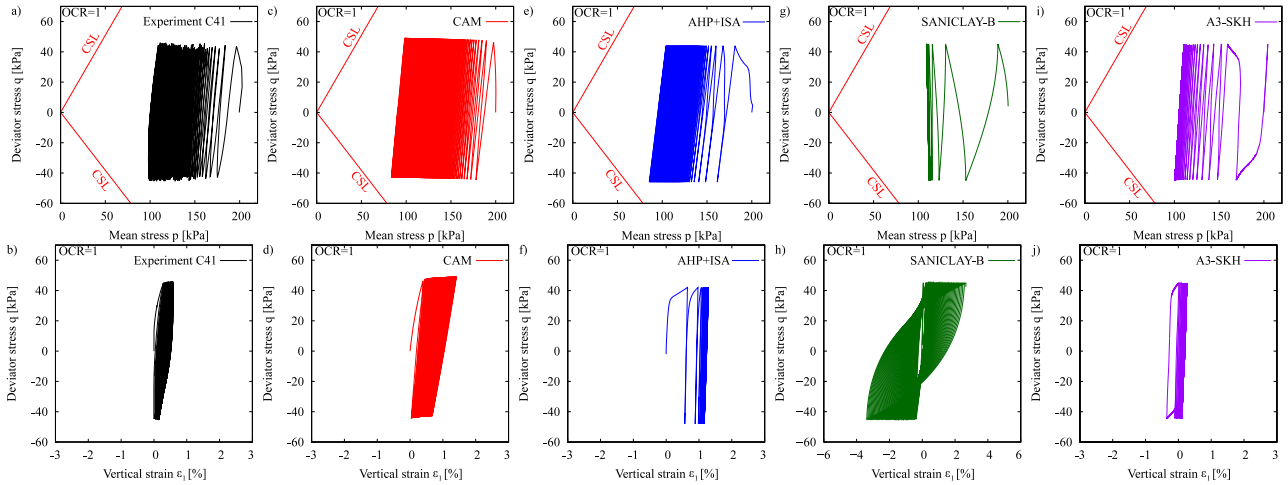

Figure 4.20: Simulations of undrained cyclic triaxial test C41 on a normally consolidated sample with constant deviatoric stress amplitude $q^{\text{amp}} = 45$ kPa, isotropic consolidation ($p_0 = 200$ kPa, $q_0 = 0$ kPa, $\eta_0 = 0$) and horizontal cutting direction: a,b) experiments by Wichtmann and Triantafyllidis [275], c,d) CAM, e,f) AHP+ISA, g,h) SANICLAY-B, i,j) A3-SKH

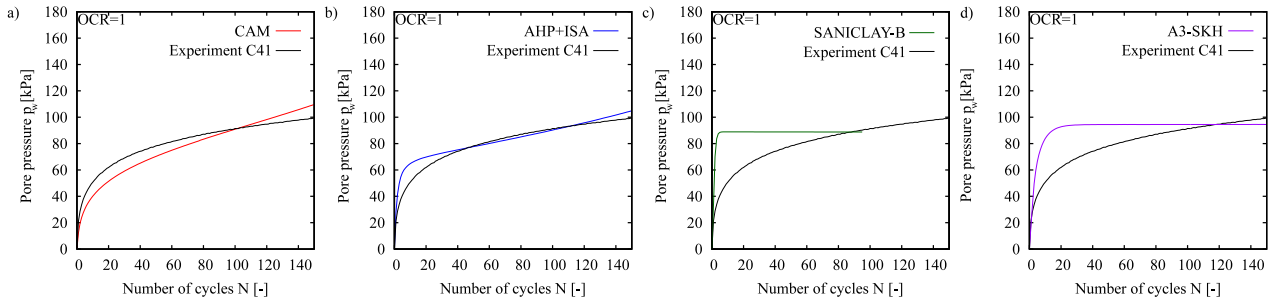

Figure 4.21: Accumulated pore water pressure in the simulation of the undrained cyclic triaxial test C41 with constant deviatoric stress amplitude $q^{\text{amp}} = 45$ kPa, isotropic consolidation ($p_0 = 200$ kPa, $q_0 = 0$ kPa, $\eta_0 = 0$) and horizontal cutting direction: a) CAM, b) AHP+ISA, c) SANICLAY-B, d) A3-SKH

4.5 Summary and conclusions

Reliable predictions of complex geotechnical problems subjected to cyclic loading require robust constitutive models for soils, able to predict the main characteristics of the material under different conditions but employing the same set of material parameters. For that purpose, the main advantage and limitations of each constitutive model should be very well known before their application on boundary value problems. In this article, the predictions capabilities of four advanced constitutive models for anisotropic fine-grained soils, namely: CAM, AHP+ISA, SANICLAY-B and A3-SKH, were inspected under a wide range of test conditions. The comparison between experimental and element test results suggests the following main findings:

- The inspected models perform well under undrained monotonic loading. They were able to accurately reproduce the experimental effective stress paths and the maximum deviatoric stresses on tests with different initial mean effective pressures.
- The eight-shaped effective stress paths observed on undrained cyclic triaxial tests, with constant deviatoric stress amplitude, and with isotropic consolidation are only reproduced to some extent by the CAM model. In addition, only the SANICLAY-B model was able to realistically reproduce the always increasing double strain amplitude after cyclic mobility. While the AHP+ISA model presents a bias in the strain accumulation, the CAM model reproduced the double strain amplitude with accumulation in extension instead of compression as observed in the laboratory data. The A3-SKH model failed to reproduce the double strain amplitude. Models having problems to reproduce the behaviour at large deformations are limited in applications dealing with earthquake loading.
- The analysis of the CSR-N_f curves on cyclic undrained tests with isotropic consolidation is still a challenge with the inspected models. For their correct reproduction, two important features need to be correctly accounted: a) accurate reproduction of the influence of the deviatoric stress amplitude in the accumulation rates, and b) the capability to (at least qualitatively) reach the defined failure criteria. The first item was fairly well reproduced by the CAM and AHP+ISA models. The second item was correctly reproduced by the CAM and SANICLAY-B models. It should be remarked that the accurate performance on the first item with the CAM and AHP+ISA models is compensated with a higher number of model parameters in comparison to the SANICLAY-B and A3-SKH models.
- Simulations on tests with different initial stress ratios suggest a less accurate performance in comparison to simulations on tests with isotropic consolidation. While the A3-SKH and SANICLAY-B models show an excessive accumulation of vertical strains, the AHP+ISA model presents an underestimation of the strains, especially on tests with initial average stress ratios in the triaxial extension regime.
- Simulation results with the inspected models suggest that the influence of the OCR on the pore water pressure accumulation is partly well predicted by the CAM model and AHP-ISA model, and moderately predicted by the SANICLAY-B and A3-SKH models.
- The degree of anisotropy plays a major role in the mechanical behavior of kaolin under cyclic loading. The experiments suggest different stiffnesses, accumulations rates and inclination of the effective stress paths depending on the cutting direction. These experimental evidences were fairly well reproduced by the CAM and AHP+ISA models, partially reproduced by the A3-SKH model and not well reproduced by the SANICLAY-B model. A simple way to fix this shortcoming of SANICLAY-B model is by scaling the isotropic hypoelastic stiffness and introducing an additional material parameter α, controlling the degree of anisotropy.

- In general, taking into account the complexity of the models, all show good agreement with the experiments. Of course, at the expense of other laboratory tests, one could reproduce each experiment more accurately using a different set of parameters. The parameter set shown in this work has been selected as the mean best fit for all experiments. This approach should also be followed for the application of the models on boundary value problems. Of course, if the loading conditions of the boundary value problem are known, then the models should be calibrated specifically based on these conditions.

4.6 Acknowledgements

The first and fourth authors appreciate the financial support given by the INTER-EXCELLENCE project LTACH19028 by the Czech Ministry of Education, Youth and Sports. The first author appreciates the financial support given by the Charles University Grant Agency (GAUK) with project number 200120. The first and fourth authors acknowledge the institutional support by the Center for Geosphere Dynamics (UNCE/SCI/006). The second author gratefully acknowledges the financial support from the German Research Community (DFG, Project: TR 218/27-1).

Chapter 5

Characteristic limitations of advanced plasticity and hypoplasticity models for cyclic loading of sands - Article 4

Summary of the article

Numerous constitutive models have been developed for the simulation of the response of granular soils under cyclic loading. While most models have succeeded in capturing certain aspects of the stress-strain response under a number of idealized loading paths, certain common limitations are encountered in simulating these and other paths, and also certain complex aspects of response. These deficiencies deserve to be discussed and carefully analyzed in order to explore their causes and to propose solutions to avoid them. Examples of them include overshooting after reverse loading/immediate reloading paths, bias in shear strain accumulation in cyclic mobility, inadequate simulation of cyclic liquefaction strength curves, inability to reach stress attractors on dense samples subjected to undrained cyclic loading, improper accumulation of strains and/or pore water pressure in cyclic shearing with small amplitudes, inaccurate cyclic oedometric stiffness, improper reproduction of preloadings, among others. These limitations are rather crucial for the end-users. Therefore, it is worthwhile to identify the common limitations of the advanced constitutive models for cyclic loading and carefully investigate their causes with the goal to come up with the corresponding mechanisms and formulations to avoid them.

Relying on cyclic tests on Toyoura and Karlsruhe fine sands, this article presents a direct comparison between the experiments and the corresponding simulation results using four advanced constitutive models for granular soils: the bounding surface plasticity model accounting for fabric changes on dilatancy proposed by Dafalias and Manzari [39], the recently proposed SANISAND-MSf model incorporating memory surface and semifluidized state by Yang et al. [286], the hypoplastic model for sands with Intergranular Strain by Niemunis and Herle [170] and the hypoplastic model for sands extended with Intergranular Strain Anisotropy by Fuentes et al. [76]. The presented results elaborate on the characteristic limitations of these advanced models in simulating several essential aspects of cyclic loading of sands. Some hints about how to solve each discussed limitation are given.

Characteristic limitations of advanced plasticity and hypoplasticity models for cyclic loading of sands

Duque, J.[1], Fuentes, W.[2], Yang, M.[3], Mašín, D.[1], Taiebat, M.[3]

[1]Charles University, Prague, Czech Republic

[2]Findeter, Bogotá, Colombia

[3]University of British Columbia, Vancouver, Canada

Abstract

Numerous studies in the literature are concerned with proposing new constitutive models for sands to simulate cyclic loading. Despite considerable progress in this area, there are various limitations on their simulation capabilities that are either overlooked or not communicated clearly by the developers. A number of these limitations are rather crucial for the end-users, and therefore, providing discussion and analysis of them would be of great value for both applications and future developments. The present work is devoted to discussing seven characteristic limitations, which are frequently observed in cyclic loading simulations. Four advanced constitutive models are considered in this study: two bounding surface elastoplasticity and two hypoplasticity models – with the models in each category following a hierarchical order of complexity. Relevant cyclic loading experimental test data on Toyoura and Karlsruhe fine sands support the analysis. The key issues discussed include stress overshooting, one-way ratcheting in cyclic strain accumulation, liquefaction strength curves, stress attractor in strain-controlled shearing, hypoelasticity, cyclic oedometer stiffness, and effect of drained pre-loading. The presented results elaborate on the specific limitations and capabilities of these rather advanced models in simulating several essential aspects of cyclic loading of sands.

5.1 Introduction

During the last decades, a number of advanced constitutive models have been proposed to simulate the mechanical behavior of sands under cyclic loading, [e.g., 10, 39, 54, 74, 75, 176, 187, 258, 277, 279, 287, 293], just to mention a few. Their capabilities include the consideration of dependency of stiffness and strength on stress and void ratio, incorporation of a Lode angle-dependent critical state surface, reproduction of small strain effects upon loading reversal, cyclic mobility under undrained cyclic shearing, among many others. Assessment of their capabilities is frequently carried out through direct comparison of their simulation results with a set of routine monotonic and cyclic experiments, such as undrained and drained cyclic triaxial tests, oedometer tests, cyclic simple shear tests, etc. Although this methodology guarantees some consistent features and cyclic loading response capabilities for the proposed models, their extended validity can be further judged by simulation of some particular paths of more complicated nature. They can be attained by combining the aforementioned routine tests sequentially, such as drained loading followed by undrained loading [43, 45, 46, 48], cyclic loading where different principal stress/strain components are simultaneously imposed [83, 111, 116, 144, 189, 199, 212, 227, 268, 283], constant mean effective stress p' paths triaxial tests [184–186, 242], and closed loops at the $q - p'$ space [180, 268]. Under these situations, some particular limitations of models for cyclic loading are repeatedly revealed, for example, overshooting effects, improper accumulation of plastic strains, spoiled dilatancy-contractancy characteristics, or in general, poorly reproduced stiffness. These and other limitations are commonly realized by users. However, they have been less discussed by the model developers.

Different types of constitutive model limitations for simulating cyclic loading are frequently reported in

the literature. For example, the overshooting phenomenon has been revealed by some authors and some have proposed solutions for it [e.g., 37, 41, 68, 121, 168, 183]. One-way ratcheting in strain accumulation of undrained cyclic triaxial tests along with cyclic mobility paths have been exhibited by many models [e.g., 39, 72, 76]. Some authors have adopted Lode angle independent critical state which would result in symmetric evolution of shear strain in both directions, that is also not desirable in cyclic triaxial shearing [23, 55, 255]. Excessive plastic accumulation on closed stress loops of small amplitudes, where an elastic behavior is shown by experiments, has been detected by Poblete et al. [180]. Discussion about the lack of plastic deformation obtained under constant stress ratio paths using models with open-wedge yield surfaces can be found elsewhere [e.g., 238, 239]. The recent work by Wichtmann et al. [265] inspected the accuracy of three well-known "advanced" models for cyclic loading, and as a conclusion, a lack of congruence was evidenced on many simulations. Indeed, they also showed that many limitations are shared by the three models, despite the remarked differences in their formulations. All these considerations suggest that models for cyclic loading sharing same limitations are frequently proposed in the literature. In contrast, works oriented to show and discuss these issues from the formulation perspective are scarcely found. This is disappointing, since such a work can serve as a serious warning for future developments and motivate future developers to find key solutions to these characteristic limitations.

The aim of the present paper is to show and discuss some characteristic limitations shared by many constitutive models for cyclic loading of sands. For the purpose of illustration, four constitutive models that have achieved certain success in simulating cyclic loading tests, are adopted: the bounding surface plasticity model accounting for fabric change effects on dilatancy upon loading reversal by Dafalias and Manzari [39], hereafter denoted as DM04, the recently proposed model incorporating memory surface and semifluidized state into DM04 by Yang et al. [286], denoted as SANISAND-MSf, the hypoplastic model for sands by Von Wolffersdorf [277] with the Intergranular Strain (IS) extension by Niemunis and Herle [170], henceforth denoted as HP+IS model, and the hypoplastic model for sands extended with Intergranular Strain Anisotropy (ISA) by Fuentes et al. [76], denoted as HP+ISA model. A brief description of their formulations is given in the next section. The present work is not meant to evaluate the accuracy of these models in simulating the experiments, but rather focuses on discussion of the limitations emerging from the lack of constitutive features in their formulations. These carefully selected limitations can pose a challenge to development of new models and meanwhile provide guidance to improvement on the existing models. To the authors' knowledge, there still does not exist a constitutive model that can properly tackle all the limitations listed in this paper.

The structure of this paper is organized as follows. At the beginning, a brief description of the constitutive models is provided. Subsequently, the testing materials and model parameters are briefly described. Then, each limitation is expounded by explaining the test, discussing the mechanism, and providing illustrative simulations with the selected models for cyclic loading. At the end, concluding remarks are given. Notation is described in appendix 5.7.1.

5.2 Brief description of models for cyclic loading

Numerical simulations of element tests will be presented in the sequel to illustrate some characteristic limitations of constitutive models for cyclic loading of sands, attributed to certain inadequate considerations or missing ingredients in the mathematical formulations. Two plasticity and two hypoplasticity constitutive models for sand are selected here because they account for various useful features such as stress and void ratio dependency allowing for successful simulations for different stresses and densities, and also have achieved certain success in simulation of cyclic response of sands.

The first model is the DM04 proposed by Dafalias and Manzari [39], an extension of a two-surface plasticity model by Manzari and Dafalias [140]. This model is critical state compatible and built in the framework

of bounding surface plasticity [38]. It has four conical surfaces in the deviatoric stress space, including a small yield surface centered at the back-stress ratio that obeys kinematic hardening, and three other origin-concentric surfaces: bounding surface, critical state surface and dilatancy surface. The distances between the current back-stress ratio and its images on bounding and dilatancy surfaces control the plastic modulus and dilatancy, respectively. In addition, the DM04 incorporates a fabric dilatancy tensor to reproduce the cyclic mobility effects observed under undrained cyclic shear tests.

The second model is the SANISAND-MSf proposed by Yang et al. [286]. This model is formulated by introducing two major and two minor modifications into the DM04 model platform with the aim to improve the reference model performance in simulation of undrained cyclic shear tests. The major modifications consist of the incorporation of two new constitutive ingredients, memory surface to well control excess pore pressure generation in pre-liquefaction stage and semifluidized state that allows to capture large shear strain development in post-liquefaction stage. The minor modifications consist of improvement in the accuracy of the non-associative flow rule in non-proportional loading and the simulation of the cyclic shear stress-strain loops shifting under cyclic triaxial loading. Constitutive relations of the DM04 and SANISAND-MSf models are presented in Table 5.5, Appendix 5.7.2.

The third model is the HP+IS, a hypoplasticity sand model proposed by Von Wolffersdorf [277] extended with Intergranular Strain (IS) according to Niemunis and Herle [170]. The hypoplasticity model without IS extension is characterized by being written through a single tensorial equation, where the stress rate depends directly on the stress, strain rate and void ratio. Despite its accuracy on the simulation of sands under medium and large amplitude cycles ($\| \Delta\boldsymbol{\varepsilon} \| > 10^{-3}$) [166, 170, 277], this particular model delivers an excessive plastic accumulation (ratcheting) under cycles of small and medium amplitudes ($\| \Delta\boldsymbol{\varepsilon} \| < 10^{-3}$). The intergranular strain (IS) extension proposed by Niemunis and Herle [170] is frequently used to overcome this deficiency, and also endows the model with the capabilities in simulations of cyclic tests. This extension incorporates an additional strain-type tensorial variable called the intergranular strain $\mathbf{h}$ to store information about the recent strain history, being properly formulated to increase the stiffness and reduce the plastic accumulation after any event of strain reversal loading. It should be noted that this IS formulation lacks an elastic locus.

The fourth model is the HP+ISA proposed by Fuentes et al. [76]. Similar to the HP+IS model, HP+ISA extends the hypoplasticity model by Von Wolffersdorff [277] by employing the more recently IS formulation proposed originally by Fuentes and Triantafyllidis [74] and enhanced in Fuentes et al. [76]. Important differences compared to the conventional IS formulation by Niemunis and Herle [170] lie in: a) the evolution of the intergranular strain is now elastoplastic allowing for the incorporation of an elastic locus to the model, b) the proposed yield surface hardens kinematically, in such fashion, that reproduces a smooth transition between the elastic and plastic behavior, c) the formulation accounts for a proper reduction mechanism of the plastic strain rate on sets of identical cycles. Besides these, the mechanism to reproduce cyclic mobility proposed by Fuentes et al. [76] is also adopted. Constitutive relations of the HP+IS and HP+ISA models are provided in Table 5.6, Appendix 5.7.2.

5.3 Description of test materials and model parameters

Two sets of laboratory experimental database on Toyoura and Karlsruhe fine sands, respectively, are considered in this study to analyze the material response under cyclic loading, in comparison with the corresponding simulations. Toyoura sand has a maximum void ratio $e_{\max} = 0.977$, a minimum void ratio $e_{\min} = 0.597$, a mean diameter $D_{50} = 0.17$ mm and a uniformity coefficient $c_{\mathrm{u}} = 1.7$ [113]. Karlsruhe fine sand (KFS), mainly composed of grains with subangular shape, has a maximum void ratio of $e_{\max} = 1.054$, a minimum void ratio of $e_{\min} = 0.677$, a mean diameter of $D_{50} = 0.14$ mm and a uniformity coefficient of $c_{\mathrm{u}} = 1.5$ [263]. Tables 5.1, 5.2, 5.3 and 5.4 present the material parameters for the DM04, SANISAND-

MSf, HP+IS and HP+ISA models for Toyoura and Karlsruhe fine sands, respectively. Most of the model parameters are directly taken from the previous works [39, 50, 76, 163, 180, 241, 265, 273, 286] and some of them are tuned a bit to obtain better simulation results. Note that due to different model formulations, parameters with similar physical meaning may have different numerical values in different models. As an example, $e_{\mathrm{c}}^{\mathrm{ref}}$ of elasto-plastic models differs from e_{c0} of hypoplastic models, although both models predict comparable critical state lines in the space of void ratio versus mean effective stress. This is because the functions defining dependency of critical state void ratio on mean effective stress are different.

Table 5.1: Parameters of the DM04 model for Toyoura sand reported by Dafalias and Manzari [39] and Karlsruhe fine sand modified from Wichtmann et al. [265]

Parameter	Nomenclature	Value Toyoura	Value KFS	Units	Useful test
Elasticity	G_0	125	150	[-]	DMT, UCT
	ν	0.05	0.05	[-]	OED
Critical state	M_{c}	1.25	1.34	[-]	UMT
	c	0.712	0.7	[-]	UMT
	λ_{c}	0.019	0.122	[-]	DMT, UMT
	$e_{\mathrm{c}}^{\mathrm{ref}}$	0.934	1.103	[-]	OED
	ξ	0.7	0.205	[-]	DMT, UMT
Yield surface	m	0.01	0.05	[-]	-
Kinematic hardening	h_0	7.05	10.5	[-]	DMT, UCT
	c_h	0.968	0.95	[-]	DMT
	n^{b}	1.1	1.2	[-]	DMT
Dilatancy	A_0	0.704	0.9	[-]	DMT
	n^{d}	3.5	2.0	[-]	DMT
Fabric dilatancy	$z_{\max}$	4.0	15.0	[-]	UCT
	c_z	600	2000	[-]	UCT

OED: Oedometric test, DMT: Drained monotonic triaxial test, UMT: Undrained monotonic triaxial test, UCT: Undrained cyclic triaxial test

Table 5.2: Parameters of the SANISAND-MSf model for Toyoura sand and Karlsruhe fine sand

Parameter	Nomenclature	Value Toyoura	Value KFS	Units	Useful test
Elasticity	G_0	125	150	[-]	DMT, UCT
	ν	0.05	0.05	[-]	OED
Critical state	M_{c}	1.25	1.34	[-]	UMT
	c	0.712	0.7	[-]	UMT
	λ_{c}	0.019	0.122	[-]	DMT, UMT
	$e_{\mathrm{c}}^{\mathrm{ref}}$	0.934	1.103	[-]	OED
	ξ	0.7	0.205	[-]	DMT, UMT
Yield surface	m	0.01	0.05	[-]	-
Kinematic hardening	h_0	7.05	10.5	[-]	DMT, UCT
	c_h	0.968	0.95	[-]	DMT
	n^{b}	1.1	1.2	[-]	DMT
Dilatancy	A_0	0.704	0.9	[-]	DMT
	n^{d}	3.5	2.0	[-]	DMT
	n_{g}	0.95	0.92	[-]	UCT
Fabric dilatancy	$z_{\max}$	4.0	15.0	[-]	UCT
	c_z	600	2000	[-]	UCT
Memory surface	μ_0	0.5	2.5	[-]	UCT
	u	2.0	1.2	[-]	UCT
Semifluidized state	x	4.3	5.5	[-]	UCT
	c_ℓ	25	30	[-]	UCT

OED: Oedometric test, DMT: Drained monotonic triaxial test, UMT: Undrained monotonic triaxial test, UCT: Undrained cyclic triaxial test

Table 5.3: Parameters of the HP+IS model for Toyoura sand modified from Ng et al. [163] and Karlsruhe fine sand reported by Wichtmann and Triantafyllidis [273]

Parameter	Nomenclature	Value Toyoura	Value KFS	Units	Useful test
Critical state friction angle	φ_c	30	33.1	[°]	UMT
Granular hardness	h_s	2600	4000	[MPa]	OED
Barotropy exponent	n	0.27	0.27	[-]	OED
Dilatancy exponent	α	0.14	0.14	[-]	DMT
Pyknotropy exponent	β	3.0	2.5	[-]	OED
Minimum void ratio at $p' = 0$	e_{d0}	0.61	0.677	[-]	$e_{\min}$ test
Critical void ratio at $p' = 0$	e_{c0}	0.98	1.054	[-]	$e_{\max}$ test
Maximum void ratio at $p' = 0$	e_{i0}	1.10	1.212	[-]	$e_{\max}$ test
Elastic strain amplitude	R	1×10^{-4}	1×10^{-4}	[-]	UCT
Stiffness factor for reversal loading	m_R	5.5	2.2	[-]	UCT
Stiffness factor for transverse loading	m_T	2.75	1.1	[-]	UCT
Parameter controlling stiffness decay	β_r	0.08	0.1	[-]	UCT
Parameter controlling stiffness decay	χ	1.0	5.5	[-]	UCT

OED: Oedometric test, DMT: Drained monotonic triaxial test, UMT: Undrained monotonic triaxial test, UCT: Undrained cyclic triaxial test

Table 5.4: Parameters of the HP+ISA model for Toyoura sand reported by Poblete et al. [180] and Karlsruhe fine sand modified from Fuentes et al. [76]

Parameter	Nomenclature	Value Toyoura	Value KFS	Units	Useful test
Critical state friction angle	φ_c	30	33.1	[°]	UMT
Granular hardness	h_s	2600	4000	[MPa]	OED
Barotropy exponent	n	0.27	0.27	[-]	OED
Dilatancy exponent	α	0.14	0.14	[-]	DMT
Pyknotropy exponent	β	3.0	2.5	[-]	OED
Minimum void ratio at $p' = 0$	e_{d0}	0.61	0.677	[-]	$e_{\min}$ test
Critical void ratio at $p' = 0$	e_{c0}	0.98	1.054	[-]	$e_{\max}$ test
Maximum void ratio at $p' = 0$	e_{i0}	1.10	1.212	[-]	$e_{\max}$ test
Elastic strain amplitude	R	1×10^{-4}	1×10^{-4}	[-]	UCT
Stiffness factor for reversal loading	m_R	5.0	5.0	[-]	UCT
Minimum IS hardening parameter	β_{h0}	0.3	0.2	[-]	UCT
Maximum IS hardening parameter	β_{hmax}	3.0	3.0	[-]	UCT
Minimum IS exponent	χ_0	5.0	5.0	[-]	UCT
Maximum IS exponent	χ_{max}	18.0	17.7	[-]	UCT
Accumulation rate factor	c_a	0.01	0.018	[-]	UCT
Cyclic mobility factor	c_z	600	300	[-]	UCT

OED: Oedometric test, DMT: Drained monotonic triaxial test, UMT: Undrained monotonic triaxial test, UCT: Undrained cyclic triaxial test

5.4 Analysis of some frequent limitations on models for cyclic loading

The frequent limitations observed on models for cyclic loading are discussed in this section, according to comparisons between laboratory experiments and the corresponding simulations from the selected models.

5.4.1 Limitation 1: overshooting after reverse loading/immediate reloading paths

In the scenario of reverse loading/immediate reloading, a so-called overshooting phenomenon is observed in many models. Overshooting implies a stress–strain curve which unrealistically overshoots the continuation of a previous curve had the event of reverse loading/immediate reloading not taken place [41]. A simulation example on Karlsruhe fine sand using the HP+IS model is presented in Fig. 5.1 to illustrate this issue. Initially, an undrained triaxial compression is performed until the vertical strain ε_1 reaching 5%, as the reference. Then four additional tests are conducted according to the following procedure: an undrained triaxial compression until $\varepsilon_1 = 0.5\%$ followed by a small reverse loading with $\Delta\varepsilon_1$ of 0.01%, 0.03%, 0.06%, or 0.09%, respectively, and subsequent reloading until $\varepsilon_1 = 5\%$. For all these reverse loading/immediate reloading scenarios, the simulations tend to present a reloading stress-strain response well above the reference monotonic curve. The level of the simulated overshooting decreases with the increasing amplitude of reverse loading. However, for such very small reverse loading/immediate reloading scenarios any overshooting is contradictory to what would be expected from experiments [e.g., 186].

To more precisely illustrate this issue, Fig. 5.2a, b presents two experimental triaxial tests on Toyoura sand from Ishihara [113], including a "monotonic" one and a "cyclic" one. Both experiments were conducted on isotropically consolidated samples with an initial mean stress $p'_0 = 100$ kPa and relative density $D_r = 16\%$. The "monotonic" experiment consists of a drained triaxial compression test ending at a deviatoric stress $q = 80$ kPa and a subsequent undrained triaxial compression test until reaching a vertical strain $\varepsilon_1 = 20\%$.

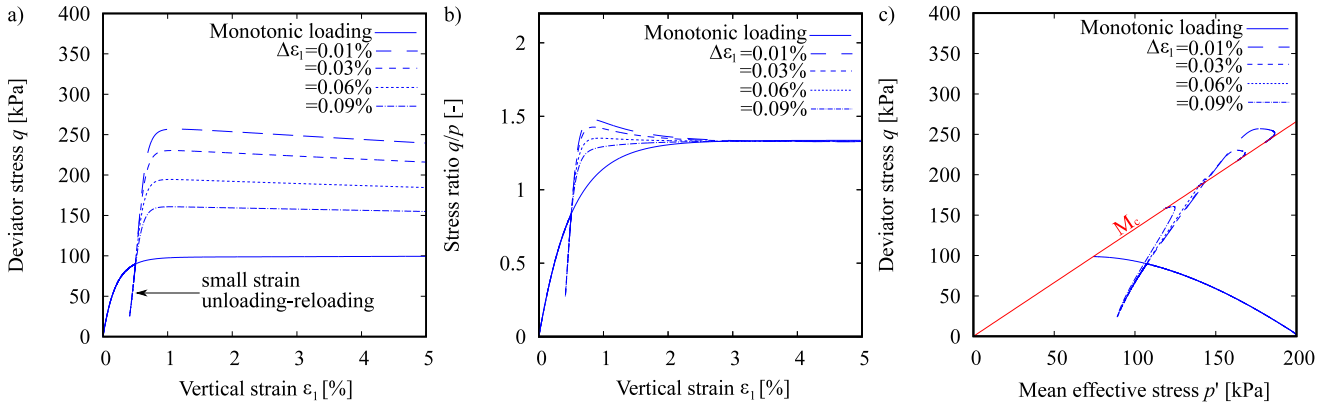

Figure 5.1: Simulations with the HP+IS model of an undrained triaxial test with different small strain unloading-reloading cycles on a loose sample ($e_0 = 0.98$) with isotropic consolidation ($p'_0 = 200$ kPa)

The "cyclic" experiment follows a similar procedure as the "monotonic" one, and the only difference is that five small undrained reverse loading-reloading cycles are introduced between the drained and undrained loadings. Each cycle follows the sequence: a loading of $\Delta\varepsilon_1 = 0.3\%$, an unloading of $\Delta\varepsilon_1 = 0.03\%$, and a reloading of $\Delta\varepsilon_1 = 0.03\%$. The experimental path clearly follows the monotonic loading path after the reverse loading/immediate reloading process.

Simulation results of these two experiments using the four selected models are shown in Fig. 5.2c-j. The simulated stress-strain curve and stress path are quite similar for the DM04 and SANISAND-MSf models, both presenting the overshooting response. This overshooting is caused by the use of a discrete memory variable updated at any stress-reversal, which in such small reverse loading/immediate reloading scenarios would lead to an overestimation of the stiffness. Fortunately, the nature of bounding surface plasticity "bounds" the extent of such overshooting to an acceptable level [41].

The simulated stress-strain curve of the HP+IS model in Fig. 5.2g indicates a significant over-prediction of the stiffness after each reloading path, inducing such massive overshooting. This undesired effect can be explained as follows: the IS formulation delivers a sudden increase of stiffness and reduction of the hypoplastic strain rate after each unloading-reloading event, which remains active upon a certain strain amplitude. The size of this amplitude is only controlled by parameters R, β and χ [71, 166]. If the reloading strain amplitude is smaller, an overshooting response is then reproduced by the IS model. This issue is aggravated in this specific simulation since the magnitude of the strain unloading is very small. Simulation results of the HP+ISA model in Fig. 5.2i,j do not indicate the issue of overshooting but the path after each loading cycle stays below the monotonic one, which can be termed as "undershooting". This is because an elastic threshold strain accounting for memory effects is incorporated in the HP+ISA model, one of the key improvements from HP+IS, however, once the elastic threshold strain is reached, the remaining strain amplitude in which the IS effect is active, does not necessarily coincide with the unloading-reloading strain amplitude, which causes the undershooting problem.

To mitigate the overshooting limitation in bounding surface plasticity models, it may be necessary to memorize the recent loading history to adjust the updating of the related discrete memory variable. Dafalias [38] outlined a way of updating the back-stress ratio at the initiation of a new loading process, and the implementation details were expounded in Dafalias and Taiebat [41]. This overshooting correction scheme can be easily incorporated in the SANISAND-MSf model. The improved simulation results are presented in Fig. 5.3, illustrating the effectiveness of the scheme. For addressing the overshooting problem in the hypoplastic models, Niemunis [166] suggested using an overlay approach. This idea still requires further investigation. A simpler solution may be coupling the intergranular strain model with the asymptotic state boundary surface (ASBS) of the hypoplastic models in such a way that the ASBS

defines the maximum stress states of the model [18]. Such an approach would however only correct major overshooting events where stress reaches states outside ASBS. Overshooting inside ASBS, such as the one presented in Figure 5.1b, would still be present.

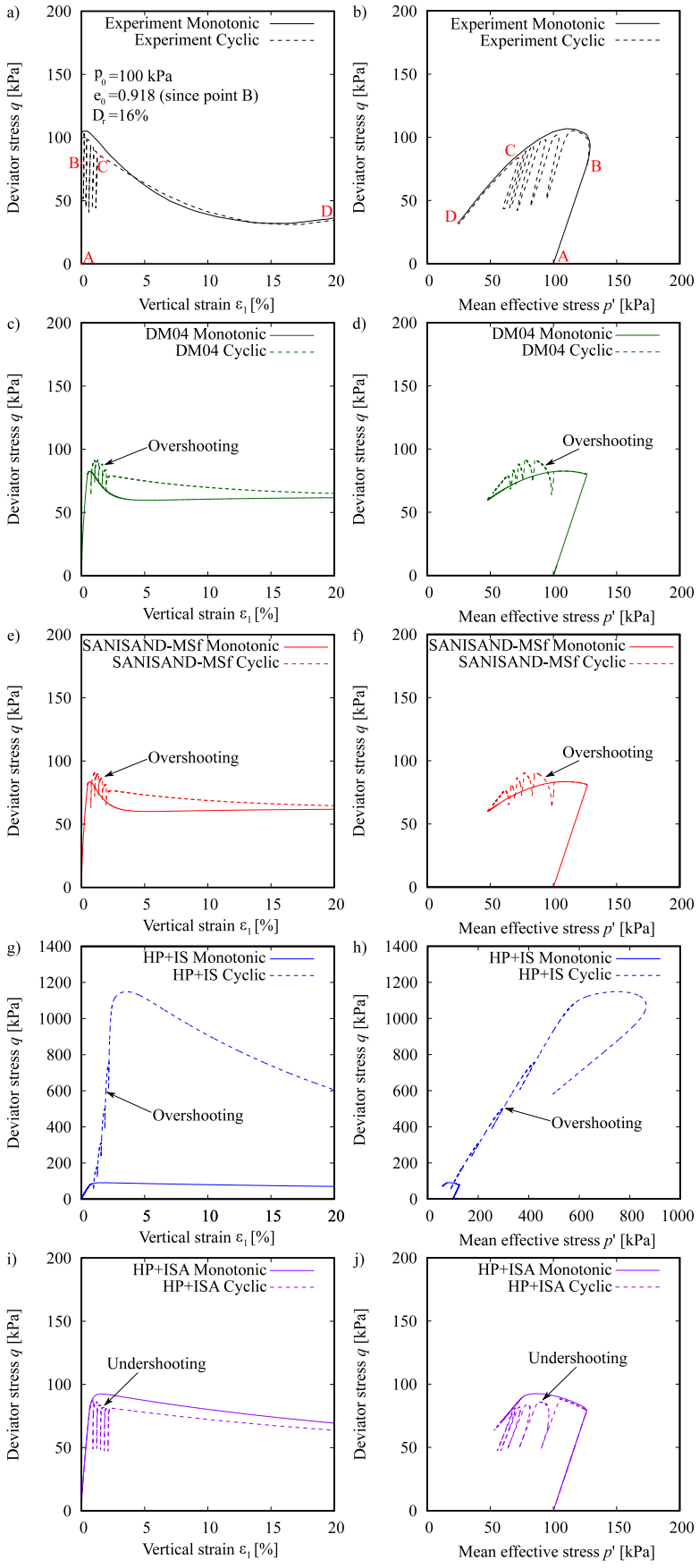

Figure 5.2: Monotonic and cyclic triaxial tests on Toyoura sand. Loose sample ($D_r = 16\%$) with isotropic ~~consolidation ($p'_0 = 100$ kPa). a,b) Experiments reported by Ishihara [113], and the corresponding simu-~~ lations using c,d) DM04; e,f) SANISAND-MSf; g,h) HP+IS; i,j)HP+ISA

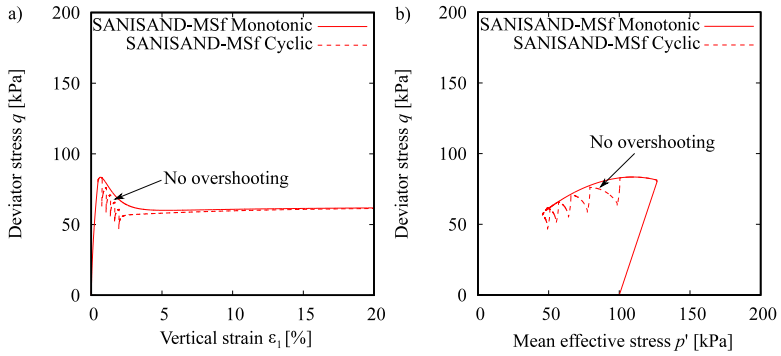

Figure 5.3: Simulations of the monotonic and cyclic triaxial tests on Toyoura sand with the SANISAND-MSf model and the overshooting correction proposed by Dafalias and Taiebat [41]

5.4.2 Limitation 2: shear strain accumulation in cyclic mobility

When medium dense or dense sand elements are subjected to undrained cyclic shearing with a constant shear stress amplitude, the samples present a gradual reduction of mean effective stress p'. Eventually the material undergoes the so-called cyclic mobility, in which the stress path experiences typical butterfly shape with momentary liquefaction state (p' near zero) while the cyclic shear strain amplitude increases cycle by cycle. Large but limited shear strain develops after a sufficient number of loading cycles. The simple shear experiments usually manifest rather symmetric stress-strain loops while the triaxial ones tend to accumulate more strain in the extension side compared with the compression side but still with stress-strain loops expanding on both sides. An undrained cyclic triaxial test of $q^{\text{amp}} = 60$ kPa on Karlsruhe fine sand with initial mean stress $p'_0 = 200$ kPa and $D_{\text{r}} = 67\%$ [273] is presented in Fig. 5.4a, b. Clearly one can observe the butterfly shape in Fig. 5.4a and gradually increasing amplitude of axial strain in subsequent loading cycles in Fig. 5.4b.

To adequately capture the response in these undrained cyclic triaxial tests, a model should have at least three considerations: i) elevated contraction in reverse loading following a dilation response, bringing the stress path to a nearly lock-up butterfly shape, ii) progressive reduction of shear stiffness at the liquefaction state in subsequent cycles, and iii) modeling the two-way non-symmetric evolution of shear strain, i.e. in both compression and extension directions. The first two considerations have been discussed in a number of constitutive modeling studies [e.g., 10, 55, 108, 134, 293], and the third one has been studied and addressed more recently by Yang et al. [286].

Simulation results of the undrained cyclic triaxial test using DM04, SANISAND-MSf, HP+IS and HP+ISA models are presented in Fig. 5.4c-j. Clearly all the models except HP+IS can achieve a satisfying butterfly shape in the stress path, as they account for consideration i mentioned above by incorporating the fabric dilatancy tensor initially proposed by Dafalias and Manzari [39]. However, the simulated stress-strain loops of DM04, HP+IS and HP+ISA manifest an unrealistic one-way ratcheting, as they do not have mechanisms for the considerations ii and iii mentioned above. The SANISAND-MSf is the only model able to reproduce the increasing double amplitude of cyclic shear strains as it tackles the two aforementioned issues by introducing the following additional constitutive ingredients. The first is significantly reducing the dilatancy and plastic modulus at low mean effective stresses or the so-called semifluidized state, via a novel internal variable called "strain liquefaction factor" (SLF), which evolves only at low mean effective stresses. This mechanism, originally proposed by Barrero et al. [10], is to reproduce shear strain development in the liquefaction state. The second consists of dividing the dilatancy and plastic modulus by a common term with n_{g} a model parameter as listed in Table 5.2, with the goal to balance the relative magnitude of shear strain amplitudes in triaxial compression and extension.

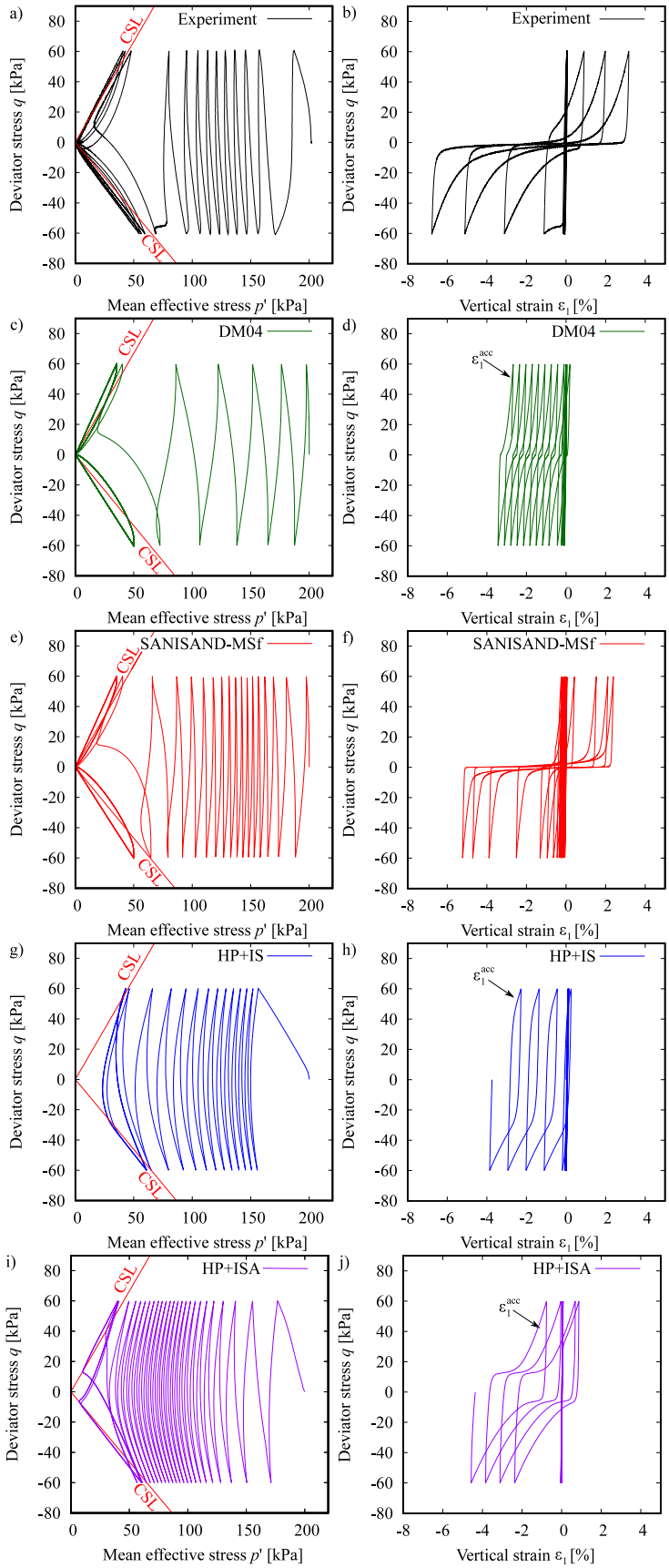

Figure 5.4: Undrained cyclic triaxial test on Karlsruhe fine sand. Medium density sample ($D_r = 67\%$) with isotropic consolidation ($p'_0 = 200$ kPa) and stress cycles of $q^{amp} = 60$ kPa: a,b) Experiments reported by Wichtmann and Triantafyllidis [273]; and the corresponding simulations using c,d) DM04; e,f) SANISAND-MSf; g,h) HP+IS; i,j)HP+ISA

5.4.3 Limitation 3: cyclic liquefaction strength curves

Cyclic liquefaction failure or initial liquefaction is usually defined as the point at which excess pore pressure ratio approaches 1, or the single or double strain amplitudes reach some limiting values. Cyclic liquefaction of saturated sand can be triggered by different combinations of uniform cyclic stress ratio (CSR), which is the uniform cyclic shear stress divided by initial effective confining stress, and the number of loading cycles [109]. The liquefaction strength curve, i.e., the plot of CSR versus the number of cycles to initial liquefaction N_{ini}, are of practical importance for assessing the success of a sand constitutive model in simulation of cyclic liquefaction.

Under cyclic triaxial conditions, the CSR is defined as the ratio of the deviatoric stress to two times the initial mean effective stress, i.e., $\text{CSR} = q^{\text{amp}}/(2p'_0)$. In the literature, different criteria were proposed to define initial liquefaction. A common approach is based on the excess pore pressure ratio $r_u = u_w^{\text{acc}}/p'_0 = 0.95$ [e.g., 7, 42, 194] or $r_u = 1$ [e.g., 109, 263, 273], where u_w^{acc} is the excess pore water pressure. In addition, some other works defined initial liquefaction based on a single strain amplitude (maximum strain in a given cycle only in compression or extension) of $\varepsilon_1^{\text{SA}} = 2.5\%$ [e.g., 81, 182, 211, 216] or double strain amplitudes (the strain amplitude of a given cycle in compression and extension) of $\varepsilon_1^{\text{DA}} = 5\%$ [e.g., 104, 112, 251]. While these three criteria preserve consistence of cyclic liquefaction resistance in the experiments, the simulations may present different response due to some deficiencies or missing features in the adopted constitutive models. For example, under undrained cyclic triaxial shearing some models may not reach $r_u = 0.95$ or $\varepsilon_1^{\text{DA}} = 5\%$ for certain states, but still develop sufficient one-way accumulation of strain to meet $\varepsilon_1^{\text{SA}} = 2.5\%$. To give a thorough evaluation of the capabilities of the constitutive models in capturing cyclic liquefaction resistance, three different criteria for initial liquefaction were considered in this paper to generate the $\text{CSR} - N_{\text{ini}}$ curves: a) excess pore pressure ratio $r_u = 0.95$, b) axial strain in single amplitude of $\varepsilon_1^{\text{SA}} = 2.5\%$, and c) axial strain in double amplitude of $\varepsilon_1^{\text{DA}} = 5\%$, with the definitions illustrated in Fig. 5.5.

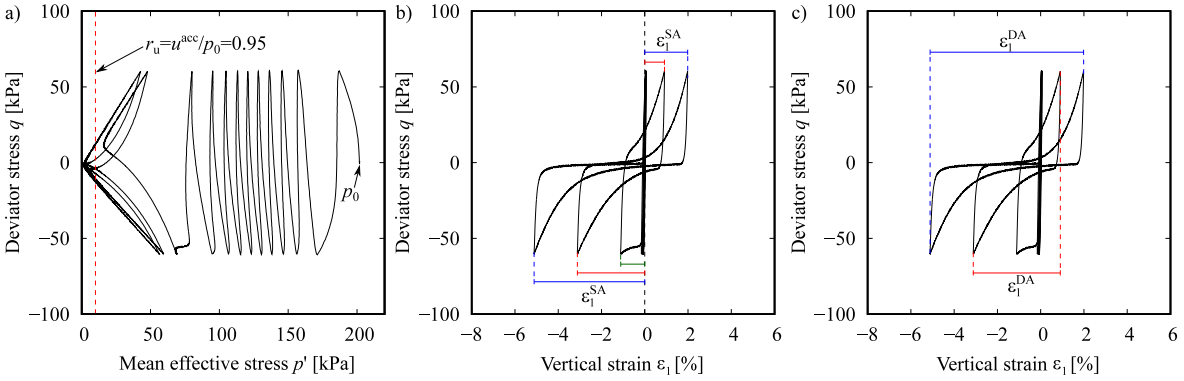

Figure 5.5: Schematic illustration of the meanings of excess pore pressure ratio r_u, single strain amplitude $\varepsilon_1^{\text{SA}}$, and double strain amplitude $\varepsilon_1^{\text{DA}}$ in undrained cyclic triaxial shearing, for checking the corresponding selected liquefaction criteria based on $r_u = 0.95$, $\varepsilon_1^{\text{SA}} = 2.5\%$, and $\varepsilon_1^{\text{DA}} = 5\%$.

To adequately simulate the cyclic liquefaction strength curves, in addition to the three consideration mentioned in section 5.4.2, the model should have a mechanism to control the pace of reduction of effective stress or development of shear strain in various undrained cyclic loading scenarios. Considering that the models can often be calibrated to reasonably reproduce cyclic accumulation at a single loading scenario (but, with the same set of parameters, fail in other loading scenarios), the most straightforward approach to correct the shape of CSR–N_{ini} is to consider state-dependent model parameters. Of course, such a dependency needs to introduce further parameters, which complicates the model formulation and

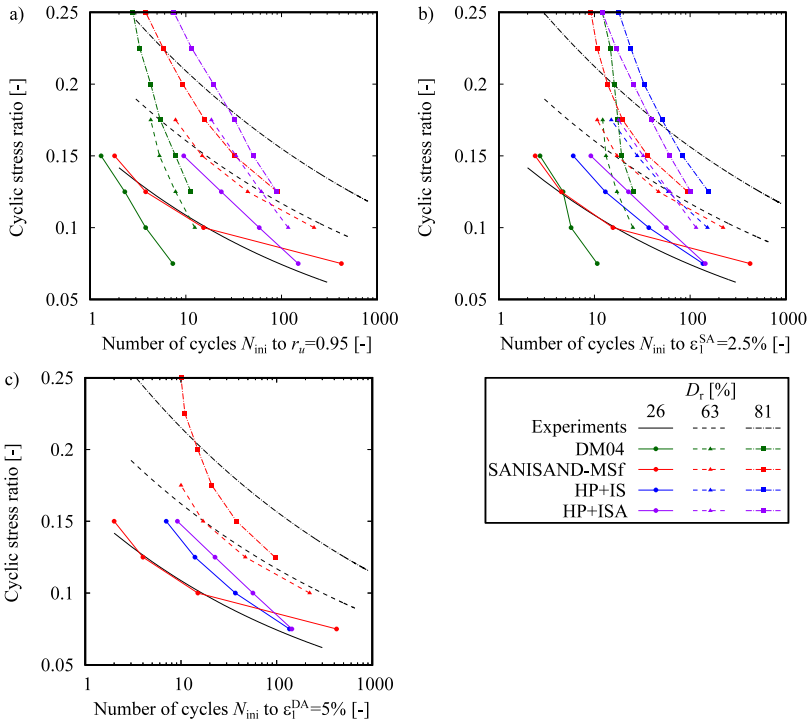

Figure 5.6: Liquefaction strength curves of Karlsruhe fine sand at different densities and for different liquefaction criteria: a) $r_u = 0.95$, b) $\varepsilon_1^{SA} = 2.5\%$ and c) $\varepsilon_1^{DA} = 5\%$

calibration. Adequacy of such a change would thus have to be thoroughly evaluated using experimental data sets on different soils.

To assess the performance of the four constitutive models in the present work in capturing the corresponding liquefaction strength curves, the experimental CSR–N_{ini} curves for Karlsruhe fine sand were constructed using the database of 22 undrained cyclic triaxial tests reported by Wichtmann and Triantafyllidis [273]. Samples were categorized in three range of densities: loose, medium dense and dense with mean relative densities of 26, 63, and 81%, respectively. The CSR–N_{ini} curves of Karlsruhe sand for all these three criteria are presented in Fig. 5.6. The corresponding simulations were performed considering the experimental average density of each range, an initial mean effective pressure $p'_0 = 100$ kPa, and a range of CSR. The results presented also in Fig. 5.6 show a number of limitations in the simulation capabilities that deserve to be discussed.

In particular, the DM04 simulations show much steeper strength curves than the experiments for the criteria of $r_u = 0.95$ and $\varepsilon_1^{SA} = 2.5\%$ as shown in Fig. 5.6a,b. This points to a deficiency in the model formulation to control the pace of reduction of effective stress in various levels of CSR. Setting this aside, note that the DM04 simulations do not reach the $\varepsilon_1^{DA} = 5\%$ and so they are absent from Fig. 5.6c. Recalling the stress-strain plots from the previous section, contrary to the experiments the DM04 shows a one-way ratcheting of strains in the extension direction, but with a locked ε_1^{DA} much smaller than 5%.

The SANISAND-MSf simulations show a significantly improved performance for all three criteria. More specifically, it shows much improved performance in the number of cycles to reach $r_u = 0.95$ as shown in Fig. 5.6a. This is due to the memory surface mechanism controlling the stiffness in the pre-liquefaction stage. The simulations of SANISAND-MSf also reach the $\varepsilon_1^{DA} = 5\%$ contrary to what was observed in case of DM04, with a reasonable performance as shown in Fig. 5.6b. This is due to the semifluidized state mechanism controlling the stiffness in the post-liquefaction stage. One still can observe that despite its

excellent performance in capturing the cyclic liquefaction curves of loose and medium dense states, the SANISAND-MSf simulations show slightly steeper curves than the experiments for the dense states.

The performance of the HP+IS model is rather poor considering that it cannot reach the criterion $r_u = 0.95$ in any of the three densities, and $\varepsilon_1^{\mathrm{DA}} = 5\%$ for medium dense and dense states, due to missing features accounting for the considerations i and ii of Section 5.4.2, respectively. The simulations can reach the $\varepsilon_1^{\mathrm{SA}} = 2.5\%$ because this model simulates a non-realistic ratcheting of cyclic shear strain shown in Fig. 5.4h. However the simulated curves look steeper than the experiments, implying that the model is incapable of controlling the pace of shear strain development in various levels of CSR.

In contrast to the HP+IS, the HP+ISA simulations can reach $r_u = 0.95$ due to incorporation of fabric-dilatancy tensor but produce a steeper CSR-N_{ini} curves than the experiments. The HP+ISA model needs improvement to handle the pace of pore pressure generation in various levels of CSR and D_{r}. The model performance related to the $\varepsilon_1^{\mathrm{SA}} = 2.5\%$ is very similar to that of the HP+IS, with the same reason explained above. The criterion $\varepsilon_1^{\mathrm{DA}} = 5\%$ is only reached for the loose state, and not the medium dense and dense states. This is because the model can not simulate large shear strain development sufficiently, related to consideration ii of Section 5.4.2.

5.4.4 Limitation 4: reaching liquefaction for dense samples under undrained cyclic shearing with constant large strain amplitude

Laboratory experiments of undrained cyclic triaxial tests with constant large strain amplitude $\| \boldsymbol{\varepsilon}_1^{\mathrm{amp}} \| > 10^{-2}$ on dense sand samples of $D_{\mathrm{r}} > 70\%$ indicate occurrence of liquefaction state after sufficient shearing [124, 142, 252, 263]. According to Gudehus [88], the liquefaction state of $p' = q = 0$ is an attractor of the stress path. In addition, the deviatoric stress amplitude q^{amp} progressively decreases along the cyclic shearing till its vanishment $q^{\mathrm{amp}} = 0$ at the liquefaction state. Fig. 5.7a,b presents an experimental test with $\varepsilon_1^{\mathrm{amp}} = 1\%$ from Wichtmann and Triantafyllidis [274] imposed on an isotropically consolidated dense sample of Karlsruhe fine sand with initial mean stress $p'_0 = 700$ kPa and relative density $D_{\mathrm{r}} = 101\%$. Along the undrained cyclic shearing, one can observe the gradual degradation of mean effective stress and progressive reduction of q^{amp}. The sample falls into liquefaction state after 57 loading cycles, where $q^{\mathrm{amp}} = 0$ and the stiffness vanishes. Note that tests on dense samples have been selected in this section to demonstrate model shortcomings, as predictions are typically more problematic than predictions of equivalent experiments on medium dense and loose samples.

To properly capture such behavior, the model should have the capabilities of i) dragging stress path to liquefaction state upon reverse loading from a considerable dilation period, and ii) liquefaction-induced degradation of stiffness. These required capabilities are same as the first two considerations mentioned in Section 5.4.2.

Simulation results of the experiment using the DM04 model are presented in Fig. 5.7c,d. The model is able to capture the attractor $p' = q = 0$ despite missing the number of cycles to get there. The latter is partly related to the choices of fabric dilatancy parameters, i.e., c_z and $z_{\max}$ in Table 5.1, which following the dilation response result in significant contraction upon reverse loading. To improve the simulation of the number of cycles to liquefaction in this case, one may consider making the c_z density-dependent. The DM04 simulation results also show that the stress path and stress-strain loops get lock-up after the first loading cycle, and do not replicate the reduction of q^{amp} as shown in the experiment. This is because in the subsequent locked-up stress loops around the liquefaction state, the DM04 does not progressively degrade the plastic modulus. The SANISAND-MSf simulation results are shown in Fig. 5.7e,f. Here, the model can gradually decrease the plastic modulus at low effective stresses by incorporating the semifluidized state. Therefore it captures the progressive reduction of q^{amp} and degradation of stress-strain loops to a nearly flat one after several loading cycles, comparable with the experiment.

Simulations with the HP+IS model are presented in Fig. 5.7g,h and show a serious flaw: the stress path gets locked-up before reaching $p' = 0$ and therefore they do not reach the attractor $p' = q = 0$. As a result, the model also cannot simulate the progressive reduction of q^{amp}. The underlying reasons for these shortcomings are same as those presented earlier for simulation of cyclic mobility. It is worth noting that by incorporating the anisotropic critical state theory to influence the dilation and shear strength, Liao and Yang [134] successfully simulated this type of experiment using a modified version of the HP+IS model. Finally, simulations with HP+ISA model are presented in Fig. 5.7i,j and show that the model approaches (but not sufficiently) the attractor $p' = q = 0$. Similar to the DM04, this model also does not adequately capture the continued reduction of q^{amp} in subsequent cycles. This is because the model adopts a strain-based version of the fabric dilatancy feature of DM04, to capture the cyclic mobility effect, but does not degrade the stiffness in a progressive fashion.

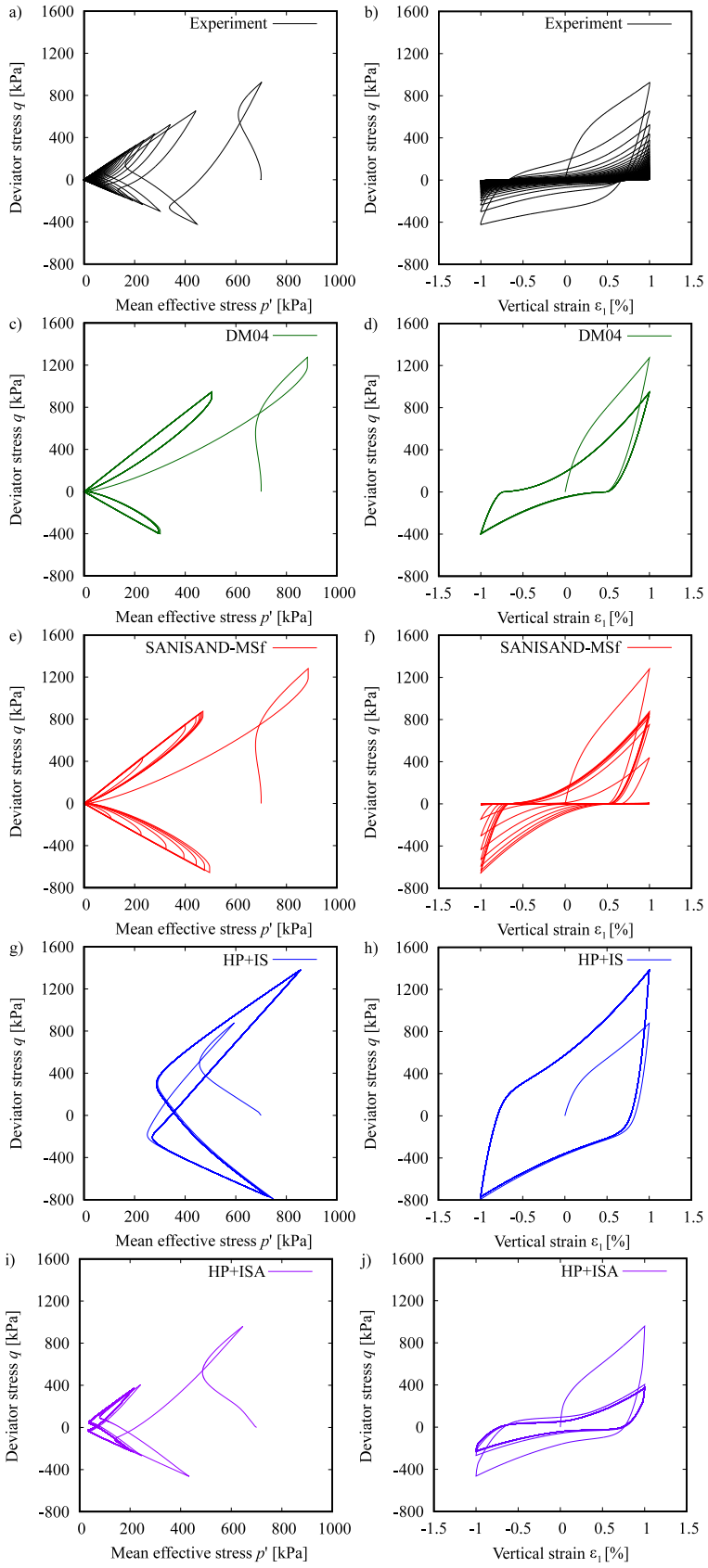

Figure 5.7: Undrained cyclic triaxial test on Karlsruhe fine sand. Dense sample ($D_\mathrm{r} = 101\%$) with isotropic consolidation ($p'_0 = 700$ kPa) and strain cycles of large amplitude ($\varepsilon_1^{\mathrm{amp}} = 1\%$): a,b) Experiments reported by Wichtmann and Triantafyllidis [274]; and the corresponding simulations using c,d) DM04; e,f) SANISAND-MSf; g,h) HP+IS; i,j) HP+ISA

5.4.5 Limitation 5: significant plastic accumulation on small $q - p'$ closed loop cycles and artificial accumulation

In addition to the popular one-dimensional cyclic loading type such as cyclic triaxial or simple shear tests, multidimensional cyclic loading generated by varying multiple components of the stress or strain tensor is also very interesting and meaningful considering the three-dimensional nature of the loading conditions in the field. One such example was performed by Poblete et al. [180] on Karlsruhe fine sand and is illustrated in Fig. 5.8. The test consists of a multidimensional stress path under triaxial conditions, describing a circle in the space of the invariants $P = \sqrt{3}p'$ and $Q = \sqrt{2/3}q$ (note that $P^2 + Q^2 = \| \boldsymbol{\sigma} \|^2$). To achieve this, Q and P were simultaneously controlled through the following parametric equations:

$$P(t) = 200\sqrt{3} + 20\sin\left(\frac{2\pi}{200}t\right), \quad \text{and} \quad Q(t) = 100\sqrt{\frac{2}{3}} + 20\sin\left(\frac{2\pi}{200}t + \frac{\pi}{2}\right) \tag{5.1}$$

or equivalently,

$$\sigma_1 = \frac{800}{3} + \frac{20}{\sqrt{3}}\sin\left(\frac{2\pi}{200}t\right) + \frac{40}{3}\sqrt{\frac{3}{2}}\sin\left(\frac{2\pi}{200}t + \frac{\pi}{2}\right) \tag{5.2}$$

$$\sigma_2 = \sigma_3 = \frac{500}{3} + \frac{20}{\sqrt{3}}\sin\left(\frac{2\pi}{200}t\right) - \frac{20}{3}\sqrt{\frac{3}{2}}\sin\left(\frac{2\pi}{200}t + \frac{\pi}{2}\right) \tag{5.3}$$

where t is the time. The corresponding experimental results within 30 loading cycles are given in Fig. 5.9a-c. One can observe a negligible accumulation of vertical strains ($\varepsilon_1^{\text{acc}} \approx 0$) along the cyclic shearing and the void ratio does not change noticeably either, implying an almost elastic response. It can be used to calibrate model parameters related to elasticity or judge the model performance in handling the plastic modulus during the transition from purely elastic to elastoplastic loading.

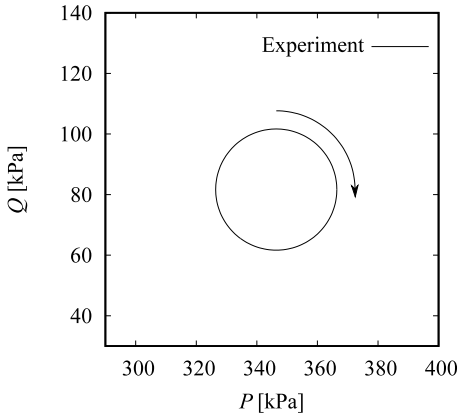

Figure 5.8: Cyclic loading path in the $Q - P$ space

We now proceed to provide some simulation results with the aforementioned four constitutive models. The initial conditions of the sample follow $\sigma_1 = 283.0$ kPa, $\sigma_2 = \sigma_3 = 158.5$ kPa and $e_0 = 0.857$. The simulations were performed by controlling the Roscoe stress invariants according to Equation 5.1 and are sequentially shown in Figs. 5.9d-o. Unlike the experiment, all the simulations exhibit significant accumulations of plastic strain and noticeable contraction except the HP+ISA model.

The mismatch between simulations of these three models and the experiment is attributed to the inability to deactivate the plastic strain rate. For DM04 (Figs. 5.9d-f) and SANISAND-MSf (Figs. 5.9g-i) models, this inability comes from a) the rather small size of yield surface (model parameter m in Tables 5.1 and 5.2), and b) the small values of model parameters related to plastic modulus (such as h_0). Had these two been increased by a certain amount, the simulations would match the experiment better. An improvement of the SANISAND-MSf simulation compared with DM04 is due to the new constitutive ingredient of memory surface, which stiffens the model when reverse loading occurs. In particular the simulation of void ratio versus N is very promising and the magnitude of strain components is also reduced a bit. The HP+IS model does not incorporate any elastic locus, but delivers a linear form of the equation when the condition ($\overrightarrow{\mathbf{h}} : \overrightarrow{\dot{\boldsymbol{\varepsilon}}} = -1$) holds for the whole cycle. The latter condition is only possible when performing a very small strain amplitude under one-directional loading conditions. Hence, it is not possible to have such condition on a $q - p'$ loop. The HP+ISA model incorporates a bubble shaped elastic locus within the strain space. From the four selected models, this is the only one able to deactivate completely the plastic strain rate under such path. However, it is still producing very small plastic strain rate, related to the second cause explained in the next paragraph, but remains the most successful in the simulation of this type of loading. These results show us the advantage of using a strain based yield surface, as in HP+ISA, rather than a stress based yield surface.

One may doubt the artificial accumulation due to incorporation of hypo-elasticity in the models, a quite common feature adopted in sand models. The selection of a hypo-elastic stiffness is usually justified by researchers with the argument that the resulting artificial accumulation is almost negligible for most practical problems. However, Poblete et al. [180] showed that multidimensional stress paths under triaxial conditions in the $q - p'$ space, such as a circle in the $q - p'$ space, provides much more artificial accumulation than unidirectional loading (e.g., conventional undrained cyclic triaxial loading), the latter frequently used to test the performance of models. The accumulation by the hypo-elastic tensors is analyzed in Fig. 5.10 through the simulation of the same experimental test. The plastic component of each model are thereby not considered. Note that the vertical axes of Figs. 5.9 and 5.10 are different to observe in detail the effect of the artificial accumulation. The simulation results show an accumulation of strains with all models and a reduction in the void ratio by the hypoplastic-type models. The magnitude of the exhibited accumulation is small but not negligible. In order to address this issue, models may be extended considering hyperelastic stiffness. Comparison of Figs. 5.9 and 5.10, however, demonstrates that hypoelastic stiffness is not the major cause of excessive accumulation in closed loop cycles.

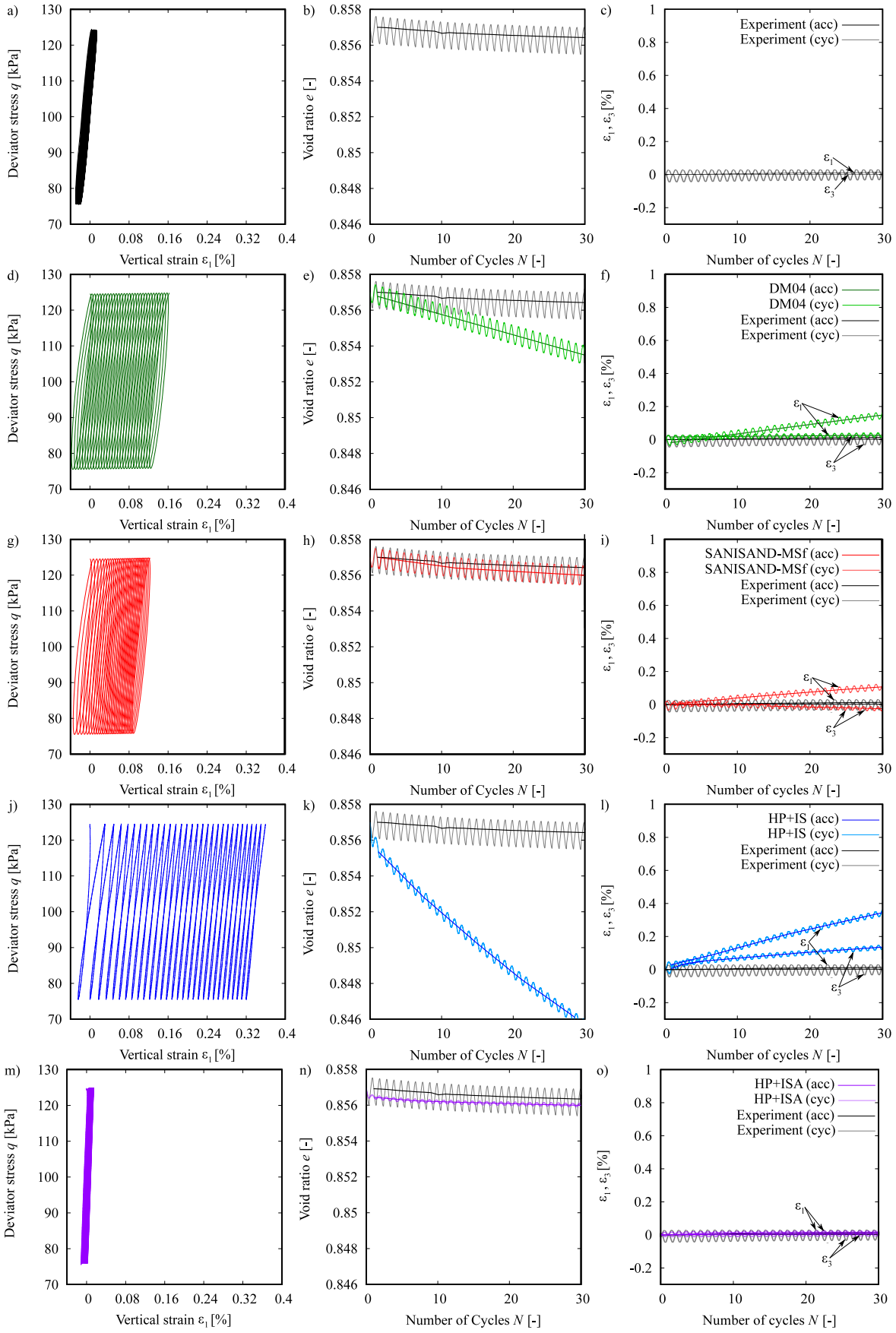

Figure 5.9: a-c) Experiment on Karlsruhe fine sand reported by Poblete et al. [180]; and the corresponding simulations using d-f) DM04, g-i) SANISAND-MSf, j-l) HP+IS, m-o) HP+ISA

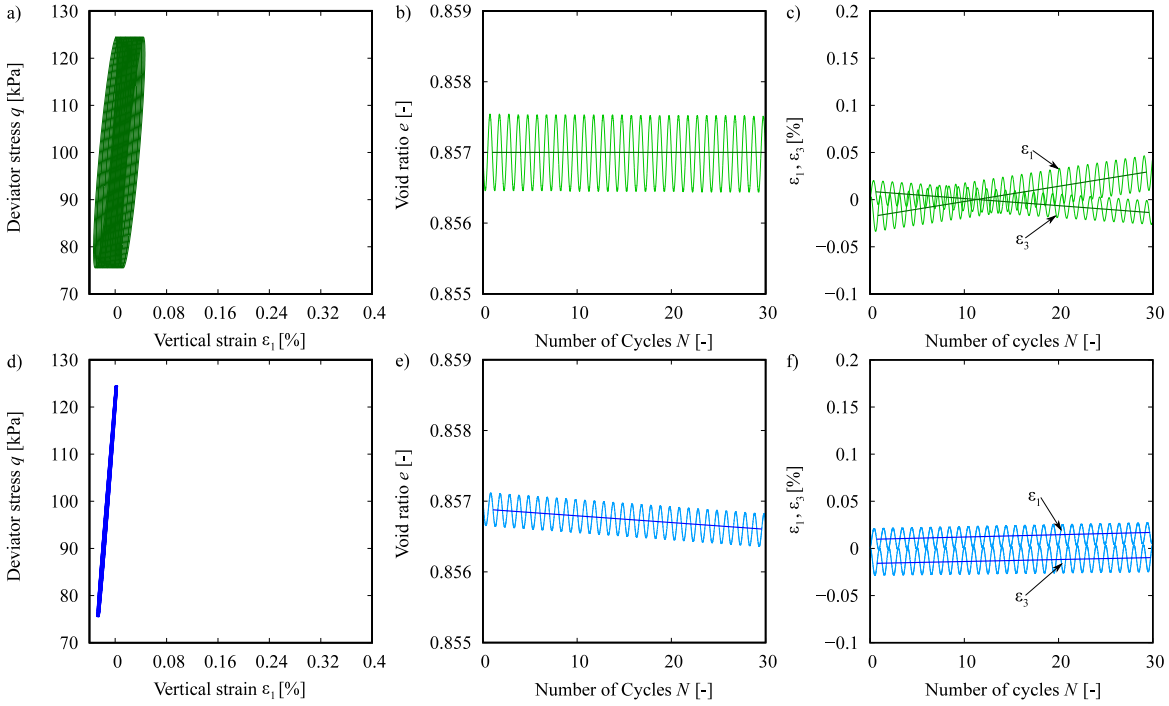

Figure 5.10: Simulations with the (hypo-)"elastic" tensor of: a-c) DM04/SANISAND-MSf models; d-f) hypoplastic models

5.4.6 Limitation 6: Wrong oedometric stiffness

Oedometric tests are of particular importance for settlement predictions on many engineering problems. When the vertical loading is of cyclic nature, and occurs under drained conditions, correct assessment of cyclic models on the reproduction of oedometric cycles is of crucial relevance. Although a cyclic oedometer test is considered to be simple, yet important, many deficiencies have been seen on their simulations. Problems concerning to the resulting oedometric stiffness, and overshooting/subshooting effects are characteristic drawbacks on these simulations. For illustration and analysis purposes, the cyclic oedometer reported by Wichtmann and Triantafyllidis [274] on Karlsruhe fine sand is used and shown in Figure 5.11. The following initial conditions are thereby given: $e_0 = 0.8894$, $D_r = 44\%$, $\sigma_1 = 0.221$ kPa. It includes multiple unloading-reloading cycles with the following description: loading/reloading paths increases the axial stress to: a) $\sigma_1 = 20.53$ kPa, b) $\sigma_1 = 55.72$ kPa, c) $\sigma_1 = 142.14$ kPa, d) $\sigma_1 = 407.1$ kPa and e) $\sigma_1 = 407.1$ kPa, respectively. All unloading paths reach always $\sigma_1 = 1$ kPa.

Simulations with the four models for cyclic loading are also included in Figure 5.11, and their lack of congruence is evident: to start with, the DM04 and SANISAND-MSf models showed in general a stiffer behavior. This is because of the basic formulation of these models with an open ended narrow cone-type yield surface, hence not generating any plasticity under constant stress ratio loading. The main logic behind this assumption is that in sands, due to their granular nature, the predominant mechanism of plastic deformation is due to a change in stress ratio. The appropriateness of various choices of yield surface shape for sand and clay elastoplasticity models was discussed in Taiebat and Dafalias [240]. In particular, it was proposed that yield surface for sands must be narrow with a shape that is more or less along a constant stress ratio line in the triaxial space, and for higher values of p' such shape must be closed, since high pressure can create plastic deformation by crushing of the sand grains. On that basis, Taiebat and Dafalias [239] proposed an additional mechanism in the SANISAND family for generating plastic strains under constant stress ratio loading, hence improving the model response in the related loading scenarios. The HP+IS and HP+ISA models perform better in regard to stiffness because they consider the void ratio characteristic loading curves, corresponding to the maximum, minimum and critical state void ratios in their formulations. However, they simulate wrong in reloading paths: while overshooting is observed on the HP+IS model for all cases, undershooting is delivered by the HP+ISA model on larger strain amplitudes. Hence it is shown that strain based formulations, as the intergranular strain theory considered by the HP+IS and HP+ISA models, should be enhanced for correct assessment of memory effects where cycles with different strain amplitudes is reproduced. It is highly recommended to investigate how memory effects can be improved on IS-type formulations. The major overshooting of monotonic paths can be eliminated by coupling the IS formulation with ASBS [18], as already discussed in Section 5.4.1. The brick model by Simpson [209] gives some hints about using multiple internal variables related to different strain amplitudes.

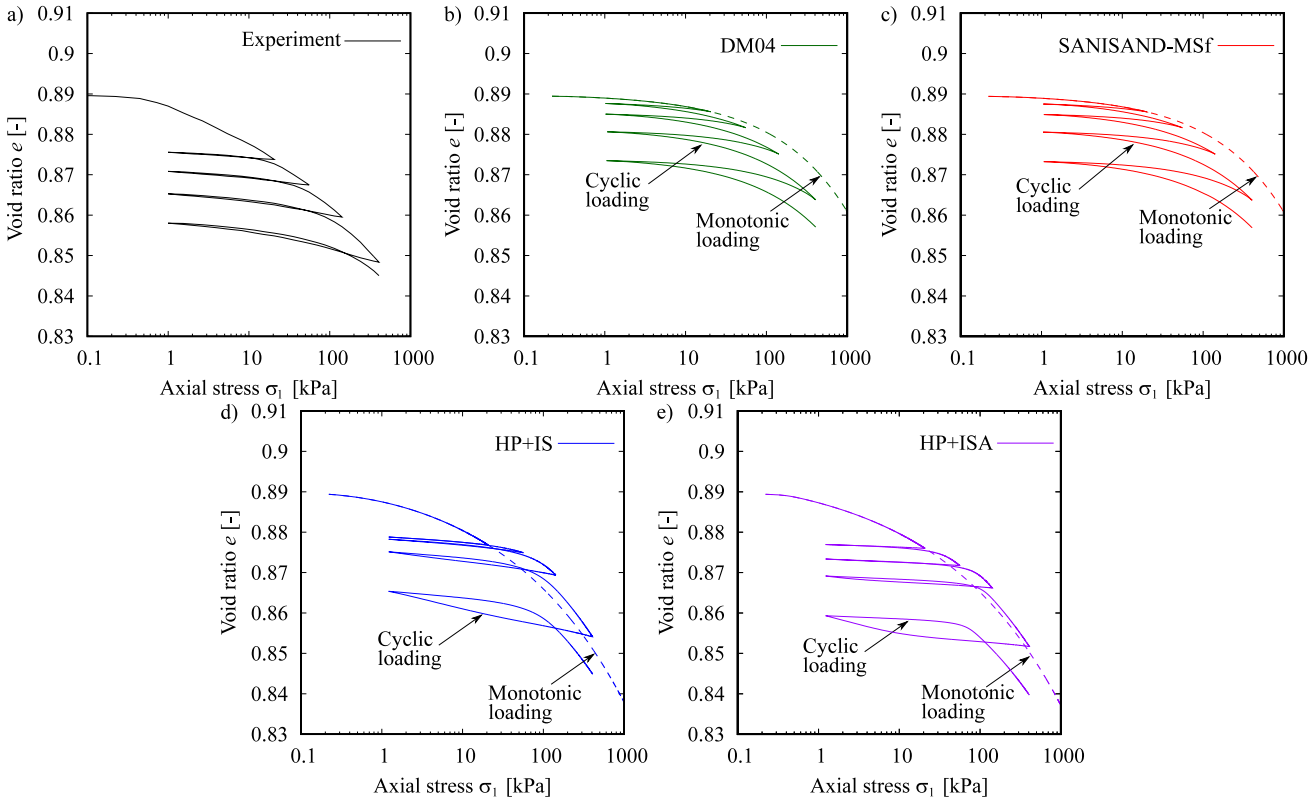

Figure 5.11: Oedometric test with multiple unloading-reloading cycles: a) Experiment on Karlsruhe fine sand reported by Wichtmann and Triantafyllidis [274]; and the corresponding simulations using b) DM04; c) SANISAND-MSf; d) HP+IS; e) HP+ISA

5.4.7 Limitation 7: Effect of drained preloading in undrained shearing

Drained preloading events have shown a strong influence on subsequent undrained shearing paths. This effect is of particular importance in many engineering problems, were "slow" loading cycles under drained conditions may eventually occur before any rapid loading. Many problems dealing with environmental loads (winds, waves, flooding, etc) may experience this effect, considering the stochastic nature of their velocities. A triaxial test including a drained preloading stage before an undrained shearing gives to researchers some hints about the material response under these conditions. These tests have clearly shown a strong influence of the drained preloading on the undrained shearing path [43, 45, 46, 48, 263], effect which is frequently disregarded on cyclic models.

For analysis purposes, three triaxial experiments performed on Karlsruhe fine sand by Wichtmann [263], two of them with drained preloading, are shown in Fig. 5.12a,b. They were performed as follows: a) undrained triaxial test with no drained preloading. Its initial conditions are ($e_0 = 0.941$, $D_r = 30\%$, $p'_0 = 300$ kPa). The undrained shearing ends at an axial strain of $\varepsilon_1 = 30\%$. b) Undrained triaxial test with isotropic ($q = 0$) drained preloading to $p' = 800$ kPa. The preloading path follows the points $\mathrm{A} \rightarrow \mathrm{B} \rightarrow \mathrm{A}$ as shown in Fig. 5.12a. The initial conditions (before the drained preloading) are ($e_0 = 0.937$, $D_r = 31\%$, $p'_0 = 300$ kPa). A subsequent undrained triaxial test was performed till reaching $\varepsilon_1 = 30\%$. c) Undrained triaxial test with drained triaxial preloading. Same as the last test, with the difference, that a drained triaxial test was used as the preloading path. The drained triaxial test follows the points $\mathrm{A} \rightarrow \mathrm{C} \rightarrow \mathrm{A}$ shown in Fig. 5.12a. The initial conditions (before the drained preloading) are ($e_0 = 0.937$, $D_r = 31\%$, $p'_0 = 300$ kPa). Subsequently, an undrained shearing till $\varepsilon_1 = 30\%$ was performed.

The experimental results are presented in Fig. 5.12a,b and show a serious affection of the undrained response due to the drained preloading. This is attributed to both small strain effects and memory effects. Simulations show that the SANISAND-MSf and HP+IS are the only ones to capture partly well the influence of the drained preloading effect on the undrained shearing. The SANISAND-MSf model reproduces the influence of the deviatoric preloading due to the introduction of memory surface, whose evolution during the deviatoric preloading increases the stiffness of the model. On the other hand, the HP+IS reproduces this behavior due to the fact that the IS approach by Niemunis and Herle [170] accounts for small strain effects depending on the angle formed by loading and unloading strain rate. The HP+ISA model did not simulate this effect, consistently with the fact that an undershooting is usually obtained on reloading paths of medium strain amplitudes. The DM04 model has a similar effect as the HP+ISA model, because its yield surface is narrow, and lacks of memory effects on cycles of larger amplitudes.

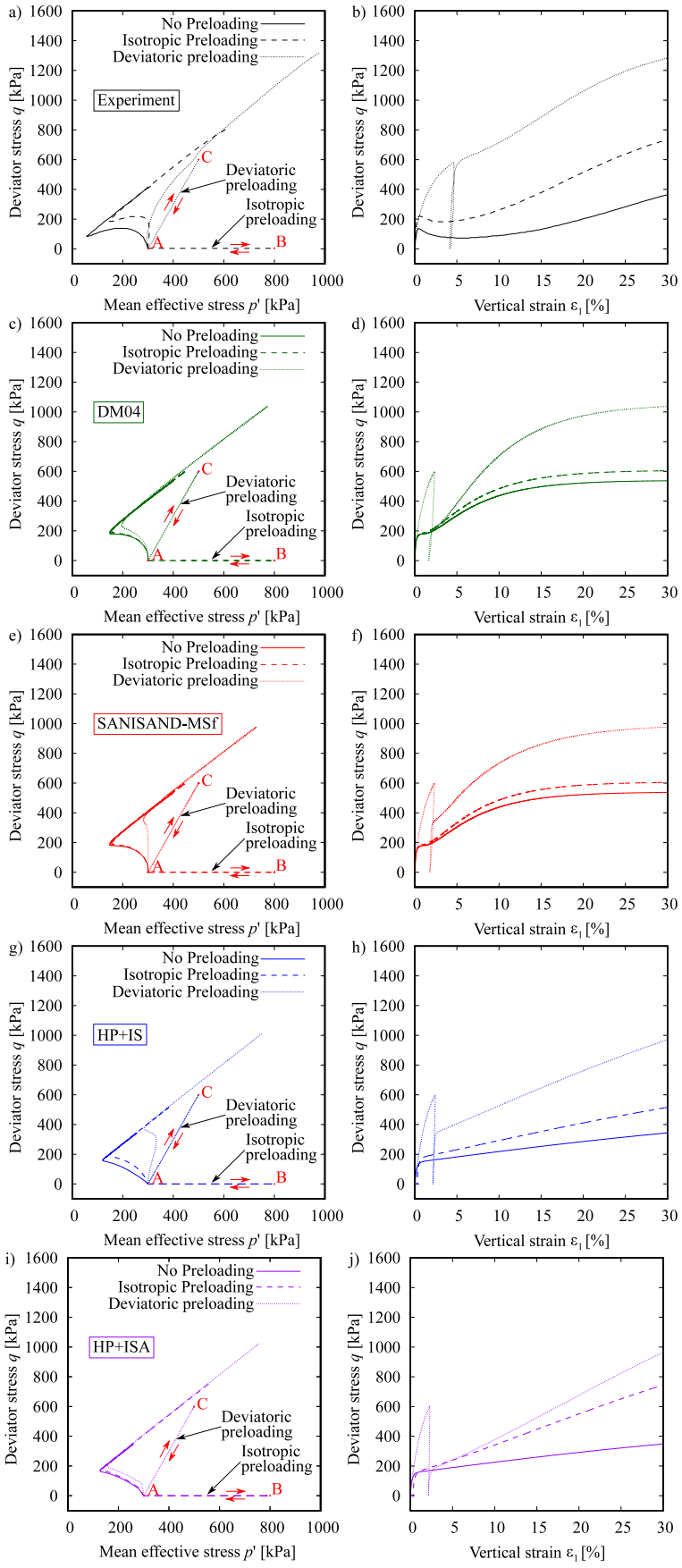

Figure 5.12: Undrained monotonic triaxial tests with isotropic consolidation ($p'_0 = 300$ kPa) and different types of preloadings: a,b) Experiments on Karlsruhe fine sand reported by Wichtmann [263], and the corresponding simulations using c,d) DM04; e,f) SANISAND-MSf; g,h) HP+IS; i,j) HP+ISA

5.5 Summary and conclusions

In this work, seven characteristic limitations of models for cyclic loading for sands are presented and discussed, from which suggestions are given to help further development of cyclic constitutive models. Components of some formulations which are responsible for these limitations, for example, yield surface, elastic stiffness, plastic strain rate, among others, are mentioned for the sake of clarity, considering that these components may be shared by many existing models. In the analysis, two models from the bounding surface plasticity family and two models from the hypoplastic family were considered. Some of the exposed limitations are described in the following lines:

1. Overshooting (or undershooting) phenomenon after reverse loading/immediate reloading paths is a characteristic artificial drawback in model simulations of the cyclic loading of sands. To adequately address this issue, considering the memory effects of recent reverse loading history in the cyclic models is recommended.

2. Simulation of cyclic mobility with undrained cyclic triaxial tests of symmetric deviator stress amplitude ($q^{\min} = q^{\max}$) is in general accompanied with one-way ratcheting in strain accumulation. Two specific considerations can be incorporated to adequately resolve this issue. The first is to induce a degrading stiffness cycle by cycle so as to generate large shear strain in the liquefaction state. The other is to control the balance of the shear modulus in the compression and extension side.

3. To adequately model the cyclic liquefaction strength curves or CSR–N_{ini} considering various criteria for reaching initial liquefaction, is a challenge in majority of available constitutive models. To reach the criterion of r_u, the model needs to induce a large amount of contraction upon unloading after dilation. To properly capture the shear strain-based initial liquefaction, a mechanism for generating large shear strain in liquefaction state is necessary. To quantitatively simulate cyclic liquefaction strength curves, one needs to consider effects of CSR, relative densities, and initial confinement.

4. Simulation performance on very dense samples subjected to undrained cycles of constant large strain amplitudes also reveals some missing features in the constitutive models. A good amount of contraction should be generated upon unloading after dilation. The stress path attractor is accompanied by a degrading shear modulus.

5. The plastic strain accumulation is unrealistic when dealing with cyclic loading with closed stress loops of small amplitude, whereby much less accumulation of strains is expected. Attention should be given to the strain accumulation provided by the hypoelastic component of the models, to properly reduce the resulting strain accumulation.

6. The constitutive models when formulated only in terms of stress ratio changes for generating plasticity, may deliver inadequate oedometric loading stiffness. Thus in the formulation one may need to also account for plastic strains under constant stress ratio loading.

7. Drained preloading affects significantly the subsequent undrained shearing. This effect should not be neglected by constitutive models. Inadequate memory effects in the formulation of some models hinder the reproduction of this important aspect in modeling the subsequent undrained shearing.

5.6 Acknowledgements

The first and fourth authors appreciate the financial support given by the INTER-EXCELLENCE project LTACH19028 by the Czech Ministry of Education, Youth and Sports. The first author appreciates the financial support given by the Charles University Grant Agency (GAUK) with project number 200120. The

fourth author acknowledges institutional support by Center for Geosphere Dynamics (UNCE/SCI/006). The third and fifth authors acknowledge the support from the Natural Sciences and Engineering Research Council of Canada (NSERC). Yannis F. Dafalias help in reviewing the parts related to the plasticity models is acknowledged.

5.7 Appendix

5.7.1 Notation and variables

The notation and convention is as follows: scalar magnitudes (e.g., a, b) are denoted by italic fonts, vectors (e.g., $\mathbf{a}, \mathbf{b}$) with bold lowercase fonts, second-rank tensors (e.g., $\mathbf{A}$, $\mathbf{B}$) with bold capital letter or bold symbols, higher ranked tensors with special fonts (e.g., E, L). Components of these tensors are denoted through indicial notation (e.g., A_{ij}). δ_{ij} is the Kronecker delta, also represented with ($1_{ij} = \delta_{ij}$). The unit fourth-rank tensor for symmetric tensors is denoted by I, where $\mathsf{I}_{ijkl} = \frac{1}{2}\big(\delta_{ik}\delta_{jl} + \delta_{il}\delta_{jk}\big)$. The following operations hold: $\mathbf{A} : \mathbf{B} = A_{ij}B_{ij}$, $\mathbf{A} \otimes \mathbf{B} = A_{ij}B_{kl}$, $\parallel \mathbf{A} \parallel = \sqrt{A_{ij}A_{ij}}$, $\overrightarrow{\square} = \frac{\square}{\|\square\|}$, $\mathbf{A}^{\mathrm{dev}} = \mathbf{A} - \frac{1}{3}(\mathrm{tr}\mathbf{A})\mathbf{1}$, $\hat{\mathbf{A}} = \frac{\mathbf{A}}{\mathrm{tr}(\mathbf{A})}$. Components of the effective stress tensor $\boldsymbol{\sigma}$ or strain tensor $\boldsymbol{\varepsilon}$ in compression are negative. Roscoe variables are defined as $p' = -\sigma_{ii}/3$, $q = \sqrt{\frac{3}{2}} \parallel \boldsymbol{\sigma}^{\mathrm{dev}} \parallel$, $\varepsilon_v = -\varepsilon_{ii}$ and $\varepsilon_s = \sqrt{\frac{2}{3}} \parallel \boldsymbol{\varepsilon}^{\mathrm{dev}} \parallel$. The stress ratio η is defined as $\eta = q/p'$.

5.7.2 Summary of constitutive equations for models for cyclic loading

Table 5.5 provides a summary of the constitutive equations of the DM04 model by Dafalias and Manzari [39] and the SANISAND-MSf model by Yang et al. [286]. A detailed guide for the calibration of the DM04 and SANISAND-MSf parameters can be found in Dafalias and Manzari [39], Taiebat and Dafalias [239] and Yang et al. [286].

Table 5.5: Constitutive relations of the elasto-plastic models

Bounding surface plasticity model by Dafalias and Manzari [39]	
$\mathrm{d}\varepsilon_{\mathrm{v}}^{\mathrm{e}} = \mathrm{d}p'/K$; $\mathrm{d}\mathbf{e}^{\mathrm{e}} = \mathrm{d}\mathbf{s}/(2G)$	$\mathrm{d}\varepsilon_{\mathrm{v}}^{\mathrm{p}} = \langle L\rangle D$; $\mathrm{d}\mathbf{e}^{\mathrm{p}} = \langle L\rangle \mathbf{R}'$
$G = G_0 p_{\mathrm{at}}(2.97 - e)^2/(1+e)(p'/p_{\mathrm{at}})^{1/2}$	$K = 2(1+\nu)/[3(1-2\nu)G]$
$f = \sqrt{(\mathbf{s} - p'\boldsymbol{\alpha}) : (\mathbf{s} - p'\boldsymbol{\alpha})} - \sqrt{2/3}pm$	$D = A_0(1 + \langle \mathbf{z} : \mathbf{n}\rangle)(\boldsymbol{\alpha}_\theta^{\mathrm{d}} - \boldsymbol{\alpha}) : \mathbf{n}$
$\mathbf{R}' = B\mathbf{n} - C[\mathbf{n}^2 - (1/3)\mathbf{I}]$	$\mathbf{n} = (\mathbf{r} - \boldsymbol{\alpha})/\|\mathbf{r} - \boldsymbol{\alpha}\|$
$B = 1 + 3(1-c)/(2c)g(\theta, c)\cos 3\theta$	$C = 3\sqrt{3/2}(1-c)g(\theta,c)/c$
$g(\theta, c) = 2c/[(1+c) - (1-c)\cos 3\theta]$	$\mathrm{d}\boldsymbol{\alpha} = \langle L\rangle (2/3)h(\boldsymbol{\alpha}_\theta^{\mathrm{b}} - \boldsymbol{\alpha})$
$\mathrm{d}\mathbf{z} = -c_z\langle -\mathrm{d}\varepsilon_{\mathrm{v}}^{\mathrm{p}}\rangle(-z_{\max}\mathbf{n} + \mathbf{z})$	$h = b_0/[(\boldsymbol{\alpha} - \boldsymbol{\alpha}_{\mathrm{in}}) : \mathbf{n}]$
$b_0 = G_0 h_0(1 - c_h e)(p'/p_{\mathrm{at}})^{-1/2}$	$\boldsymbol{\alpha}_\theta^{\mathrm{d}} = \sqrt{2/3}[g(\theta,c)M\exp(n^{\mathrm{d}}\psi) - m]\mathbf{n}$
$\boldsymbol{\alpha}_\theta^{\mathrm{b}} = \sqrt{2/3}[g(\theta,c)M\exp(-n^{\mathrm{b}}\psi) - m]\mathbf{n}$	$e_{\mathrm{c}} = e_{\mathrm{c}}^{\mathrm{ref}} - \lambda_{\mathrm{c}}(p'/p_{\mathrm{at}})^{\xi}$
SANISAND-MSf model by Yang et al. [286]	
$\mathrm{d}\mathbf{e}^{\mathrm{p}} = \langle L\rangle \mathbf{R}^*$; $\mathbf{R}^* = x_\alpha^2\mathbf{n} + (1 - x_\alpha^2)\mathbf{R}'/\|\mathbf{R}'\|$	$x_\alpha = \langle \alpha_{\theta_\alpha}^{\mathrm{b}} - \|\boldsymbol{\alpha}\|\rangle/\alpha_{\theta_\alpha}^{\mathrm{b}}$
$\alpha_{\theta_\alpha}^{\mathrm{b}} = \sqrt{2/3}[g(\theta_\alpha, c)M\exp(-n^{\mathrm{b}}\psi) - m]$	$\cos 3\theta_\alpha = \sqrt{6}\mathrm{tr}(\mathbf{n}_\alpha^3)$; $\mathbf{n}_\alpha = \boldsymbol{\alpha}/\|\boldsymbol{\alpha}\|$
$D = A_0 g(\theta,c)^{-n_{\mathrm{g}}}(1 + \langle \mathbf{z} : \mathbf{n}\rangle)(\boldsymbol{\alpha}_\theta^{\mathrm{d}} - \boldsymbol{\alpha}) : \mathbf{n}$	$b_0 = G_0 h_0 g(\theta,c)^{-n_{\mathrm{g}}}(1 - c_h e)(p'/p_{\mathrm{at}})^{-1/2}$
$f^{\mathrm{M}} = \sqrt{(\boldsymbol{\alpha}_\theta^{\mathrm{M}} - \boldsymbol{\alpha}^{\mathrm{M}}) : (\boldsymbol{\alpha}_\theta^{\mathrm{M}} - \boldsymbol{\alpha}^{\mathrm{M}})} - \sqrt{2/3}m^{\mathrm{M}}$	$\boldsymbol{\alpha}_\theta^{\mathrm{M}} = \boldsymbol{\alpha}^{\mathrm{M}} + \sqrt{2/3}m^{\mathrm{M}}\mathbf{n}$
$\mathrm{d}\boldsymbol{\alpha}^{\mathrm{M}} = \langle L\rangle (2/3)h^{\mathrm{M}}(\boldsymbol{\alpha}_\theta^{\mathrm{b}} - \boldsymbol{\alpha}_\theta^{\mathrm{M}})$	
$\mathrm{d}m^{\mathrm{M}} = \langle L\rangle[\sqrt{2/3}c_{\mathrm{c}}h^{\mathrm{M}}\langle(\boldsymbol{\alpha}_\theta^b - \boldsymbol{\alpha}_\theta^{\mathrm{M}}) : \mathbf{n}\rangle - m^{\mathrm{M}}/\varsigma\|(\boldsymbol{\alpha}_\theta^{\mathrm{b}} - \boldsymbol{\alpha}_\theta^{\mathrm{M}}) : \mathbf{n}\|\langle -D\rangle]$	
$h^{\mathrm{M}} = \{h + \sqrt{3/2}(m^{\mathrm{M}}/\varsigma)\mathrm{sgn}[(\boldsymbol{\alpha}_\theta^{\mathrm{b}} - \boldsymbol{\alpha}_\theta^{\mathrm{M}}) : \mathbf{n}]\langle -D\rangle\}/(1 + c_{\mathrm{c}}\mathcal{H}[(\boldsymbol{\alpha}_\theta^{\mathrm{b}} - \boldsymbol{\alpha}_\theta^{\mathrm{M}}) : \mathbf{n}])$	
$h = \{b_0/[(\boldsymbol{\alpha} - \boldsymbol{\alpha}_{\mathrm{in}}) : \mathbf{n}]\}\exp[\{\mu_0/(\|\boldsymbol{\alpha}_{\mathrm{in}}\|^u + \varepsilon)\}(b^{\mathrm{M}}/b_{\mathrm{ref}})^w]$	$b^{\mathrm{M}} = (\boldsymbol{\alpha}_\theta^{\mathrm{M}} - \boldsymbol{\alpha}) : \mathbf{n}$; $b_{\mathrm{ref}} = (\boldsymbol{\alpha}_\theta^{\mathrm{b}} - \boldsymbol{\alpha}_{\theta+\pi}^{\mathrm{b}})$
$\mathrm{d}\ell = \langle L\rangle[c_\ell\langle 1 - p_{\mathrm{r}}\rangle(1-\ell)^{n_\ell}] - c_{\mathrm{r}}\ell\,\mathrm{d}\varepsilon_{\mathrm{v}}\|$	$p_{\mathrm{r}} = p'/p_{\mathrm{th}}$
$h_0 = h_0'[(1 - \langle 1 - p_{\mathrm{r}}\rangle)^{x\ell} + f_\ell]$	$A_0 = A_0'[(1 - \langle 1 - p_{\mathrm{r}}\rangle)^{x\ell} + f_\ell]$

The constitutive equations of the hypoplastic model for sands by Von Wolffersdorff [277] and the two

different intergranular strain approaches by Niemunis and Herle [170] and Fuentes et al. [76] are presented in Table 5.6. A detailed guide for the calibration of the hypoplastic and conventional intergranular strain parameters can be found in Herle and Gudehus [90] and Niemunis and Herle [170], respectively. On the other hand, a guide for the calibration of the ISA-hypoplasticity parameters can be found in Fuentes [68] and Fuentes et al. [76].

Table 5.6: Constitutive relations of the hypoplastic models

Hypoplastic model for sands by Von Wolffersdorff [277]	
$\mathring{\boldsymbol{\sigma}} = \mathsf{M} : \dot{\boldsymbol{\varepsilon}}$	
$\mathsf{L}^{\text{hyp}} = f_b f_e \dfrac{1}{\hat{\boldsymbol{\sigma}} : \hat{\boldsymbol{\sigma}}}(F^2 \mathsf{I} + a^2 \hat{\boldsymbol{\sigma}}\hat{\boldsymbol{\sigma}})$	$\mathbf{N}^{\text{hyp}} = f_d f_b f_e \dfrac{Fa}{\hat{\boldsymbol{\sigma}} : \hat{\boldsymbol{\sigma}}}(\hat{\boldsymbol{\sigma}} + \hat{\boldsymbol{\sigma}}^{\text{dev}})$
$f_b = \dfrac{h_s}{n}\left(\dfrac{1+e_i}{e_i}\right)\left(\dfrac{e_{i0}}{e_{c0}}\right)^{\beta}\left(-\dfrac{\text{tr}\boldsymbol{\sigma}}{h_s}\right)^{1-n}\left[3 + a^2 - \sqrt{3}a\left(\dfrac{e_{i0}-e_{d0}}{e_{c0}-e_{d0}}\right)^{\alpha}\right]^{-1}$	$f_e = \left(\dfrac{e_c}{e}\right)^{\beta}$
$F = \sqrt{\dfrac{1}{8}\tan^2(\psi) + \dfrac{2-\tan^2(\psi)}{2+2\sqrt{2}\tan(\psi)\cos(3\theta)}} - \dfrac{1}{2\sqrt{2}\tan(\psi)}$	$f_d = \left(\dfrac{e-e_d}{e_c-e_d}\right)^{\alpha}$
$e_c = e_{c0}\exp(-(3p'/h_s)^n)$	$a = \dfrac{\sqrt{3}(3-\sin(\varphi_c))}{2\sqrt{2}\sin(\varphi_c)}$
$e_d = e_{d0}\exp(-(3p'/h_s)^n)$	$e_i = e_{i0}\exp(-(3p'/h_s)^n)$
$\cos(3\theta) = \sqrt{6}\dfrac{\text{tr}(\hat{\boldsymbol{\sigma}}^{\text{dev}}\hat{\boldsymbol{\sigma}}^{\text{dev}}\hat{\boldsymbol{\sigma}}^{\text{dev}})}{(\hat{\boldsymbol{\sigma}}^{\text{dev}} : \hat{\boldsymbol{\sigma}}^{\text{dev}})^{3/2}}$	$\tan\psi = \sqrt{3}\|\hat{\boldsymbol{\sigma}}^{\text{dev}}\|$
Intergranular Strain model by Niemunis and Herle [170]	
$\mathsf{M} = m_1\mathsf{L}^{\text{hyp}} + m_2\mathsf{L}^{\text{hyp}} : \overrightarrow{\mathbf{h}}\overrightarrow{\mathbf{h}} + \rho^{\chi}\mathbf{N}^{\text{hyp}}\overrightarrow{\mathbf{h}}$ for $\overrightarrow{\mathbf{h}} : \dot{\boldsymbol{\varepsilon}} > 0$	$\dot{\mathbf{h}} = (\mathsf{I} - \overrightarrow{\mathbf{h}}\overrightarrow{\mathbf{h}}\rho^{\beta_r}) : \dot{\boldsymbol{\varepsilon}}$ for $\overrightarrow{\mathbf{h}} : \dot{\boldsymbol{\varepsilon}} > 0$
$\mathsf{M} = m_1\mathsf{L}^{\text{hyp}} + m_3\mathsf{L}^{\text{hyp}} : \overrightarrow{\mathbf{h}}\overrightarrow{\mathbf{h}}$ for $\overrightarrow{\mathbf{h}} : \dot{\boldsymbol{\varepsilon}} \le 0$	$\dot{\mathbf{h}} = \dot{\boldsymbol{\varepsilon}}$ for $\overrightarrow{\mathbf{h}} : \dot{\boldsymbol{\varepsilon}} \le 0$
$m_1 = \rho^{\chi} m_T + (1-\rho^{\chi})m_R$	$m_2 = \rho^{\chi}(1-m_T)$
$m_3 = \rho^{\chi}(m_R - m_T)$	$\rho = \parallel \mathbf{h} \parallel / R$
ISA-hypoplasticity by Fuentes et al. [76]	
$\mathsf{M} = m(\mathsf{L}^{\text{hyp}} + \rho^{\chi}\mathbf{N}^{\text{hyp}}\mathbf{N})$ for $F_H = 0$	$F_H = \parallel \mathbf{h} - \mathbf{c} \parallel - R/2$
$\mathsf{M} = m_R\mathsf{L}^{\text{hyp}}$ for $F_H < 0$	$\mathbf{N} = (\mathbf{h}-\mathbf{c})^{\rightarrow}$
$m = m_R + (1-m_R)y_h$	$\dot{\lambda}_H = \dfrac{\langle \mathbf{N} : \dot{\boldsymbol{\varepsilon}} \rangle}{1 + \mathbf{N} : \bar{\mathbf{c}}}$
$\dot{\mathbf{h}} = \dot{\boldsymbol{\epsilon}} - \dot{\lambda}_H \mathbf{N}$	$\dot{\mathbf{c}} = \dot{\lambda}_H \bar{\mathbf{c}}$
$\mathbf{c}_b = (R/2)\overrightarrow{\dot{\boldsymbol{\varepsilon}}}$	$\mathbf{h}_b = R\mathbf{N}$
$y_h = \rho^{\chi}\langle \mathbf{N} : \dot{\boldsymbol{\varepsilon}} \rangle$	$\rho = 1 - \dfrac{\|\mathbf{d}_b\|}{2R}$
$\mathbf{d}_b = \mathbf{h}_b - \mathbf{h}$	$\bar{\mathbf{c}} = \beta_h(\mathbf{c}_b - \mathbf{c})/R$
$\chi = \chi_0 + \varepsilon_{\text{acc}}(\chi_{\max} - \chi_0)$	$\dot{\varepsilon}_{\text{acc}} = \dfrac{c_a}{R}(1 - y_h - \varepsilon_{\text{acc}}) \parallel \dot{\boldsymbol{\varepsilon}} \parallel$
$\beta_h = \beta_{\text{hmax}} + (\beta_{h0} - \beta_{\text{hmax}})(1-f_z)f_h$	$\dot{\mathbf{Z}} = c_z\langle F_d \rangle(\mathbf{N} - \mathbf{Z}) \parallel \dot{\boldsymbol{\varepsilon}} \parallel$
$f_h = \mid \overrightarrow{\dot{\boldsymbol{\varepsilon}}} : \overrightarrow{\mathbf{d}_b} \mid$	$\overrightarrow{\mathbf{d}_b} = (R\overrightarrow{\dot{\boldsymbol{\varepsilon}}} - \mathbf{h})^{\rightarrow}$
$f_e = f_{e0} - f_z\langle f_{e0} - 1 \rangle$	$f_{e0} = \left(\dfrac{e_c}{e}\right)^{\beta}$
$f_d = f_{d0} + f_z\langle 1 - f_{d0} \rangle$	$f_{d0} = \left(\dfrac{e-e_d}{e_c-e_d}\right)^{\alpha}$
$F_d = \dfrac{q/p'}{M_c F f_{d0}}$	$f_z = \langle -\mathbf{Z} : \mathbf{N} \rangle$

Chapter 6

Improvement to the intergranular strain model for larger numbers of repetitive cycles - Article 5

Summary of the article

The experience with hypoplastic models suggest that they present a good performance on monotonic loading, or equivalently, under medium and large strain amplitudes. On the other hand, they present some serious deficiencies under very small to small strain amplitudes (e.g. under cyclic loading), where small strain effects take relevance. A solution to properly include small-strain effects in hypoplasticity was proposed by Niemunis and Herle [170] with the so-called "Intergranular Strain" theory as an extension of hypoplastic models. It proposes a new strain-type state variable that stores information about the recent strain history, and this enables to detect whether the material has been subjected to monotonic or loading reversal, which needs to be properly identified for predicting cyclic loading. This information is used to increase the stiffness and reduce the strain accumulation on cyclic loading. With this, most of the issues of the basic hypoplasticity in the small-strain range were addressed.

The experimental evidence under cyclic loading suggest that when the soil is subjected to a set of repetitive cycles, the strain and pore water pressure accumulation rate reduces as the number of cycles increases, increasing subsequently when the state approaches cyclic mobility. However, the experience with hypoplasticity extended with intergranular strain suggest that the performance on the aforementioned tests is not accurate enough. This article presents a simple yet efficient extension of the original intergranular strain model with focus to cyclic loading episodes with sets of repetitive cycles. For validation purposes, the hypoplastic model for sands by Von Wolffersdorff [277] is extended with the original intergranular strain model, the extension proposed by Wegener and Herle [260] and with the herein proposed. Subsequently, multiple drained and undrained cyclic triaxial tests were simulated with the different intergranular strain models and compared. The results indicate that a better agreement with the experimental results is provided by the proposed extension than with the previous ones.

Improvement to the Intergranular Strain model for larger numbers of repetitive cycles

Duque, J.[1], Mašín, D.[1], Fuentes, W.[2]

[1]Charles University, Prague, Czech Republic

[2]Findeter, Bogotá, Colombia

Abstract

The analysis of geotechnical problems involving saturated soils under cyclic loading requires the use of advanced constitutive models. These models need to describe the main characteristics of the material under cyclic loading and undrained conditions, such as the rate of the pore water pressure accumulation and the stress attractors. When properly doing so, the models are expected to be reliable for their use in boundary value problems. In this work, an extension of the widely implemented Intergranular Strain (IS) model by Niemunis and Herle [170] is proposed. The modification is aimed to improve the capabilities of the model when simulating a number of repetitive cycles, where a proper reduction of the strain accumulation is expected. For validation purposes, the reference model and proposed improvement are compared against some monotonic and cyclic triaxial tests. The results indicate that the Intergranular Strain Improvement (ISI) model provides a more realistic prediction of the accumulation rates under cyclic loading, without spoiling the advantages of the original formulation.

6.1 Introduction

Hypoplasticity for soils is a family of constitutive models with the following characteristics: a) it can be written in a single tensorial equation, which interrelates the stress tensor rate $\dot{\boldsymbol{\sigma}}$ with the strain tensor rate $\dot{\boldsymbol{\varepsilon}}$, b) it can be decomposed into a linear and non-linear component in $\dot{\boldsymbol{\varepsilon}}$, while the $\dot{\boldsymbol{\varepsilon}}$ is not decomposed into elastic and plastic parts, c) it accounts for at least the stress-dependency (barotropy), and d) it provides smooth responses envelopes. Different versions of Hypoplasticity have been proposed in the literature for the simulation of granular (e.g. [11, 261, 277, 279, 280]) and fine-grained (e.g. [72, 73, 91, 146, 147, 150, 151]) soils. The experience with this model family is that it provides a good performance on monotonic loading, or equivalently, under medium and large strain amplitudes ($\| \Delta\boldsymbol{\varepsilon} \| > 10^{-3}$), but in the basic form it presents some serious deficiencies when simulating cyclic loading where small strain effects take relevance [147, 166, 262, 277].

One can summarize the main limitations of hypoplastic models on cyclic loading as follows: a) the inability to properly reproduce the increase in stiffness upon reversal loading, b) excessive strain accumulation (ratcheting) upon cyclic loading, and c) lack of memory upon reloading paths [68, 70, 74, 166, 183]. In order to overcome these shortcomings, Niemunis and Herle [170] proposed the so-called 'Intergranular Strain' (IS) theory as an extension of hypoplastic models. It proposes a new strain-type state variable that stores information about the recent strain history, and this enables to detect whether the material has been subjected to monotonic or loading reversal, which needs to be properly identified for predicting cyclic loading. This information is used to increase the stiffness and reduce the strain accumulation on cyclic loading, such that some of the aforementioned limitations are addressed. The extended hypoplastic model with IS has been widely used in the literature, whether to simulate cyclic element tests, boundary value problems involving cyclic loading [93, 95, 162, 163, 163, 188, 191] or boundary value problems involving small strain stiffness effects [149, 161, 163]. Despite of this achievement, deficiencies have recently been detected under the simulation of a greater numbers of cycles ($N > 10$), as explained in the following.

Several experimental works have shown, that when a soil is subjected to a set of repetitive cycles of small strain amplitudes ($\| \Delta\boldsymbol{\varepsilon} \| < 10^{-3}$), the strain accumulation rate reduces as the number of cycles increases [177, 263, 273–275]. In other words, under such cyclic conditions, the strain accumulation rate depends somehow on the number of previously performed cycles, effect which has been by some authors referred to as "historiotropy" (path-dependency) [171, 262, 263]. However, a mechanism to reproduce historiotropic effects is not provided by the IS model. Therefore, the performance of the IS-hypoplastic model is rather poor on simulations with a higher number of cycles ($N > 10$). Many users are aware of this drawback, especially, when dealing with tests with small cyclic stress ratios or dense/overconsolidated soils [17, 76, 180, 265, 273], whereby a greater number cycles are required to reach failure.

In this work, a simple yet efficient extension of the original intergranular strain model with focus to cyclic loading with sets of repetitive cycles is proposed. The modification enables to reproduce the reduction of the strain accumulation rate upon repetitive cycles. With this, the modified IS model provides a more accurate estimation of the experimental behavior on cyclic loading. For validation purposes, the hypoplastic model for sands by Von Wolffersdorff [277] is extended with the original IS model and with the herein proposed. Monotonic and cyclic triaxial tests are then simulated using both approaches for comparison purposes. The results indicate that a better agreement with the experimental data is provided by the proposed approach than with the original one. Notation is summarized in Appendix 6.8.1.

6.2 Brief description of the Intergranular Strain model

As mentioned before, the Intergranular Strain (IS) tensor, denoted by $\mathbf{h}$, is a strain-type (second ranked) tensor providing information about the recent strain loading history. For this aim, its evolution equation $\dot{\mathbf{h}}$ was proposed as follows [170]:

$$\dot{\mathbf{h}} = \begin{cases} \left(\mathsf{I} - \overrightarrow{\mathbf{h}}\,\overrightarrow{\mathbf{h}}\,\rho^{\beta_r}\right) : \dot{\boldsymbol{\varepsilon}} & \text{for } \overrightarrow{\mathbf{h}} : \dot{\boldsymbol{\varepsilon}} > 0 \\ \dot{\boldsymbol{\varepsilon}} & \text{for } \overrightarrow{\mathbf{h}} : \dot{\boldsymbol{\varepsilon}} \leq 0 \end{cases} \tag{6.1}$$

$$\rho = \| \mathbf{h} \| / R \tag{6.2}$$

where β_r, χ and R are parameters. In particular, β_r controls the strain amplitude at which small strain effects are active, χ controls the stiffness decay, and R imposes the bounding condition $\| \mathbf{h} \| \leq R$. The condition $\| \mathbf{h} \| = R$ implies a fully mobilized state of the IS, usually captured at monotonic loading or at cycles with medium or large amplitudes, while $\| \mathbf{h} \| < R$ suggests cyclic loading. Niemunis and Herle [170] proposed an IS-dependent constitutive relation to consider the increase of stiffness and reduction of strain accumulation rate as follows:

$$\dot{\boldsymbol{\sigma}} = \mathsf{M} : \dot{\boldsymbol{\varepsilon}} \tag{6.3}$$

where the tangent modulus M is defined as:

$$\mathsf{M} = \begin{cases} m_1 \mathsf{L}^{\text{hyp}} + m_2 \mathsf{L}^{\text{hyp}} : \overrightarrow{\mathbf{h}}\,\overrightarrow{\mathbf{h}} + \rho^{\chi} \mathbf{N}^{\text{hyp}} \overrightarrow{\mathbf{h}} & \text{for } \overrightarrow{\mathbf{h}} : \dot{\boldsymbol{\varepsilon}} > 0 \\ m_1 \mathsf{L}^{\text{hyp}} + m_3 \mathsf{L}^{\text{hyp}} : \overrightarrow{\mathbf{h}}\,\overrightarrow{\mathbf{h}} & \text{for } \overrightarrow{\mathbf{h}} : \dot{\boldsymbol{\varepsilon}} \leq 0 \end{cases} \tag{6.4}$$

where L^{hyp} is the hypoelastic stiffness (fourth ranked) tensor, $\mathbf{N}^{\text{hyp}}$ is a hypoplastic (second ranked) tensor, and m_1, m_2 and m_3 are scalar functions controlling the reversal and transverse stiffness when performing cyclic loading. The latter scalars (m_1, m_2 and m_3) were carefully proposed considering the

following conditions: at reversed strain loading $\overrightarrow{\dot{\boldsymbol{\varepsilon}}} : \overrightarrow{\mathbf{h}} = -1$, the tangent stiffness delivers $\mathsf{M} = m_R \mathsf{L}^{\text{hyp}}$, where factor m_R is a parameter ($m_R > 1$). At transverse strain loading $\overrightarrow{\dot{\boldsymbol{\varepsilon}}} : \overrightarrow{\mathbf{h}} = 0$, the tangent stiffness renders $\mathsf{M} = m_T \mathsf{L}^{\text{hyp}}$, where m_T is a material constant ($1 \leq m_T < m_R$). Finally, at monotonic paths, or equivalently, when reaching medium or large strain amplitudes ($\| \Delta\boldsymbol{\varepsilon} \| > 10^{-3}$), the conditions $\rho = 1$ and $\overrightarrow{\mathbf{h}} : \overrightarrow{\dot{\boldsymbol{\varepsilon}}} = 1$ hold, and the tangent modulus M for the current strain rate direction $\overrightarrow{\dot{\boldsymbol{\varepsilon}}}$ coincides with the one of the hypoplastic equation without IS extension ($\mathsf{M} = \mathsf{L}^{\text{hyp}} + \mathbf{N}^{\text{hyp}} \overrightarrow{\dot{\boldsymbol{\varepsilon}}}$), see details in Niemunis and Herle [170]. The scalar factors m_1, m_2, m_3 were defined as:

$$m_1 = \rho^{\chi} m_T + (1 - \rho^{\chi}) m_R \tag{6.5}$$

$$m_2 = \rho^{\chi} (1 - m_T) \tag{6.6}$$

$$m_3 = \rho^{\chi} (m_R - m_T) \tag{6.7}$$

In summary, the set of parameters needed by the IS model are R, m_R, m_T, β_r and χ. Since the development of the original IS model by Niemunis and Herle [170], a few modifications to the theory have been proposed, among them:

- Wegener and Herle [260] replaced exponent χ in the term $\rho^{\chi} \mathbf{N}^{\text{hyp}} \overrightarrow{\mathbf{h}}$ (see equation 6.4) with a new parameter γ, being $\gamma > \chi$, see equation 6.8. This modification proved accurate reproduction of the stiffness degradation of the material. In addition, it allowed for a greater reduction of strain accumulation upon cyclic loading and showed some improvement on simulations with greater number of cycles (e.g. $N > 10$). However, since γ is a fixed parameter, it is unable to adapt its value on cycles of larger strain amplitudes ($\| \Delta\boldsymbol{\varepsilon} \| > 10^{-3}$), where the strain accumulation rate increases [71].

$$\mathsf{M} = \begin{cases} m_1 \mathsf{L}^{\text{hyp}} + m_2 \mathsf{L}^{\text{hyp}} : \overrightarrow{\mathbf{h}} \overrightarrow{\mathbf{h}} + \rho^{\gamma} \mathbf{N}^{\text{hyp}} \overrightarrow{\mathbf{h}} & \text{for } \overrightarrow{\mathbf{h}} : \dot{\boldsymbol{\varepsilon}} > 0 \\ m_1 \mathsf{L}^{\text{hyp}} + m_3 \mathsf{L}^{\text{hyp}} : \overrightarrow{\mathbf{h}} \overrightarrow{\mathbf{h}} & \text{for } \overrightarrow{\mathbf{h}} : \dot{\boldsymbol{\varepsilon}} \leq 0 \end{cases} \tag{6.8}$$

- The Intergranular Strain Anisotropy (ISA) model by Fuentes and Triantafyllidis [74]. In this work, the IS theory was completely reformulated, based on a novel approach which brought two main features compared to the original IS model: a) an elastoplastic evolution of IS to provide some memory effects, and b) the model incorporates a yield surface which can be adjusted to the elastic threshold strain amplitude. Although the new model was completely reformulated, both models shared the same underlying theory. A new extension was later proposed to ISA on Poblete et al. [180], whereby parameter χ, controlling the rate of the stiffness decay, was converted into a function, that smoothly increases when performing a sequence of repetitive cycles with small strain amplitudes ($\| \Delta\boldsymbol{\varepsilon} \| < 10^{-3}$), and decays on monotonic loading or larger strain amplitudes. This achieved to reproduce the observed reduction of the strain accumulation rate on tests where the number of cycles is higher (e.g. $N > 10$). Since then, satisfactory results have been evidenced with ISA on cyclic tests with several cycles e.g. [71, 75, 76, 180].

The aforementioned works concluded that the original IS model by Niemunis and Herle [170] requires some enhancements with focus to cyclic loading with larger number of repetitive cycles, in order to improve the poorly predicted accumulation rates reported by many users e.g. [17, 76, 263, 265, 273]. The latter limitation is tackled in the present work, adopting and simplifying the ideas of Poblete et al. [180], while including the enhancement by Wegener and Herle [260].

6.3 Proposed Intergranular Strain improvement

Two experimental examples having repetitive cycles are presented, the first in Figure 6.1a for a fine-grained soil, and the second in Figure 6.1b,c for a granular soil. Three different stages can be identified, thereby indicated as "A", "B" and "C", which clearly show the remarked variation of the pore water pressure accumulation rate upon cyclic loading. At stage "A", the pore water pressure shows a rapid accumulation rate, which decelerates with increasing number of cycles. Soon, stage "B" is reached, where an almost constant accumulation rate of the pore water pressure is exhibited. Finally, at stage "C" close to the critical state, an increase of the pore water pressure accumulation rate is once more experienced, and the development of large strain amplitudes occur.

The proposed extension considers the developments by Wegener and Herle [260] and Poblete et.al. [180], and presents the two following components: First, exponent χ in term $\rho^{\chi}\mathbf{N}^{\text{hyp}}\overrightarrow{\mathbf{h}}$ (see equation 6.4) is replaced with a new function γ, with $\gamma = \gamma_{\chi}\chi$, where γ_{χ} is a new model parameter and χ is a function. In addition, a new mechanism is proposed to account for historiotropic (path-dependent) effects. Hence, we propose an internal variable Ω, which evolves towards one ($\Omega \to 1$) as long as the IS is not mobilized ($\rho \approx 0$), and decays to zero on monotonic loading paths, or when reaching large strain amplitudes, whereby the approximation $\rho \approx 1$ holds. The following evolution equation for Ω suits the aforementioned conditions:

$$\dot{\Omega} = C_{\Omega}(1 - \rho^{\gamma} - \Omega) \parallel \dot{\boldsymbol{\varepsilon}} \parallel \tag{6.9}$$

where C_{Ω} is a parameter controlling its rate. The latter evolution equation allows Ω to be interpreted as an indicator of the intensity of the recent repetitive loading experienced by the material: when $\Omega = 0$, a monotonic loading, or a path with large strain amplitude has been recently performed. On the other hand, when $\Omega \approx 1$, several consecutive cycles with small strain amplitude have been experienced. This information, related to the path-dependency, is accounted by exponent χ, to affect the strain accumulation rate. We therefore propose χ to be a function, such that it smoothly evolves from a minimum value $\chi = \chi_0$ when $\Omega = 0$ (monotonic loading) to a maximum value $\chi = \chi_{max}$ when $\Omega = 1$ (recently experienced repetitive cycles with small strain amplitude). The following interpolation function is proposed:

$$\chi = \chi_0 + \Omega(\chi_{\max} - \chi_0) \tag{6.10}$$

Having Ω and χ defined, we now proceed to explain their behavior in an undrained cyclic triaxial test, see Figure 6.1d:

- The initial value of Ω is zero ($\chi = \chi_0$), because an isotropic consolidation (monotonic loading) had been previously performed. Stage "A" therefore begins with $\chi = \chi_0$, and with the reproduction of a high rate of pore water pressure accumulation.
- As long as the number of cycles (with small strain amplitudes) during stage "A" increases, Ω evolves towards one ($\Omega \approx 1$), and thus, exponent χ approaches to $\chi \approx \chi_{\max}$. Stage "B" is characterized by the states $\Omega \approx 1$ and $\chi \approx \chi_{\max}$, which consequently is accompanied by a low reproduction of the rate of pore water pressure accumulation.
- At stage "C", close to failure conditions, cycles now reach larger strain amplitudes. Therefore, Ω decays once more to zero, providing an increase in the pore water pressure accumulation rate through $\chi \approx \chi_0$.

Considering the aforementioned mechanism, a short guide for the calibration of parameters χ_0, $\chi_{\max}$ and C_{Ω} has been provided in Appendix 6.8.4. The next section is aimed to evaluate the performance of the proposed modification. It will be shown that the results are considerably better than the reference model.

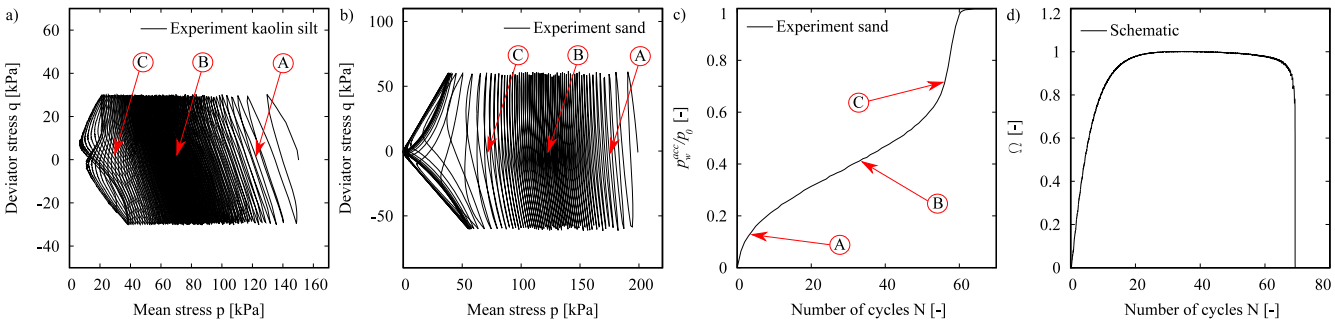

Figure 6.1: Experimental variation of the accumulation rate: a) Typical result on Kaolin silt by Wichtmann and Triantafyllidis [275], b) Typical result on Karlsruhe fine sand by Wichtmann and Triantafyllidis [273], c) Normalized pore water pressure accumulation, and d) Schematic evolution of Ω

6.4 Numerical implementation and test material

For comparison purposes, the hypoplastic model for sands proposed by Von Wolffersdorff [277], is extended with: a) the original IS model by Niemunis and Herle [170], hereafter referred as HP+IS, b) the modification by Wegener and Herle [260], referred to as HP+ISW, and c) the proposed Intergranular Strain Improvement (ISI), hereafter referred as HP+ISI. Constitutive equations of the selected hypoplastic model are summarized in Appendix 6.8.2. The implementation of the models used a substepping explicit scheme, with a constant strain length of $\| \Delta\boldsymbol{\varepsilon} \| = R/10$ to provide numerical convergence. A FORTRAN code was written according to the subroutine UMAT from the commercial software ABAQUS Standard and provided for free use through soilmodels.com website.

The Karlsruhe fine sand data by Wichtmann and Triantafyllidis [273] were adopted in the present work to test the model. This sand is mainly composed of subangular shaped grains and has a maximum void ratio of $e_{max} = 1.054$, a minimum void ratio of $e_{min} = 0.677$, a mean diameter of $D_{50} = 0.14$ mm and a uniformity coefficient of $c_u = 1.5$. For the evaluation of the performance of the models, the following tests were considered: 3 oedometric compression tests (OC) with an unloading-reloading cycle and different initial densities, 8 undrained monotonic triaxial tests (UT) either in compression or extension, 5 drained monotonic triaxial tests (DT), 4 undrained cyclic triaxial tests (UCT) and 3 drained cyclic triaxial tests (TCD), see Table 6.1. The nomenclature of the experimental tests is the same as reported by Wichtmann and Triantafyllidis [273]. The parameters of the HP+IS, HP+ISW and HP+ISI models are presented in Tables 6.2 through 6.5, respectively. Parameters of the HP+IS were previously calibrated in the work by Wichtmann and Triantafyllidis [273]. The new parameters from the proposed improvement (χ_0, $\chi_{\max}$, C_Ω), were herein calibrated following the procedure given in Appendix 6.8.4.

Table 6.1: Testing program with Karlsruhe fine sand. Experiments reported by Wichtmann [263] and Wichtmann and Triantafyllidis [273]

Test name	Test type	e_0 [-]	D_{r0} [%]	p_0 [kPa]	q_0 [kPa]	q^{amp} [kPa]	N [-]
OE8	OC	0.833	59	-	-	-	-
OE9	OC	0.808	65	-	-	-	-
OE10	OC	0.777	73	-	-	-	-
TMU1	UT†	0.828	60	100	0	-	-
TMU2	UT†	0.814	64	200	0	-	-
TMU3	UT†	0.822	62	300	0	-	-
TMU4	UT†	0.819	62	400	0	-	-
TMU7	UT‡	0.828	60	100	0	-	-
TMU8	UT‡	0.853	53	200	0	-	-
TMU9	UT‡	0.828	60	300	0	-	-
TMU10	UT‡	0.827	60	400	0	-	-
TMD1	DT†	0.996	15	50	0	-	-
TMD2	DT†	0.975	21	100	0	-	-
TMD3	DT†	0.975	21	200	0	-	-
TMD4	DT†	0.970	22	300	0	-	-
TMD5	DT†	0.960	25	400	0	-	-
TCUI6	UCT	0.964	24	300	0	45	144
TCUI12	UCT	0.814	64	200	0	50	83
TCUI19	UCT	0.760	78	100	0	40	14
TCUI21	UCT	0.755	80	200	0	60	69
TCD1	DCT	0.827	60	200	150	80	100
TCD2	DCT	0.827	60	200	150	60	100
TCD3	DCT	0.827	60	200	150	20	100

† Triaxial compression
‡ Triaxial extension

Table 6.2: Parameters of the hypoplastic model for the Karlsruhe fine sand, as calibrated by Wichtmann and Triantafyllidis [273]

φ_c	h_s	n	α	β	e_{d0}	e_{c0}	e_{i0}
[°]	[MPa]	[−]	[−]	[−]	[−]	[−]	[−]
33.1	4000	0.27	0.14	2.5	0.677	1.054	1.212

Table 6.3: Parameters of the IS model for the Karlsruhe fine sand, as calibrated by Wichtmann and Triantafyllidis [273]

R	m_R	m_T	β_r	χ
[−]	[−]	[−]	[−]	[−]
1×10^{-4}	2.2	1.1	0.1	5.5

Table 6.4: Parameters of the ISW model for the Karlsruhe fine sand calibrated in this work

R	m_R	m_T	β_r	χ	γ
[−]	[−]	[−]	[−]	[−]	[−]
1×10^{-4}	2.2	1.1	0.1	2.5	3

Table 6.5: Parameters of the ISI model for the Karlsruhe fine sand calibrated in this work

R	m_R	m_T	β_r	χ_0	χ_{max}	C_Ω	γ_χ
[−]	[−]	[−]	[−]	[−]	[−]	[−]	[−]
1×10^{-4}	2.2	1.1	0.1	0.95	3.55	48	3

6.5 Simulations

In this section, the performance of the HP+IS, HP+ISW and HP+ISI models is evaluated under cyclic loading using element test simulations, while simulations on monotonic loading are presented in Appendix 6.8.3. Figures 6.2 and 6.3 show the experimental and simulation results of four undrained cyclic triaxial tests in the $q-p$ and $q-\varepsilon_1$ spaces, respectively. The experimental tests considered variations of the deviator stress amplitude, $q^{\text{amp}} = \{40, 45, 50, 60\}$ kPa, and the initial density, $D_r = \{24, 64, 78, 80\}$ %, allowing different behaviors of the pore water pressure accumulation curves to be observed. All the undrained cyclic triaxial tests presented a drained cycle before the undrained shearing stage. This additional loading stage was also considered in the simulations. The results suggest that the number of cycles needed to reach failure conditions, or equivalently, to develop large strains ($\varepsilon_1 > 5\%$), was better captured by the modified model (HP+ISI) than by the HP+IS and HP+ISW models. This was actually the expected advantage of the improved model, considering its modification for repetitive cycles. In addition, the HP+ISI model showed the ability to change the strain accumulation rate upon cycles, as shown by the experiments. On the other hand, none of the models was able to reproduce the "butterfly-shaped" effective stress paths that are observed during the cyclic mobility phase on tests TCUI12,19 and 21. This is actually a deficiency of the base hypoplastic model, and not of the IS approach, since the cyclic mobility is a large strain amplitude effect. Considering this, an improvement to account for proper cyclic mobility effect is out of the scope of the present work. However, it is mentioned, that the lack of cyclic mobility effects in the hypoplastic model by Von Wolffersdorff [277] is attributed to the fact, that it does not consider any fabric evolution mechanisms describing neither the stiffness degradation nor dilatancy-contractancy changes due to the rearrangement of the particles at large strain amplitudes [76].

The accumulation of the normalized pore water pressure p_w^{acc}/p_0, p_0 being the initial mean pressure before the cycles, is plotted in Figure 6.4. Simulation results with the HP+IS model suggest that it is able to somehow reproduce the accumulation rate on tests where few cycles are required to reach failure conditions (e.g. TCUI19). On tests TCUI6,12 and 21, where the number of cycles to reach cyclic mobility is higher (e.g. $N_f > 20$), the experiments show a reduction in the accumulation rate which is not properly reproduced by the HP+IS model. Consequently, a poor estimation of the accumulation of the normalized pore water pressure is found on these tests. Simulations with the HP+ISW model suggest similar conclusions, in which the accumulation rate is not well reproduced. On the other hand, the simulation results with the HP+ISI model showed to be consistent with the experiments.

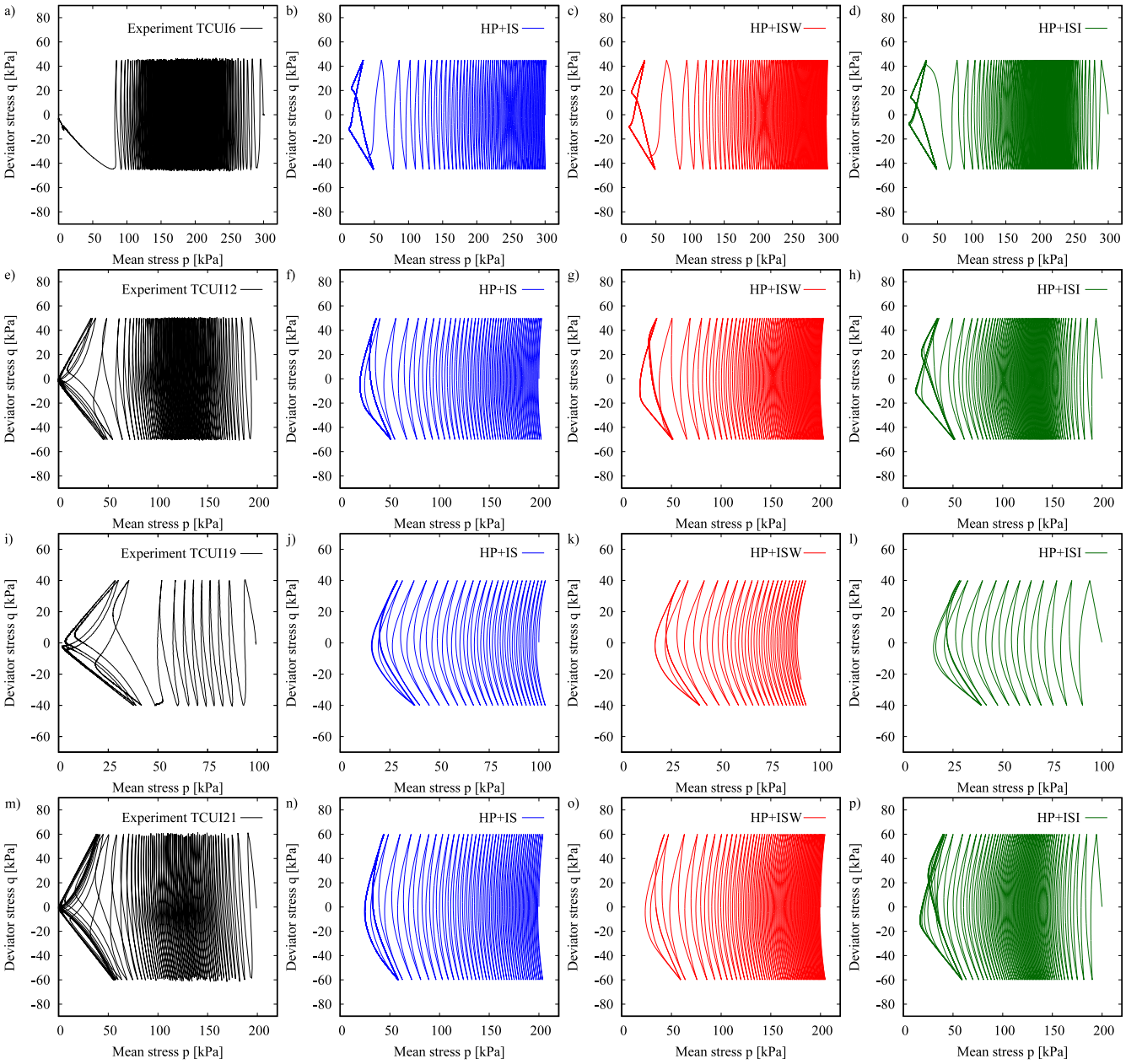

Figure 6.2: Simulations of undrained cyclic triaxial tests TCUI6,12,19,21 with isotropic consolidation ($q_0 = 0$ kPa) and variation of the initial density $D_r = \{24, 64, 78, 80\}$ % and stress amplitude $q^{\text{amp}} = \{40, 45, 50, 60\}$ kPa, $q - p$ space

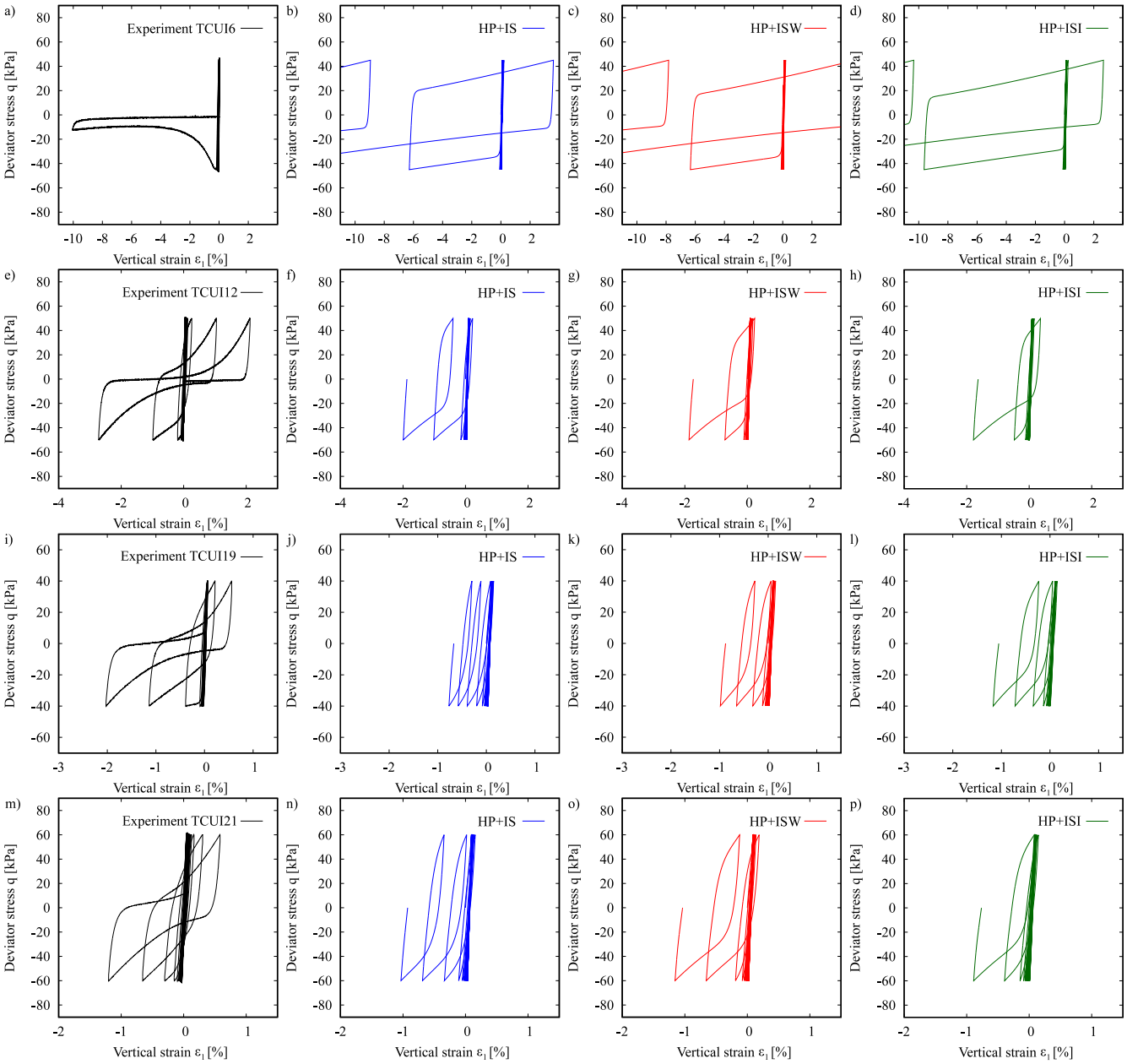

Figure 6.3: Simulations of undrained cyclic triaxial tests TCUI6,12,19,21 with isotropic consolidation ($q_0 = 0$ kPa) and variation of the initial density $D_r = \{24, 64, 78, 80\}$ % and stress amplitude $q^{\text{amp}} = \{40, 45, 50, 60\}$ kPa, $q - \varepsilon_1$ space

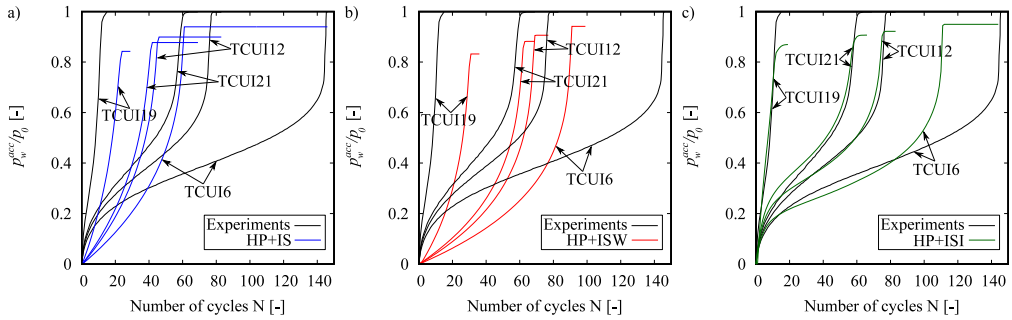

Figure 6.4: Accumulation of the normalized pore water pressure p_w^{acc}/p_0 in the simulations of undrained cyclic triaxial tests with isotropic consolidation ($q_0 = 0$ kPa) and variation of the initial density $D_r = \{24, 64, 78, 80\}$ % and stress amplitude $q^{\text{amp}} = \{40, 45, 50, 60\}$ kPa

The behavior under drained cyclic triaxial tests is now analyzed. Figure 6.5a presents the schematic stress path performed under drained conditions. Only regular cycles were considered in the analyzes, as depicted in Figure 6.5b. Experimental results of drained cyclic triaxial tests reported by Wichtmann [263] are presented in Figure 6.6a. The results suggest a decrease in the strain accumulation $\varepsilon^{acc} = \sqrt{(\varepsilon_1^{acc})^2 + 2(\varepsilon_3^{acc})^2}$ rate as the number of cycles increases. Simulation results with HP+IS and HP+ISW show an unsatisfactory behavior showing an excessive accumulation in test TCD1, with accumulation rate unaffected by cycle number. Indeed, an almost linear accumulation rate vs. the number of cycles is inconsistently delivered by the HP+IS and HP+ISW models. This is contrasted by the HP+ISI performance, which successfully reproduced the change in the accumulation rate. However, an underestimation of the accumulated strains is given on test TCD2. One can show that the performance of the HP+ISI can be improved under drained cyclic loading at the cost of reducing the accurate performance on the pore water pressure accumulation given in Figure 6.4.

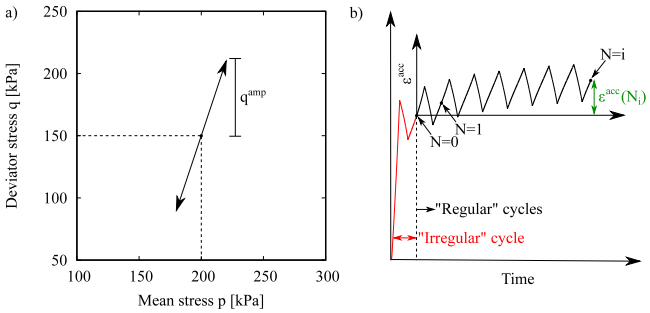

Figure 6.5: Typical curves in drained cyclic triaxial tests: a) stress path, and b) evolution of the accumulated strain ε^{acc}

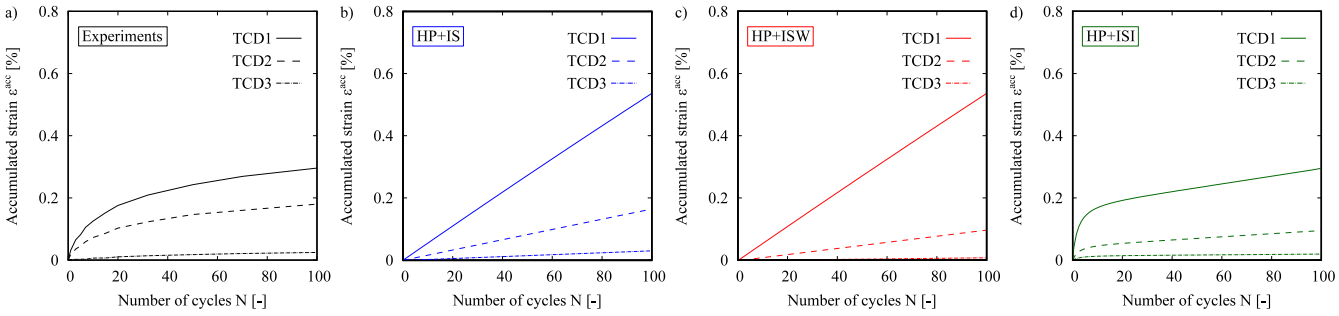

Figure 6.6: Accumulation of strains ε^{acc} in the simulations of drained cyclic triaxial tests TCD1-TCD3

6.6 Summary and conclusions

In this work, a simple yet efficient modification to the original IS model by Niemunis and Herle [170] was proposed. The modification consists on an additional mechanism to reduce the strain accumulation rate on paths with repetitive cycles of small strain amplitudes. The improvement allows to adapt its response at cycles of larger strain amplitudes, where the strain accumulation rate is expected to increase. The original and modified models were implemented together with the hypoplastic model for sands by Von Wolffersdorff [277] and compared to each other under cyclic loading. The results showed that the modified model is able to capture with better accuracy most of the observed effects under cyclic loading, as for example: a) the number of cycles required to reach failure conditions, b) the behavior of the normalized accumulated pore water pressure p_w^{acc}/p_0, under undrained conditions, and c) the tendency of the accumulated strains under drained conditions. The proposed modification requires the calibration of parameters χ_0, $\chi_{\max}$ and C_Ω (instead of χ) which can be adjusted according to the methodology presented in Appendix 6.8.4.

Users should be aware that, although the proposed modification showed a better congruence on the simulation of the pore water pressure accumulation, some limitations of the reference hypoplastic model extended by the original IS approach are still remaining. Among them, it is important to remark the following: a) accumulation due to closed strain cycles of very small amplitude ($\| \Delta\boldsymbol{\varepsilon} \| \leq R$), b) overshooting on reloading paths after cycles of small strain amplitudes, and c) unrealistic hysteresis loops during large strain cycles in dense conditions. These limitations are currently being investigated by the authors to improve the model formulation.

6.7 Acknowledgements

The first and second authors appreciate the financial support given by the INTER-EXCELLENCE project LTACH19028 by the Czech Ministry of Education, Youth and Sports. The first author appreciates the financial support given by the Charles University Grant Agency (GAUK) with project number 200120. The second author acknowledges institutional support by Center for Geosphere Dynamics (UNCE/SCI/006).

6.8 Appendix

6.8.1 Notation

Table 6.6 summarizes some symbols, notation, and tensorial operations. Indicial notation is used (e.g. A_{ij}). δ_{ij} is the Kronecker delta, also represented with ($1_{ij} = \delta_{ij}$).

Table 6.6: Summary of some symbols and operations

Example	Description	Operations	
a, b	scalar magnitudes	$\mathbf{AB} = A_{ij}B_{kl}$	dyadic product
$\mathbf{A}$,$\boldsymbol{\sigma}$	second ranked tensors	$\mathbf{A} : \mathbf{B} = A_{ij}B_{ij}$	double contraction
E, L	fourth ranked tensors	$\parallel \mathbf{A} \parallel = \sqrt{A_{ij}A_{ij}}$	Euclidean norm
$\mathsf{I}_{ijkl} = \frac{1}{2}\left(\delta_{ik}\delta_{jl} + \delta_{il}\delta_{jk}\right)$	unit symmetrical tensor	$\overrightarrow{\sqcup} = \frac{\sqcup}{\parallel \sqcup \parallel}$	Extracts unit tensor

Components of the effective stress tensor $\boldsymbol{\sigma}$ or strain tensor $\boldsymbol{\varepsilon}$ in compression are negative. Roscoe variables are defined as $p = -\sigma_{ii}/3$, $q = \sqrt{\frac{3}{2}} \parallel \boldsymbol{\sigma}^{\text{dev}} \parallel$, $\varepsilon_v = -\varepsilon_{ii}$ and $\varepsilon_s = \sqrt{\frac{2}{3}} \parallel \boldsymbol{\varepsilon}^{\text{dev}} \parallel$. The stress ratio η is defined as $\eta = q/p$. The deviator stress tensor is defined as $\boldsymbol{\sigma}^{\text{dev}} = \boldsymbol{\sigma} + p\,\mathbf{1}$.

6.8.2 Summary of the hypoplastic model for sands by Von Wolffersdorff

In this appendix, a summary of the constitutive relations of the hypoplastic model for sands by Von Wolffersdorff [277] is provided, see Table 6.7:

Table 6.7: Constitutive relations of the hypoplastic model by Von Wolffersdorff [277]

$\mathsf{L}^{\text{hyp}} = f_b f_e \frac{1}{\hat{\boldsymbol{\sigma}} : \hat{\boldsymbol{\sigma}}} (F^2 \mathsf{I} + a^2 \hat{\boldsymbol{\sigma}} \hat{\boldsymbol{\sigma}})$	$\hat{\boldsymbol{\sigma}} = \frac{\boldsymbol{\sigma}}{\text{tr}(\boldsymbol{\sigma})}$
$\mathbf{N}^{\text{hyp}} = f_d f_b f_e \frac{Fa}{\hat{\boldsymbol{\sigma}} : \hat{\boldsymbol{\sigma}}} (\hat{\boldsymbol{\sigma}} + \hat{\boldsymbol{\sigma}}^{\text{dev}})$	$\hat{\boldsymbol{\sigma}}^{\text{dev}} = \hat{\boldsymbol{\sigma}} - \frac{1}{3}\mathbf{1}$
$f_e = \left(\frac{e_c}{e}\right)^{\beta}$	$e_i = e_{i0} \exp(-(3p/h_s)^n)$
$f_d = \left(\frac{e - e_d}{e_c - e_d}\right)^{\alpha}$	$e_d = e_{d0} \exp(-(3p/h_s)^n)$
$f_b = \frac{h_s}{n_B} \left(\frac{1 + e_i}{e_i}\right) \left(\frac{e_{i0}}{e_{c0}}\right)^{\beta} \left(-\frac{\text{tr}\boldsymbol{\sigma}}{h_s}\right)^{1-n} \left[3 + a^2 - \sqrt{3}a \left(\frac{e_{i0} - e_{d0}}{e_{c0} - e_{d0}}\right)^{\alpha}\right]^{-1}$	$e_c = e_{c0} \exp(-(3p/h_s)^n)$
$F = \sqrt{\frac{1}{8}\tan^2(\psi) + \frac{2 - \tan^2(\psi)}{2 + 2\sqrt{2}\tan(\psi)\cos(3\theta)}} - \frac{1}{2\sqrt{2}\tan(\psi)}$	$a = \frac{\sqrt{3}(3 - \sin(\varphi_c))}{2\sqrt{2}\sin(\varphi_c)}$
$\cos(3\theta) = \sqrt{6} \frac{\text{tr}(\hat{\boldsymbol{\sigma}}^{\text{dev}} \hat{\boldsymbol{\sigma}}^{\text{dev}} \hat{\boldsymbol{\sigma}}^{\text{dev}})}{(\hat{\boldsymbol{\sigma}}^{\text{dev}} : \hat{\boldsymbol{\sigma}}^{\text{dev}})^{3/2}}$	$\tan\psi = \sqrt{3}\|\hat{\boldsymbol{\sigma}}^{\text{dev}}\|$

6.8.3 Simulations of monotonic loading

In this Appendix, some simulations of the HP+ISI model under monotonic loading are shown. The tests correspond to three oedometric compression tests with an unloading-reloading cycle, 8 undrained and 5 drained monotonic triaxial tests, with variation of the initial mean effective pressure. Simulation results

are presented in Figures 6.7, 6.8 and 6.9, respectively, and showed a satisfactory agreement with the experimental data.

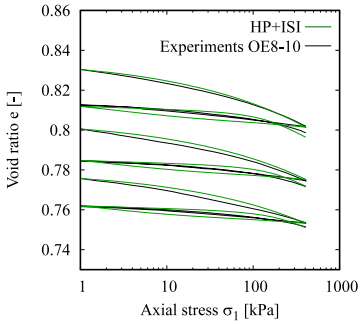

Figure 6.7: Simulations of three oedometric tests OED8-10 with an unloading-reloading cycle, $e-$ Log σ_1 space. Initial conditions given in Table 6.1.

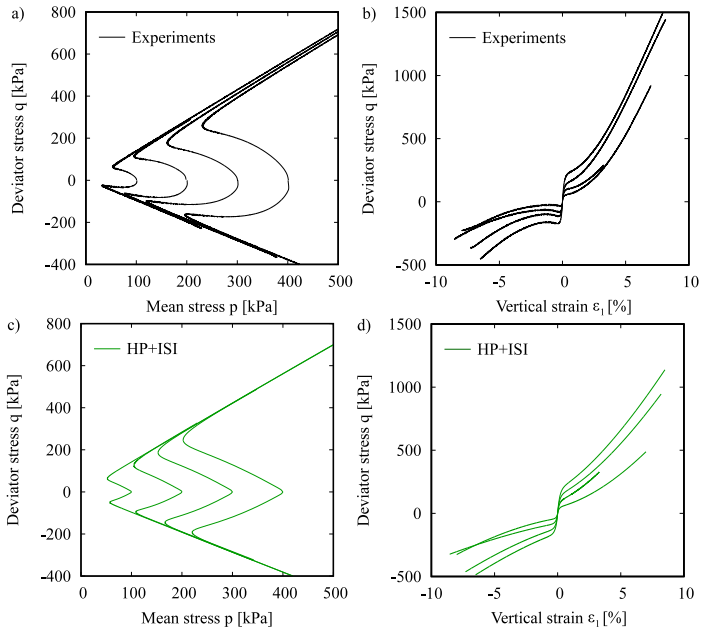

Figure 6.8: Simulations of undrained monotonic triaxial tests with isotropic consolidation ($q_0 = 0$ kPa) under extension and compression with variation of the initial mean effective pressure $p_0 = \{100, 200, 300, 400\}$ kPa. Initial conditions given in Table 6.1.

6.8.4 Short guide for the determination of parameters χ_0, $\chi_{\max}$ and C_Ω

In this section, a short guide for the determination of the new parameters is given:

- Parameter χ_0 controls the accumulation rate on the first cycles. Its calibration can be performed simulating the first cycles (e.g. $N < 5$) on an undrained cyclic triaxial test. An example of the influence of this parameter is given in Figure 6.10a.
- Parameter $\chi_{\max}$ controls the rate of the accumulation after a larger number of repetitive cycles with small strain amplitudes (e.g. $N > 10$). It should be adjusted to reproduce the reduction of the

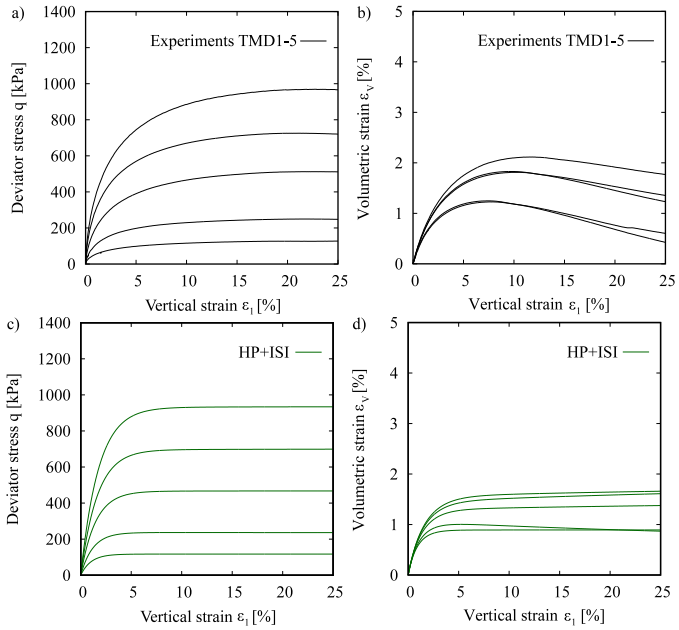

Figure 6.9: Simulations of drained monotonic triaxial tests with isotropic consolidation ($q_0 = 0$ kPa) and variation of the initial mean effective pressure $p_0 = \{50, 100, 200, 300, 400\}$ kPa. Initial conditions given in Table 6.1.

strain accumulation rate observed in the experiments. Figure 6.10b provides an example of its effect on the normalized pore water pressure accumulation.

- Parameter C_Ω controls how fast the strain accumulation rate reduces and the model changes the IS exponent χ from $\chi = \chi_0$ to $\chi = \chi_{max}$. It should be adjusted to reproduce the observed behavior of the pore water pressure accumulation on undrained cyclic triaxial tests, see Figure 6.10c.

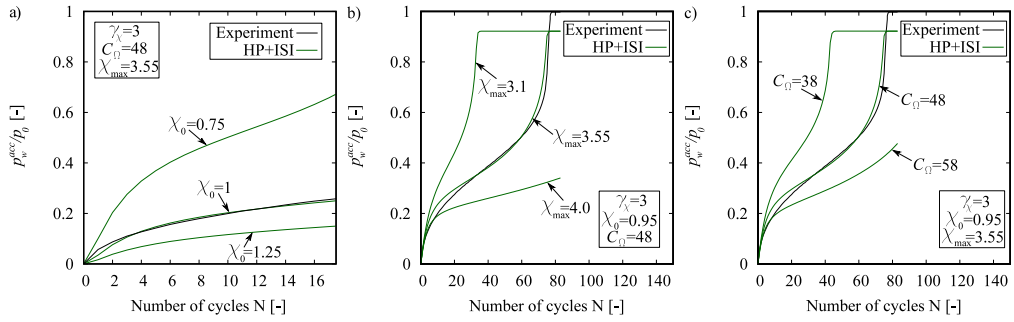

Figure 6.10: Accumulation of the normalized pore water pressure p_w^{acc}/p_0 in the undrained cyclic triaxial test TCUI12. Influence of parameters: a) χ_0, b) $\chi_{\max}$ and c) C_Ω

A detailed guide for the calibration of the hypoplastic and intergranular strain parameters can be found in Herle and Gudehus [90] and Niemunis [166], respectively. The calibration procedure of parameter γ_χ is explained in detail in Wegener and Herle [260], considering that $\gamma = \gamma_\chi \chi$.

Chapter 7

Numerical study of monopiles subjected to multiple episodes of cyclic loading and reconsolidation - Article 6

Summary of the article

This article presents the numerical simulations of the centrifuge tests performed by Lai et al. [126]. The centrifuge tests consisted of large diameter monopiles, typical of offshore foundations, embedded in a soft normally consolidated kaolin and subjected to either monotonic or cyclic lateral loading. Initially, a pair of monopiles were laterally loaded to determine its ultimate lateral capacity. Subsequently, other monopiles with the same characteristics were subjected to intermittent episodes of cyclic loading (that may represent storm conditions) in which there is pore water pressure accumulation, followed by episodes of reconsolidation (that may represent calm conditions), which allowed a full dissipation of the accumulated pore water pressure. The experimental results showed that the accumulation rates of pore water pressure and displacements decreased with increasing number of cycles. In addition, an interesting increase in the soil-pile stiffness was observed after each reconsolidation episode.

The numerical simulations of the centrifuge tests were performed using the free finite element software Tochnog Professional. The soil was simulated with a hypoplastic model with intergranular strain. In order to calibrate the parameters of the constitutive model for clays, three undrained monotonic and three undrained cyclic triaxial tests were performed in the same material used in the centrifuge tests. Element test simulations suggested an accurate performance on the monotonic triaxial tests and a relatively good agreement in the cyclic triaxial tests. It should be remarked that the undrained cyclic triaxial tests where performed considering deviatoric stresses only in the compression side. Therefore, all the strain accumulation was obtained in compression. Most cyclic simulations reported in the literature with hypoplasticity extended with intergranular strain are performed on tests with symmetric deviatoric stress amplitude (i.e. $q^{\max} = -q^{\min}$), in which the main focus of the calibration lies in the prediction of the accumulated pore water pressure and less importance is given to the strain accumulation since most hypoplastic models present a bias in strain accumulation. The latter is not the case of the presented simulations, which rises the level of complexity of the calibration since the authors needed to predict with accuracy both, the accumulated pore water pressure and strains in tests with different deviatoric stress amplitudes.

Finite element simulation results suggested an accurate reproduction of the monopile monotonic behavior. In addition, a relatively good agreement was found in the accumulated pore water pressure and displace-

ments under cyclic loading. However, the finite element simulations failed to reproduce the increase in the soil-pile stiffness after each reconsolidation episode. In the author's opinion, before to propose any mechanism to capture these effects, more experimental tests are needed. In particular, laboratory cyclic tests with episodes of undrained cyclic loading that lead to different magnitudes of the accumulated pore water pressures, followed by episodes of reconsolidation till the initial mean effective pressure and further re-shearing, similar to the tests performed in Zbraslav sand and reported in chapter 3. These tests will quantify the stiffness and cyclic resistance variation depending on the type and amount of the undrained cyclic preloadings. Based on that, the constitutive model may be extended to account for these effects.

On the behavior of monopiles subjected to multiple episodes of cyclic loading and reconsolidation in cohesive soils

Duque, J.[1], Ochmański, M.[1,2], Mašín, D.[1], Hong, Y.[3], Wang, L.[3]

[1]Charles University, Prague, Czech Republic

[2]Silesian University of Technology, Gliwice, Poland

[3]Zhejiang University, Hangzhou, China

Abstract

The study of cyclic loading on saturated natural clay deposits is of great interest for the analysis of offshore and onshore structures. Recent experimental research in the field of offshore engineering has indicated that the mechanical behavior of monopiles is strongly influenced by the reconsolidation processes that take place during calm conditions. After the reconsolidation episodes, the soil-pile stiffness considerably increases. Unfortunately, the previous behavior is usually disregarded in the numerical analysis and design of monopiles. In this work, the behavior of monopiles subjected to multiple episodes of cyclic loading and reconsolidation is analyzed from a numerical point of view. For that purpose, the sophisticated hypoplastic model for clays by Mašín [151] with intergranular strain by Niemunis and Herle [170] is carefully evaluated under element test conditions and by back-calculating some centrifuge tests. For the calibration of the constitutive model, three undrained monotonic and three undrained cyclic triaxial tests were performed. At the end, the influence of reconsolidation stages on the design of monopiles and the model capabilities to reproduce this behavior are discussed.

7.1 Introduction

Rapid population growth and economic development lead to high energy demand [24, 53, 259]. This increasing demand for energy results in rapidly rising carbon dioxide emissions, which highlights the need for more affordable, accessible and sustainable energy sources [33, 47]. One of the most promising clean energy alternatives is the one generated by Offshore Wind Turbines (OWTs) [34, 56, 97, 159]. Special attention is given to the foundations for OWTs since they constitute from 20% to 40% of the overall installation cost [29, 32, 98, 160, 257]. Several different types of foundations for OWTs have been developed through years. However, more than 80% of them are monopile foundations [159]. Therefore, many experimental and numerical efforts have been performed to understand the behavior of monopiles under monotonic and cyclic loading, e.g. [1, 67, 94, 143, 195, 220, 221, 256].

Foundations for OWTs are subjected to short episodes of extreme cyclic loading (i.e. during storm events) before the actual design history, followed by long episodes of low-magnitude environmental conditions (i.e. calm conditions) where reconsolidation processes take place [120, 190]. The influence of reconsolidation on foundations for OWTs was recently investigated by Lai et al. [126] by performing centrifuge tests on monopiles with diameter $D = 4$ m and $D = 6$ m (in prototype scale) embedded in a soft normally consolidated kaolin. The centrifuge tests considered intermittent stages of cyclic loading and reconsolidation. The experimental results suggested that the lateral soil-pile stiffness degrades after cyclic loading, but it is fully recovered and exceeds the initial stiffness up to 20% after the reconsolidation episodes. These findings highlight the importance of considering the influence of reconsolidation stages when evaluating the soil-pile stiffness of monopiles, specially since it controls their cumulative displacement and dynamic

response. Unfortunately, these effects are usually disregarded and can lead to unrealistic numerical predictions of the soil-pile behavior under cyclic loading.

The most important question that arises from the numerical point of view is whether sophisticated constitutive models are able to accurately reproduce the stiffness recovery after reconsolidation processes. In the present work, the capabilities of the sophisticated hypoplastic model for clays by Mašín [151] are investigated. This model was selected as it has been widely validated under element tests and finite element simulations (e.g. [94, 147, 149, 161, 173, 192, 193, 196]). In order to account for small strain stiffness, the model was extended with the Intergranular Strain model by Niemunis and Herle [170]. For the model calibration, three undrained monotonic and three undrained cyclic triaxial tests were performed on specimens of Malaysian kaolin.

The structure of the article is as follows: first, the reference experimental study is described. Then, the test material and selected experiments for calibration purposes are presented. Subsequently, details on the constitutive model and its calibration are provided. Following this, the construction of the boundary value problem is described. Finally, the results of the simulations are shown and carefully analyzed.

7.2 Reference experimental study

The present study considered the centrifuge results by Lai et al. [126] as a benchmark for the numerical simulations. The centrifuge tests were performed at the Hong Kong centrifuge facility at a centrifugal acceleration of 100 g. The tests were performed on four model piles embedded in soft normally-consolidated Malaysian kaolin. The model piles were designed to simulate steel monopiles. Two of the monopiles had a diameter in prototype scale of $D = 4$ m, while the other two had $D = 6$ m. The embedded and total length of the piles in prototype scale were equal to 60 m and 75 m respectively. Flexural rigidities of 3.11×10^8 kNm^2 and 11.05×10^8 kNm^2 were determined for the piles with $D = 4$ m and $D = 6$ m, respectively.

Initially, one monopile from each pair was subjected to monotonic loading to determine their ultimate lateral capacity (F_u). Afterwards, the second pile was subjected to multiple stages of one-way cyclic loading with an amplitude of $0.25F_u$. Each episode of cyclic loading was composed of 100 cycles and followed by a stage of reconsolidation that allowed for a full dissipation of the excess pore water pressure before the subsequent stage of cyclic loading. The performed loading and reconsolidation sequence is schematized in Figure 7.1. The centrifuge tests were monitored with two sets of transducers: a linear variable differential transformer (LVDT), to measure the displacements of the monopiles in the surface, and a pore water pressure transducer (PPT) to register the excess pore water pressure generated by cyclic loading. The PPT was located at a depth of 24 m in prototype scale, see Figure 7.7a. A detailed description of the experimental procedure is given in Lai et al. [126]. The experimental results are described in detail in section 7.5.5 and suggest that the initial soil-pile stiffness considerably increases after each subsequent stage of reconsolidation.

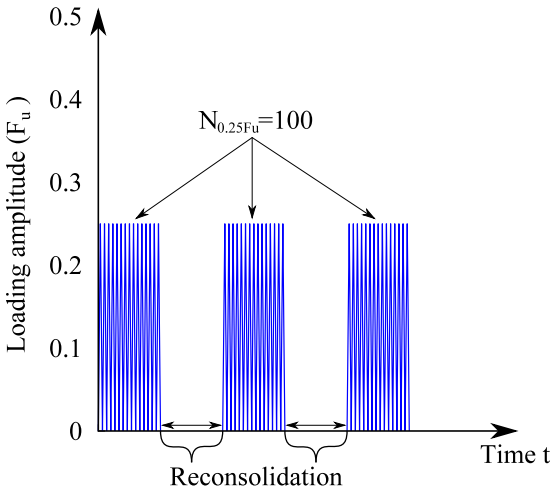

Figure 7.1: Sequence of the loading and reconsolidation stages

7.3 Test material

This section describes the main characteristics of the Malaysian kaolin which was used as test material in the centrifuge analysis and has been widely implemented in many geotechnical model tests (e.g. [96, 110, 281, 295]). The Malaysian kaolin presents a specific gravity of the solids of $G_s = 2.71$, a liquid limit of $LL = 65\%$ and a plastic limit of $PL = 38\%$, and is classified as a silt with high plasticity (MH), see Figure 7.2a. The material is composed of fine-sand (2%), silt (70%) and clay (28%) particles, see Figure 7.2b. The kaolin presents a coefficient of permeability (at 100 kPa) of $k = 2 \times 10^{-8}$ m/s [126].

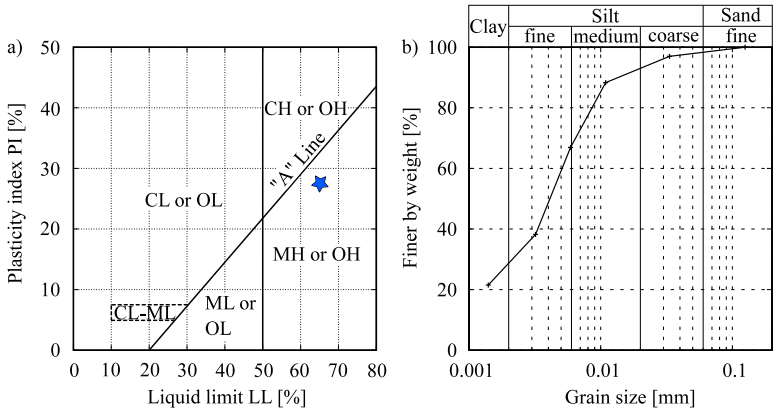

Figure 7.2: Characterization of the kaolin: a) position of the Malaysian kaolin in the Casagrande diagram, b) grain size distribution

Undrained monotonic and cyclic triaxial tests were performed on specimens of the Malaysian kaolin to calibrate the constitutive model. The samples were prepared from a dry kaolin powder which was mixed with demineralized water with an initial water content equal to two times the liquid limit ($w_i = 2LL$). The samples were initially pre-consolidated with a maximum effective vertical stress of $\sigma'_v = 60$ kPa. Then, the samples were located in the triaxial cell and the initial mean effective pressure was increased up to the desired value. Saturation was always checked before starting the shearing stage by calculating the Skempton coefficient B. Values of $B > 0.99$ were always obtained. A summary of all the performed

tests and their initial conditions is presented in Table 7.1. The first tests correspond to three undrained monotonic triaxial tests (UMT) with variation of the mean effective pressure $p_0 = \{200, 300, 600\}$ kPa and isotropic consolidation. The test results are presented in Figure 7.5 and suggest a clear failure envelope, shown as "CSL" in the $q-p$ space. In addition, three undrained cyclic triaxial tests (UCT) with variation of the cyclic stress amplitude $q^{\text{amp}} = (q_{max} - q_{min})/2$ were performed. The results from those tests suggest an increase in the accumulation of vertical strains and pore water pressure with increasing cyclic stress amplitude. The observed behavior is in agreement with many results reported in the literature for fine-grained soils, e.g. [21, 22, 31, 263, 275]. Each cyclic test considered a total of $N = 150$ cycles, which was not enough to reach failure conditions in any of the undrained cyclic triaxial tests.

Table 7.1: Testing program with the Malaysian kaolin

Test name	Test type	p_0 [kPa]	q_0 [kPa]	q^{amp} [kPa]	OCR [-]	e_0 [-]	N [-]
UMT1	UMT	200	0	-	1	1.405	-
UMT2	UMT	300	0	-	1	1.276	-
UMT3	UMT	600	0	-	1	1.096	-
UCT1	UCT	200	0	24	1	1.406	150
UCT2	UCT	200	0	36	1	1.395	150
UCT3	UCT	200	0	42	1	1.381	150

7.4 Constitutive model

7.4.1 Brief model description

The sophisticated hypoplastic model for clays by Mašín [151], hereafter denoted as the HP model, was adopted for the numerical simulations. This model was selected as it has been widely validated under element test simulations and boundary value problems (e.g. [94, 147, 149, 161, 173, 192, 193, 196]).

The HP model itself is composed five parameters $\{\varphi_c, N, \lambda^*, \kappa^*, \nu\}$ and is suitable for the simulation of large strain amplitudes (e.g. monotonic loading). However, hypoplastic models alone present multiple problems under cyclic loading as excessive strain accumulation, lack of memory upon reloading paths, inability to properly increase the stiffness upon loading reversals, among others [50, 70, 166]. For that reason, Niemunis and Herle [170] developed the so-called hypoplastic model with Intergranular Strain (IS) which addressed most of the aforementioned limitations. The extended hypoplastic model with intergranular strain is hereafter referred to as HP+IS model and can be expressed in terms of the tangent modulus M as:

$$\dot{\boldsymbol{\sigma}} = \mathsf{M} : \dot{\boldsymbol{\varepsilon}} \tag{7.1}$$

$$\mathsf{M} = \begin{cases} \left[\rho^{\chi} m_T + (1-\rho^{\chi}) m_R\right] \mathsf{L}^{\text{hyp}} + \rho^{\chi}(1-m_T)\mathsf{L}^{\text{hyp}} : \overrightarrow{\mathbf{h}}\overrightarrow{\mathbf{h}} + \rho^{\chi}\mathbf{N}^{\text{hyp}}\overrightarrow{\mathbf{h}} & \text{for } \overrightarrow{\mathbf{h}} : \dot{\boldsymbol{\varepsilon}} > 0 \\ \left[\rho^{\chi} m_T + (1-\rho^{\chi}) m_R\right] \mathsf{L}^{\text{hyp}} + \rho^{\chi}(m_R - m_T)\mathsf{L}^{\text{hyp}} : \overrightarrow{\mathbf{h}}\overrightarrow{\mathbf{h}} & \text{for } \overrightarrow{\mathbf{h}} : \dot{\boldsymbol{\varepsilon}} \leq 0 \end{cases} \tag{7.2}$$

where $\dot{\boldsymbol{\sigma}}$ is the stress rate tensor, $\dot{\boldsymbol{\varepsilon}}$ is the strain rate tensor, $\mathbf{h}$ is a strain-type state variable which store information about the recent strain loading history, L^{hyp} and $\mathbf{N}^{\text{hyp}}$ are the fourth and second rank state-dependent constitutive tensors, respectively. Function ρ quantifies the degree of mobilization of the additional stiffness and is defined as $\rho = \| \mathbf{h} \| / R$. Scalars m_1, m_2 and m_3 were defined in such a way that at reversed strain loading the tangent stiffness delivers $\mathsf{M} = m_R \mathsf{L}^{\text{hyp}}$, at transverse strain loading the

tangent stiffness renders $\mathsf{M} = m_T \mathsf{L}^{\text{hyp}}$ and at large strain deformations the tangent modulus M is equal to the one of the hypoplastic model without IS extension ($\mathsf{M} = \mathsf{L}^{\text{hyp}} + \mathbf{N}^{\text{hyp}} \overrightarrow{\dot{\boldsymbol{\varepsilon}}}$). The IS model composed by parameters $\{R, m_{rat}, A_g, n_g, \beta_r, \chi\}$. In this study, tensors L^{hyp} and $\mathbf{N}^{\text{hyp}}$ were adopted from Mašín [151] to simulate the mechanical behavior of clays. The full constitutive description of the HP and IS models are detailed in Mašín [151] and Niemunis and Herle [170], respectively.

7.4.2 Model calibration and implementation

The calibration procedure of the hypoplastic parameters $\{\varphi_c, N, \lambda^*, \kappa^*, \nu\}$ was as follows:

- The critical state friction angle $\{\varphi_c\}$ was adjusted with the three undrained monotonic triaxial tests at the critical state ($\varepsilon_1 \approx 20\%$). The slope of the critical state line in the $q - p$ space was fitted with the relation $q/p = M_c = 6 \sin \varphi_c / (3 - \sin \varphi_c)$, where M_c is the critical state slope for triaxial compression.
- Parameters $\{N, \lambda^*\}$ were adjusted to fit the initial states of the six undrained triaxial tests in the $e-$ log p space, see Figure 7.3. Parameter $\{\kappa^*\}$ was assumed as $\kappa^* = \lambda^*/10$ following typical relations for this type of material [153].
- The Poisson's ratio $\{\nu\}$ was calibrated to reproduce the shape of the effective stress path and the stress-strain behavior on the $q - \varepsilon_1$ space on undrained monotonic triaxial tests.

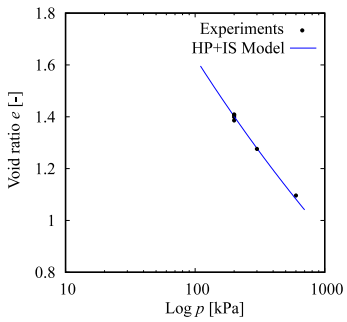

Figure 7.3: Adjustment of the model equation describing the behavior in the $e-$ Log p space and different initial states of undrained monotonic and cyclic triaxial tests

Parameters $\{R, m_{rat}\}$ of the IS model were defined with "default" values for "kaolins" [153]. On the other hand, parameters $\{A_g, n_g, \beta_r, \chi\}$ of the IS model were calibrated to reproduce the rate of the pore water pressure and strain accumulation in the undrained cyclic triaxial tests. A detailed procedure for the calibration of the IS parameters can be found elsewhere, e.g. [153, 166, 170]. The calibrated parameters of the HP+IS model are presented in Table 7.2. The model was implemented in a Fortran subroutine as a user-defined material (UMAT) for the commercial software Abaqus. The model adopts an explicit Runge-Kutta algorithm with a substepping scheme controlled by the difference between 3-rd and 2-nd order accuracy solution (RKF23). Accuracy and cumulative numerical errors due to the integration approach are important when dealing with the application of a large number of cycles. Figure 7.4 presents the simulation of 1000 closed strain loops with the HP+IS model and the RKF23 integration algorithm. The strain loops were analyzed considering different number of increments per cycle $N_{inc} = 10, 100, 1000$. The results of the simulations suggest that the accumulated stress is approximately the same regardless of the number of increments per cycle. Different results are obtained when adopting simpler integration

schemes (such as Euler forward) for which excessive cumulative errors have been reported [171]. The element test simulations were performed with the element test driver TRIAX [152]. The implementation of the HP+IS model is freely available at the soilmodels.com website [89].

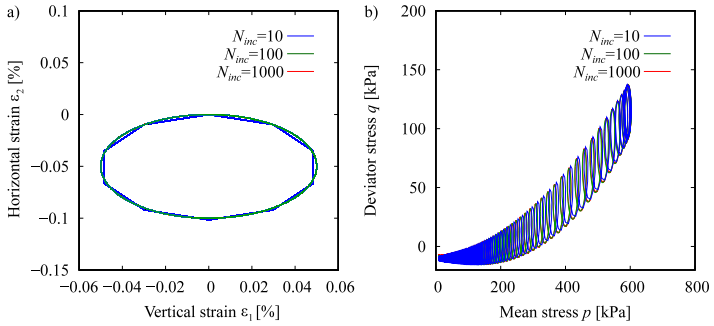

Figure 7.4: Simulation of 1000 strain cycles with the HP+IS model and the RKF23 integration algorithm for different number of increments per cycle

Table 7.2: Parameters of the HP+IS model for the Malaysian kaolin

φ_c	N	λ^*	κ^*	ν	A_g	n_g	R	β_r	χ	m_{rat}
[°]	[-]	[-]	[-]	[-]	[-]	[-]	[-]	[-]	[-]	[-]
30	1.565	0.13	0.013	0.1	350	0.66	0.0001	0.014	5.25	0.7

7.4.3 Element test simulations

This section analyzes the performance of the HP+IS model under element test conditions (homogeneous stress and strain fields). For the element test simulations, an initial full mobilization of the intergranular strain ($h_{ii} = -R/\sqrt{3}$) was assumed. Simulations of the undrained monotonic triaxial tests are presented in Figure 7.5 and show a reasonably accurate prediction of the undrained shearing stage. Figure 7.6 presents the experimental and simulation results of the undrained cyclic triaxial tests. The simulations considered the same number of cycles that were performed in the experiments ($N = 150$). The element test simulation results suggest a reasonable prediction of the undrained cyclic triaxial tests. However, one can note an underprediction of the vertical strain accumulation for the test UCT1 (with the smallest cyclic stress amplitude) along with an overprediction of the pore water pressure and strain accumulation for the test UCT3 (with the highest cyclic stress amplitude). Simulations of each particular test can be improved at the cost of decreasing the overall performance of the model. Therefore, the model was calibrated with "average" parameters that reproduce reasonable results for all the cyclic stress amplitudes. The decreased performance of constitutive models for fine-grained materials using tests with different cyclic stress amplitudes and a single set of parameters has been discussed in the literature by for example Wichtmann [263], Varun [250] and Fuentes et al. [71] for the anisotropic visco-hypoplastic model by Niemunis et al. [169], the SANICLAY-B model by Seidalinov and Taiebat [203] and the three surface kinematic hardening model by Stallebras and Taylor [219], respectively.

7.5 FEM simulations

Numerical simulations of the centrifuge tests were performed using the free finite element method (FEM) software TOCHNOG PROFESSIONAL [89, 243]. The following subsections describe the main characteristics

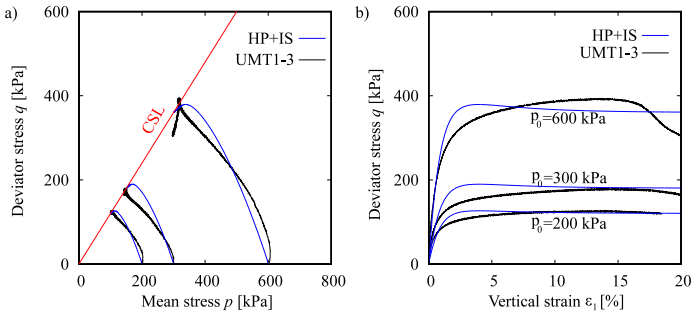

Figure 7.5: Simulations of undrained monotonic triaxial tests UMT1-UMT3 with isotropic consolidation ($q_0 = 0$ kPa, $\eta_0 = 0$) and variation of the initial mean effective pressure $p_0 = \{200, 300, 600\}$ kPa

of the FEM model and the simulation results. All simulations were performed in model scale.

7.5.1 Geometry and discretization

The geometric layout of the model is illustrated in Figure 7.7 and follows from the reference centrifuge tests by Lai et al. [126]. In the experimental study, four monopiles (a pair with $D = 40$ mm and a pair with $D = 60$ mm) were tested. However, the numerical simulations of monotonic and cyclic loading were only performed on the monopile with larger diameter ($D = 60$ mm). The model boundaries were set at a distance of 1.2 m, which is far enough to neglect their effects on the simulation results. The nodes on the bottom surface were fixed in all directions, while the ones located on the lateral boundary surfaces were fixed in the perpendicular direction to the surface. Water flow was prevented through all model boundaries except for the upper surface that serves as drainage and overlaps with the phreatic level.

The monopile geometry was modelled as a cylinder with a length of 750 mm, an outer diameter of 60 mm and a wall thickness of 2 mm. The pile was embedded 600 mm into the soil. The lateral loading was applied to the pile at a distance of 70 mm from the pile's top end. The model geometry has been discretized using 45000 finite elements of variable sizes, e.g. smallest near the monopile, where stress concentration appears and then gradually coarsen in the direction of the model boundaries. Linear fully integrated coupled stress/displacement and pore pressure 8-node hexahedral and 6-node prism elements were used for the soil block, while stress/displacement 8-node hexahedral elements reproduced the pile's geometry.

7.5.2 Pile behaviour

The monopile was made from aluminium alloy and was simulated as a linear-elastic material with Young's modulus of 72 GPa and Poisson's ratio of 0.33. The soil-pile interface was modelled using hexahedral interface elements with zero thickness described by a simple linear-elastic model with the Mohr-Coulomb failure criterion. The elastic stiffnesses of the interface in the normal and tangential direction were defined as 72 GPa and 7.5 MPa, respectively. The plastic frictional behaviour of the interface was defined by setting the friction and dilation angles as 14° and 0° [136], respectively.

7.5.3 Simulation steps

In the first step, an equilibrium calculation between gravitational loads and initial stress states is performed. For simplicity, the centrifuge spin up was omitted and 100 g conditions were directly modelled

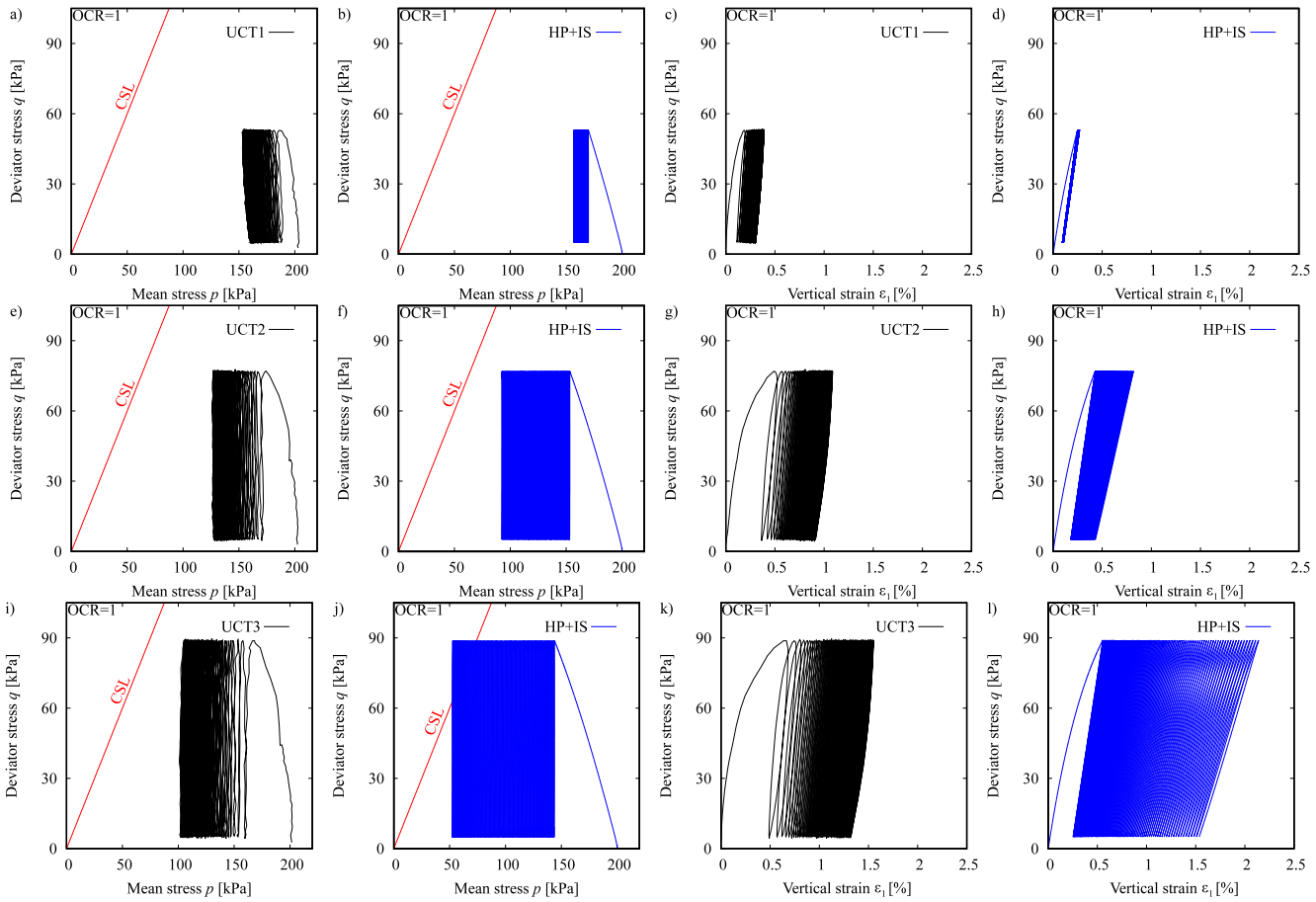

Figure 7.6: Simulations of undrained cyclic triaxial tests UCT1-UCT3 with isotropic consolidation ($p_0 = 200$ kPa, $q_0 = 0$ kPa, $\eta_0 = 0$) and variation of the cyclic stress amplitude q^{amp}

assuming them as initial conditions. The initial horizontal stresses were calculated using the K_0 coefficient reported by Mayne [145] for clays, i.e. $K_0 = (1 - \sin\varphi_c)\text{OCR}^{\sin\varphi_c}$, and Jaky [117] for sands, i.e. $K_0 = 1 - \sin\varphi_c$. To initialize the stress states and void ratios in the kaolin layer, an average OCR = 1.32 was used. In addition, hydrostatic groundwater conditions with phreatic level at the upper surface of the model were assumed.

Further simulations were performed separately for monotonic and cyclic loading. In both cases, the initial state of the intergranular strain was assumed fully mobilized in the vertical direction ($h_{11} = -R, h_{22} = h_{33} = 0$). In the simulation of monotonic loading, a single loading step was used, while the simulation of cyclic loading was performed with successive loading and reconsolidation steps. The consolidation analysis was performed by calculating the groundwater flow equations in each increment. The loading period of each cyclic stage was equal to 100 s while the reconsolidation after each loading step took 4100, 2850 and 2200 s, respectively. Despite the use of a high performance computational unit (AMD Ryzen$^{\text{TM}}$ Threadripper$^{\text{TM}}$ 2990WX with 64 threads and 128 GB of memory), about one week was needed to perform the simulation of the 300 cycles.

7.5.4 Drainage layer

A 50 mm layer of Toyoura sand was considered in the centrifuge tests to act as a drainage layer. Toyoura sand is a well tested uniform clean sand with a specific gravity of $G_s = 2.656$ and minimum and maximum

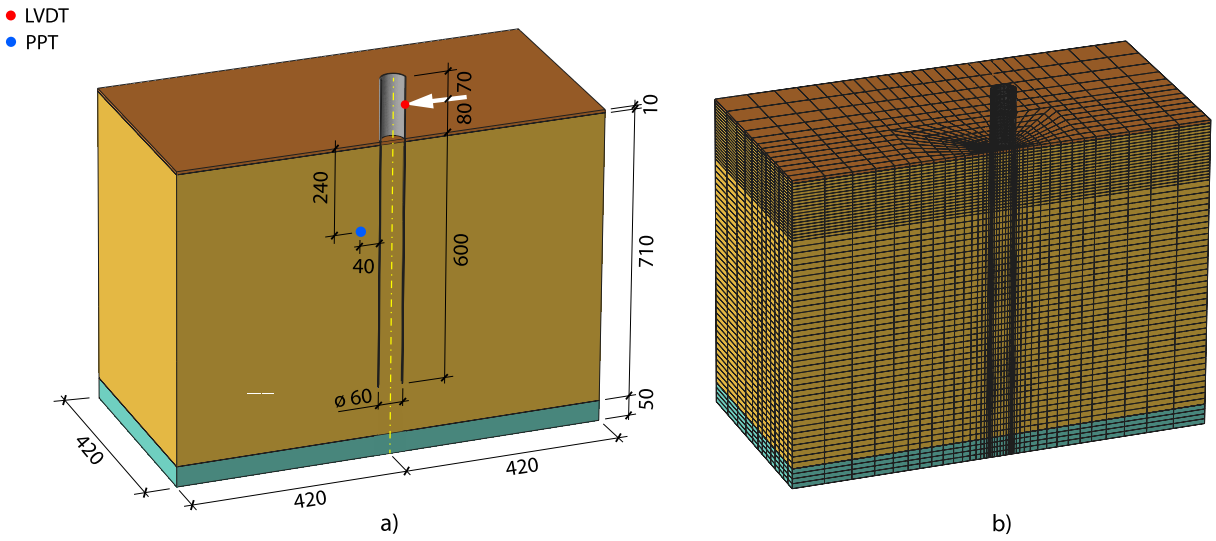

Figure 7.7: Geometry of the FEM model: a) main parts, dimensions and locations of the transducers, b) mesh discretization (in model scale, unit: mm).

void ratios of $e_{min} = 0.597$ and $e_{max} = 0.977$, respectively. An initial relative density of $D_r = 80\%$ ($e_0 = 0.673$) was assumed. The mechanical behaviour of the sand was reproduced using the hypoplastic model for granular soils by von Wolffersdorff [277] extended with IS. Parameters of the constitutive model for the sand were taken from the literature e.g. [161] and are presented in Table 7.3. For the simulation of the drainage layer, a coefficient of permeability $k = 1 \times 10^{-6}$ m/s was adopted.

Table 7.3: Parameters of the hypoplastic model for sands with intergranular strain for Toyoura sand

φ_c	h_s	n	e_{d0}	e_{c0}	e_{i0}	α	β	R	m_R	m_T	β_r	χ
[°]	[MPa]	[-]	[-]	[-]	[-]	[-]	[-]	[-]	[-]	[-]	[-]	[-]
30	2600	0.27	0.61	0.98	1.1	0.14	3.0	2×10^{-5}	8.0	4.0	0.1	1.0

7.5.5 Simulation results

This section presents the back-calculation of the centrifuge tests results with the HP+IS model. All the results presented in this section are in model scale except otherwise stated. The simulation results for the monotonically loaded monopile with $D = 60$ mm are given in Figure 7.8. The results suggest an accurate prediction of the force-displacement response with the HP+IS model, along with a small deviation in the prediction of the ultimate limit capacity. The previous behavior is in accordance with the good prediction obtained under monotonic loading in the element test simulations, see Figure 7.5.

The behavior of the monopile with $D = 60$ mm subjected to cyclic loading is now analyzed. The experimental and simulation results of the normalized excess pore water pressure $\Delta u/\sigma'_v$ vs the number of cycles are presented in Figure 7.9. The experiment shows an increase in $\Delta u/\sigma'_v$ during the first loading stage. During the second loading stage, $\Delta u/\sigma'_v$ remains almost constant after the first cycle. Finally, in the third loading stage, $\Delta u/\sigma'_v$ increases and then decreases with the number of cycles. In contrast, the simulation results show an increase in $\Delta u/\sigma'_v$ with the number of cycles in each loading stage. The experimental and numerical results are in the same order of magnitude. However, an overestimation of the excess pore water pressure was always reproduced by the model. These results are in accordance with the cyclic element test simulations, see Figure 7.6f,j, where an overestimation of the pore water

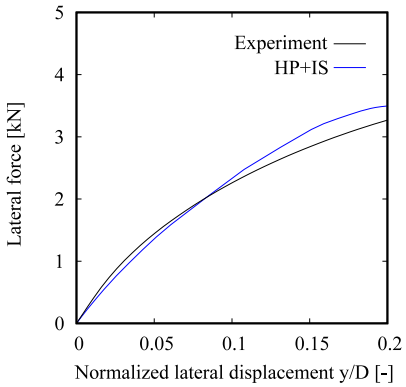

Figure 7.8: Measured and predicted monotonic load-displacement relationship of the monopile

pressure was reproduced by the model. The predictions of the pore water pressure accumulation in the element test simulations, which affect the FEM model results, can be improved at the cost of decreasing the performance in the prediction of vertical strains. Additionally, Figure 7.10 presents the simulated normalized excess pore water pressure $\Delta u/\sigma'_v$ vs time after each loading and reconsolidation stage. A full dissipation of $\Delta u/\sigma'_v$ was always reached before proceeding to the subsequent stage of cyclic loading.

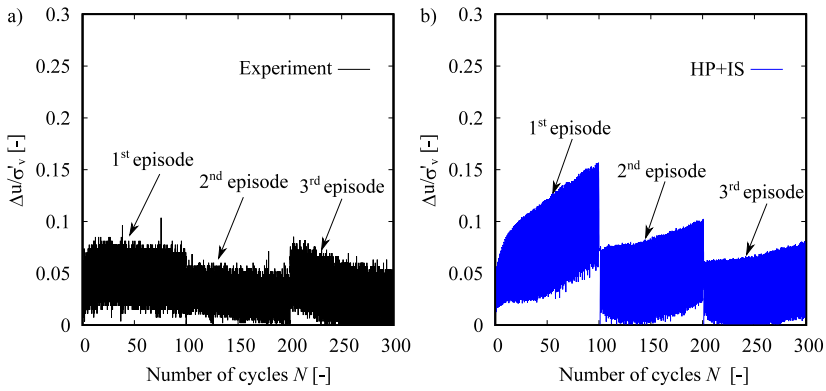

Figure 7.9: Normalized excess pore-water pressure $\Delta u/\sigma'_v$ in the episodes of cyclic loading and reconsolidation: a) Experiment, b) HP+IS model

Figure 7.11 presents the comparison between experimental and numerical force-displacement curves for each of the cyclic loading episodes. The numerical results suggest a satisfactory prediction of the normalized lateral displacements y/D. A small underestimation is revealed in the second and third stages, where the experimental results show a small increase in stiffness while the model predicts an almost identical stiffness regardless of the loading stage. On the other hand, the magnitudes of the cumulative peak and residual displacements, y_p and y_r respectively, are evaluated against the number of cycles in Figure 7.12. The experimental results suggest an increase in y_p and y_r with the number of cycles. However, the initial magnitudes of y_p and y_r are strongly reduced after each subsequent loading stage. The previous effect was well predicted by the HP+IS model. One can mention that the peak residual displacements during the first loading episode are particularly well predicted. However, a small overestimation is presented in the second and third stages due to the fact that the model does not reproduce the increase in the stiffness after the reconsolidation episodes.

The evolution of the soil-pile stiffness is of crucial importance in the analysis of monopiles since it governs their cumulative displacements and dynamic response. The soil-pile stiffness was evaluated with the unloading stiffness ratio k_{ep_i}/k_{ep_1} that is defined as the unloading stiffness (secant stiffness between

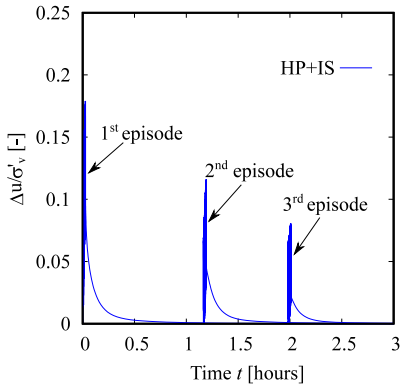

Figure 7.10: Predicted behavior of the normalized excess pore-water pressure $\Delta u/\sigma'_v$ during the episodes of cyclic loading and reconsolidation

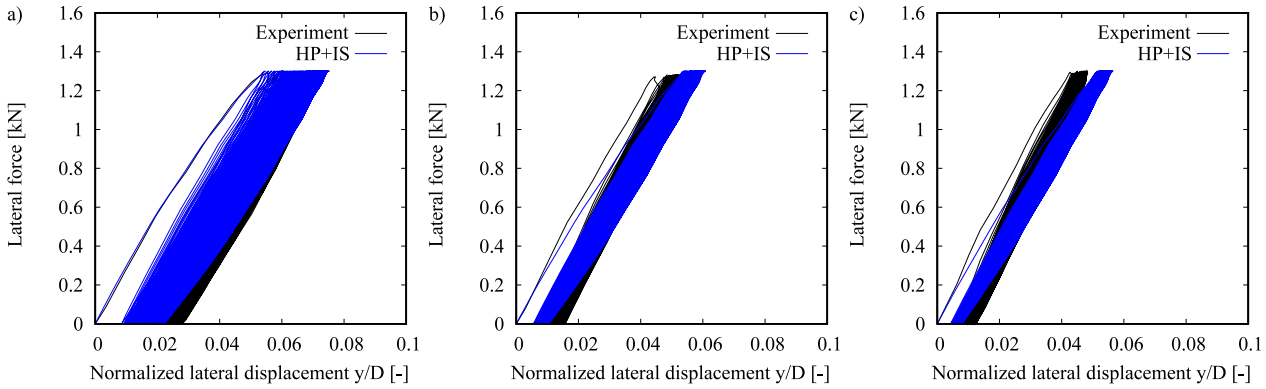

Figure 7.11: Cyclic load-displacement curves of the monopile during the stages of cyclic loading: a) first episode, b) second episode, c) third episode

loading reversal points) of the first cycle of each stage divided by the unloading stiffness of the first cycle of the first loading stage. The experimental results show an increase of the unloading stiffness ratio with each subsequent loading stage, see Figure 7.13. On the other hand, the simulation results reveal almost identical unloading stiffness ratios after full dissipation of the excess pore water pressure, which is not consistent with the experimental results. This, however, represents a conservative design scenario. Further experiments on monopiles subjected to multiple stages of cyclic loading and reconsolidation are still needed to propose a new mechanism to reproduce the stiffness recovery with the constitutive model. In addition, laboratory experiments with intermittent episodes of cyclic loading and reconsolidation are still required in order to analyze and quantify these complex effects. With this, the capabilities of the HP+IS or any other constitutive model can be extended. In the author's opinion, the modification of the HP+IS should be performed directly in intergranular strain model, which controls the behavior at small strain deformations (e.g. under cyclic loading).

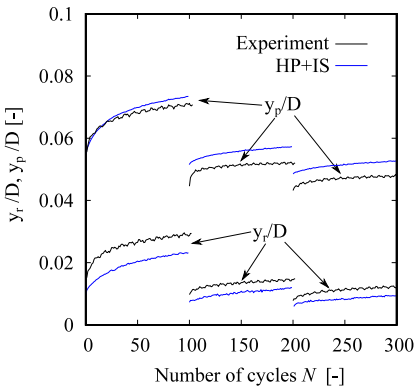

Figure 7.12: Cumulative peak and residual displacements of the monopile

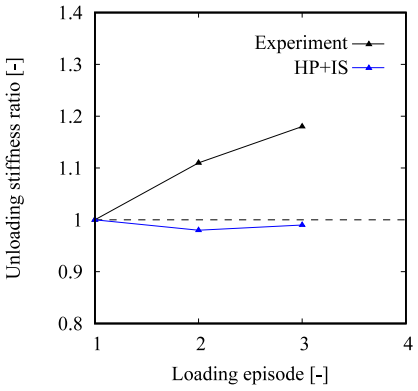

Figure 7.13: Variation of the unloading stiffness ratio k_{ep_i}/k_{ep_1} with the loading episodes

7.6 Summary and conclusions

The prediction of the cyclic soil-pile behavior in saturated fine-grained soils is a challenging task from the numerical point of view. In this work, three undrained monotonic and three undrained cyclic triaxial tests were performed on a Malaysian kaolin to calibrate a sophisticated hypoplastic model for clays with intergranular strain. To investigate the model capabilities, numerical simulations of monopiles subjected to multiple episodes of cyclic loading and reconsolidation were performed following the experimental setup from the centrifuge tests by Lai et al. [126]. The main findings are given below:

- A very clear relation between the results of simulations for element tests and boundary value problems was observed. Both presented a very accurate response under monotonic loading while a small overprediction of the pore water pressure on the boundary value problem and two of the elemental simulations. Therefore, the calibration of constitutive models for its application on cyclically-loaded boundary value problems should be based on multiple monotonic and cyclic tests with different controls (e.g. cyclic stress amplitudes, initial mean effective stresses, over-consolidation ratios and so on) that represent the possible conditions in the field.
- The HP+IS model reproduced in a satisfactory manner the undrained monotonic and cyclic triaxial tests. However, the overall performance of the model decreased when dealing with tests with different cyclic stress amplitudes and $N > 100$ cycles. This problem is currently being investigated to improve the predictive capabilities of the HP+IS model.
- The magnitudes of the cumulative peak and residual displacements of the monopile increase with the number of cycles. However, they are strongly reduced after each episode of reconsolidation. The previous behavior was well reproduced by the model. The cyclic lateral force-displacement response was also reasonably well predicted. An overestimation of the excess pore water pressure was reproduced by the model during the first loading stage.
- The experiment suggested an increase of the unloading stiffness ratio k_{ep_i}/k_{ep_1} after each subsequent stage of reconsolidation. The model failed to reproduce this behavior and instead reproduced an almost constant unloading stiffness ratio $k_{ep_i}/k_{ep_1} \approx 1$. Further experimental research on tests with multiple episodes of cyclic loading and reconsolidation on monopiles and laboratory experiments (e.g. undrained cyclic triaxial tests) are still needed in order to quantify and propose a mechanism in the constitutive model to reproduce the stiffness recovery.

7.7 Acknowledgements

The authors appreciate the financial support given by the INTER-EXCELLENCE project LTACH19028 by the Czech Ministry of Education, Youth and Sports. The first author appreciates the financial support given by the Charles University Grant Agency (GAUK) with project number 200120. The first and third authors acknowledge the institutional support by the Center for Geosphere Dynamics (UNCE/SCI/006).

Chapter 8

Numerical study of tripod suction bucket foundations - Article 7

Summary of the article

This article presents the numerical simulations of a tripod suction bucket foundation for offshore wind turbines embedded on a coarse-grained soil. As a reference, the centrifuge tests reported by Wang et al. [257] were used. In the aforementioned tests, the behavior of a tripod suction bucket foundation was studied by means of accumulated rotation, displacements and change of dynamic stiffness when subjected to lateral cyclic loading. The centrifuge results showed that the cumulative rotation initially increases along with the direction of the applied load. However, after several cycles, the whole foundation change the rotation direction to the opposite side, effect which is usually referred as "stiffness recovery effect" or "self-healing". Unfortunately, a clear discussion about this mechanism and the capabilities of advanced constitutive models to reproduce this behavior was not available in the literature and deserved further investigation.

The numerical simulations of the centrifuge tests were performed using the free finite element software Tochnog Professional. The tripod and soil were simulated with a linear-elastic and hypoplastic with intergranular strain models, respectively. Parameters of the constitutive model for granular materials were calibrated based on drained cyclic triaxial tests with different stress paths prior to the shearing. The comparison between centrifuge results and numerical simulations reveals that the model accurately reproduces the magnitude of peak and residual cumulative rotation. Irrespectively of the load amplitude at the initial loading stage (after few cycles) the whole foundation rotates along with the direction of the applied load. With subsequent cycles, the uneven progressive change in soil state leads to a significant change in stress state around both buckets. Finally, when the cumulative settlement of the pulled bucket overcome those for the pushed one, the whole foundation change rotation to the one against loading direction producing the "self-healing" effect.

Performance of tripod foundations for offshore wind turbines: a numerical study

Ochmański, M.[1,2], Mašín, D.[1], Duque, J.[1], Hong, Y.[3], Wang, L.[3]

[1]Charles University, Prague, Czech Republic

[2]Silesian University of Technology, Gliwice, Poland

[3]Zhejiang University, Hangzhou, China

Abstract

Around 80% of offshore wind turbines (OWTs) are founded on deep seabed using large-diameter monopiles that reach length up to 60 m. In a race to seek cost-effectiveness, tripod foundation made with suction caissons represent a promising solution. Safety and serviceability of these structures require to analyze, understand and predict their response to the repetitive loads acting on the wind turbines. For instance, the deformation mechanism induced by cyclic lateral loading on the tripod bucket embedded in sand reveals recovery of dynamic stiffness with the number of cycles that influences the subsequent dynamic response of the structure-foundation complex. This "self-healing" and the coupled increase of settlement rate are caused by uneven change in soil fabric and density among the buckets. A clear explanation is thus needed of the ground flow around the caissons. Yet the capability of the recently developed constitutive models to predict this effect is limited. To address this issue, a series of centrifuge tests performed at Zhejiang University are herein back-analyzed with a three-dimensional FEM model. The implicit approach has been implemented using an advanced rate-independent hypoplastic model coupled with the conventional intergranular strain theory able to reproduce the mechanical response of the cyclically loaded sand preceded by various stress paths. The model captures the magnitude of the peak and residual cumulative rotation. The results indicate that the push-pull mechanism turns into a horizontal translation, with active wedges formed behind the pulled bucket. After about a hundred cycles, due to significant redistribution of mean stresses, wedges are formed around both pushed and pulled buckets.

8.1 Introduction

With the rapidly growing market of offshore wind farms, around 80% of them are founded using large-diameter (4-6 m) monopiles [57]. Due to the lack of easily accessible shallow waters, their length may reach even up to 60 m. Thus, in pursuit of more economically and viable solutions, various types of foundations have been proposed. In the variety of possible schemes, suction caissons installed in the form of tripod seems to be especially promising.

The response of tripod foundations subjected to cyclic loading is usually studied in the reduced form of a single suction caisson subjected to vertical cyclic loading [13, 27, 28, 30, 36, 66, 78, 100, 101, 122, 292, 294, 296]. Such simplification comes from the assumption that the lateral load applied to the tripod is transferred to caissons either into vertical compression or tension. However, this doubtful assumption was proven to be wrong as interaction among caissons leads to complex load redistribution [225] and should be taken into account at the design stage (e.g. IEC [35]). Nevertheless, The referred studies commonly point out that the compression/extension cycles affect significantly the caisson stiffness at an increasing rate with the mean applied load. Under relatively high compressive loads, settlements accumulate even tough load cyclically produce tension. Furthermore, during high-frequency cycles, caissons reveal significant tension capacity.

The experimental assessment of the cyclic lateral response of tripod is limited to Kim et al. [123] and Wang et al. [257]. These works present a comparative study of the cyclic lateral response between monopod and tripod bucket foundations based on centrifuge tests. The results suggested that the rotation of monopod cumulatively increases with the number of cycles although with a progressively decreasing rate. On the other hand, tripods showed a lower residual cumulative rotation that reduces with the number of cycles. The stiffness of this foundation system increases producing the so-called "stiffness recovery effect". Houlsby et al. [100] pointed out that such effect can be related to damage in soil fabrics. Furthermore, this effect was also observed in 1g laboratory tests and numerical simulations of shallow foundations and monopiles [214, 223, 226]. Its physical explanation was given by Gudehus [87] as a result of dilatancy or recompaction, respectively triggered by alternating shear or pressure induced in the adjacent to foundation portion of soil. However, in the case of tripod bucket foundation, the lack of a clear description of the deformation mechanism does not enable to clarify this phenomenon. On the other hand, the observed response of tripod does not agree with the in-situ monitoring from Borkum Riffgrund 1 wind farm reported by Shonberg et al. [208] where stiffness tends to reduce during periods of low production and goes back to its original value when the load is reapplied with no stiffness degradation in time. This result can be related to the fact that in the laboratory, the loading is precisely controlled in one-way, which could be far from real loading scenarios exhibited in the field.

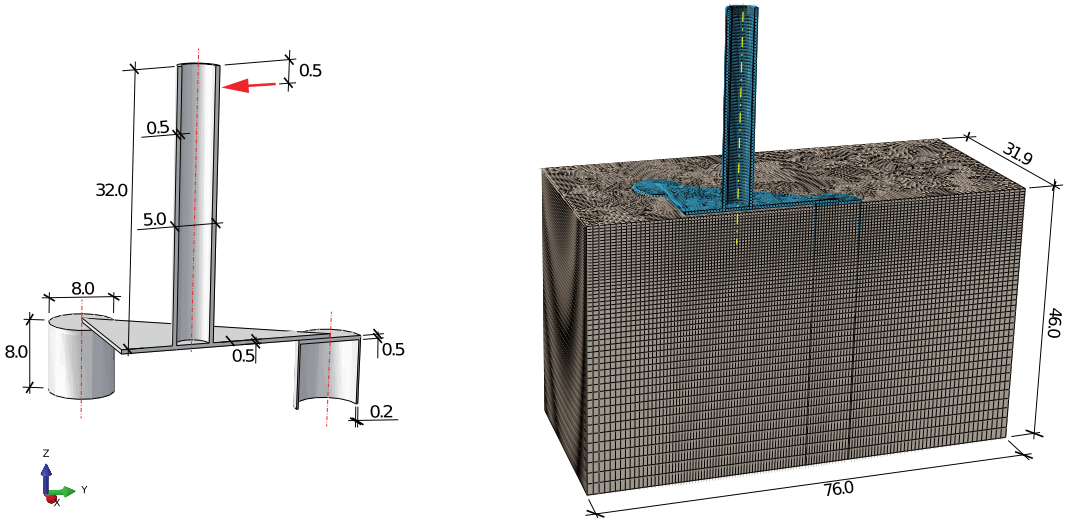

Figure 8.1: Geometry and discretization of the computational model (in prototype scale, unit: m)

The idea behind the present work is to use numerical tools validated versus experimental data to get a deep insight into the deformation mechanism of tripod subjected to cyclic loading. For this purpose, traditional implicit approach, i.e. precisely simulating each cycle, was adopted. Alternatively, for a large number of cycles, explicit models such as High-Cycle Accumulation (HCAM) model developed and thoroughly validated by Wichtmann et al. [221, 262, 269, 273] can be used. A 3D numerical model with an advance non-linear, irreversible and rate-independent hypoplastic constitutive law has been implemented. The lateral cyclic response is qualitatively and quantitatively assessed in terms of the accumulation of rotation, displacements and change of dynamic stiffness. The revealed soil flow mechanism at different stages of cyclic loading has been analysed from the deformation vectors and map of mobilized friction angle.

8.2 Computational model

The numerical simulations have been carried out using the free FEM code Tochnog professional. The model set-up reproduces centrifuge tests on the tripod bucket foundations performed at Zhejiang University [257].

8.2.1 Model set-up

The tripod geometry and its discretization illustrated in Figure 8.1 has been optimized exploiting symmetry. The model boundaries have been set at the same distance as in the centrifuge test, i.e. 24.7 and 51.3 m in YZ plane, 31.9 m in XZ plane from the tower axis and 46.0 m in XZ plane from the top surface of the soil block. Displacements at the bottom surface of the model have been fixed in all directions, while those at the model vertical sides have been fixed in the perpendicular direction.

The tripod geometry consists of three buckets with a centre-to-centre distance of 30 m connected to each other by triangular base plate thick on 0.5 m. The diameter and height of each bucket are equal to 8 m (an aspect ratio equal to 1), while the thickness of the buckets skirts and caps are equal to 0.2 m and 0.5 m, respectively. Such a high value of caisson's aspect ratio can lead to serious problems during the installation in sand, thus usually lower aspect ratios in the range of 0.3-0.7 are recommended (e.g.[28, 99, 101, 245]). A rigid loading tower with 32 m height, 5 m diameter and a wall thickness of 0.5 m is attached at the centroid of the base. The tripod was made of an aluminium alloy with elastic modulus equal to 72 GPa and Poisson's ratio equal to 0.3 [257]. The interaction between suction buckets and soil was modelled with hexahedral elements with zero thickness described by a linear-elasticity with Mohr-Coulomb failure criterion. The friction angle of the interface has been estimated as $2/3\tan(\varphi_c)$ (acc. to [95]), while cohesion was set to 0.1 kPa to eliminate numerical instabilities. The interface model has a stiffness of 1000 and 10 MPa in the normal and tangential direction, respectively and it does not allow any separation between surfaces in contact.

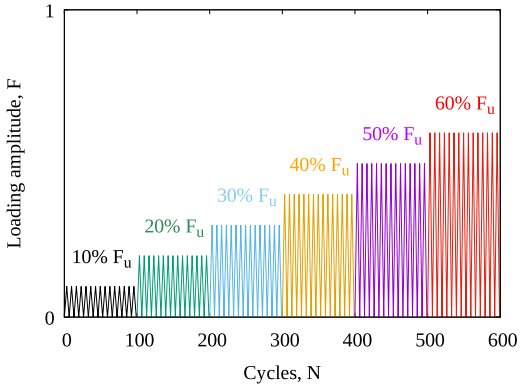

Figure 8.2: Loading sequence with increasing amplitude

Table 8.1: Calibrated parameters of hypoplastic constitutive model for Fujian sand

	φ_c [°]	h_s [MPa]	n [-]	e_{d0} [-]	e_{c0} [-]	e_{i0} [-]	α [-]	β [-]	R [-]	m_R [-]	m_T [-]	β_r [-]	χ [-]
Set I	32.5	25000	0.31	0.607	0.952	1.14	0.08	1.8	0.0001	4.9	2.6	0.4	0.8
Set II	32.5	25000	0.31	0.607	0.952	1.14	0.08	1.8	0.0001	3.9	2.6	0.1	0.8

According to Wang et al. [257], Fujian sand presents the following properties: $G_s = 2.633$, $\gamma_d = 17\ \mathrm{kN/m^3}$

and an initial void ratio at 100 kPa for $D_r = 60\%$ of $e_0 = 0.745$. The tripod foundation has been subjected to six episodes of one-way cyclic loading (see Figure 8.2) with amplitude from 10 up to 60% of the ultimate limit force (F_u). In the experiment, 1000 cycles were applied with amplitudes 10-40% F_u and 2000 cycles with 50-60% F_u while, in simulations the number of cycles was limited to 100 per each episode to reduce the computational effort. The load has been applied to the face of a single finite element of tripod tower at a height of 31.5 m above the top surface of the soil block (see Figure 8.1). Furthermore, the simulation of each loading episode has been performed separately neglecting possible effects of previous loading (taking advantage of the fact that each loading episode has higher loading magnitude than the preceding episode). This assumption comes from the need to reduce the computational effort to a reasonable level.

Simulation of each episode has been performed using two steps. In the first one, the equilibrium for the initial stress state and applied loads has been obtained with the K_0 coefficient calculated using Jaky [117] relation, i.e. $K_0 = 1 - \sin\varphi$. Despite the fact that in centrifuge tests the gravitational acceleration vary slightly over each point of the model, due to the different distances and directions from spinning centre, for simplicity, this effect has been neglected and constant value of acceleration was used. Furthermore, the centrifugal gravity increase from 1 g to 100 g has been omitted and the initial stress state refers directly to 100 g conditions. In the second step, 100 loading cycles for each of six episodes have been simulated.

The FEM mesh consists of around 260000 linear stress/displacement 8-node hexahedral and 6-node prism elements of variable sizes.

8.2.2 Soil characterization

The soil used for the experiments is a medium-dense dry Fujian sand. Its mechanical behaviour is simulated with an advanced rate independent hypoplastic constitutive model for granular materials. The large-strain response of soil has been reproduced using von Wolffersdorff [277] model which requires to define 8 parameters, namely ϕ_c, h_s, n, e_{d0}, e_{c0}, e_{i0}, α and β. Additionally, the past strain history and stiffness in the small-strain range is described by the Intergranular Strain Concept (ISC) introduced by Niemunis and Herle [170]. This extension requires to calibrate five more parameters, i.e. R, β_r, χ, m_R and m_T.

The UMAT (ABAQUS^{TM} user-defined format for material's mechanical behaviour) implementation of von Wolffersdorff [277] model with ISC is freely available at the soilmodels project website (www.soilmodels.info after Gudehus et al. [89]). This model has been calibrated against the drained cyclic triaxial tests with various stress paths imposed prior shearing [257]. The stress paths illustrated in Figure 8.3 (a) were designed to obtain 0°, 90°, −90° and 180° reversal of stress path direction moving along the same effective stress path with constant p'. The calibrated response of hypoplastic model with ISC illustrated in 8.3 (d-e) shows a good agreement with the experimental data (Fig. 8.3(b-c)). However, this initial calibration of the hypoplastic model with the conventional intergranular strains denoted as "Set I" in Table 8.1 is known to overpredict the accumulation of strains in drained cyclic loading [50, 71]. For this reason, constitutive parameters (m_R and β_r) have been retuned (Set II in Table 8.1) to catch response of tripod in centrifuge tests (see Figure 8.5). The average initial relative density of the cyclic experiments ($D_r = 60\%$) and range of effective stresses is the same observed in the centrifuge tests. For that reason, the calibration of the model is representative for the simulations of the BVP.

To guarantee same relative density as in the experiment throughout the whole depth of soil, the initial void ratio e_0 has been corrected for pressure dependency according to Bauer [11] relation. Furthermore, the effects induced during the installation of foundation have been neglected as they are significantly disrupted by gravity increase during spin-up of centrifuge. Thus, the past deformation history was taken into account in a simplified manner by initializing the vertical component of intergranular strain δ to $-1 \cdot 10^{-4}$.

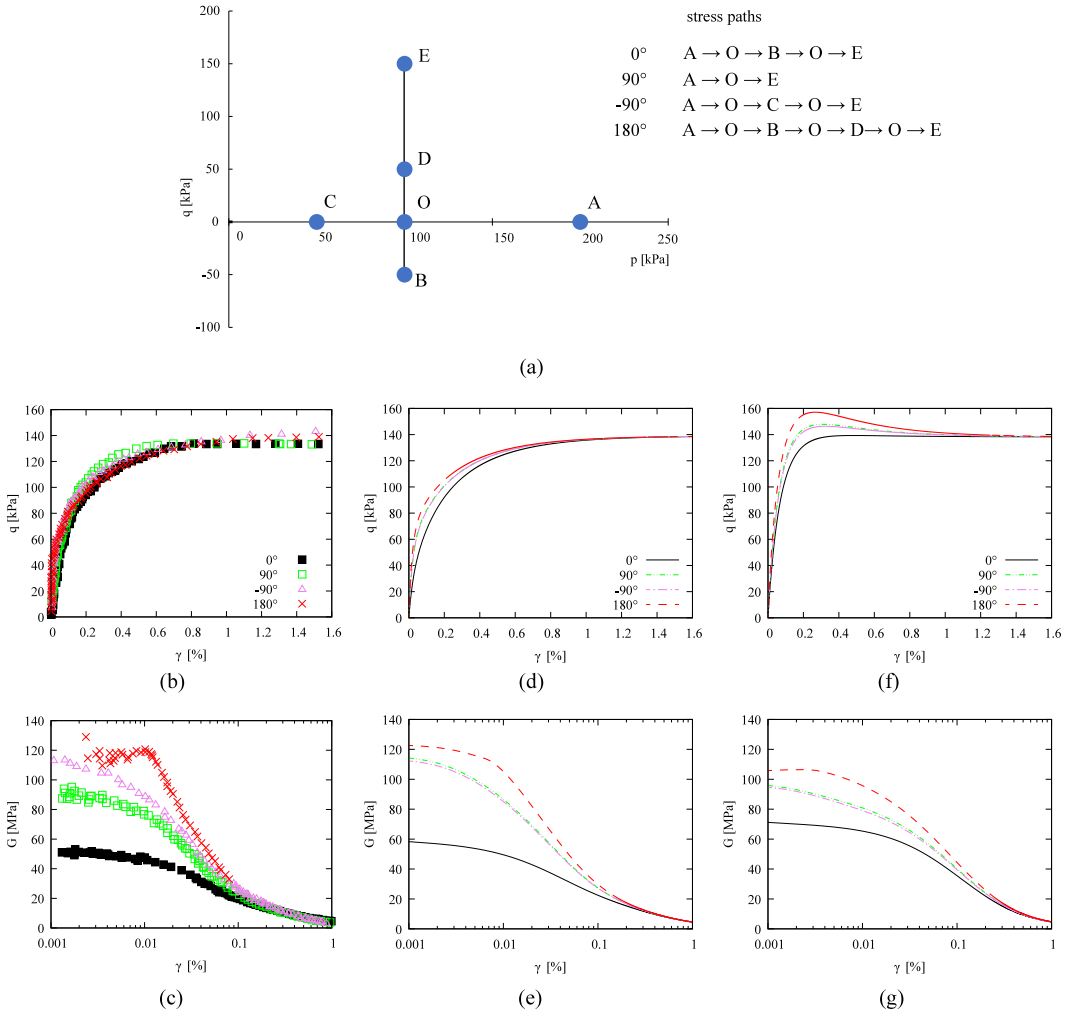

Figure 8.3: Simulation of drained cyclic triaxial tests of Fujian sand: (a) stress paths; (b-c) experiments; (d-e) calculation with Set I; (f-g) calculation with Set II

It is known that the convergence rate of the finite element solution in zones with low mean stress is poor when hypoplastic models are used, due to the stiffness stress-dependency and singular stiffness matrix at stress-free states. To eliminate this problem, a thin linear-elastic layer was introduced at the top of the model with elastic modulus equal to 500 kPa and Poisson's ratio equal to 0.3. The Fortran implementation of the used hypoplastic constitutive model adopts an explicit Runge-Kutta algorithm with a substepping scheme controlled by the difference between 3-rd and 2-nd order accuracy solution (RKF23). This approach provides a considerably higher accuracy level with a low number of increments than simpler integration schemes [137, 138]. Figure 8.4 which shows simulation of the first loading episode with 2, 10 and 20 increments per each cycle. Thus, to ensure low numerical error, 10 increments per each cycle has been used together with a ratio of unbalance forces equal to 0.0001.

8.3 Soil deformation mechanism induced by cyclic loading

The observed and computed rotation of the tripod foundation induced by cyclic loading is illustrated in Figure 8.5. The experimental evidence suggests that the rotation increase during the first cycles for each

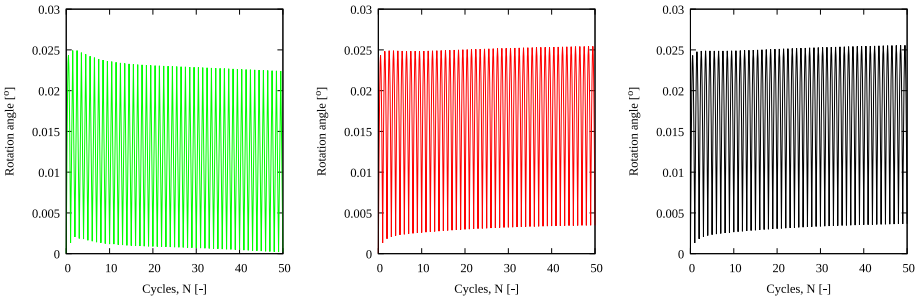

Figure 8.4: Simulation of the first loading episode (50 cycles) with a different number of increments per each cycle

episode with a typical shakedown response which then turns into decrease for remaining ones. Both peak and residual cumulative rotation decrease with the number of cycles for all loading amplitudes, where the former one reaches almost zero at the end of each episode. This effect called "self-healing" is probably caused by irreversible change in soil fabric and density [5] in a larger extent near the rear bucket than near two front buckets. Uneven change in soil fabrics and density among tripod caissons exhibited as reduction of mean stresses and development of ground deformation lead to the backward tilt of foundation. The comparison reveals that the model accurately reproduces the magnitude of peak and residual cumulative rotation. The parameters of ISC (m_R and β_r) have been recalibrated to obtain similar decreasing trend of cumulative rotation (see Set II in Table 8.1).

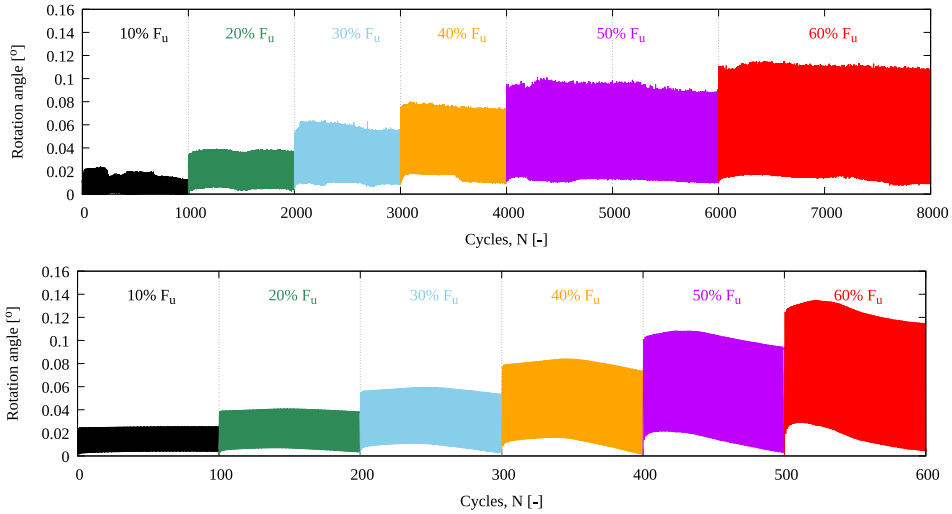

Figure 8.5: Comparison of measured (a) and computed with Set II (b) rotation of tripod during the multi-amplitude lateral cyclic loading

Figure 8.6 shows the deformation mechanism and mean stresses induced after 10 and 100 cycles for loading amplitude of 10% F_u. Deformation mechanism is illustrated by the residual displacement vectors, map of mobilized friction angle and relative void ratio defined as $r_e = (e - e_d)/(e_c - e_d)$ [278]. At the initial loading state (after 10 cycles) a slight reduction of mean stresses around pulled bucket skirts is observed which comes together with a drop of mobilized friction angle (ϕ_{mob}) and relative void ratio. Computed displacements vectors reveal that at this state whole foundation rotates in loading direction with the left bucket being pushed and the right pulled-out. Nevertheless, this push-pull mechanism identified by Senders [204] and confirmed by Houlsby [97] comes together with the horizontal translation of foundation in a loading direction. The progressive change in soil state during consequent cycles leads to a further

drop of mean stresses around both buckets skirts. At the same time, a slight increase of mobilized friction angle indicates an initial formation stage of active wedges on both sides of the pulled bucket and front of the pushed one. The rotation of foundation in loading direction turns progressively opposite as settlement rate of pulled bucket increases.

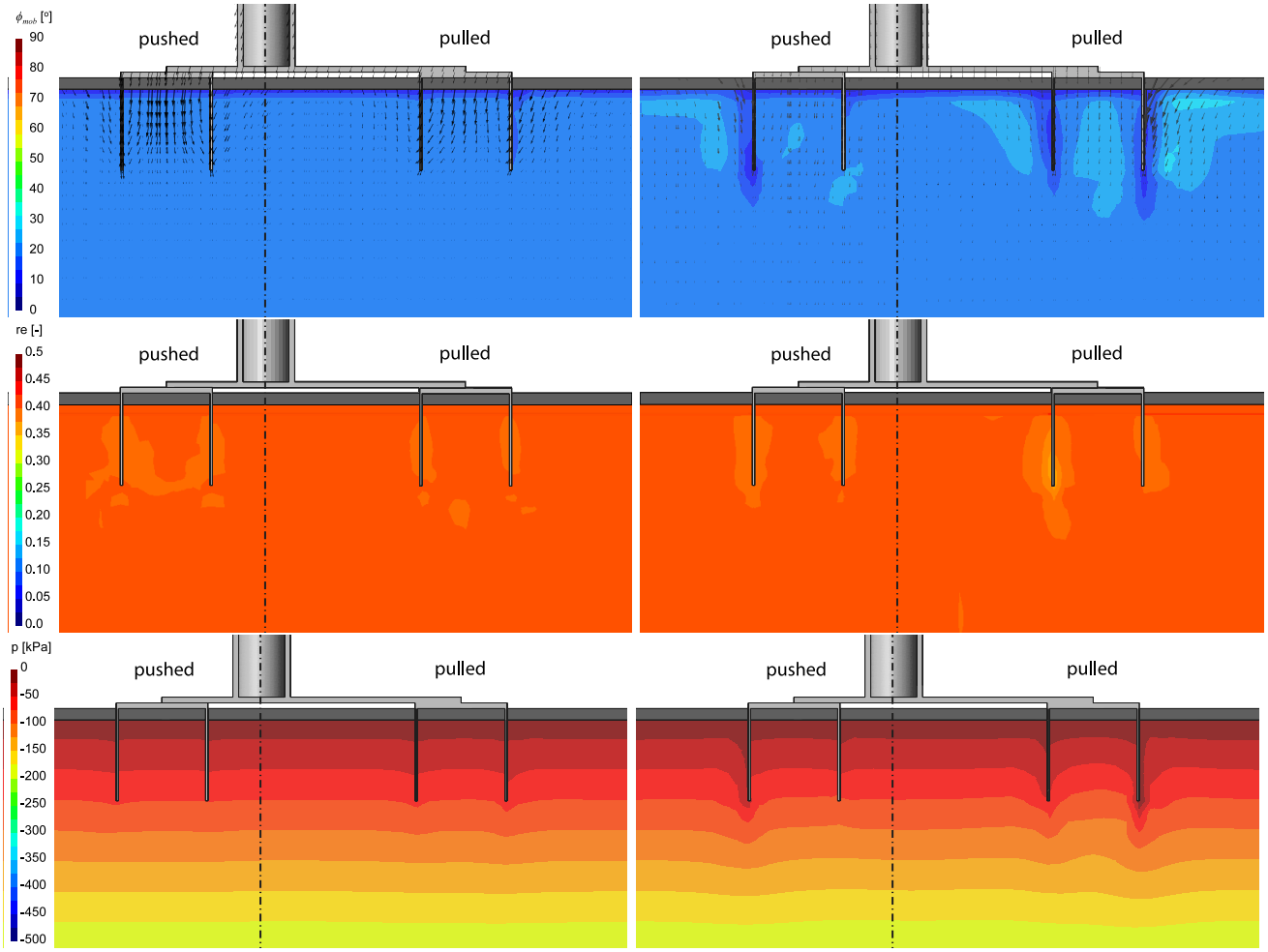

Figure 8.6: Computed mobilised friction angle with displacements vectors, relative void ratio and mean effective stress for 10% F_u: (a-c) after 10 cycles; (d-f) after 100 cycles

With the increase of loading amplitude up to 60% F_u (see Figure 8.7), state after first 10 cycles is similar to that corresponding to 10% F_u after 100 cycles. However, with formed active wedge behind the pulled bucket, the displacement vectors indicate that the whole foundation still undergoes rotation with loading direction. Despite higher load amplitude, change in soil state at this stage is not extensive enough to change the settlement rate of the pulled bucket. On the other hand, the subsequent cycles lead to a drastic stress change around both buckets due to progressive and at this stage already severe change in soil state. Around skirts of the pushed bucket mean stress drops almost to zero and concentrates below the right one. Moreover, the significant stress drop around the pulled bucket with concentration below its centre result in a change of its settlement rate. With the increasing cumulative settlements pulled bucket drags downward soil around which fully develop active wedges at both sides. The mobilized friction angle increases up to 50° in the zones of active wedges while inside pulled bucket up to almost 80°. Such a high value of ϕ_{mob} (with theoretical max. limit of 90°) is possible when soil undergoes dilative behaviour, i.e. increases it's void ratio due to the drastic stress reduction [153]. Furthermore, the relative void ratio reduces significantly around skirts of the pulled caisson down to around 0.25. When the cumulative

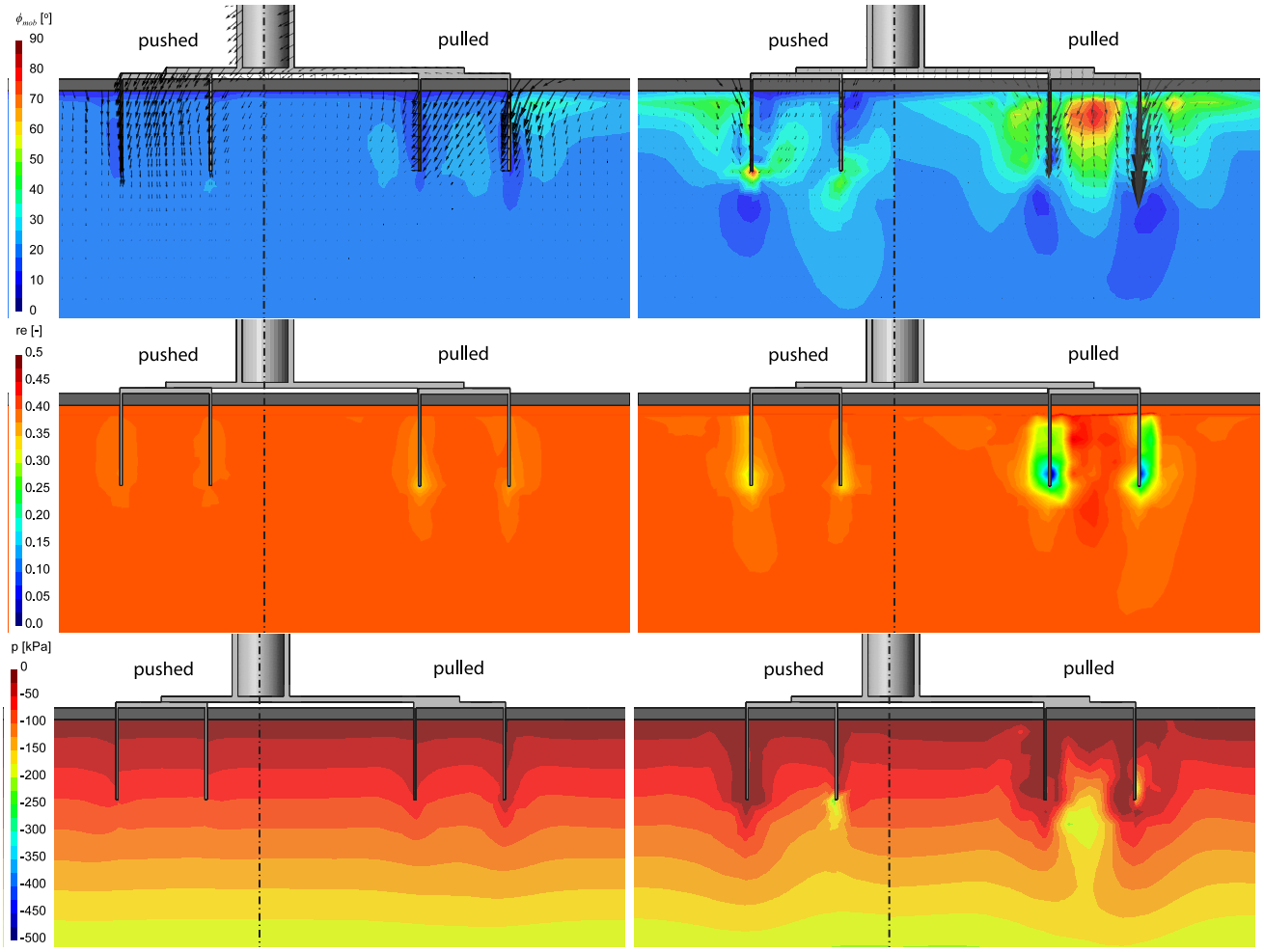

Figure 8.7: Computed mobilised friction angle with displacements vectors, relative void ratio and mean effective stress for 60% F_u: (a-c) after 10 cycles; (d-f) after 100 cycles

settlement of the pulled bucket overcome those for the pushed one, the whole foundation change direction of rotation to opposite, i.e. against loading direction.

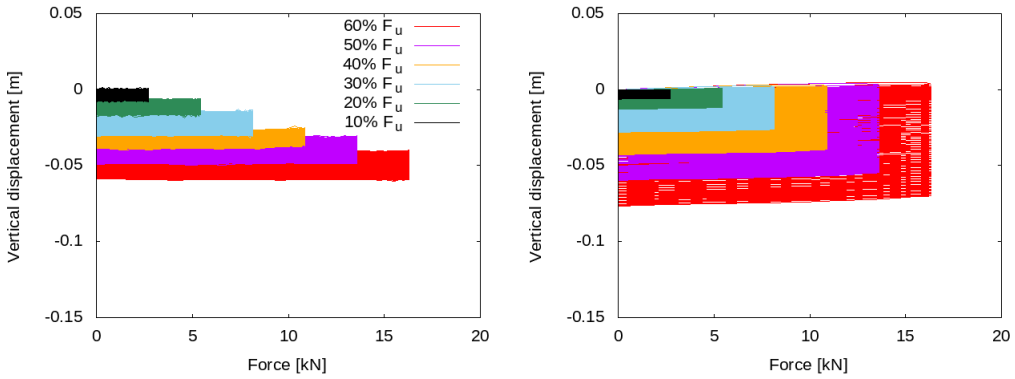

Figure 8.8: Comparison of measured (left) and computed (right) vertical displacement induced by cyclic loading for pulled caisson. Note that, as the numerical simulations have been performed separately for each episode, computed results start for each episode from zero displacement, whereas measured data include displacements from previous loading steps

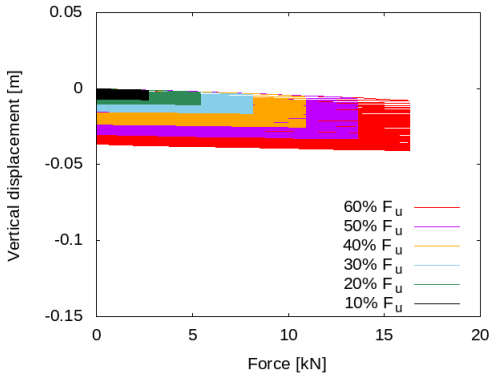

Figure 8.9: Computed vertical displacement induced by cyclic loading for pushed caisson

Measured and computed vertical displacements of pulled caisson at the centre of the bucket lid are shown in Figure 8.8. While for the pushed caisson, due to the lack of experimental data only computed vertical displacements are presented (Figure 8.9). Simulation results reveal that the pulled bucket after unloading from the first cycle exhibits some residual upward movement, while the pushed one goes back almost to the initial position with small residual settlement due to stiffness degradation. This leads to the initial rotation in loading direction for each loading episode (see Figure 8.5). With subsequent cycles pulled caisson starts to settle with a higher rate than the pushed one, in consequence reducing rotation of tripod. The presented trend remain unchanged for all loading amplitudes with a small deviation in peak displacements. Experimental data for the pulled caisson show the same response as from the simulation, however, the slope of the vertical displacements for loading/unloading cycles and residual settlements are much smaller for loading levels 30% and higher. It could be caused by a different structure stiffness when compared to the assumed aluminium alloy stiffness of 72 GPa and due to presence of structural joints [224, 225].

8.4 Summary and conclusions

Results of the numerical simulations presented in this work provide an insight into the deformation mechanism of tripod subjected to cyclic loading. Despite the load amplitude at the initial loading stage (after few cycles) the whole foundation rotates accordingly with the direction of the applied load. With the subsequent cycles, the uneven progressive change in soil state leads to a significant change in stress state around both buckets. It comes together with the increase of mobilized friction angle to around 50° in the zones of active wedges, and even almost to 80° inside the pulled bucket. Finally, when the cumulative settlement of the pulled bucket overcome those for the pushed one, the whole foundation change rotation to the one against loading direction producing "self-healing" effect.

Acknowledgement

The financial support provided by the research grant LTACH19028 Inter-Excellence (Inter-Action) of the Czech Ministry of Education, Youth and Sports is greatly appreciated. The second and third authors acknowledges institutional support by the Center for Geosphere Dynamics (UNCE/SCI/006). The third author appreciates the financial support given by the Charles University Grant Agency (GAUK) with project number 200120.

Chapter 9

Summary and conclusions

This cumulative dissertation presented some contributions to the experimental investigation and numerical description of soil cyclic behavior. Initially, an experimental database on a high-plasticity Malaysian kaolin under monotonic and cyclic loading was presented. The results of undrained monotonic triaxial tests on normally consolidated samples showed a contractive behavior. Increasing the mean effective pressure of the tests leads to higher undrained shear strengths. In addition, an increase in the initial overconsolidation ratio leads to more dilative responses, lower initial void ratios and higher undrained shear strengths. The results of undrained cyclic triaxial tests with isotropic consolidation suggested a remarkable influence of the deviatoric stress amplitude in the accumulation rates of pore water pressure and strains, and therefore, in the number of cycles to reach failure conditions. A similar effect was found with the initial stress ratio η_0, in which an increase of η_0 drastically reduces the number of cycles to reach the failure criterion.

Like tests on medium to high plasticity soils from the literature, the state with zero effective stress, hence the liquefaction state, was not reached with the tested kaolin. In addition, the Malaysian kaolin does not exhibit eight-shaped effective stress paths in the final phase of tests with isotropic consolidation, which are usually observed on some fine-grained soils. The comparison of the obtained results with some former studies suggest that, with all other conditions remaining the same, an increase in soil plasticity considerably increases the number of cycles to reach failure. Undrained cyclic tests performed considering packages of cycles in different sequences suggested that, independently of η_0, Miner's rule is not valid under undrained conditions. A modified Stewart's approach was proposed to analytically estimate the accumulated pore water pressure and strains on tests with variable loading magnitudes based on single-amplitude tests. Its validity suggested that constitutive models developed using single-magnitude loading packages can be used in simulations of problems with variable cyclic loading magnitudes. Undrained cyclic triaxial tests with a drained cyclic preloading presented a substantial reduction in the accumulation rates of strains and pore water pressure, and therefore, an increase the number of cycles to reach failure conditions. These behavioral features are associated with effects of recent stress history and fabric changes due to stress/strain induced anisotropy.

An experimental database on Zbraslav sand under monotonic and cyclic loading was presented. It included undrained monotonic triaxial tests, oedometric compression tests with multiple unloading-reloading cycles and undrained cyclic triaxial tests with and without cyclic preloadings. Undrained monotonic triaxial tests on medium dense samples showed a contractive behavior followed by dilation. Increasing the initial relative density of the samples leads to a less compressive response at the initial phase of the tests. The results of undrained cyclic triaxial tests with isotropic consolidation suggest a remarkable influence of the deviatoric stress amplitude in the accumulation rates of pore water pressure and strains, and therefore, in the number of cycles to reach failure conditions. In addition, their final phase is characterized by butterfly-shaped effective stress paths accompanied with a progressive increase of the axial strain amplitude with

each subsequent cycle. Similar to former studies on undrained cyclic triaxial tests, and differing from typical results on undrained cyclic simple shear tests, the vertical strain accumulation is asymmetric with higher accumulation in the extension side compared with the compression side. The experimental results suggested that drained cyclic preloadings remarkably modified the subsequent rate of pore water pressure accumulation and increased the number of cycles to reach the defined failure criterion without affecting the shape of the stress-strain hysteresis. On the other hand, undrained cyclic preloadings presented a threshold which separated positive and negative effects in the subsequent undrained cyclic resistance.

A detailed review of the prediction capabilities, advantages and limitations of four advanced constitutive models for fine-grained soils, namely: CAM, AHP+ISA, SANICLAY-B and A3-SKH was presented. These models were carefully selected since they are based on different mathematical frameworks and claim to reproduce the monotonic and cyclic behavior of fine-grained soils. As expected, the four constitutive models performed well under undrained monotonic loading. However, many issues were found on the simulations of cyclic tests. The experiments showed eight-shaped effective stress paths in the last stage of tests with isotropic consolidation and stress-cycles. They were only partially reproduce by the CAM model. However, it should be noted that these eight-shaped effective stress paths are "erased" with increasing plasticity as remarked by e.g. [21, 105]. This is an important difference in comparison to tests on coarse-grained soils. Therefore, the models need to be extended with a mechanism that phenomenologically reproduce the influence of soil plasticity in the shape of the effective stress paths. The accumulated pore water pressure was well reproduced by the AHP+ISA and CAM models. The pore water pressure accumulation with the SANICLAY-B and A3-SKH stops as soon as mean effective stress reaches critical state value. This limits the predictive capabilities of these models on boundary value problems whereby the prediction of pore water pressure is of interest. Only the SANICLAY-B model was able to realistically reproduce the ever increasing double strain amplitude after cyclic mobility. Models having problems to reproduce the behaviour at large deformations are limited in applications dealing with earthquake loading. The analysis of the CSR-N_{f} curves on undrained cyclic tests with isotropic consolidation is still a challenge with the inspected models. For their correct reproduction, two important features need to be correctly accounted for: a) accurate reproduction of the influence of the deviatoric stress amplitude in the accumulation rates, and b) the capability to (at least qualitatively) reach the defined failure criteria. Variation of the initial conditions such as the initial stress ratio, OCR and strain-cycles suggest a less accurate performance with all the models. The influence of the inherent anisotropy was only well reproduced by the CAM and AHP+ISA models.

Seven characteristic limitations of models for cyclic loading for sands were presented and discussed. They were exemplified with the simulations of two models from the bounding surface plasticity family and two models from the hypoplastic family. The results suggest that overshooting and undershooting effects after reverse loading/immediate reloading paths is a characteristic artificial drawback on simulations with models for cyclic loading of sands. To properly address this issue, a proper consideration of the memory effects of recent loading history in the cyclic models is necessary. Simulation of cyclic mobility with undrained cyclic triaxial tests of symmetric deviator stress amplitude is usually accompanied with one-way ratcheting in strain accumulation. Two specific considerations can be incorporated to adequately resolve this issue. The first is to induce a degrading stiffness cycle by cycle so as to generate large shear strain in the liquefaction state. The other is to control the balance of the shear modulus in the compression and extension side. The adequate modeling of cyclic liquefaction strength curves or CSR–N_{ini} considering various criteria for reaching initial liquefaction, is a challenge in majority of available constitutive models. To reach the criterion of r_u, the model needs to induce a large amount of contraction upon unloading after dilation. To properly capture the shear strain-based initial liquefaction, a mechanism for generating large shear strain in liquefaction state is necessary. To quantitatively simulate cyclic liquefaction strength curves, one need to consider effects of CSR, relative densities, and initial confinement. Simulation performance on very dense samples subjected to undrained cycles of constant large strain amplitudes

also reveals some missing features in the constitutive models. A good amount of contraction should be generated upon unloading after dilation. The stress path attractor is accompanied by a degrading shear modulus. The plastic strain accumulation is unrealistic when dealing with cyclic loading with closed stress loops of small amplitude, whereby an elastic response is expected. Attention should be given to the yield surface geometry, and the accumulation provided by the hypoelastic tensor, to properly reduce the resulting plastic accumulation. The constitutive models, when formulated in terms of stress-ratio changes for generating plasticity, may deliver inadequate oedometric loading stiffness. Thus, one may need an additional plastic mechanism, implying some modifications in the yield surface, which allows for proper reproduction of plastic strains under this path. Drained preloading affects significantly subsequent undrained shearing. Definitely, this effect should not be neglected by constitutive models. The lack of memory effects on the formulation of some models disables the reproduction of this important effect.

A simple yet efficient modification to the original intergranular strain model by Niemunis and Herle [170] was proposed. The modification consists on an additional mechanism to reduce the strain accumulation rate on paths with repetitive cycles of small strain amplitudes. The improvement allows to adapt its response at cycles of larger strain amplitudes, where the strain accumulation rate is expected to increase. The original and modified models were implemented together with the hypoplastic model for sands by Von Wolffersdorff [277] and compared to each other under cyclic loading. The results showed that the modified model is able to capture with better accuracy most of the observed effects under cyclic loading, as for example: a) the number of cycles required to reach failure conditions, b) the evolution with number of cycles of the normalized accumulated pore water pressure u_w^{acc}/p_0, under undrained conditions, and c) the evolution with number of cycles of the accumulated strains under drained conditions. The proposed modification requires the calibration of parameters χ_0, $\chi_{\max}$ and C_Ω (instead of χ).

Finite element simulations of the centrifuge tests reported by Lai et al. [126] showed that the hypoplastic model for clays with intergranular strain was able to accurately reproduce the magnitude of the ultimate lateral monotonic loading. In addition, the cumulative peak and residual displacements of the monopile under cyclic loading were also well predicted. The cyclic lateral force-displacement response was reasonably well predicted. An overestimation of the excess pore water pressure was reproduced by the model during the first loading stage. The centrifuge tests suggested an increase of the unloading stiffness ratio k_{ep_i}/k_{ep_1} after each subsequent stage of reconsolidation. The model failed to reproduce this behavior and instead reproduced an almost constant unloading stiffness ratio $k_{ep_i}/k_{ep_1} \approx 1$. Further experimental research on tests with multiple episodes of cyclic loading and reconsolidation on monopiles and laboratory experiments (e.g. undrained cyclic tests) are still needed in order to quantify and propose a mechanism in the constitutive model to reproduce the stiffness recovery.

Finite element simulations were performed to provide an insight into the deformation mechanism of tripod suction bucket foundations subjected to cyclic loading. The results suggest that independently of the loading amplitude, the foundation initially rotates according to the direction of the applied load. Then, after several cycles, the uneven progressive change in soil state leads to a significant change in stress state around both buckets. It comes together with the increase of mobilized friction angle to around 50° in the zones of active wedges, and even almost to 80° inside the pulled bucket. Finally, when the cumulative settlement of the pulled bucket overcome those for the pushed one, the whole foundation change rotation to the one against loading direction producing the so-called "self-healing" effect. This is actually an important difference in the deformation mechanism in comparison to the one observed on the monopile simulations.

In the author's opinion, soil cyclic behavior is one of the main directions of geotechnical research. There are many open questions from the experimental point of view and huge space for further developments or improvements from the modelling side. Some of them, which are related with this thesis, are remarked in Chapter 10 and will be one of the focus of the author subsequent research.

Chapter 10

Outlook

Some further experimental and numerical works are still necessary, and will be the focus of the author subsequent research. Some of the most important issues to address are summarized as follows:

- The experimental evidence on cyclic tests with episodes of undrained cyclic loading, reconsolidation and further undrained cyclic re-shearing suggest a considerable variation of the stiffness, undrained shear strength and cyclic resistance on fine-grained e.g. [288–290] and coarse-grained soils e.g. [102, 114, 115, 174, 181, 182, 200, 201, 213, 217, 228, 249]. The mechanism controlling this behavior is more or less known on coarse-grained soils and depends on whether the effective stress path of the preloading goes beyond the phase transformation line on loose samples or a strain threshold after initial liquefaction in the case of dense samples. However, this behavior seems much less straightforward on fine-grained soils, in which the distance between the state $p = 0$ and the asymptotic state $p > 0$ where the pore water pressure accumulation stops depends on the mineralogical composition of the material. Therefore, additional undrained cyclic triaxial tests on fine-grained soils are necessary to investigate the variation of the cyclic resistance on tests with different amounts of undrained cyclic preloadings, similar to the ones performed on Zbraslav sand.

- The improved intergranular strain model presented in chapter 6 shows improved capabilities in the prediction of the accumulation rates under cyclic loading. However, the model failed to reproduce cyclic mobility effects, and instead of that, presented a bias in the vertical strain accumulation. As remarked by Fuentes et al. [76], this issue is a consequence of the mathematical formulation of the hypoplastic model by Von Wolffersdorff [277] and not due to the intergranular strain model. An attempt to address this limitation was proposed by Fuentes et al. [76], by introducing a fabric-dilatancy tensor, similar to the one proposed by Dafalias and Manzari [39] for the SANISAND 2004 model. Simulation results with the improved hypoplastic model by Fuentes et al. [76] show an accurate behavior during the first mobilized cycles but a bias in the vertical strain accumulation thereafter, see Figure 5.4. The recent work by Liao and Yang [134] proposed an extension of the hypoplastic model to account for cyclic mobility effects by incorporating the anisotropic critical state theory by Li and Dafalias [133]. Even though that their improved hypoplastic model presents much improved capabilities, the model incorporates 6 additional parameters to the basic hypoplastic model. In the author's opinion, some of the most attractive features of the hypoplastic model by Von Wolffersdorff [277] are its simple mathematical structure and the incorporation of rather "few" model parameters, the latter lost in the version by Liao and Yang [134]. Therefore, the author thinks that more research in the incorporation of cyclic mobility effects on hypoplasticity is still necessary.

- Simulation results presented in chapter 5 suggest that the overshooting problem is probably the

most critical issue of the intergranular strain model by Niemunis and Herle [170] and its further extensions e.g. [50, 260]. Although this limitation is strongly mitigated using the intergranular strain anisotropy (ISA) model by Fuentes [68], the problem is not fully addressed. This issue requires further research. A first attempt could be coupling the intergranular strain model with the asymptotic state boundary surface of the hypoplastic models in such a way that the asymptotic state boundary surface defines the maximum stress states of the model.

Bibliography

[1] C. Abadie, B. Byrne, and G. Houlsby. Rigid pile response to cyclic lateral loading: laboratory tests. *Géotechnique*, 69(10):863–876, 2019.

[2] T. Adachi, F. Oka, T. Hirata, T. Hashimoto, J. Nagaya, M. Mimura, and T. Pradhan. Stress-strain behavior and yielding characteristics of eastern osaka clay. *Soils and Foundations*, 35(3):1–13, 1995.

[3] S. Afifi and R. J. Stress-history effects on shear modulus of soils. *Soils and Foundations*, 13(1):77–95, 1973.

[4] A. Al Tabbaa and D. Wood. An experimentally based "bubble" model for clay. In *Proceedings of the third International Conference on Numerical Models in Geomechanics*, pages 91–99, Niagara Falls, 1989.

[5] K. Andersen. Cyclic soil parameters for offshore foundation design. In *Frontiers in Offshore Geotechnics III: Proceedings of the 3rd International Symposium on Frontiers in Offshore Geotechnics*, pages 5–82, Leiden, 2015.

[6] A. Arab, M. Sadek, M. Belkhatir, and I. Shahrour. Monotonic preloading effect on the liquefaction resistance of chlef silty sand: A laboratory study. *Arabian Journal For Science and Engineering*, 39(2):685–694, 2014.

[7] R. Armstrong. Numerical analysis of leap centrifuge tests using a practice-based approach. *Soil Dynamics and Earthquake Engineering*, 113:793–803, 2018.

[8] J. Atkinson, D. Richardson, and S. Stallebrass. effect of recent stress history on the stiffness of overconsolidated soil. *Géotechnique*, 40(4):531–540, 1990.

[9] A. Azzouz and M. Malek, A. Baligh. Cyclic behavior of clays in undrained simple shear. *Journal of Geotechnical Engineering*, 115(5):637–657, 1989.

[10] A. Barrero, M. Taiebat, and Y. Dafalias. Modeling cyclic shearing of sands in the semifluidized state. *International Journal for Numerical and Analytical Methods in Geomechanics*, 44(3):371–388, 2020.

[11] E. Bauer. Calibration of a comprehensive constitutive equation for granular materials. *Soils and Foundations*, 36(1):13–26, 1996.

[12] J. Benoot, W. Haegeman, S. François, and G. Degrande. Experimental study of strain accumulation of silica sand in a cyclic triaxial test. In *Proceedings of the 23rd European Young Geotechnical Engineers Conference*, pages 3–6, Barcelona, 2014.

[13] B. Bienen, R. Klinkvort, C. O'Loughlin, F. Zhu, and B. Byrne. Suction caissons in dense sand, part II: vertical cyclic loading into tension. *Géotechnique*, 68(11):953–967, 2018.

[14] O. Blaker and K. Andersen. Shear strength of dense to very dense dogger bank sand. In *Frontiers in Offshore Geotechnics III: Proceedings of the 3rd International Symposium on Frontiers in Offshore Geotechnics*, pages 1167–1172, Leiden, 2015.

[15] O. Blaker and K. Andersen. Cyclic properties of dense to very dense silica sand. *Soils and Foundations*, 59(4):982–1000, 2019.

[16] D. Bobei, D. Wanatowski, M. Rahman, S. Lo, and C. Gnanendran. The effect of drained preshearing on the undrained behaviour of loose sand with a small amount of fines. *Acta Geotechnica*, 8:311–322, 2013.

[17] M. Bode, W. Fellin, D. Mašín, G. Medicus, and A. Ostermann. An intergranular strain concept for material models formulated as rate equations. *International Journal for Numerical and Analytical Methods in Geomechanics*, 44(7):1003–1018, 2020.

[18] W. Bode, M.and Fellin and G. Medicus. Reloading in barodesy employing the asymptotic state boundary surface. *International Journal for Numerical and Analytical Methods in Geomechanics*, 2021. https://doi.org/10.1002/nag.3258.

[19] J. Boháč and J. Feda. Membrane penetration in triaxial tests. *Geotechnical Testing Journal*, 15(3):288–294, 1992.

[20] G. Bouckovalas, R. Whitman, and W. Marr. Permanent displacement of sand with cyclic loading. *Journal of Geotechnical Engineering*, 110(11):1606–1623, 1984.

[21] R. Boulanger and I. Idriss. Liquefaction susceptibility criteria for silts and clays. *Journal of Geotechnical and Geoenvironmental Engineering*, 132(11):1413–1426, 2006.

[22] R. Boulanger and I. Idriss. Evaluation of cyclic softening in silts and clays. *Journal of Geotechnical and Geoenvironmental Engineering*, 133(6):641–652, 2007.

[23] R. W. Boulanger and K. Ziotopoulou. Formulation of a sand plasticity plane-strain model for earthquake engineering applications. *Soil Dynamics and Earthquake Engineering*, 53:254–267, 2013.

[24] BP. Statistical review of world energy 2019. Technical report, BP plc, 2019.

[25] S. Brown, A. Lashine, and A. Hyde. Repeated load triaxial testing of a silty clay. *Géotechnique*, 25(1):95–114, 1975.

[26] J. Burland. On the compressibility and shear strength of natural clays. *Géotechnique*, 40(3):329–378, 1990.

[27] B. Byrne. *Investigations of Suction Caissons in dense Sand*. PhD thesis, University of Oxford, Oxford, U.K., 2000.

[28] B. Byrne and G. Houlsby. Experimental investigations of response of suction caissons to transient vertical loading. *Journal of Geotechnical and Geoenvironmental Engineering*, 128(11):926–939, 2002.

[29] B. Byrne and G. Houlsby. Foundations for offshore wind turbines. *The Royal Society*, 361(1813):2909–2930, 2003.

[30] B. Byrne and G. Houlsby. Experimental investigations of the response of suction caissons to transient combined loading. *Journal of Geotechnical and Geoenvironmental Engineering*, 130(3):240–253, 2004.

[31] Y. Cai, C. Gu, J. Wang, C. Juang, C. Xu, and X. Hu. One-way cyclic triaxial behavior of saturated clay: Comparison between constant and variable confining pressure. *Journal of Geotechnical and Geoenvironmental Engineering*, 139(5):797–809, 2013.

[32] K. Chew, K. Tai, E. Ng, and M. Muskulus. Analytical gradient-based optimization of offshore wind turbine substructures under fatigue and extreme loads. *Marine Structures*, 47:23–41, 2016.

[33] S. Chu and A. Majumdar. Opportunities and challenges for a sustainable energy future. *Nature*, 488:294–303, 2012.

[34] A. Colmenar, J. Perera, D. Borge, and C. Palacio. Offshore wind energy: A review of the current status, challenges and future development in spain. *Renewable and Sustainable Energy Reviews*, 64:1–18, 2016.

[35] I. E. Commission. Wind turbines – part 3: Design requirements for offshore wind turbines. Standard, International Electrotechnical Commission (IEC), 2009.

[36] J. Cox, C. O'Loughlin, M. Cassidy, S. Bhattacharya, C. Gaudin, and B. Bienen. Centrifuge study on the cyclic performance of caissons in sand. *International Journal of Physical Modelling in Geotechnics*, 14(4):99–115, 2014.

[37] M. Cudny and A. Truty. Refinement of the hardening soil model within the small strain range. *Acta Geotechnica*, 15:2031–2051, 2020.

[38] Y. Dafalias. An anisotropic critical state soil plasticity model. *Mechanical Research Communications*, 13(6):341–347, 1986.

[39] Y. Dafalias and M. Manzari. Simple plasticity sand model accounting for fabric change effects. *Journal of Engineering Mechanics*, 130(6):662–634, 2004.

[40] Y. Dafalias, M. Manzari, and A. Papadimitriou. SANICLAY: simple anisotropic clay plasticity model. *International Journal for Numerical and Analytical Methods in Geomechanics*, 30(12):1231–1257, 2006.

[41] Y. Dafalias and M. Taiebat. SANISAND-Z: zero elastic range sand plasticity model. *Géotechnique*, 66(12):999–1013, 2016.

[42] K. Darby, G. Hernandez, J. DeJong, and R. Boulanger. Centrifuge model testing of liquefaction mitigation via microbially induced calcite precipitation. *Journal of Geotechnical and Geoenvironmental Engineering*, 145(10), 2019.

[43] T. Doanh, P. Dubujet, and G. Touron. Exploring the undrained induced anisotropy of Hostun rf loose sand. *Acta Geotechnica*, 5(4):239–256, 2010.

[44] T. Doanh, Z. Finge, and S. Boucq. Effects of previous deviatoric strain histories on the undrained behaviour of hostun rf loose sand. *Geotechnical and Geological Engineering*, 30(4):697–712, 2012.

[45] T. Doanh, Z. Finge, S. Boucq, and P. Dubujet. Histotropy of Hostun RF loose sand. In *Modern Trends in Geomechanics*, pages 399–411, 2006.

[46] T. Doanh, E. Ibraim, and R. Matiotti. Undrained instability of very loose Hostun sand in triaxial compression and extension. part 1: experimental observations. *Mechanics of Cohesive-frictional Materials*, 2(1):47–70, 1997.

[47] M. Dolores, J. Javier, J. López, and V. Negro. Why offshore wind energy? *Renewable Energy*, 36(2):444–450, 2011.

[48] P. Dubujet and T. Doanh. Undrained instability of very loose Hostun sand in triaxial compression and extension. part 2: theoretical analysis using an elastoplasticity model. *Mechanics of Cohesive-frictional Materials*, 2(1):71–92, 1997.

[49] J. Duque. Experimentación y modelación constitutiva de arcillas anisotrópicas y su aplicación en monopiles. Master Thesis. University del Norte, 2018.

[50] J. Duque, D. Mašín, and W. Fuentes. Improvement to the intergranular strain model for larger numbers of repetitive cycles. *Acta Geotechnica*, 15:3593–3604, 2020.

[51] J. Duque, D. Mašín, and W. Fuentes. Hypoplastic model for clays with stiffness anisotropy. In *Proceedings of IACMAG 2021: Challenges and Innovations in Geomechanics*, pages 414–421, Turin, Italy, 2021.

[52] J. Duque, M. Ochmański, D. Mašín, Y. Hong, and L. Wang. On the behavior of monopiles subjected to multiple episodes of cyclic loading and reconsolidation in cohesive soils. *Computers and Geotechnics*, 134, 2021.

[53] EIA. Annual energy outlook 2020. Technical report, U.S. Energy Information Administration, 2020.

[54] A. Elgamal, Z. Yang, and E. Parra. Computational modeling of cyclic mobility and post-liquefaction site response. *Soil Dynamics and Earthquake Engineering*, 22(4):259–271, 2002.

[55] A. Elgamal, Z. Yang, E. Parra, and A. Ragheb. Modeling of cyclic mobility in saturated cohesionless soils. *International Journal of Plasticity*, 19(6):883–905, 2003.

[56] M. Esteban, J. Diez, M. López, and V. Negro. Integral management applied to offshore wind farms. *Journal of Coastal Research*, 56:1204–1208, 2009.

[57] EWEA. Offshore wind in europe. key trends and statistics 2017-2019. Technical report, WindEurope, Brussels, Belgium, 2019.

[58] P. Fardad, D. Huang, G. Wang, and F. Jin. Effects of strain history and induced anisotropy on reliquefaction resistance of toyoura sand. *Journal of Geotechnical and Geoenvironmental Engineering*, 147(9):04021094, 2021.

[59] J. Feda. *Základy mechaniky partikulárních látek*. Československá akademie věd, Prague, 1977.

[60] J. Feda. *Mechanics of Particulate Materials, the principles*. Elsevier Science, Prague, 1982.

[61] J. Feda. Stress-path dependent shear strength of sand. *Journal of Geotechnical Engineering*, 120(6):958–974, 1994.

[62] J. Feda. Notes on the effect of grain crushing on the granular soil behaviour. *Engineering Geology*, 63(1-2):93–98, 2002.

[63] Z. Finge, T. Doanh, and P. Dubujet. Undrained anisotropy of hostun rf loose sand: new experimental investigations. *Canadian Geotechnical Journal*, 43(11):1195–1212, 2006.

[64] L. Finn, P. Bransby, and D. Pickering. Effect of strain history on liquefaction of sand. *Journal of the Soil Mechanics and Foundations Division*, 96(6):1917–1934, 1970.

[65] R. Finno and C. Chung. Stress-strain-strength responses of compressible chicago glacial clays. *Journal of Geotechnical Engineering*, 118(10):1607–1625, 1992.

[66] A. Foglia and L. Ibsen. Monopod bucket foundations under cyclic lateral loading. Technical report, DCE Technical Memorandum, 2014.

[67] D. Frick and M. Achmus. An experimental study on the parameters affecting the cyclic lateral response of monopiles for offshore wind turbines in sand. *Soils and Foundations*, 60(6):1570–1587, 2020.

[68] W. Fuentes. *Contributions in mechanical modelling of fill materials.* PhD thesis, Karlsruhe Institute of Technology, Germany, 2014.

[69] W. Fuentes, J. Duque, and C. Lascarro. Constitutive simulation of a kaolin clay with vertical and horizontal sedimentation axes. *DYNA*, 85(207):227–235, 2018.

[70] W. Fuentes, M. Gil, and J. Duque. Dynamic simulation of the sudden settlement of a mine waste dump under earthquake loading. *International Journal of Mining, Reclamation and Environment*, 33(6):425–443, 2019.

[71] W. Fuentes, D. Mašín, and J. Duque. Constitutive model for monotonic and cyclic loading on anisotropic clays. *Géotechnique*, 71(8):657–673, 2021.

[72] W. Fuentes, M. Tafili, and T. Triantafyllidis. Constitutive model for clays under the ISA framework. In *Holistic Simulation of Geotechnical Installation Processes, Benchmarks and Simulations*, chapter 6, pages 115–129. Springer, 2017.

[73] W. Fuentes, M. Tafili, and T. Triantafyllidis. An ISA-plasticity-based model for viscous and non-viscous clays. *Acta Geotechnica*, 13(3):367–386, 2018.

[74] W. Fuentes and T. Triantafyllidis. ISA model: A constitutive model for soils with yield surface in the intergranular strain space. *International Journal for Numerical and Analytical Methods in Geomechanics*, 39(11):1235–1254, 2015.

[75] W. Fuentes, T. Triantafyllidis, and C. Lascarro. Evaluating the performance of an ISA-hypoplasticity constitutive model on problems with repetitive loading. In *Holistic Simulation of Geotechnical Installation Processes, Theoretical Results and Applications*, chapter 16, pages 341–362. Springer, 2017.

[76] W. Fuentes, T. Wichtmann, M. Gil, and C. Lascarro. ISA-Hypoplasticity accounting for cyclic mobility effects for liquefaction analysis. *Acta Geotechnica*, 15:1513–1531, 2020.

[77] A. Gajo and L. Piffer. The effects of preloading history on the undrained behaviour of saturated loose sand. *Soils and Foundations*, 39(6):43–53, 1999.

[78] Y. Gao, Y. Qiu, B. Li, D. Li, C. Sha, and X. Zheng. Experimental studies on the anti-uplift behavior of the suction caissons in sand. *Applied Ocean Research*, 43:37–45, 2013.

[79] I. Gazibaric. Untersuchungen zum einfluss des salzgehaltes während der sedimentation auf das materialverhalten von kaolinton unter monotoner und zyklischer belastung. Master Thesis. Karlsruhe Institute of Technology, 2017.

[80] V. Ghionna and D. Porcino. Liquefaction resistance of undisturbed and reconstituted samples of a natural coarse sand from undrained cyclic triaxial tests. *Journal of Geotechnical and Geoenvironmental Engineering*, 132(2):194–202, 2006.

[81] M. Ghoraiby, H. Park, and M. Manzari. Physical and mechanical properties of ottawa f65 sand. In *Model Tests and Numerical Simulations of Liquefaction and Lateral Spreading. LEAP-UCD-2017*, pages 45–67, 2020.

[82] A. Gotschol and H. Kempfert. Zyklisch viskoelastisch-viskoplastischer stoffansatz nichtbindiger boden und schotter. *Bautechnik*, 81(4):279–285, 2004.

[83] P. Grabe and C. Clayton. Effects of principal stress rotation on permanent deformation in rail track foundations. *Journal of Geotechnical and Geoenvironmental Engineering*, 135(4):555–565, 2009.

[84] J. Graham and G. Houlsby. Anisotropic elasticity of a natural clay. *Géotechnique*, 33(2):165–180, 1983.

[85] C. Gu, J. Wang, Y. Cai, Z. Yang, and Y. Gao. Undrained cyclic triaxial behavior of saturated clays under variable confining pressure. *Soil Dynamics and Earthquake Engineering*, 40:118–128, 2012.

[86] G. Gudehus. Attractors for granular storage and flow. In *Third European Symposium – Storage and Flow of Particulate Solids*, page 333–345, Nürnberg, Germany, 1995.

[87] G. Gudehus. Psammodynamics: attractors and energetic. In *Proceedings of 9th HSTM International Conference on Mechanics*, 2010.

[88] G. Gudehus. *Physical Soil Mechanics*. Springer, Berlin, 2011.

[89] G. Gudehus, A. Amorosi, A. Gens, I. Herle, D. Kolymbas, D. Mašín, D. Wood, A. Niemunis, R. Nova, M. Pastor, C. Tamagnini, and G. Viggiani. The soilmodels.info project. *International Journal for Numerical and Analytical Methods in Geomechanics*, 32(12):1571–1572, 2008.

[90] I. Herle and G. Gudehus. Determination of parameters of a hypoplastic constitutive model from properties of grain assemblies. *Mechanics of Cohesive-Frictional Materials*, 4(5):461–486, 1999.

[91] I. Herle and D. Kolymbas. Hypoplasticity for soils with low friction angles. *Computers and Geotechnics*, 31(5):365–373, 2004.

[92] A. Hettler. *Verschiebungen starrer und elastische Gründungskörper in Sand bei monotoner und zyklischer Belastung*. PhD thesis, Karlsruhe Institute of Technology, 1981.

[93] J. Hleibieh, D. Wegener, and I. Herle. Numerical simulation of a tunnel surrounded by sand under earthquake using a hypoplastic model. *Acta Geotechnica*, 9(4):631–640, 2014.

[94] Y. Hong, B. He, L. Wang, Z. Wang, W. Ng, and D. Mašín. Cyclic lateral response and failure mechanisms of semi-rigid pile in soft clay: centrifuge tests and numerical modelling. *Canadian Geotechnical Journal*, 54(6):806–824, 2017.

[95] Y. Hong, M. Soomro, and C. Ng. Settlement and load transfer mechanism of pile group due to side-by-side twin tunnelling. *Computers and Geotechnics*, 64:105–119, 2015.

[96] Y. Hong, L. Wang, C. Ng, and B. Yang. Effect of initial pore pressure on undrained shear behaviour of fine-grained gassy soil. *Canadian Geotechnical Journal*, 54(11):1592–1600, 2017.

[97] G. Houlsby. Interactions in offshore foundation design. *Géotechnique*, 66(10):791–825, 2016.

[98] G. Houlsby and B. Byrne. Suction caisson foundations for offshore wind turbines and anemometer masts. *Wind Engineering*, 24(4):249–255, 2000.

[99] G. Houlsby, L. Ibsen, and B. Byrne. Suction caissons for wind turbines. In *Frontiers in Offshore Geotechnics: IS-FOG 2005*, pages 75–93, London, UK, 2005.

[100] G. Houlsby, R. Kelly, and B. Byrne. The tensile capacity of suction caissons in sand under rapid loading. In *Frontiers in Offshore Geotechnics: IS-FOG 2005*, pages 405–410, London, UK, 2005.

[101] G. Houlsby, R. Kelly, J. Huxtable, and B. Byrne. Field trials of suction caissons in sand for offshore wind turbine foundations. *Géotechnique*, 56(1):3–10, 2006.

[102] M. Hussain and A. Sachan. Post-liquefaction reconsolidation and undrained cyclic behaviour of chang dam soil. In *Proceedings of IACMAG 2019: Advances in Computer Methods and Geomechanics*, pages 77–90, 2019.

[103] A. Hyde, T. Higuchi, and K. Yasuhara. Postcyclic recompression, stiffness, and consolidated cyclic strength of silt. *Journal of Geotechnical and Geoenvironmental Engineering*, 133(4):416–423, 2007.

[104] M. Hyodo, A. Hyde, and N. Aramaki. Liquefaction of crushable soils. *Géotechnique*, 48(4):527–543, 1998.

[105] M. Hyodo, A. Hyde, Y. Yamamoto, and T. Fujii. Cyclic shear strength of undisturbed and remoulded marine clays. *Soils and foundations*, 39(2):45–58, 1999.

[106] M. Hyodo, H. Tanimizu, N. Yasufuku, and H. Murata. Undrained cyclic and monotonic triaxial behaviour of saturated loose sand. *Soils and foundations*, 34(1):19–32, 1994.

[107] M. Hyodo, Y. Yamamoto, and M. Sugiyama. Undrained cyclic shear behaviour of normally consolidated clay subjected to initial static shear stress. *Soils and foundations*, 34(4):1–11, 1994.

[108] S. Iai, T. Tobita, O. Ozutsumi, and K. Ueda. Dilatancy of granular materials in a strain space multiple mechanism model. *International Journal for Numerical and Analytical Methods in Geomechanics*, 35(3):360–392, 2011.

[109] I. Idriss and R. Boulanger. *Soil liquefaction during earthquakes*. Earthquake Engineering Research Institute, Oakland, CA, 2008. Monograph MNO-12, 261 pp.

[110] T. Ilyas, C. Leung, Y. Chow, and S. Budi. Centrifuge model study of laterally loaded pile groups in clay. *Journal of Geotechnical and Geoenvironmental Engineering*, 130(3):274–283, 2004.

[111] A. Inam, T. Ishikawa, and S. Miura. Effect of principal stress axis rotation on cyclic plastic deformation characteristics of unsaturated base course material. *Soils and Foundations*, 52(3):465–480, 2012.

[112] K. Ishihara. Liquefaction and flow failure during earthquakes. *Géotechnique*, 43(3):351–415, 1993.

[113] K. Ishihara. *Soil behaviour in earthquake geotechnics*. Oxford University Press, New York, 1996.

[114] K. Ishihara and S. Okada. Effects of stress history on cyclic behavior of sand. *Soils and foundations*, 18(4):31–45, 1978.

[115] K. Ishihara and S. Okada. Effects of large preshearing on cyclic behavior of sand. *Soils and foundations*, 22(3):109–125, 1982.

[116] K. Ishihara and F. Yamazaki. Cyclic simple shear tests on saturated sand in multidirectional loading. *Soils and Foundations*, 20(1):45–59, 1980.

[117] J. Jaky. The coefficient of earth pressure at rest (in hungarian). *Journal of the society of Hungarian Architects and Engineering*, 78(22):355–358, 1944.

[118] J. Jerman and D. Mašín. Hypoplastic and viscohypoplastic models for soft clays with strength anisotropy. *International Journal for Numerical and Analytical Methods in Geomechanics*, 44(10):1396–1416, 2020.

[119] W. Kaggwa, J. Booker, and J. Carter. Residual strains in calcareous sand due to irregular cyclic loading. *Journal of Geotechnical Engineering*, 117(2):201–218, 1991.

[120] S. Kalving, E. Manger, B. Hjertager, and J. Jakobsen. Wave influenced wind and the effect on offshore wind turbine performance. *Energy Procedia*, 53:202–213, 2014.

[121] M. Kan and H. Taiebat. On implementation of bounding surface plasticity models with no overshooting effect in solving boundary value problems. *Computers and geotechnics*, 55:103–116, 2014.

[122] R. Kelly, G. Houlsby, and B. Byrne. Transient vertical loading of model suction caissons in a pressure chamber. *Géotechnique*, 56(10):665–675, 2006.

[123] D. Kim, Y. Choo, J. Kim, S. Kim, and D. Kim. Investigation of monotonic and cyclic behavior of tripod suction bucket foundations for offshore wind towers using centrifuge modeling. *Journal of Geotechnical and Geoenvironmental Engineering*, 140(5):04014008, 2014.

[124] S. Kumar, A. Krishna, and A. Dey. Assessment of dynamic response of cohesionless soil using strain-controlled and stress-controlled cyclic triaxial tests. *Geotechnical and Geological Engineering*, 38:1431–1450, 2020.

[125] P. Lade. *The stress-strain and strength characteristics of cohesionless soils*. PhD thesis, University of California, Berkeley, 1972.

[126] Y. Lai, L. Wang, Y. Hong, and B. He. Centrifuge modeling of the cyclic lateral behavior of large-diameter monopiles in soft clay: Effects of episodic cycling and reconsolidation. *Ocean Engineering*, 200:1–17, 2020.

[127] J. Lambrechts and G. Leonards. Effects of stress history on deformation of sand. *Journal of the Geotechnical Engineering Division*, 104(11):1371–1387, 1978.

[128] G. Lanzano, C. Visone, E. Bilotta, and F. de Magistris. Experimental assessment of the stress–strain behaviour of leighton buzzard sand for the calibration of a constitutive model. *Geotechnical and Geological Engineering*, 34(4):991–1012, 2016.

[129] C. Leblanc, B. Byrne, and G. Houlsby. Response of stiff piles to random two-way lateral loading. *Géotechnique*, 60(9):715–721, 2010.

[130] K. Lee and A. Albaisa. Earthquake induced settlements in saturated sands. *Journal of the Geotechnical Engineering Division*, 100(4):387–406, 1974.

[131] L. Li, H. Dan, and L. Wang. Undrained behavior of natural marine clay under cyclic loading. *Ocean Engineering*, 38(16):1792–1805, 2011.

[132] W. Li, D. Igoe, and K. Gavin. Field tests to investigate the cyclic response of monopiles in sand. In *Proceedings of the Institution of Civil Engineers - Geotechnical Engineering*, pages 407–421, 2015.

[133] X. Li and Y. Dafalias. Anisotropic critical state theory: role of fabric. *Journal of engineering mechanics*, 138(3):263–275, 2012.

[134] D. Liao and Z. Yang. Hypoplastic modeling of anisotropic sand behavior accounting for fabric evolution under monotonic and cyclic loading. *Acta Geotechnica*, 16(7):2003–2029, 2021.

[135] S. Lin and J. Liao. Permanent strains of piles in sand due to cyclic lateral loads. *Journal of Geotechnical and Geoenvironmental Engineering*, 125(9):798–802, 1999.

[136] I. Littleton. An experimental study of the adhesion between clay and steel. *Journal of Terramechanics*, 13(3):141–152, 1976.

[137] H. Liu, J. Abell, A. Diambra, and F. Pisanò. Modelling the cyclic ratcheting of sands through memory-enhanced bounding surface plasticity. *Géotechnique*, 69(9):783–800, 2019.

[138] H. Liu, E. Kementzetzidis, J. Abell, and F. Pisanò. From cyclic sand ratcheting to tilt accumulation of offshore monopiles: 3d FE modelling using SANISAND-MS. *Géotechnique*, pages 1–16, 2021.

[139] S. López and M. Coop. Drained cyclic behaviour of loose dogs bay sand. *Géotechnique*, 62(4):281–289, 2012.

[140] M. Manzari and Y. Dafalias. A critical state two-surface plasticity model for sands. *Géotechnique*, 47(2):255–272, 1997.

[141] W. Marr and J. Christian. Permanent displacements due to cyclic wave loading. *Journal of the Geotechnical Engineering*, 107(8):1129–1149, 1981.

[142] S. Marshall and T. Park. Liquefaction potential evaluated from cyclic strain-controlled properties tests on sands. *Soils and foundations*, 16(3):51–65, 1976.

[143] H. Matlock. Correlations for design of laterally loaded piles in clay. In *Offshore Technology Conference, Houston, Paper OTC1204*, pages 577–588, 1970.

[144] H. Matsuda, A. Hendrawan, R. Ishikura, and S. Kawahara. Effective stress change and post-earthquake settlement properties of granular materials subjected to multi-directional cyclic simple shear. *Soils and Foundations*, 51(5):873–884, 2011.

[145] P. Mayne and F. Kulhawy. K0-OCR relationships in soil. *Journal of the Geotechnical Engineering Division*, 108(6):851–872, 1982.

[146] D. Mašín. A hypoplastic constitutive model for clays. *International Journal for Numerical and Analytical Methods in Geomechanics*, 29(4):311–336, 2005.

[147] D. Mašín. *Hypoplastic models for fine-grained soils*. PhD thesis, Charles University, Prague, 2006.

[148] D. Mašín. Incorporation of meta-stable structure into hypoplasticity. In *Proceedings of the International Conference on Numerical Modelling of Construction Processes in Geotechnical Engineering for Urban Environment*, pages 283–290, Bochum, Germany, 2006.

[149] D. Mašín. 3D modeling of an natm tunnel in high k0 clay using two different constitutive models. *Journal of Geotechnical and Geoenvironmental Engineering*, 135(9):1326–1335, 2009.

[150] D. Mašín. Clay hypoplasticity with explicitly defined asymptotic states. *Acta Geotechnica*, 8(5):481–496, 2013.

[151] D. Mašín. Clay hypoplasticity model including stiffness anisotropy. *Géotechnique*, 64(3):232–238, 2014.

[152] D. Mašín. *Triax user's manual, https://soilmodels.com/triax*. Charles University, Czech Republic, 2018.

[153] D. Mašín. *Modelling of Soil Behaviour with Hypoplasticity: Another Approach to Soil Constitutive Modelling*. Springer, Switzerland, 2019.

[154] D. Mašín and J. Rott. Small strain stiffness anisotropy of natural sedimentary clays: review and a model. *Acta Geotechnica*, 9(2):299–312, 2014.

[155] M. Miner. Cumulative damage fatigue. *Journal of Applied Mechanics*, 12:159–164, 1945.

[156] R. Mohamad and R. Dobry. Undrained monotonic and cyclic triaxial strength of sand. *Journal of Geotechnical Engineering*, 112(10):941–958, 1986.

[157] C. Monismith, N. Ogawa, and C. Freeme. Permanent deformation characteristics of subgrade soils due to repeated laoding. *Transportation Research Record*, 537:1–17, 1975.

[158] R. Nazir, M. Hussain, and A. Sachan. Influence of stress history, strain rate and end effects on undrained shear behaviour and strain localization of laterite soil. *International Journal of Geotechnical Engineering*, 14(8):888–901, 2020.

[159] V. Negro, J. López, M. Dolores, P. Alberdi, M. Imaz, and M. Serraclara. Monopiles in offshore wind: Preliminary estimate of main dimensions. *Ocean Engineering*, 133:253–261, 2017.

[160] V. Negro, J. López, M. Dolores, and C. Matutano. Uncertainties in the design of support structures and foundations for offshore wind turbines. *Renewable Energy*, 63:125–132, 2014.

[161] C. Ng, T. Boonyarak, and D. Mašín. Three-dimensional centrifuge and numerical modeling of the interaction between perpendicularly crossing tunnels. *Canadian Geotechnical Journal*, 50(9):935–946, 2013.

[162] C. Ng, Q. Ma, and A. Gunawan. Horizontal stress change of energy piles subjected to thermal cycles in sand. *Computers and Geotechnics*, 78:54–61, 2016.

[163] W. Ng, H. Sun, G. Lei, J. Shi, and D. Mašín. Ability of three different soil constitutive models to predict a tunnel's response to basement excavation. *Canadian Geotechnical Journal*, 52(11):1685–1698, 2015.

[164] J. Ni, B. Indraratna, X. Geng, and J. Phillip. Model of soft soils under cyclic loading. *International Journal of Geomechanics*, 15(4):04014067, 2015.

[165] A. Niemunis. Beiträge zum workshop: Boden unter fast zyklischer belastung: Erfahrungen und forschungsergebnisse, veröffentlichungen des institutes für grundbau und bodenmechanik, Ruhr-universität bochum, heft 32, 2000.

[166] A. Niemunis. *Extended Hypoplastic Models for Soils*. Habilitation, Institute for Foundation Engineering and Soil Mechanics, Ruhr-University Bochum, Germany, 2003.

[167] A. Niemunis. *Incremental Driver, user's manual, https://soilmodels.com/idriver*. University of Karlsruhe KIT, Germany, 2008.

[168] A. Niemunis and M. Cudny. Poor performance of the HSS model: Discussion on "dynamic soil-structure interaction: A three-dimensional numerical approach and its application to the lotung case study." Computers and Geotechnics, 2018.

[169] A. Niemunis, C. Grandas, and L. Prada. Anisotropic visco-hypoplasticity. *Acta Geotechnica*, 4(4):293–314, 2009.

[170] A. Niemunis and I. Herle. Hypoplastic model for cohesionless soils with elastic strain range. *Mechanic of cohesive-frictional materials*, 2(4):279–299, 1997.

[171] A. Niemunis, T. Wichtmann, and T. Triantafyllidis. A high-cycle accumulation model for sand. *Computers and Geotechnics*, 32(4):245–263, 2005.

[172] M. Ochmański, D. Mašín, J. Duque, Y. Hong, and L. Wang. Performance of tripod suction bucket foundations for offshore wind turbines: a numerical study. *Géotechnique letters*, 11(3):1–24, 2021.

[173] M. Ochmański, G. Modoni, and J. Bzówka. Automated numerical modelling for the control of epb technology. *Tunnelling and Underground Space Technology*, 75:117–128, 2018.

[174] M. Oda, K. Kawamoto, K. Suzuki, H. Fujimori, and M. Sato. Microstructural interpretation on reliquefaction of saturated granular soils under cyclic loading. *Journal of Geotechnical and Geoenvironmental Engineering*, 127(5):416–423, 2001.

[175] Y. Pan, K.and Cai, Z. Yang, and X. Pan. Liquefaction of sand under monotonic and cyclic shear conditions: Impact of drained preloading history. *Soil Dynamics and Earthquake Engineering*, 126:105775, 2019.

[176] A. Papadimitriou and G. Bouckovalas. Plasticity model for sand under small and large cyclic strains: a multiaxial formulation. *Soil Dynamics and Earthquake Engineering*, 22(3):191–204, 2002.

[177] A. Parra. *Ottawa F-65 sand characterization*. PhD thesis, University of California, Davis, 2016.

[178] R. Parry. Triaxial compression and extension tests on remoulded saturated clay. *Géotechnique*, 10(4):166–180, 1960.

[179] H. Patiño, A. Soriano, and J. González. Failure of a soft cohesive soil subjected to combined static and cyclic loading. *Soils and foundations*, 53(6):910–922, 2013.

[180] M. Poblete, W. Fuentes, and T. Triantafyllidis. On the simulation of multidimensional cyclic loading with intergranular strain. *Acta Geotechnica*, 11(6):1263–1285, 2016.

[181] D. Porcino and G. Caridi. Pre- and post-liquefaction response of sand in cyclic simple shear. In *Geo-Denver 2007: New Peaks in Geotechnics*, pages 1–10, 2007.

[182] D. Porcino, V. Marciano‘, and V. Ghionna. Influence of cyclic pre-shearing on undrained behaviour of carbonate sand in simple shear tests. *Geomechanics and Geoengineering*, 4(2):151–161, 2009.

[183] L. Prada. *Paraelastic description of small-strain behaviour*. PhD thesis, Karlsruhe Institute of Technology, Germany, 2011.

[184] T. Pradhan and F. Tatsuoka. On stress-dilatancy equations of sand subjected to cyclic loading. *Soils and foundations*, 29(1):65–81, 1989.

[185] T. Pradhan, F. Tatsuoka, Y. Mohri, and Y. Sato. An automated triaxial testing system using a simple triaxial cell for soils. *Soils and foundations*, 29(1):151–160, 1989.

[186] T. Pradhan, F. Tatsuoka, and Y. Sato. Experimental stress-dilatancy relations of sand subjected to cyclic loading. *Soils and foundations*, 29(1):45–64, 1989.

[187] J. Prevost. A simple plasticity theory for frictional cohesionless soils. *Soil Dynamics and Earthquake Engineering*, 4(1):9–17, 1985.

[188] T. Pucker and J. Grabe. Numerical simulation of the installation process of full displacement piles. *Computers and Geotechnics*, 45:93–106, 2012.

[189] R. Pyke, H. Seed, and C. Chan. Settlement of sands under multidirectional shaking. *Journal of the Geotechnical Engineering Division*, 101(4):379–398, 1975.

[190] C. Pérez and D. Iglesias. A review of combined wave and offshore wind energy. *Renewable and Sustainable Energy Reviews*, 42:141–153, 2015.

[191] G. Qiu and S. Henke. Controlled installation of spudcan foundations on loose sand overlying weak clay. *Marine Structures*, 24(4):528–550, 2011.

[192] R. Ragni, B. Bienen, D. Wang, D. Mašín, and M. Cassidy. Numerical modelling of the effects of consolidation on the undrained spudcan capacity under combined loading in silty clay. *Computers and Geotechnics*, 86:33–51, 2017.

[193] R. Ragni, D. Wang, D. Mašín, B. Bienen, M. Cassidy, and S. Stanier. Numerical modelling of the effects of consolidation on jack-up spudcan penetration. *Computers and Geotechnics*, 78:25–37, 2016.

[194] D. Rayamajhi. *Shear reinforcement effects of discrete columns in liquefiable soils.* PhD thesis, Oregon State University, 2014.

[195] I. Richards, B. Byrne, and G. Houlsby. Monopile rotation under complex cyclic lateral loading in sand. *Géotechnique*, 70(10):916–930, 2020.

[196] J. Rott, D. Mašín, J. Boháč, M. Krupička, and T. Mohyla. Evaluation of K0 in stiff clay by back-analysis of convergence measurements from unsupported cylindrical cavity. *Acta Geotechnica*, 10:719–733, 2015.

[197] A. Sawicki and W. Swidzinski. Mechanics of a sandy subsoil subjected to cyclic loadings. *International Journal For Numerical And Analytical Methods in Geomechanics*, 13(5):511–529, 1989.

[198] B. Schädlich and H. Schweiger. Influence of anisotropic small strain stiffness on the deformation behavior of geotechnical structures. *International Journal of Geomechanics*, 13(6):861–868, 2013.

[199] B. Seed, G. Martin, and R. Pyke. Effect of multidirectional shaking on pore pressure development in sands. *Journal of the Geotechnical Engineering Division*, 104(1):27–44, 1978.

[200] H. Seed, K. Mori, and C. Chan. Influence of seismic history on liquefaction of sands. *Journal of the Geotechnical Engineering Division*, 103(4):257–270, 1977.

[201] R. Seed, S. Lee, and H. Jong. Penetration and liquefaction resistances: Prior seismic history effects. *Journal of Geotechnical Engineering*, 114(6):691–697, 1988.

[202] G. Seidalinov. *Constitutive and Numerical Modeling of Clay Subjected to Cyclic Loading.* PhD thesis, The University of British Columbia, Vancouver, 2018.

[203] G. Seidalinov and M. Taiebat. Bounding surface SANICLAY plasticity model for cyclic clay behavior. *International Journal for Numerical and Analytical Methods in Geomechanics*, 38(7):702–724, 2014.

[204] M. Senders. *Suction Caissons in Sand as Tripod Foundations for Offshore Wind Turbines.* PhD thesis, University of Western Australia, Perth, Australia, 2008.

[205] S. Sharma and M. Ismail. Monotonic and cyclic behavior of two calcareous soils of different origins. *Journal of geotechnical and geoenvironmental engineering*, 132(12):1581–1591, 2006.

[206] T. Sheahan, C. Ladd, and J. Germaine. Rate dependent undrained shear behavior of saturated clay. *Journal of Geotechnical Engineering*, 122(2):99–108, 1996.

[207] T. Shibata, F. Oka, and Y. Ozawa. Characteristics of ground deformation due to liquefaction. *Soils and foundations*, 36(1):65–79, 1996.

[208] A. Shonberg, M. Harte, A. Aghakouchak, C. Brown, M. Andrade, and L. M. Suction bucket jackets for offshore wind turbines: applications from in situ observations. In *Proceedings of TC209 workshop: Foundation design of offshore wind structures*, pages 65–77. NGI, 2017.

[209] B. Simpson. Retaining structures: displacement and design, 32nd rankine lecture. *Géotechnique*, 42(4):541–576, 1992.

[210] V. Sivakumar, I. Doran, and J. Graham. Particle orientation and its influence on the mechanical behavior of isotropically consolidated reconstituted clay. *Engineering Geology*, 66(3):197–209, 2002.

[211] S. Sivathayalan. Static, cyclic and post liquefaction simple shear response of sands. Master Thesis. The University of British Columbia, 1994.

[212] S. Sivathayalan, P. Logeswaran, and V. Manmatharajan. Cyclic resistance of a loose sand subjected to rotation of principal stresses. *Journal of Geotechnical and Geoenvironmental Engineering*, 141(3), 2015.

[213] S. Sivathayalan and M. Yazdi. Influence of strain history on postliquefaction deformation characteristics of sands. *Journal of Geotechnical and Geoenvironmental Engineering*, 140(3):04013019, 2014.

[214] O. Solf, P. Kudella, and T. Triantafyllidis. Investigation of the self-healing effect of monopile foundations. In S. Springman, J. Laue, and L. Seward, editors, *Proceedings of International Conference on Physical Modelling in Geotechnic*. CRC Press/Balkema, 2010.

[215] S. Son, J. Yoon, and J. Kim. Simplified method for defining 2-dimensional design failure curve of marine silty sand under dynamic loading. *Journal of Marine Science and Engineering*, 8(1):1–15, 2020.

[216] S. Sriskandakumar. Cyclic loading response of fraser river sand for validation of numerical models simulating centrifuge tests. Master Thesis. The University of British Columbia, 2004.

[217] S. Sriskandakumar, D. Wijewickreme, and P. Byrne. Multiple cyclic loading response of loose air-pluviated fraser river sand. In *Proceedings of the 15th World Conference on Earthquake Engineering*, pages 1–10, Lisbon, Portugal, 2012.

[218] S. Stallebrass. *Modelling the effect of recent stress history on the deformation of overconsolidated soils*. PhD thesis, City, University of London, London, UK, 1990.

[219] S. Stallebrass and R. Taylor. The development and evaluation of a constitutive model for the prediction of ground movements in overconsolidated clay. *Géotechnique*, 47(2):235–253, 1997.

[220] P. Staubach, M. Machaček, M. Moscoso, and T. Wichtmann. Impact of the installation on the long-term cyclic behaviour of piles in sand: A numerical study. *Soil Dynamics and Earthquake Engineering*, 138:106223, 2020.

[221] P. Staubach and T. Wichtmann. Long-term deformations of monopile foundations for offshore wind turbines studied with a high-cycle accumulation model. *Computers and Geotechnics*, 124:1–15, 2020.

[222] H. Stewart. Permanent strains from cyclic variable-amplitude loadings. *Journal of Geotechnical Engineering*, 112(6):646–660, 1986.

[223] H. Sturm. Numerical investigation of the stabilisation behaviour of shallow foundations under alternate loading. *Acta Geotechnica*, 4(4):283–292, 2009.

[224] H. Sturm. Geotechnical performance of a novel gravity base type shallow foundation for offshore wind turbines. *Geotechnik*, 34(2):85–96, 2011.

[225] H. Sturm. Design aspects of suction caissons for offshore wind turbine foundations. In Y. Shin, editor, *Proceedings of TC209 workshop: Foundation design of offshore wind structures*, pages 45–63. NGI, 2017.

[226] H. Sturm, O. Solf, and P. Kudella. Self-healing effects of shallow foundations for offshore wind turbine structures. In Z. Młynarek, S. Z., and E. Dembicki, editors, *Proceedings of 11th Baltic Sea Geotechnical Conference on Geotechnics in Maritime Engineering*, pages 45–63. Polish Committee on Geotechnics, 2008.

[227] D. Su and X. Li. Impact of multidirectional shaking on liquefaction potential of level sand deposits. *Géotechnique*, 58(4):259–267, 2008.

[228] T. Suzuki and S. Toki. Effects of preshearing on liquefaction characteristics of saturated sand subjected to cyclic loading. *Soils and foundations*, 24(2):16–28, 1984.

[229] H. Sze and J. Yang. Failure modes of sand in undrained cyclic loading: impact of sample preparation. *Journal of geotechnical and geoenvironmental engineering*, 140(1):152–169, 2014.

[230] M. Tafili. *On the Behaviour of Cohesive Soils: Constitutive Description and Experimental Observations*. PhD thesis, Institute of Soil Mechanics and Rock Mechanics, Karlsruhe Institute of Technology, 2019.

[231] M. Tafili, W. Fuentes, and T. Triantafyllidis. A comparative study of different model families for the constitutive simulation of viscous clays. *International Journal for Numerical and Analytical Methods in Geomechanics*, 44(5):633–667, 2020.

[232] M. Tafili and T. Triantafyllidis. On constitutive modelling of anisotropic viscous and non-viscous soft soils. In *9th European Conference on Numerical Methods in Geotechnical Engineering*, pages 139–147, London, 2018.

[233] M. Tafili and T. Triantafyllidis. State-dependent dilatancy of soils: Experimental evidence and constitutive modeling. In T. Triantafyllidis, editor, *Recent Developments of Soil Mechanics and Geotechnics in Theory and Practice*, pages 54–84. Springer, 2019.

[234] M. Tafili and T. Triantafyllidis. AVISA: anisotropic visco-ISA model and its performance at cyclic loading. *Acta Geotechnica*, 15:2395–2413, 2020.

[235] M. Tafili and T. Triantafyllidis. Cyclic and monotonic response of silts and clays: experimental analysis and constitutive modelling. *European Journal of Environmental and Civil Engineering*, pages 1–10, 2020.

[236] M. Tafili and T. Triantafyllidis. A simple hypoplastic model with loading surface accounting for viscous and fabric effects of clays. *International Journal for Numerical and Analytical Methods in Geomechanics*, 44(2), 2020.

[237] M. Tafili, T. Wichtmann, and T. Triantafyllidis. Experimental investigation and constitutive modeling of the behaviour of highly plastic lower rhine clay under monotonic and cyclic loading. *Canadian Geotechnical Journal*, 58(9):1396–1410, 2021.

[238] M. Taiebat. *Advanced Elastic-Plastic Constitutive and Numerical Modeling in Geomechanics*. PhD thesis, University of California, Davis, 2008.

[239] M. Taiebat and Y. Dafalias. SANISAND: simple anisotropic sand plasticity model. *International Journal for Numerical and Analytical Methods in Geomechanics*, 32(8):915–948, 2008.

[240] M. Taiebat and Y. Dafalias. Simple yield surface expressions appropriate for soil plasticity. *International Journal of Geomechanics*, 10(4):161–169, 2010.

[241] M. Taiebat, B. Jeremić, Y. F. Dafalias, A. M. Kaynia, and Z. Cheng. Propagation of seismic waves through liquefied soils. *Soil Dynamics and Earthquake Engineering*, 30(4):236–257, 2010.

[242] F. Tatsuoka and K. Ishihara. Drained deformation of sand under cyclic stresses reversing direction. *Soils and foundations*, 14(3):51–65, 1974.

[243] Tochnog. Tochnog professional user's manual. http://tochnogprofessional.nl/, 2020. Accessed: 08-25-2020.

[244] S. Toki and S. Kitago. Effects of repeated loading on deformation behavior of dry sand. *Soils and foundations*, 14(1):95–103, 1974.

[245] N. Tran, L. Hung, and S. Kim. Evaluation of horizontal and moment bearing capacities of tripod bucket foundations in sand. *Ocean Engineering*, 140:209–221, 2017.

[246] K. Ueda, R. Vargas, and K. Uemura. Leap-asia-2018: stress-strain response of ottawa sand in cyclic torsional shear tests. *DesignSafe-CI*, 2018.

[247] Y. Vaid and J. Chern. Effect of static shear on resistance to liquefaction. *Soils and foundations*, 23(1):47–60, 1983.

[248] Y. Vaid, E. Chung, and R. Kuerbis. Preshearing and undrained response of sand. *Soils and Foundations*, 29(4):49–61, 1989.

[249] Y. Vaid and J. Thomas. Liquefaction and postliquefaction behavior of sand. *Journal of Geotechnical Engineering*, 121(2):163–173, 1995.

[250] K. Varun. A parametric study on the bounding surface SANICLAY model for cyclic behavior of kaolin clay. Master Thesis. Delft University of Technology, 2019.

[251] A. Vasko. An investigation into the behavior of ottawa sand through monotonic and cyclic shear tests. Master Thesis. George Washington University, 2015.

[252] M. Vaucetic and A. Mortezaie. Cyclic secant shear modulus versus pore water pressure in sands at small cyclic strains. *Soil Dynamics and Earthquake Engineering*, 70:60–72, 2015.

[253] R. Verdugo and K. Ishihara. The steady state of sandy soils. *Soils and foundations*, 36(2):81–91, 1996.

[254] K. Vinck, T. Liu, U. E., and R. Jardine. An appraisal of end conditions in advanced monotonic and cyclic triaxial testing on a range of geomaterials. 7th International Symposium on Deformation Characteristics of Geomaterials, 2019.

[255] G. Wang and Y. Xie. Modified bounding surface hypoplasticity model for sands under cyclic loading. *Journal of Geotechnical and Geoenvironmental Engineering*, 140(1):91–101, 2014.

[256] L. Wang, B. He, Y. Hong, Z. Guo, and L. Li. Field tests of the lateral monotonic and cyclic performance of jet-grouting reinforced cast-in-place piles. *Journal of Geotechnical and Geoenvironmental Engineering*, 141(5), 2015.

[257] L. Wang, H. Wang, B. Zhu, and Y. Hong. Comparison of monotonic and cyclic lateral response between monopod and tripod bucket foundations in medium dense sand. *Ocean Engineering*, 155:88–105, 2018.

[258] Z. Wang, Y. Dafalias, and C. Shen. Bounding surface hypoplasticity model for sand. *Journal of Engineering Mechanics*, 116(5):983–1001, 1990.

[259] WEC. World energy scenarios composing energy futures to 2050. Technical report, World Energy Council, 2013.

[260] D. Wegener and I. Herle. Prediction of permanent soil deformations due to cyclic shearing with a hypoplastic constitutive model. *Geotechnik*, 37(2):113–122, 2014.

[261] T. Weifner and D. Kolymbas. A hypoplastic model for clay and sand. *Acta Geotechnica*, 2(2):103–112, 2007.

[262] T. Wichtmann. *Explicit accumulation model for non-cohesive soils under cyclic loading*. PhD thesis, Ruhr-Universität Bochum, Germany, 2005.

[263] T. Wichtmann. Soil behaviour under cyclic loading: Experimental observations, constitutive description and applications. Habilitation, Karlsruhe Institute of Technology (KIT), 2016.

[264] T. Wichtmann, K. Andersen, M. Sjursen, and T. Berre. Cyclic tests on high-quality undisturbed block samples of soft marine norwegian clay. *Canadian Geotechnical Journal*, 50(4):400–412, 2013.

[265] T. Wichtmann, W. Fuentes, and T. Triantafyllidis. Inspection of three sophisticated constitutive models based on monotonic and cyclic tests on fine sand: Hypoplasticity vs. Sanisand vs. ISA. *Soil Dynamics and Earthquake Engineering*, 124:172–183, 2019.

[266] T. Wichtmann, I. Kimmig, and T. Triantafyllidis. On correlations between "dynamic"(small-strain) and "static"(large-strain) stiffness moduli–an experimental investigation on 19 sands and gravels. *Soil Dynamics and Earthquake Engineering*, 98:72–83, 2017.

[267] T. Wichtmann, A. Niemunis, and T. Triantafyllidis. Gilt die miner'sche regel für sand? *Bautechnik*, 83(5):341–350, 2007.

[268] T. Wichtmann, A. Niemunis, and T. Triantafyllidis. On the influence of the polarization and the shape of the strain loop on strain accumulation in sand under high-cyclic loading. *Soil Dynamics and Earthquake Engineering*, 27(1):14–28, 2007.

[269] T. Wichtmann, A. Niemunis, and T. Triantafyllidis. Prediction of long-term deformations for monopile foundations of offshore wind power plants. In Z. Młynarek, S. Z., and E. Dembicki, editors, *Proceedings of 11th Baltic Sea Geotechnical Conference on Geotechnics in Maritime Engineering*, pages 45–63. Polish Committee on Geotechnics, 2008.

[270] T. Wichtmann, A. Niemunis, and T. Triantafyllidis. Strain accumulation in sand due to drained cyclic loading: On the effect of monotonic and cyclic preloading (miner's rule). *Soil Dynamics and Earthquake Engineering*, 30(8):736–745, 2010.

[271] T. Wichtmann, A. Niemunis, T. Triantafyllidis, and M. Poblete. Correlation of cyclic preloading with the liquefaction resistance. *Soil Dynamics and Earthquake Engineering*, 25(12):923–932, 2005.

[272] T. Wichtmann, K. Steller, and T. Triantafyllidis. On the influence of the sample preparation method on strain accumulation in sand under high-cyclic loading. *Soil Dynamics and Earthquake Engineering*, 131:106028, 2020.

[273] T. Wichtmann and T. Triantafyllidis. An experimental data base for the development, calibration and verification of constitutive models for sand with focus to cyclic loading. part I: tests with monotonic loading and stress cycles. *Acta Geotechnica*, 11(4):739–761, 2016.

[274] T. Wichtmann and T. Triantafyllidis. An experimental data base for the development, calibration and verification of constitutive models for sand with focus to cyclic loading. part II: tests with strain cycles and combined loading. *Acta Geotechnica*, 11(4):763–774, 2016.

[275] T. Wichtmann and T. Triantafyllidis. Monotonic and cyclic tests on kaolin: a database for the development, calibration and verification of constitutive models for cohesive soils with focus to cyclic loading. *Acta Geotechnica*, 13(5):1103–1128, 2018.

[276] D. Wijewickreme, S. Sriskandakumar, and P. Byrne. Cyclic loading response of loose air-pluviated fraser river sand for validation of numerical models simulating centrifuge tests. *Canadian Geotechnical Journal*, 42(2):550–561, 2005.

[277] V. Wolffersdorff. A hypoplastic relation for granular materials with a predefined limit state surface. *Mechanics of cohesive-frictional materials*, 1(3):251–271, 1996.

[278] W. Wu and E. Bauer. A hypoplastic model for barotropy and pyknotropy of granular soils. In *Proceedings of International Workshop on Modern Approaches to Plasticity*, pages 225–245. Elsevier, 1993.

[279] W. Wu and E. Bauer. A simple hypoplastic constitutive model for sand. *International Journal for Numerical and Analytical Methods in Geomechanics*, 18(12):833–862, 1994.

[280] W. Wu, J. Lin, and X. Wang. A basic hypoplastic constitutive model for sand. *Acta Geotechnica*, 12:1373–1382, 2017.

[281] Y. Xie, C. Leung, and Y. Chow. Centrifuge modelling of spudcan–pile interaction in soft clay. *Géotechnique*, 62(9):799–810, 2012.

[282] S. Yamada, T. Takamori, and K. Sato. Effects on reliquefaction resistance produced by changes in anisotropy during liquefaction. *Soils and Foundations*, 50(1):9–25, 2010.

[283] Y. Yamada and K. Ishihara. Undrained deformation characteristics of sand in multidirectional shear. *Soils and foundations*, 23(1):61–79, 1983.

[284] J. Yang and H. Sze. Cyclic behaviour and resistance of saturated sand under non-symmetrical loading conditions. *Géotechnique*, 61(1):59–73, 2011.

[285] J. Yang and H. Sze. Cyclic strength of sand under sustained shear stress. *Journal of Geotechnical and Geoenvironmental Engineering*, 137(12):1275–1285, 2011.

[286] M. Yang, M. Taiebat, and Y. Dafalias. SANISAND-MSf: a memory surface and semifluidized state enhanced sand plasticity model for undrained cyclic shearing. *Accepted for publication in Géotechnique*, 2020.

[287] Z. Yang, A. Elgamal, and E. Parra. Computational model for cyclic mobility and associated shear deformation. *Journal of Geotechnical and Geoenvironmental Engineering*, 129(12):1119–1127, 2003.

[288] K. Yasuhara and K. Andersen. Effect of cyclic loading on recompresion of everconsolidate clay. In *Proceedings of the 12th International Conference on Soil Mechanics and Foundation Engineering*, pages 485–488, 1989.

[289] K. Yasuhara and K. Andersen. Recompression of normally consolidated clay after cyclic loading. *Soils and foundations*, 31(1):83–94, 1991.

[290] H. Yildirim and H. Erşan. Settlements under consecutive series of cyclic loading. *Soil Dynamics and Earthquake Engineering*, 27(6):577–585, 2007.

[291] M. Yoshimine, P. Robertson, and C. Wride. Undrained shear strength of clean sands to trigger flow liquefaction. *Canadian Geotechnical Journal*, 36(5):891–906, 1999.

[292] F. Zhang, B. Ye, T. Noda, M. Nakano, and K. Nakai. Explanation of cyclic mobility of soils: approach by stress-induced anisotropy. *Soils and foundations*, 47(4):635–648, 2007.

[293] J. Zhang and G. Wang. Large post-liquefaction deformation of sand, part I: physical mechanism, constitutive description and numerical algorithm. *Acta Geotechnica*, 7(2):69–113, 2012.

[294] B. Zhu, B. Byrne, and G. Houlsby. Long-term lateral cyclic response of suction caisson foundations in sand. *Journal of Geotechnical and Geoenvironmental Engineering*, 139(1):73–83, 2013.

[295] B. Zhu, K. Wen, D. Kong, Z. Zhu, and L. Wang. A numerical study on the lateral loading behaviour of offshore tetrapod piled jacket foundations in clay. *Applied Ocean Research*, 75:165–177, 2018.

[296] B. Zhu, W. Zhang, P. Ying, and Y. Chen. Deflection-based bearing capacity of suction caisson foundations of offshore wind turbines. *Journal of Geotechnical and Geoenvironmental Engineering*, 140(5):04014013, 2014.

[297] D. Zografou. *Investigation of shallow skirted foundations under undrained cyclic loading.* PhD thesis, University of Western Australia, 2018.